TECHNISCHE UNIVERSITÄT
BERGAKADEMIE FREIBERG
The University of Resources. Since 1765.

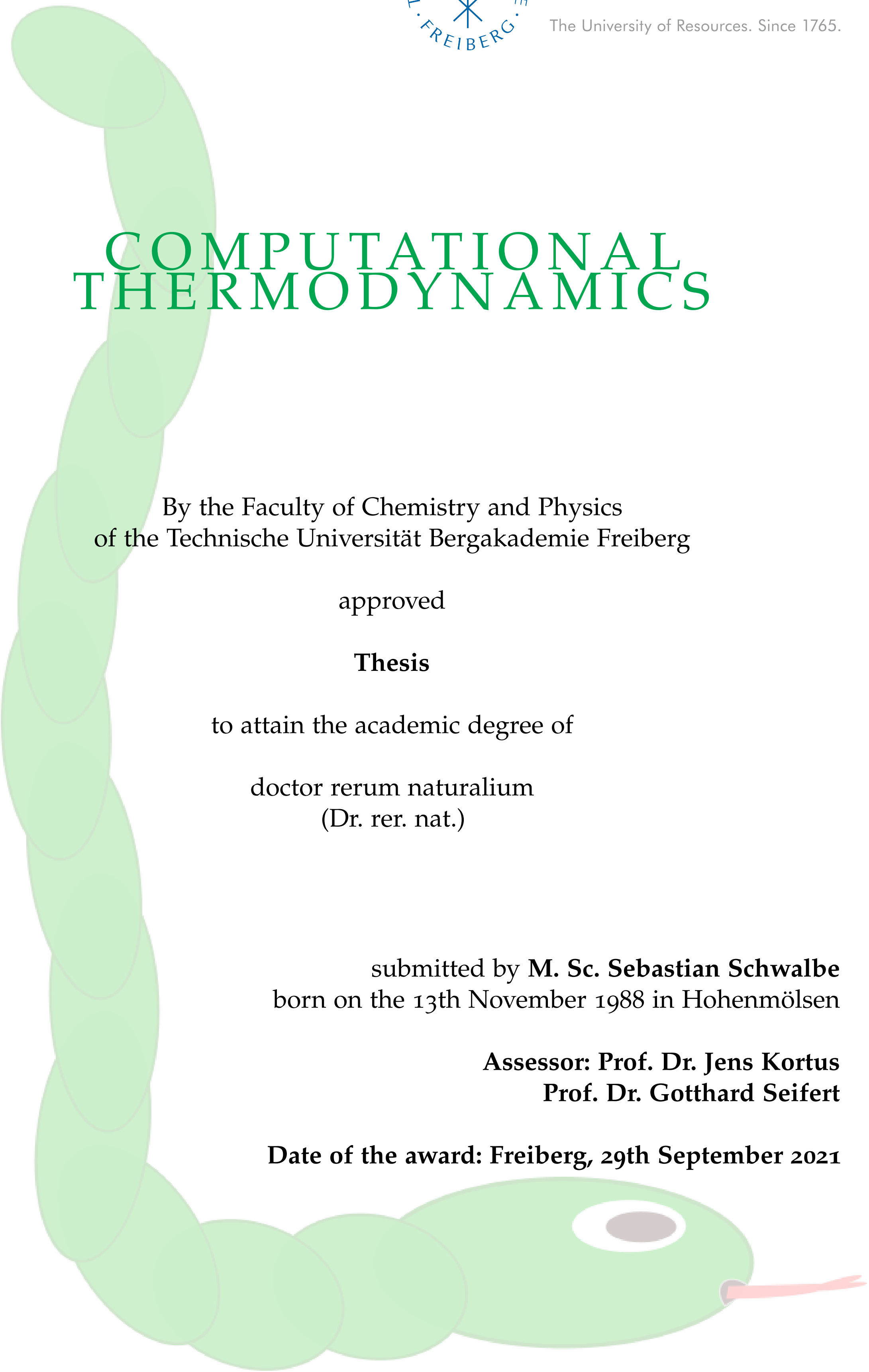

COMPUTATIONAL THERMODYNAMICS

By the Faculty of Chemistry and Physics
of the Technische Universität Bergakademie Freiberg

approved

Thesis

to attain the academic degree of

doctor rerum naturalium
(Dr. rer. nat.)

submitted by **M. Sc. Sebastian Schwalbe**
born on the 13th November 1988 in Hohenmölsen

Assessor: Prof. Dr. Jens Kortus
Prof. Dr. Gotthard Seifert

Date of the award: Freiberg, 29th September 2021

Computational Thermodynamics
submitted in fulfillment of the requirements for the degree of doctor rerum naturalium
(Dr. rer. nat.)

Institute of Theoretical Physics
TU Bergakademie Freiberg
09599 Freiberg
Germany

All I Want

Keep your hopes up high and your head down low.

—A Day to Remember, American music band

Dedicated in loving memory of my grand parents.

Annelies Schwalbe
⋆27.10.1936 – †30.05.2007

Gerhard Schwalbe
⋆25.11.1936 – †21.01.2015

Fred Winnemund
⋆03.09.1930 – †21.09.2017

And to all my family members, my friends, and my institute
for guiding me along the way.

KURZDARSTELLUNG

Diese Arbeit befasst sich mit theoretischen Konzepten der phänomenologischen und statistischen Thermodynamik und deren numerischer Umsetzung. Das Hauptziel dieser Arbeit ist es, Arbeitsabläufe für die akurate Beschreibung von thermodynamischen Eigenschaften von Molekülen und Festkörpern zur Verfügung zu stellen. Der während dieser Arbeit entwickelte C_p-*MD* Arbeitsablauf wird angewandt um binäre Batteriemateralien, wie Lithiumsilizide, zu charakterisieren. Dieser Arbeitsablauf ermöglicht eine numerisch effiziente Beschreibung von makroskopischen thermodynamischen Eigenschaften. Für Batteriematerialien und metallorganische Gerüstverbindungen wird gezeigt, dass einige makroskopische Eigenschaften hauptsächlich von mikroskopischen Eigenschaften kontrolliert sind. Diese mikroskopischen Eigenschaften können mittels zugehöriger Cluster oder Moleküle beschrieben werden. Aufgrund ihrer reduzierten Größe können diese Systeme mit genaueren und numerisch aufwendigeren Methoden berechnet werden. Standard Dichtefunktionaltheorie (DFT) und die Fermi-Löwdin-Orbital Selbstwechselwirkungskorrektur (FLO-SWK) werden für weitere Untersuchungen verwendet. Es wird gezeigt, dass die SWK einige Probleme der DFT überwinden kann. Anhand weiterer Arbeitsabläufe wird gezeigt, wie eine Kombination von verschiedenen numerischen Methoden thermodynamische Berechnungen beschleunigen kann und in der Lage ist das Verständnis der Triebkräfte von makroskopischen thermodynamischen Eigenschaften zu vertiefen.

ABSTRACT

This thesis is concerned with theoretical concepts of phenomenological and statistical thermodynamics and their computational realization. The main goal of this thesis is to provide efficient workflows for an accurate description of thermodynamic properties of molecules and solid state materials. The C_p-*MD* workflow developed within this thesis is applied to characterize binary battery materials, such as lithium silicides. This workflow enables a numerically efficient description of macroscopic thermodynamic properties. For battery materials and metal-organic frameworks, it is shown that some macroscopic properties are dominantly controlled by microscopic properties. These microscopic properties are well described by respective small clusters or molecules. Given their reduced size, these systems can be calculated using more accurate and numerically more demanding methods. Standard density functional theory (DFT) and the so called Fermi-Löwdin orbital self-interaction correction (FLO-SIC) method are used for further investigations. It will be shown that SIC is able to overcome some of the problems of DFT. Given further workflows, it is demonstrated how a combination of different computational methods can speed up thermodynamic calculations and is able to deepen the understanding of the driving forces of macroscopic thermodynamic properties.

PUBLICATIONS

This section lists all publications produced during this thesis. The publications are listed for the main chapters of the thesis.

Battery materials: Lithium silicides

- S. Schwalbe, T. Gruber, K. Trepte, F. Taubert, F. Mertens and J. Kortus
  Mechanical, elastic and thermodynamic properties of crystalline lithium silicides
  Computational Materials Science, 134, 48 - 57, 2017
- F. Taubert, S. Schwalbe, J. Seidel, R. Hüttl, T. Gruber, R. Janot, M. Bobnar, R. Gumeniuk, F. Mertens and J. Kortus
  Thermodynamic characterization of lithium monosilicide (LiSi) by means of calorimetry and DFT-calculations
  International Journal of Materials Research, 108, 942 - 958, 2017

Metal-organic frameworks

- K. Trepte, S. Schwalbe and G. Seifert
  Electronic and magnetic properties of DUT-8(Ni)
  Physical Chemistry Chemical Physics, 17, 17122 - 17129, 2015
- S. Schwalbe, K. Trepte, G. Seifert and J. Kortus
  Screening for high-spin metal organic frameworks (MOFs): density functional theory study on DUT-8(M_1,M_2) (with M_i = V,...,Cu)
  Physical Chemistry Chemical Physics, 18, 8075 - 8080, 2016
- K. Trepte, J. Schaber, S. Schwalbe, F. Drache, I. Senkovska, S. Kaskel, J. Kortus, E. Brunner and G. Seifert
  The origin of the measured chemical shift of ^{129}Xe in UiO-66 and UiO-67 revealed by DFT investigations
  Physical Chemistry Chemical Physics, 19, 10020 - 10027, 2017
- K. Trepte, S. Schwalbe, J. Schaber, S. Krause, I. Senkovska, S. Kaskel, E. Brunner, J. Kortus and Gotthard Seifert
  Theoretical and experimental investigations of ^{129}Xe NMR chemical shift isotherms in metal–organic frameworks
  Physical Chemistry Chemical Physics, 20, 25039 - 25043, 2018
- K. Trepte and S. Schwalbe
  kaitrepte/porE: porE v.1.0.3 release
  Zenodo, DOI: `http://doi.org/10.5281/zenodo.4075260`, 2020
- K. Trepte and S. Schwalbe
  porE: A code for deterministic and systematic analyses of porosities
  Journal of Computational Chemistry, 42, 630-643, 2021

- T. Hahn, S. Schwalbe, J. Kortus and M. R. Pederson
  Symmetry Breaking within Fermi-Löwdin Orbital Self-Interaction Corrected Density Functional Theory
  Journal of Chemical Theory and Computation, 13, 5823 - 5828, 2017

- S. Schwalbe, T. Hahn, S. Liebing, K. Trepte and J. Kortus
  Fermi-Löwdin orbital self-interaction corrected density functional theory: Ionization potentials and enthalpies of formation
  Journal of Computational Chemistry, 39, 2463 - 2471, 2018

- S. Schwalbe, K. Trepte, L. Fiedler, A. I. Johnson, J. Kraus,
  T. Hahn, J. E. Peralta, K. A. Jackson, J. Kortus
  Interpretation and Automatic Generation of Fermi-Orbital Descriptors
  Journal of Computational Chemistry, 40, 2843 - 2857, 2019

- K. Trepte, S. Schwalbe, T. Hahn, J. Kortus,
  D.-Y. Kao, Y. Yamamoto, T. Baruah, R. R. Zope,
  K. P. K. Withanage, J. E. Peralta and K. A. Jackson
  Analytic atomic gradients in the Fermi-Löwdin orbital self-interaction correction
  Journal of Computational Chemistry, 40, 820 - 825, 2019

- C. Shahi, P. Bhattarai, K. Wagle, B. Santra,
  S. Schwalbe, T. Hahn, J. Kortus,
  K. A. Jackson, J. E. Peralta, K. Trepte,
  S. Lehtola, N. K. Nepal, H. Myneni, B. Neupane,
  S. Adhikari, A. Ruzsinszky, Y. Yamamoto, T. Baruah, R. R. Zope,
  and J. P. Perdew
  Stretched or noded orbital densities and self-interaction correction in density functional theory
  The Journal of Chemical Physics, 150, 174102, 2019

- S. Schwalbe, L. Fiedler, J. Kraus, J. Kortus, K. Trepte and S. Lehtola
  pyflosic/pyflosic: PyFLOSIC v.1.0.1 release
  Zenodo, DOI: `http://doi.org/10.5281/zenodo.3948143`, 2020

- K. Trepte, S. Schwalbe, J. Kraus, S. Liebing and A. Johnson
  pyflosic/fodMC: fodMC release v.1.0.0
  Zenodo, DOI: `http://doi.org/10.5281/zenodo.3922473`, 2020

- S. Schwalbe, L. Fiedler, J. Kraus, J. Kortus, K. Trepte and S. Lehtola
  PyFLOSIC: Python-based Fermi-Löwdin orbital self-interaction correction
  The Journal of Chemical Physics, 153, 084104, 2020

In addition, papers are listed which are not directly connect to the thesis itself.

- S. Schwalbe, R. Wirnata, R. Starke, G. A. H. Schober and J. Kortus
  Ab initio electronic structure and optical conductivity of bismuth tellurohalides
  Physical Review B, 94, 205130, 2016
- K. Rühlig, A. Abylaikhan, A. Aliabadi, V. Kataev,
  S. Liebing, S. Schwalbe, K. Trepte, C. Ludt, J. Kortus,
  B. Büchner, T. Rüffer and H. Lang
  *Ni^{II} formate complexes with bi-and tridentate nitrogen-donor ligands:
  synthesis, characterization, and magnetic and thermal properties*
  Dalton Transactions, 46, 3963 - 3979, 2017

A more recent list of publications can be found at one of the following sources.

- ORCID
  `https://orcid.org/0000-0002-4561-0158`
- Google Scholar
  `https://scholar.google.com/citations?hl=en&user=PzLtaUgAAAAJ`
- ResearchGate
  `https://www.researchgate.net/profile/Sebastian_Schwalbe`

CONTENTS

LIST OF FIGURES

LIST OF TABLES

ACRONYMS

Methods and techniques

DFT	Density Functional Theory
SIC	Self-Interaction Correction
FLO	Fermi-Löwdin Orbital
FOD	Fermi-Orbital Descriptor
WFT	Wavefunction Theory
MD	Molecular Dynamics
MC	Monte Carlo
FF	Force Field
MEAM	Modified Embedded Atom Method
EFF	Electron Force Field
UFF	Universal Force Field
UFF4MOF	Universal Force Field For Metal-Organic Framework

Materials and structures

LIB	Lithium Ion Battery
$\mathrm{Li}_x\mathrm{Si}_y$	Lithium Silicides
MOF	Metal-Organic Frameworks
SBU	Secondary Building Unit
PUC	Primitive Unit Cell
CUC	Conventional Unit Cell

1

INTRODUCTION

Computational physics, chemistry and materials science aim to provide various kinds of information in different scientific fields. In the past, computational science was only recognized as a supplier of secondary information to verify experimental results. This point of view slowly changed, as quantum chemical calculations using wavefunction (WF) methods based on Hartree-Fock (HF) [1, 2] were able to show discrepancies between very accurate theoretical calculations and experimental findings [3]. This led to a re-investigation of the experiments, which in the end confirmed the theoretical results. Density functional theory (DFT) [4, 5] has become a widely used electronic structure method based on the compromise of suitable accuracy and low numerical effort [6, 7]. Several hundreds of atoms can be treated using numerous available implementations. For large scale simulations of thousands to millions of atoms, so called force fields (FF) [8–11] are commonly used.

In this thesis, calculations were performed to deliver additional information to complete the understanding of a specific system or even a class of materials. Often, systems containing a large number of atoms (> 100) are of general interest. Battery materials [12] and metal-organic frameworks (MOFs) [13] are material classes which fulfill the aforementioned criterion. Technological improvements such as smart phones, tablets, laptops and electrically powered cars need batteries which enable a suitable operation time of the specific device. Thus, battery materials are needed which can improve on the standard performance of lithium ion batteries (LIBs), e.g., higher specific energy, lower battery weight, higher energy density and with that an overall lower volume and cost of the battery. Anode materials need the capability to store lithium atoms. Another material class which has the capability not only to store lithium, but even other kinds of atoms, molecules or small clusters are MOFs. These frameworks are porous which allows to load them with the aforementioned systems. MOFs are of general interest based on various applications, such as gas absorbers [14], catalysts [15], optical sensors [16], and post-synthetic modification (PSM) of MOFs for modulating reaction outcomes and biomedical applications [17]. The class of amorphous MOFs (aMOFs) has possible applications as liquids or melt quenched glasses [18].

The relevance of the discussed computational methods (DFT, FF) and materials classes (LIBs, MOFs) can be shown by counting the literature occurrence of representative keywords using a database (such as google.scholar) within a given time span. DFT is represented by the key "density functional theory", FF is represented by the key "force field", LIBs are represented by the novel anode material "lithium silicides" and MOFs are represented by the key "metal organic frameworks". The occurrence of these keys within the year 1960 - 2018 is determined by using a modified Python tool [19] (see Fig. 1).

From this analysis it is obvious that DFT and FF are commonly used computational methods. Their respective high occurrence numbers might also indicate a huge scientific knowledge base, but state nothing about the quality of each entry within these databases. Intensive, but also critical literature reviews are needed before investiga-

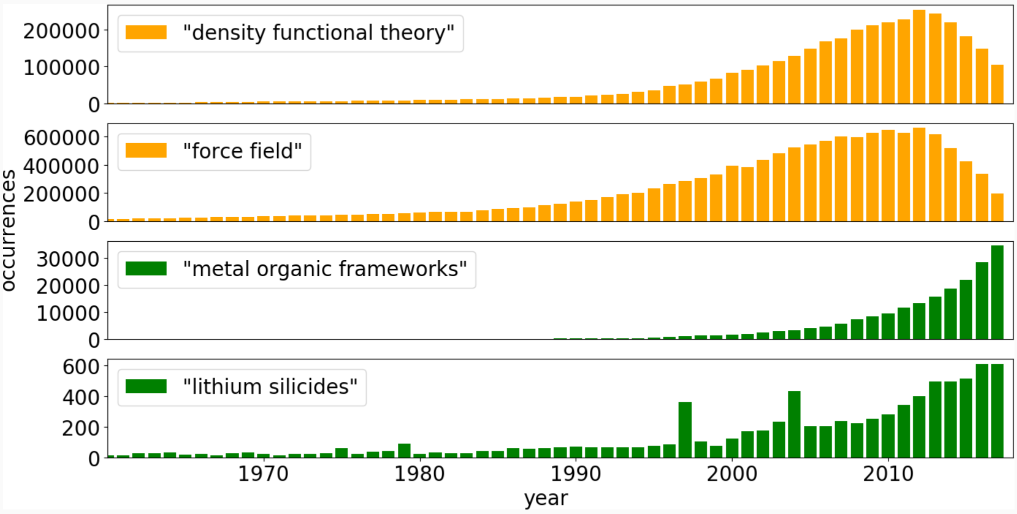

Figure 1: Literature occurrence (1960-2018) of thesis related methods (orange) and material classes (green).

tions of new materials can be performed. Out of the relevant literature one needs to determine a subset of structures or structural motifs which can be used as benchmarks to verify known trends and obtain reliable numerical parameter sets for the calculation of unknown properties.

The general interest in lithium silicides and MOFs grew enormously during the last years. Thus, these two material classes are promising candidates to start such numerical investigations. This thesis aims to provide unknown thermodynamical data to complete the general understanding of these material classes. In case of lithium silcides (Li_xSi_y) this data completes the understanding of this material class and leads to a purely theoretically derived phase diagram. In case of MOFs it will be shown that many properties are clearly dominated by the so called secondary building unit (SBU), which commonly contains transitions metals.

In addition, thermodynamical properties are calculated with force field based quasi-harmonic approximation (QHA) workflows developed within this thesis. Further, it will be shown that MOFs need to be treated with care as small changes (e.g., pressure and temperature) may introduce significant structural changes.

The first part of this thesis provides the theoretical background for the numerical methods of interest, i.e., DFT and FF. In the second part thermodynamical properties of solids with the main focus on battery materials (i.e., lithium silicides) and metal-organic frameworks are discussed. The fact that the local properties (e.g., structural motifs) of small building units influence many global properties (e.g., electronic, magnetic, and vibronic properties) introduces the third part. In this part, suitable tools for the analyses of thermodynamical properties of these small building units (e.g., atoms and molecules) are discussed and applied. The fourth part will provide a summary of the main findings as well as show how a combination of the aforementioned methods might enable large scale simulations in the future. One could treat active centers accurately while saving time by employing force field approximations to organic bridges between these centers.

2

OPEN-SOURCE AND OPEN-SCIENCE

Computational science relies on computer codes which implement the electronic structure or force field methods. Usually one starts with a paper and wants to understand how the values were produced. Therefore one needs to choose one of these codes to perform calculations.

There are various implementations, but many of them are not "freely" (free of charge) available. The most commonly used commercial codes are the Gaussian code [20] for Gaussian type orbital (GTO) basis sets, the VASP code [21–24] for plane wave (PW) basis set and the WIEN2k code [25] for linearized augumented plane waves (LAPW). Further details and explanation of basis sets will be presented in the next section. One needs to pay to use these codes, and there can be further restrictions in the usage of the produced values (e.g., reproducibility and performance tests to other codes). Users of this kind of codes get some support by the developers, thus they can use these codes without knowing exactly what is implemented and how the values are produced (i.e., "black box" usage).

In contrast to these codes, within this thesis only open-source codes will be used. These codes offer many advantages, like the possibility to have a look into the source code and modify it to the users needs. Many of these open-source codes come with a big user community which can be seen as a support for an inexperienced user. Knowing the implementations offers many advantages (e.g., reproduction of published numerical results). Checking the reproducibility of published or self-produced data is very important. Having the same numerical implementation of a method and using same numerical parameters, two independent codes should be able to produce exactly the same results. Whenever possible, calculations in this thesis were double or triple checked against reference calculations or additional calculations using the same numerical parameter space.

During this thesis, various codes were developed and made freely available. The used codes will be discussed shortly at places where they are introduced. An extended discussion and further details can be found in Appendix A. Plane wave calculations were performed with Quantum Espresso (QE) [26], GPAW [27] or CP2K [28], calculations of molecules and clusters using GTO basis sets were performed with developer versions of NRLMOL (i.e., FG-NRLMOL) [29–35], standalone executable of ORCA [36], the ERKALE [37] or the PySCF code [38]. Self-interaction corrected density functional theory calculations were performed with FG-NRLMOL [29–35], ERKALE [37] and PyFLOSIC [39]. PyFLOSIC [39] is an open-source implementation of the FLO-SIC [40–44] methodology based on PySCF. PyFLOSIC was developed during this thesis by Lenz Fiedler, Torsten Hahn and the author. Force field calculations were mainly performed with LAMMPS [45], GULP [46], eFF code [47–49] and the PyEFF code, which was developed during this thesis.

The next chapter will summarize the essential theoretical backgrounds needed for the used *ab initio* and force field methods.

Part I

THEORETICAL BASICS

The first part of this thesis provides an introduction and the theoretical foundation for all other parts.

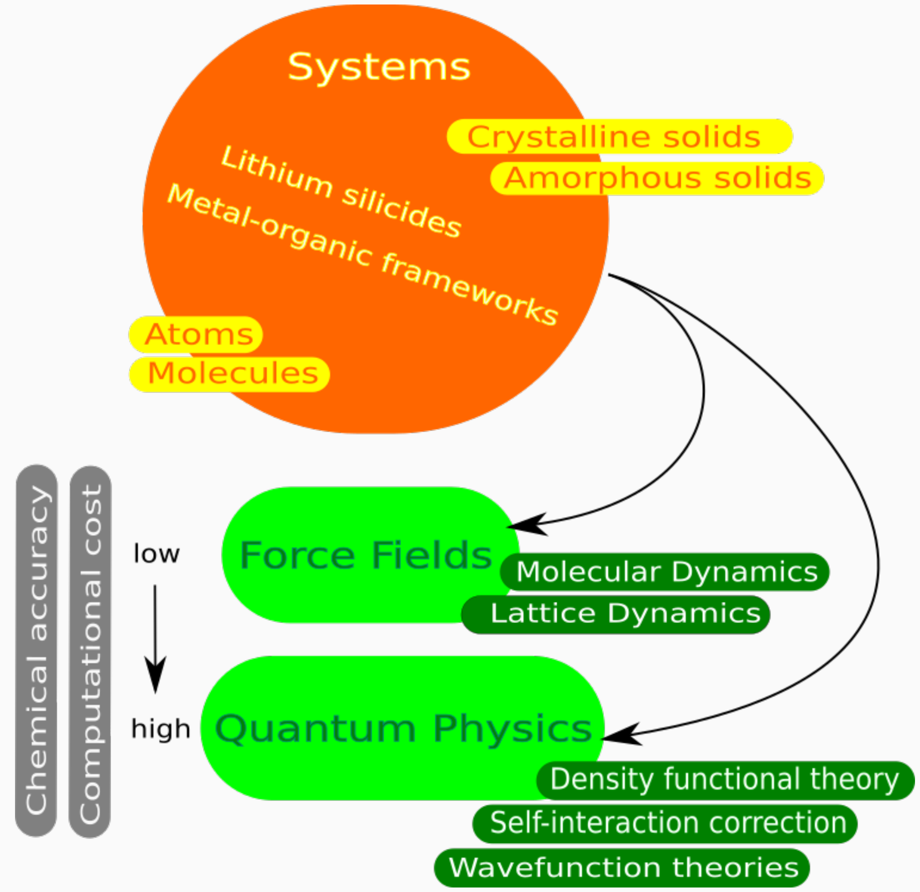

Figure 2: Determine a solution (e.g., a physical property) for specific systems (e.g., atom, molecule, cluster or solid) using a computational method (e.g., force field or electronic structure method) with a certain numerical accuracy and respective numerical effort.

3

COMPUTATIONAL METHODS

3.1 *ab initio* METHODS

Necessary details for all relevant electronic structure methods are outlined in this chapter. The notation of Lehtola et al. [37] is used, while slightly modified if needed. Such a notation is important to understand numerical implementations of Gaussian type orbitals codes like ERKALE [37] and PySCF [38]. As basis sets and self-consistent field cycles are important for both wavefunction theories (WFT) and density functional theories (DFT), both are shortly discussed. The following sections will provide details for WFT and DFT. As exchange-correlation functionals are essential for DFT calculations, some important approximations are reviewed. Further, some drawbacks of DFT are mentioned. Self-interaction correction (SIC) as a possibility to overcome some of these disadvantages is presented.

3.1.1 *Basis sets*

In the field of quantum chemistry, theoretical and computational physics there exists a variety of different implementations of WFT and DFT electronic structure methods. They differ in the way molecular orbitals (MOs) are represented. Many quantum chemistry problems are related to molecules and clusters. In this field, localized orbital basis sets like the Slater type orbitals [50] (STOs) and Gaussian type orbitals [51, 52] (GTOs, e.g., commercial GAUSSIAN code [20], open-source ERKALE code [37]) are used. In condensed matter theories often plane waves (PW, e.g., commercial VASP code [21–24], and open-source QUANTUM ESPRESSO code [26]) or linearized-augmented plane waves (LAPW, e.g., commercial WIEN2K code [25], open-source ELK code [53]) are employed. As an example, the GPAW code [27] can be used with plane waves, real-space uniform grids and a finite-difference stencils for the Laplacian in the Kohn-Sham and Poisson equations as well as atom-centered basis functions. In the next paragraphs GTO, PW and LAPW basis sets will be explained shortly.

Gaussian type orbitals (GTOs) in the form of segmented contracted Gaussians (cartesian representation Eqs. (1,2) or spherical representation Eqs. (1,3)) can be expressed by

$$\phi_\mu(\mathbf{r}) = \Omega_{\lambda_\mu}(\mathbf{r}) \sum_p d_{\mu p} e^{-\zeta_{\mu p}(\mathbf{r}-\mathbf{r}_\mu)^2} \tag{1}$$

$$\Omega^{\text{cart}}_{\lambda_\mu} = N^{\text{cart}}_\mu (x-x_\mu)^{l_\mu}(y-y_\mu)^{m_\mu}(z-z_\mu)^{n_\mu} \tag{2}$$

$$\Omega^{\text{sph}}_{\lambda_\mu} = N^{\text{sph}}_\mu |\mathbf{r}-\mathbf{r}_\mu|^{\lambda_\mu} Y_{\lambda_\mu M}(\mathbf{r}-\mathbf{r}_\mu) \tag{3}$$

with $\phi_\mu(\mathbf{r})$ being the coordinate representation of the μ-th basis function located at $r_\mu = (x_\mu, y_\mu, z_\mu)$, $\Omega_{\lambda_\mu}(\mathbf{r})$ includes the angular part of the basis functions, $\boldsymbol{\lambda}_\mu = (l_\mu, m_\mu, n_\mu)$ being the angular momenta and $Y_{\lambda_\mu M}$ being spherical harmonics. Further, $d_{\mu p}$ are the contraction coefficient and $\zeta_{\mu p}$ are the contraction exponent, respectively, of the p-th

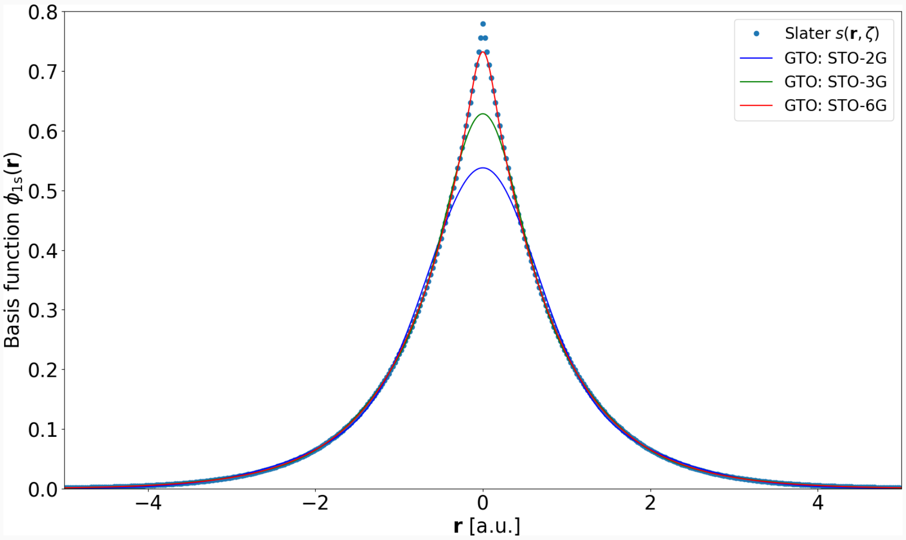

Figure 3: Gaussian type orbitals (GTOs) in comparison to Slater type orbitals (STOs) for the 1s wavefunction ϕ_{1s}. For the Slater type wavefunction $s(\mathbf{r},\zeta) = (\zeta^3/\pi)^{1/2} \exp(-\zeta \mathbf{r})$, a contraction exponent of $\zeta = 1.24$ was used. For the STO representation using GTOs $g_{\text{STO}} = \sum_k^K d_k g(\mathbf{r},\alpha_k)$ with $g(\mathbf{r},\alpha) = (2\alpha/\pi)^{3/4} \exp(-\alpha \mathbf{r}^2)$, the basis set exchange (BSE) [54] database was used to evaluate the expansion coefficients d_k and the Gaussian exponents α_k for STO-2G, STO-3G and STO-6G basis sets. The general failure of GTOs to correctly describe the nuclear cusp is observed for all three GTO basis sets. The picture was produced by the author using PYTHON (see Appendix A).

primitive Gaussian function in the μ-th basis function. N_μ^{cart} and N_μ^{sph} are normalization constants.

Advantages of GTOs are based on their simple implementation into an electronic structure method (WFT or DFT), because integrals can be computed analytically using recursion relations [37, 55, 56]. Further, the existence of libraries like LIBINT [57] as well as LIBCINT [58] enables a fast development of new GTO codes.

Drawbacks of GTOs are the incorrect asymptotic behaviour, the violation of the nuclear cusp condition and a too fast asymptotic decay [37, 59] (see Fig. 3). The nuclear cusp condition [60], also known as Kato theorem or Kato's cusp condition, states that the electron density has a cusp at the position of the nuclei. While for STOs this condition is fulfilled, GTOs are not able to reproduce the cusp correctly (see Fig. 3). In addition, atom-centered basis sets often suffer from linear dependence problems and a non-smooth basis set convergence. As pointed out by Lehtola et al. [37] these problems make it difficult to approach the complete basis set limit. Comparing calculated properties for different molecular geometries is also non trivial, as the basis set changes with the respective geometry. A Pulay-force correction [61] to the Hellmann-Feyman forces [62] is needed to evaluate correct forces. The problem is also known as the basis set superposition error (BSSE). An approach to address this problem is the so called counterpoise correction [63].

In summary, GTOs are the dominant basis sets in quantum chemical calculations, despite their shortcomings. This is due to their simple implementation, which allows not only to perform HF or DFT calculations, but also post-HF computations (e.g., Møller-Plesset [64] or coupled-cluster [65] level of theory).

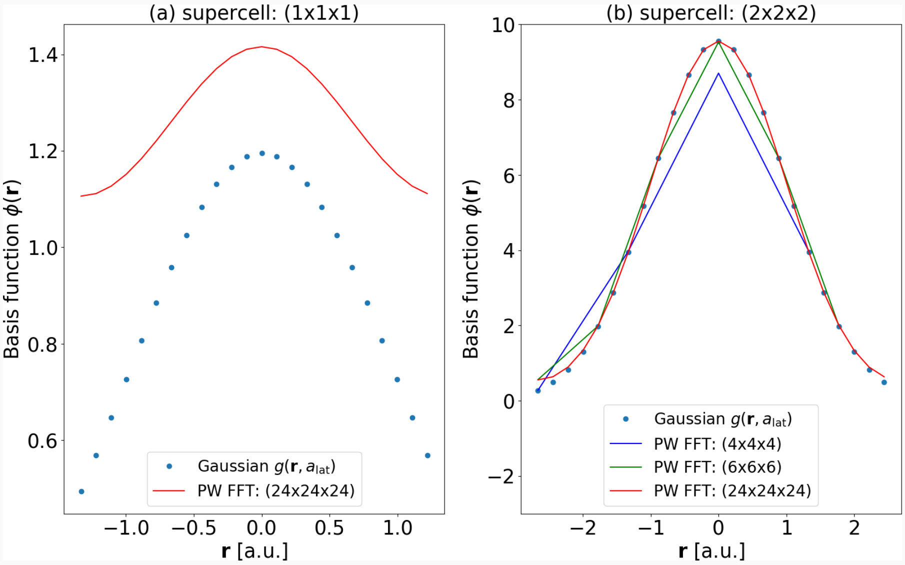

Figure 4: Plane waves (PWs) in comparison to Gaussian type orbitals (GTOs) for the usage as wave functions $\phi(\mathbf{r})$. For the representation of the Gaussian wave function $g(\mathbf{r}, a_{\text{lat}}) = (1/2\pi)^{3/2} \exp(-1/2\mathbf{r}^2) a_{\text{lat}}^3$ was used. For the plane waves a Fast-Fourier transformation (FFT) was applied on a reciprocal lattice $\mathbf{k}_{\text{grid}} = \sum_{k_x=k_y=k_z=-n_x/2}^{n_x/2} 2\pi/a_{\text{lat}} \exp(-1/2\mathbf{k}^2)$ with $a_{\text{lat}} = 2.66$ a.u. being the real-space lattice constant and $\mathbf{k} = 2/(\pi a_{\text{lat}})(kx, ky, kz)$ are the used $\mathbf{k}$ points. Sub-figure (a) shows a simple unit cell, whereas sub-figure (b) shows a (2x2x2) super cell (doubling a_{lat} in each direction). The plane wave in sub-figure (a) differs from the expected Gaussian because of the limited spatial extend of the applied FFT grid, which forces periodicity. Increasing the supercell size (see sub-figure (b)), i.e., the spatial extend of the FFT grid (24x24x24), the plane wave representation is able to reproduce the Gaussian wave function. In detail a dense FFT grid (24x24x24) (many plane waves) is needed to achieve this result. The picture was produced by the author using PYTHON (see Appendix A).

Plane waves are non-localized basis functions, which are commonly applied for solid state calculations based on their ability to treat periodic boundary conditions (PBCs). For an infinite system such a basis function can be expressed as

$$\phi_i = \frac{1}{\Omega} \sum_{G} c_i(\mathbf{G}) \exp(i\mathbf{G}\mathbf{r}), \tag{4}$$

with **G** being the reciprocal lattice vector and Ω the volume of the cell.

Advantages of plane wave in comparison to GTO basis sets are that they are independent of the atomic positions. Thus, no Pulay-force correction is necessary to get correct forces. The numerical quality of this basis set can easily be varied by changing the respective cutoff parameters (e.g., setting a maximal value for reciprocal lattice vectors $\mathbf{G}_{\text{max}}$). Thus, it is possible within this basis set to approach the basis set limit.

Drawbacks of plane wave basis sets are that they are implicitly periodic, and a large number of basis functions is needed for reasonable results. Localized functions and their properties are difficult to represent, as the inner-core wavefunction vary too rapidly. Thus, pseudo-potential approximations are usually necessary.

Linearized-augmented plane wave (LAPW) methods [66] are very accurate for performing electronic structure calculations of crystal structures. In LAPW the unit cell is divided into two regions, where the first one consists of non-overlapping spheres centered at the atomic sites and the second one is the interstitial region in-between the spheres. Inside the spheres a linear combination of radial functions and spherical harmonics $Y_{lm}(\mathbf{r})$ is used

$$\phi_{\mathbf{k}_n} = \sum_{lm}[A_{lm}(\mathbf{k}_n)u_l(\mathbf{r}, E_l) + B_{lm}(\mathbf{k}_n)\dot{u}_l(\mathbf{r}, E_l)]Y_{lm}(\mathbf{r}), \tag{5}$$

where $u_l(\mathbf{r}, E_l)$ is the regular solution of the radial Schrödinger equation and $\dot{u}_l(\mathbf{r}, E_l)$ being the energy derivative of $u_l(\mathbf{r}, E_l)$ for the same energy E_l. The coefficients $A_{lm}(\mathbf{k}_n)$ and $B_{lm}(\mathbf{k}_n)$ are determined by the condition that the corresponding basis function needs to match the basis functions in the interstitial region at the boundaries. In the interstitial region a plane wave expansion is used

$$\phi_{\mathbf{k}_n} = \frac{1}{\sqrt{\Omega}} \exp{(i\mathbf{k_n r})}, \tag{6}$$

where $\mathbf{k}_n = \mathbf{k} + \mathbf{K}$ are reciprocal lattice vectors with $\mathbf{k}$ being the wave vector in the first Brillouin zone and Ω the volume of the supercell. Each plane wave is augmented by an atomic-like function in every sphere. The Kohn-Sham equations (see Section 3.1.4) are solved using a combined basis set of LAPWs using a linear combination

$$\psi_{\mathbf{k}} = \sum_n c_n \phi_{\mathbf{k}_n}, \tag{7}$$

where the coefficients c_n may be determined by a Rayleigh-Ritz variational principle. The numerical quality of this basis set is controlled by the cutoff parameter

$$\mathbf{R}_{\mathrm{mt}}\mathbf{K}_{\mathrm{max}} \approx 7, \tag{8}$$

with $\mathbf{R}_{\mathrm{mt}}$ being the smallest radius of a Muffin-tin (MT) sphere and $\mathbf{K}_{\mathrm{max}}$ is the magnitude of the largest $\mathbf{K}$ vector. One can improve this basis set with respect to flexibility to appropriately treat semi-core and valence states by adding additional $\mathbf{k}_n$ dependent local basis function. This extended basis set might be called LAPW+lo, where lo are these additional "local orbitals".

Advantages of LAPW over pseudo-potential based methods is that core and semi-core electrons can explicitly be included in the calculations.

Drawbacks of LAPW are a higher numerical effort in comparison to pseudo-potential methods.

3.1.2 *Self-consistent field*

In both theories, WFT and DFT, we are solving the electronic Schrödinger equation

$$\mathbf{H}_{\mathrm{el}}\psi_n = \varepsilon_n \psi_n. \tag{9}$$

The spatial part of the wavefunction or the molecular orbitals (MOs) can be expressed as a sum of contracted GTOs

$$\psi_i^{\sigma}(\mathbf{r}) = \sum_{\mu} C_{\mu,i}^{\sigma} \phi_{\mu}(\mathbf{r}), \tag{10}$$

with $\psi_i^\sigma(\mathbf{r})$ being the i-th MO of spin σ and $C_{\mu,i}^\sigma$ is the coefficient of the μ-th basis function in its expansion.

A self-consistent field (scf) to solve this problem for these MO coefficients can be expressed in the Pople-Nesbet-Roothaan-Hall formulation [67, 68] as

$$\mathbf{F}^\sigma \mathbf{C}^\sigma = \mathbf{S}\mathbf{C}^\sigma \mathbf{E}^\sigma, \tag{11}$$

with $\mathbf{C}^\sigma$ being a matrix containing the molecular orbital coefficients, $\mathbf{S}$ is the overlap matrix and $\mathbf{E}$ is a diagonal matrix holding the orbital eigenvalues. The Fock matrix $\mathbf{F}^\sigma$ can be expressed as

$$\mathbf{F}^\sigma = \mathbf{H}_{\text{core}} + \mathbf{J} + \mathbf{K}^\sigma, \tag{12}$$

with $\mathbf{H}_{\text{core}}$ being the core Hamiltonian, $\mathbf{J}$ stands for the static Coulomb repulsion of the electrons with themselves and $\mathbf{K}^\sigma$ includes exchange and correlation effects (which are different for WFT and DFT). The kinetic energy $\mathbf{T}$ and the electron-nuclear interactions $\mathbf{V}$ are summed up in $\mathbf{H}_{\text{core}}$, given by

$$\mathbf{H}_{\text{core}} = \mathbf{T} + \mathbf{V}. \tag{13}$$

The energy contribution from the core Hamiltonian can be derived as the expectation value

$$E_{\text{core}} = \langle\ \psi \mid \mathbf{H}_{\text{core}} \mid \psi\ \rangle = \sum_{i=1}^{N} \int \psi_i^*(\mathbf{r}_1)\left(-\frac{1}{2}\nabla_1^2 - \sum_A \frac{Z_A}{|\mathbf{r}_1 - \mathbf{r}_A|}\right)\psi_i(\mathbf{r}_1)d\mathbf{r}_1, \tag{14}$$

with ∇ being the Nabla operator and Z_A being the nuclear charge of atom A at position $\mathbf{r}_A$. The expectation value of the Coulomb integral covering the static Coulomb repulsion of the electrons with themselves is given by

$$E_J = \langle\ \psi \mid \mathbf{J} \mid \psi\ \rangle = \sum_i^N \sum_{j>i}^N \int\int |\psi_i(\mathbf{r}_1)|^2 \left(\frac{1}{r_{12}}\right) |\psi_j(\mathbf{r}_2)|^2 d\mathbf{r}_1 d\mathbf{r}_2, \tag{15}$$

with $1/r_{12} = 1/|\mathbf{r}_1 - \mathbf{r}_2|$ being the Coulomb kernel.

3.1.3 *Wavefunction theory*

The Hartree and moreover the Hartree-Fock (HF) theory are the cornerstones of wavefunction theories. In HF the exchange-integral is expressed as

$$E_{K_x^{\text{HF}}} = \langle\ \psi \mid \mathbf{K}_x^{\text{HF}} \mid \psi\ \rangle = -\sum_i^N \sum_{j>i}^N \int\int \psi_i^*(\mathbf{r}_1)\psi_j^*(\mathbf{r}_2)\left(\frac{1}{r_{12}}\right)\psi_j(\mathbf{r}_1)\psi_i(\mathbf{r}_2)d\mathbf{r}_1 d\mathbf{r}_2, \tag{16}$$

with ψ being the wavefunction located at position $\mathbf{r}$. While in the one-electron limit (e.g., the H_2^+ molecule) HF is exact, for more realistic systems (e.g., complex molecules or solids) it delivers less accurate results. This is obvious, because HF misses correlation effects. Theoretically, standard HF scales like $\mathcal{O}(N^4)$ [69], but many implementations are identifying and neglecting small two-center integrals, which leads to $\mathcal{O}(N^3)$ scaling. Here, N describes the system size and is commonly representing the number of electrons in the system. Quantum chemists developed more sophisticated methods based on HF which are able to treat correlation effects (e.g., Møller-Plesset [64] or coupled-cluster [65] level of theory). Møller–Plesset perturbation theory in the second order (MP2) formally scales as $\mathcal{O}(N^5)$. [70], whereas the widely used coupled-cluster theory with singles and doubles (CCSD) scales as $\mathcal{O}(N^6)$ [71]. While the most accurate method of quantum chemistry might be full-configuration interaction (FCI), the *golden standard* is coupled-cluster with singles, doubles, and perturbative triples CCSD(T). The drawback of CCSD(T) is the $\mathcal{O}(N^7)$ scaling [72] which makes the method computationally very demanding. For systems containing several hundreds of atoms, other approaches like density functional theory, formally scaling like $\mathcal{O}(N^3)$, offer a compromise between accurate results and lower computational effort.

3.1.4 *Density functional theory*

The theoretical foundation of density functional theory (DFT) is provided by the Hohenberg-Kohn (HK) theorems [4]. The first HK theorem states that the external potential $V_{\text{ext}}(\mathbf{r})$ is a unique functional of the ground-state electron density $n(\mathbf{r})$ (within an arbitrary constant). Given this relation, it follows that the Hamiltonian of the system and the many-body wavefunctions are fully determined as well. Thus, any property can be derived from this ground-state density. The second HK theorem reveals that the ground-state energy can be obtained variationally, i.e., the electron density which minimizes the total energy given by an unique energy functional is the exact ground-state density.

While the HK theorems provide the theoretical foundation of DFT, they do not deal with a practical realization. Most of the implementations of DFT are based on the Kohn-Sham (KS) scheme [5], where a non-interacting system is used to obtain the electronic density of the interacting system.

The total energy in the KS DFT formalism is given by [73, 74]

$$E_{\text{KS}}[n] = E_T[n] + E_V[n] + E_J[n] + E_K[n], \tag{17}$$

with $E_{\text{KS}}[n]$ the total KS energy, $E_T[n]$ the kinetic energy of the non-interacting system

$$E_T[n] = \sum_{i=1}^{N} \int \psi_i^*(\mathbf{r}_1)\left(-\frac{1}{2}\nabla_1^2\right)\psi_i(\mathbf{r}_1)d\mathbf{r}_1, \tag{18}$$

$E_V[n]$ the external potential energy

$$E_V[n] = -\sum_A Z_A \int n(\mathbf{r}_1)\frac{1}{r_{1A}}d\mathbf{r}_1, \tag{19}$$

$E_J[n]$ the Coulomb energy

$$E_J[n] = \int\int n(\mathbf{r}_1)\left(\frac{1}{r_{12}}\right)n(\mathbf{r}_2)d\mathbf{r}_1 d\mathbf{r}_2, \tag{20}$$

and $E_K[n]$ the exchange-correlation energy. Each term is a functional of the density

$$n(\mathbf{r}_1) = \sum_\sigma \sum_{i=1}^{N^\sigma} |\psi_i^\sigma(\mathbf{r}_1)|^2 = \sum_{i=1}^{N^\alpha} |\psi_i^\alpha(\mathbf{r}_1)|^2 + \sum_{i=1}^{N^\beta} |\psi_i^\beta(\mathbf{r}_1)|^2 = n^\alpha(\mathbf{r}_1) + n^\beta(\mathbf{r}_1), \tag{21}$$

where the total density $n(\mathbf{r})$ is the sum of the spin densities of spin σ ($n^{\alpha}(\mathbf{r})$ and $n^{\beta}(\mathbf{r})$). The difference to Hartree-Fock theory is the formulation of the exchange-correlation energy, which now includes correlation effects. There exists a variety of approximations, so called exchange-correlation functionals. The exact exchange-correlation functional is not known, and needs to be approximated. Almost all commonly used exchange-correlation functionals at least partly suffer from the so called self-interaction error (see Sec. 3.1.5). John Perdew established the Jakob's ladder [75] for these exchange-correlation functionals (see Fig. 5), ranking them according to their ingredients and their corresponding accuracy. It is not clear how a proper self-interaction-correction (SIC) to DFT affects the accuracy of each rung of the original DFT Jakob's ladder, therefore a new SIC Jakob's ladder is proposed here (see Fig. 5). Further details about SIC will be discussed in the next section (see Sec. 3.1.5).

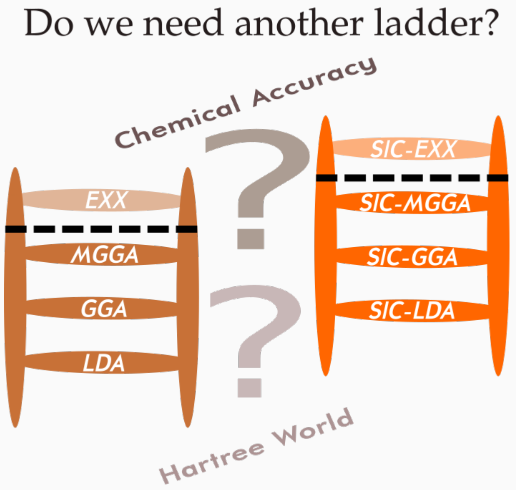

Figure 5: Jakob's ladders for density functional theory (DFT) and self-interaction correction (SIC) applied to DFT. While there is no question about the rungs of the DFT Jakob's ladder, it might not be obvious how a proper self-interaction correction changes the quality of each rung of the original Jakob's ladder. The picture was produced by the author using INKSCAPE (see Appendix A).

The first rung of the DFT Jakob's ladder is the local-(spin) density approximation (LSDA, or for short LDA) [76]

$$E_{K_{\text{xc}}^{\text{LDA}}} = \int n(\mathbf{r}_1)\varepsilon_{\text{xc}}^{\text{LDA}}[n^{\sigma}(\mathbf{r}_1)]d\mathbf{r}_1, \tag{22}$$

which only depends on the density $n^{\sigma}(\mathbf{r}_1)$. Here, $\varepsilon_{\text{xc}}^{\text{LDA}}$ is the exchange-correlation energy density per electron. The second rung is represented by the generalized-gradient approximation (GGA)

$$E_{K_{\text{xc}}^{\text{GGA}}} = \int n(\mathbf{r}_1)\varepsilon_{\text{xc}}^{\text{GGA}}[n^{\sigma}(\mathbf{r}_1), \nabla n^{\sigma}(\mathbf{r}_1)]d\mathbf{r}_1, \tag{23}$$

which next to the density $n^{\sigma}(\mathbf{r})$ now depends also on the gradient of the density $\nabla n^{\sigma}(\mathbf{r})$. The Perdew-Burke-Ernzerhof (PBE) [77] functional is one representative of the GGA rung. Meta-GGAs (mGGA) are situated on the 3rd rung

$$E_{K_{\text{xc}}^{\text{mGGA}}} = \int n(\mathbf{r})\varepsilon_{\text{xc}}^{\text{mGGA}}[n^{\sigma}(\mathbf{r}_1), \nabla n^{\sigma}(\mathbf{r}_1), \tau^{\sigma}(\mathbf{r}_1), \nabla^2 n^{\sigma}(\mathbf{r}_1)]d\mathbf{r}_1, \tag{24}$$

and depend additionally on the non-interacting kinetic energy $\tau^{\sigma}(\mathbf{r})$ and the Laplacian of the density $\nabla^2 n^{\sigma}(\mathbf{r}_1)$. The promising strongly-constrained and appropriately-normed (SCAN) [78] functional offers a very high accuracy for many calculated properties, while it is not fitted to any molecular database. The fourth rung includes a mixture of a fraction a_x of (exact) Hartree-Fock exchange and density functional exchange-correlation

$$E_{K_{\mathrm{xc}}^{\mathrm{hyb}}} = a_{\mathrm{x}} E_{K_{\mathrm{x}}^{\mathrm{HF}}} + (1 - a_{\mathrm{x}}) E_{K_{\mathrm{x}}^{\mathrm{DFT}}} + E_{K_{\mathrm{c}}^{\mathrm{DFT}}}, \tag{25}$$

the so called hybrid (hyb) functionals. In quantum chemistry, the B3LYP functional [79] is a commonly used hybrid functional.

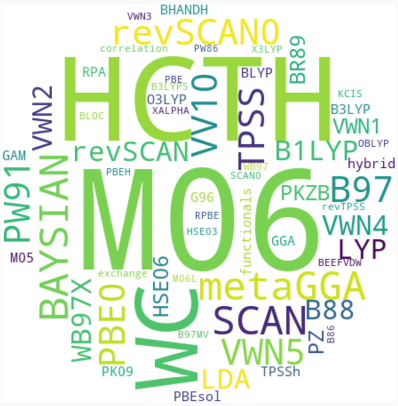

Figure 6: A schematic illustration of the variety of exchange-correlation functions within DFT. The idea of this image was inspired by the cover-figure of the work of Goerigk et al. [80]. The image shows only a selection taken from the Libxc library list. The picture was produced by the author using a Python script based on WordCloud (see Appendix A).

Libraries such as XCFun [81] or Libxc [82] offer access to a variety of exchange-correlation functionals, which allow a faster code development and an efficient usage of new exchange-correlation functionals. There exists various exchange-correlation functionals [80, 83] (see Fig. 6), while their construction is based on mainly two strategies. The first one is based on fitting to various reference values for specific properties (e.g., atomization energies, barrier heights and thermochemical data), and the second one considers the fulfillment of several exact conditions, constraints and norms [78, 84]. The M06-L [85, 86] functional has 35 empirical parameters, which are fitted to atomization energies as well as other chemical data [78]. The LDA, the PBE and the SCAN functional are constructed by fulfilling certain conditions, constraints and norms. The mGGA SCAN has only 7 fitting parameters, and fulfills 17 currently known constraints [78] for a semi-local functional, i.e.

for exchange functionals

1. negativity
2. spin-scaling
3. uniform density scaling
4. fourth-order gradient expansion
5. non-uniform density scaling

6. tight bound for two-electron densities

   for correlation functionals

7. non-positivity
8. second-order gradient expansion
9. uniform density scaling to high-density limit
10. uniform density scaling to low-density limit
11. zero correlation energy for any one-electron spin-polarized density
12. non-uniform density scaling

    for exchange-correlation functionals

13. size extensivity
14. general Lieb-Oxford bound
15. weak dependence upon relative spin polarization in the low-density limit
16. static linear response of the uniform electron gas
17. Lieb-Oxford bound for two electron densities.

In this thesis, only functionals constructed by the second route are used, because the overall understanding and correct description is more important than a better agreement of a specific value with reference values (e.g., atomization energies [87]). Some of the empirically fitted functionals even break simple conditions like the Lieb-Oxford bound (see Fig. 7). In the limit of one-electron density, it is shown here that a SIC fulfills the Lieb-Oxford bound. For all other constraints it is not obvious how a proper SIC will change the respective fulfillment of the underlying pure functional [88, 89]. Within a cooperation with John Perdew it turned out that orbital densities should be nodeless [88], thus this could also be considered as a constraint for future functional development.

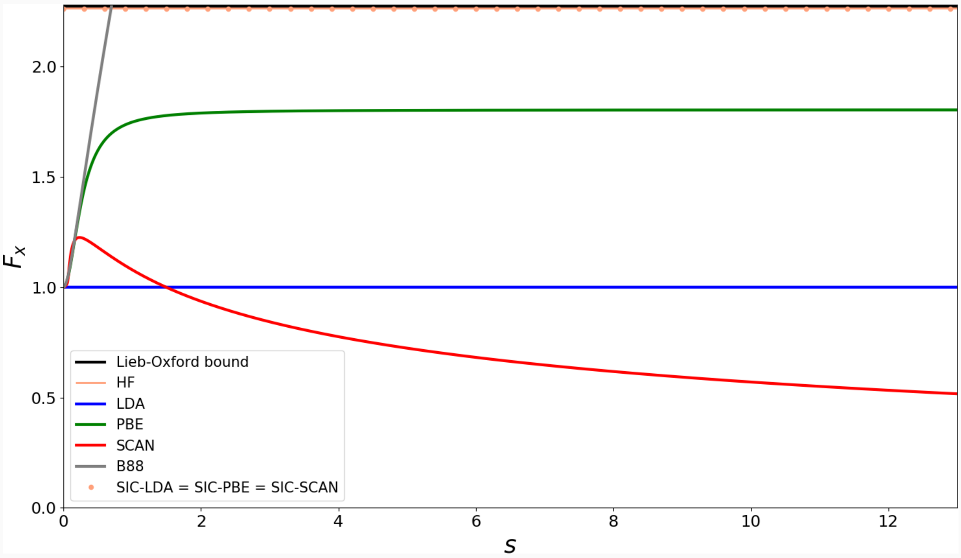

Figure 7: Exchange only enhancement factors F_x for different functionals. The exchange enhancement factor of a given exchange functional is defined as enhancement over the LDA exchange energy density per particle $\varepsilon_x^{\mathrm{DFT}} = \varepsilon_x^{\mathrm{LDA}} F_x^{\mathrm{DFT}}$. The simple H atom with STO-3G basis set was used to produce the density for the calculation, where the reduced gradient s was varied. The exchange enhancement factor is calculated using $F_x^{\mathrm{DFT}} = E_{K_x}^{\mathrm{DFT}} / E_{K_x}^{\mathrm{LDA}}$. While HF, LDA, PBE, SCAN as well as all tested SIC functionals fulfill the Lieb-Oxford condition $F_x \leq 2.27$ [90], the Becke B88 exchange functional, which is part of the commonly used BLYP and B3LYP functionals, does not fulfill this limit. The B88 is not the only functional which does not fulfill this limit [90]. In the limit of small s values, PBE, SCAN and B88 show a similar behaviour. The picture was produced by the author using a PYTHON script based on PySCF (see Appendix A).

3.1.5 *Self-interaction error*

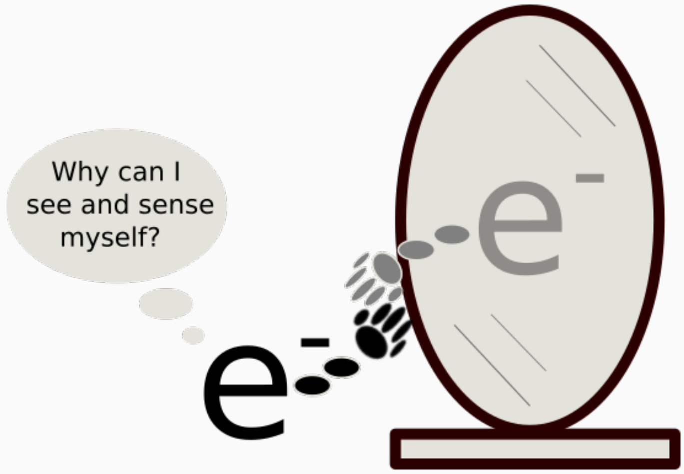

Figure 8: Why can I see and interact with myself? The idea of the picture was initiated and influenced by [91]. The picture was produced by the author using the INKSCAPE program (see Appendix A).

Using certain density functional approximations (DFAs), an electron can spuriously interact with itself (see Fig. 8). This phenomena is known as self-interaction error (SIE). The SIE is attributed to be the origin, at least to some extend, of

1. underestimation of band gaps [92, 93], reaction barriers [88] and ionization potentials [94]
2. incorrect description of bond dissociation [88]
3. incorrect $1/\mathbf{r}$ long-range behaviour of the Kohn-Sham potential [92]
4. problems with dipole-bound anions [95–97] and charge-transfer complexes [43, 44].

There are several methodical possibilities to treat SIE in DFT. The best way might be the construction of a SIE free functional. While there are attempts to realize this [98–101], these functionals are usually not SIE free. Mixing a certain amount of HF density into DFT can make the overall density more localized. With that, hybrid functional and especially long-range corrected hybrid functionals address the SIE to some extend. Within solid state calculations one of the biggest challenges is the correct description of semiconductor band gaps. A numerically cheap method to address this problem is the so called DFT+U (e.g., LDA+U or GGA+U) method, where U is a Hubbard-like parameter [102]. The U parameter opens the band gap, and accordingly also treats SIE in DFT to some extent. Other methods which open the band gap are the GW method [103] and the (modified) Becke-Johns potential [104–106].

For the exact density functional approximation (DFA) a proper self-interaction correction (SIC) needs to vanish [107, 108]. Already in 1981 Perdew and Zunger [92] proposed such a *proper* SIC (PZ-SIC), which is one of the most commonly used SIC variants. Although PZ-SIC addresses many of the aforementioned problems of DFT it is not commonly used. One drawback of PZ-SIC in comparison the pure DFT is its higher numerical effort as well as some other shortcomings [108]. Pederson et al. [40–42, 109, 110] showed that Fermi-Löwdin orbitals can be constructed in a unitarily invariant way from Kohn-Sham orbitals to perform self-consistent SIC calculations within the Fermi-Löwdin orbital self-interaction correction (FLO-SIC) method.

To introduce PZ-SIC or FLO-SIC, the SIC Hamiltonian can be formulated as an extension to Eq. (11) [67, 68], which reads

$$(\mathbf{F}^{\mathrm{KS},\sigma} + \mathbf{F}^{\mathrm{SIC},\sigma})\mathbf{C}^{\sigma} = \mathbf{S}\mathbf{C}^{\sigma}\mathbf{E}^{\sigma}, \tag{26}$$

with $\mathbf{C}^{\sigma}$ being a matrix containing the KS molecular orbital coefficients, $\mathbf{S}$ is the overlap matrix and $\mathbf{E}^{\sigma}$ is a diagonal matrix holding the energy eigenvalues as before. The SIC Hamiltonian can be derived from a unified Hamiltonian (see Harrison, Heaton, and Lin [111] and see Lehtola and Jónsson [74] Eq. (37)). One variant of unified Hamiltonian only treats the occupied-occupied (OO) space

$$\mathbf{F}^{\mathrm{SIC}}_{\mathrm{OO}} = -\frac{1}{2}\sum_{i=1}^{N^{\sigma}}(\mathbf{f}_i^{\sigma}\mathbf{p}_i^{\sigma}\mathbf{S} + \mathbf{S}\mathbf{p}_i^{\sigma}\mathbf{f}_i^{\sigma}), \tag{27}$$

while another variant includes the occupied-virtual (OV) space

$$\mathbf{F}^{\mathrm{SIC}}_{\mathrm{OO,OV}} = -\mathbf{S}\sum_{i=1}^{N^{\sigma}}(\mathbf{p}_i^{\sigma}\mathbf{f}_i^{\sigma}\mathbf{p}_i^{\sigma} + \mathbf{v}^{\sigma}\mathbf{f}_i^{\sigma}\mathbf{p}_i^{\sigma} + \mathbf{p}_i^{\sigma}\mathbf{f}_i^{\sigma}\mathbf{v}^{\sigma})\mathbf{S}. \tag{28}$$

In this context, $\mathbf{f}_i = \mathbf{J}(\mathbf{p}_i^\sigma) + \mathbf{K}(\mathbf{p}_i^\sigma)$ is the KS-Fock matrix of the i-th density matrix $\mathbf{p}_i^\sigma$ given by

$$\mathbf{p}_i^\sigma = \mathbf{c}_i^\sigma \mathbf{c}_i^{\sigma\dagger}, \tag{29}$$

with $\mathbf{c}_i^\sigma$ being the i-th column of the FLO molecular orbital coefficient matrix, containing the coefficients of FLO ϕ_i. Further, the virtual space projector can be introduced as

$$\mathbf{v}^\sigma = \sum_i^{\text{virtual}} \mathbf{C}_i^\sigma \mathbf{C}_i^{\sigma\dagger}, \tag{30}$$

with $\mathbf{C}_i^\sigma$ being the i-th column of $\mathbf{C}^\sigma$. As a guide for the eyes, the Hamiltonian can be written as a matrix

$$\mathbf{F}^{\text{SIC}} = \begin{pmatrix} \mathbf{F}_{\text{OO}} & \mathbf{F}_{\text{OV}} \\ \mathbf{F}_{\text{VO}} & \mathbf{F}_{\text{VV}} \end{pmatrix} = \begin{pmatrix} \mathbf{F}_{\text{OO}} & \mathbf{F}_{\text{OV}} \\ \mathbf{F}_{\text{VO}} & 0 \end{pmatrix}. \tag{31}$$

3.1.6 *Derivative discontinuity*

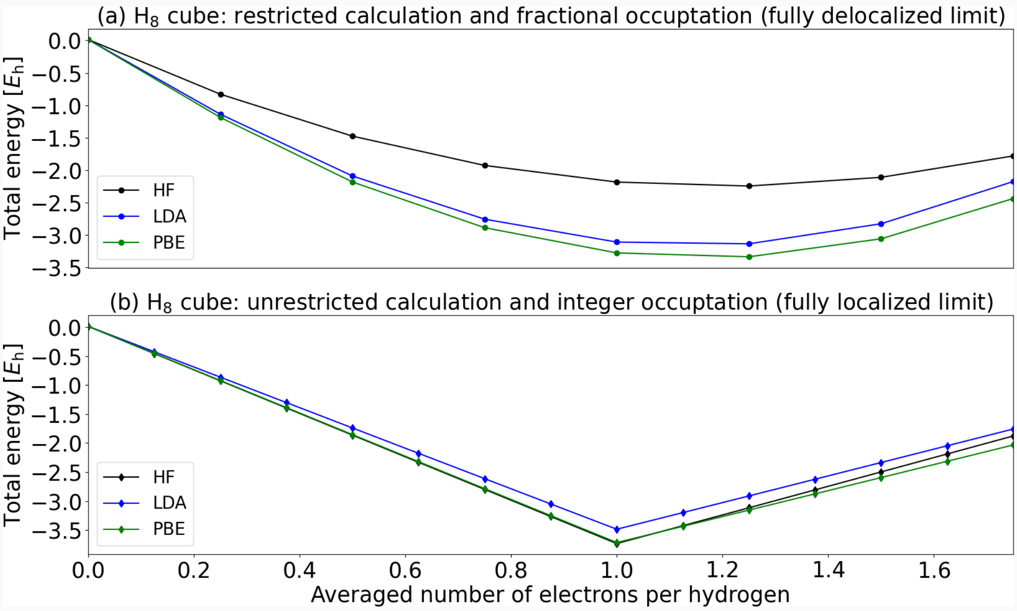

Figure 9: For a model system, consisting of 8 hydrogen atoms spaced 1000 Å apart from each other to build a cube, (a) fully delocalized calculations (RHF/RKS and fractional occupation) are compared to (b) fully localized calculations (UHF/UKS and integer occupation). While the fully delocalized calculations in (a) have the derivative discontinuity error, the fully localized calculations in (b) do not show this error. For a fully delocalized calculation each H atom has the same fractional occupation, while in the fully localized limit each H atom has integer occupation. The idea of this comparison was influenced by the work of Mori-Sánchez and Cohen [112]. The STO-3G basis set was used. The picture was produced by the author using a Python script based on PySCF (see Appendix A).

An error which is related to the SIE is the derivative discontinuity error (DDE). As a consequence of the integer nature of electrons, the energy of the system needs to exhibit derivative discontinuities when changing its charge state (see Fig. 9). The exact exchange-correlation functional needs to be piecewise linear, i.e., enforce piecewise linearity (PWL) as a function of the number of particles. Koopmans compilant (KC) functionals by Borghi et al. [113, 114] are explicitly constructed to produce this correct behaviour. There are flavours of this type of functional which are working hand-in-hand with PZ-SIC. FLO-SIC prefers integer occupation, thus FLO-SIC indirectly affects the behaviour of the DDE and can be used to remove the DDE [94]. For the prototypical H_2^+ molecule in one of the articles related to this thesis [94], it was shown that FLO-SIC is also able to produce the correct PWL behaviour.

3.1.7 *Localized orbitals*

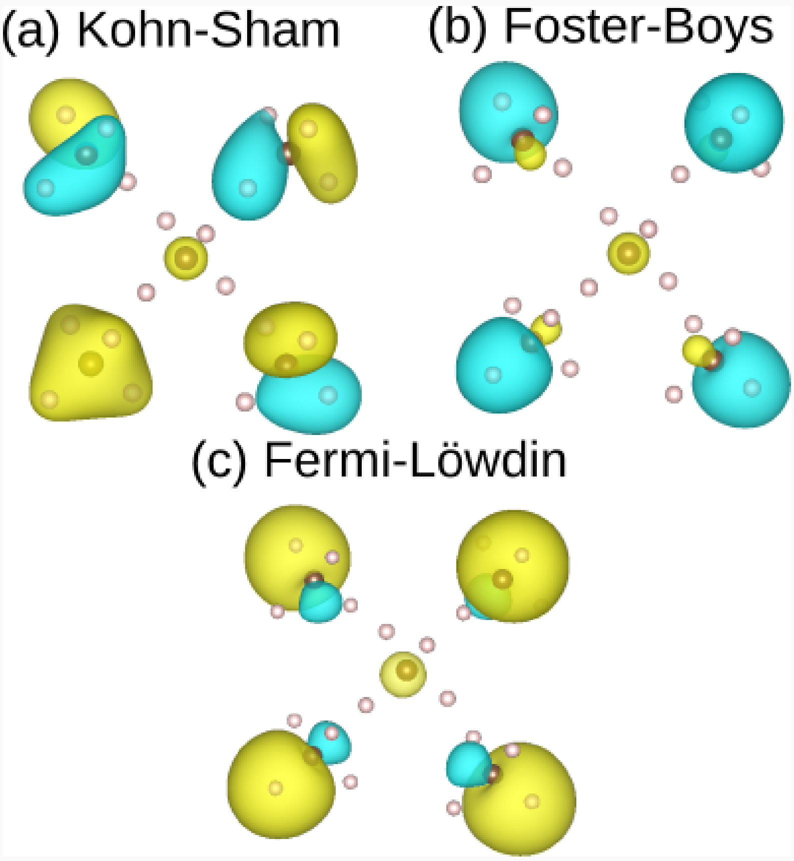

Figure 10: Comparison of Kohn-Sham orbitals (KSOs), Foster-Boys orbitals (FBOs) and Fermi-Löwdin orbitals (FLOs) for the CH_4 molecule. While the KSOs are delocalized, the FBOs and FLOs are clearly localized. The picture was produced by the author using PYTHON scripts based on PYSCF and PYFLOSIC using the LDA-PW exchange-correlation functional and the cc-pVQZ basis set (see Appendix A).

It has been shown that localized orbitals deliver lower self-interaction energies and, accordingly, play an essential role for a proper SIC [92, 111, 115]. As discussed several decades ago, the exchange hole (Fermi hole) can be expressed for single determinant cases by means of so called Fermi orbitals [116]. Luken [117] showed that there are regions in space where the Fermi hole resembles localized orbitals. In these regions the Fermi orbital only weakly depends on the position of the reference electron. The corresponding Fermi hole can be approximated by the square of the localized Fermi orbital.

Fermi orbitals and Fermi-Löwdin orbitals are well-localized (see Fig. 10), comparable to Foster-Boys [118], Edmiston-Ruedenberg [119] or Pipek-Mezey [120] localized orbitals. Fermi-Löwdin orbitals and other localized orbitals can be interpreted as core, lone pair or bonding orbitals [116]. Fermi orbitals depend on the Fermi-orbital descriptors (FODs), as will be explained later in the text, for a given density, thus one can argue that the optimized set of these descriptors carries bonding information.

Fermi orbitals (FO, $|FO_i\rangle$) can be constructed from the original Kohn-Sham wavefunctions ψ_α via

$$|FO_i\rangle = \sum_{\alpha=1}^{N} R_{i\alpha} \, |\psi_\alpha\rangle \ , \tag{32}$$

where the transformation matrix $\mathbf{R}$ is defined as

$$R_{i\alpha} = \frac{\psi_\alpha^*(\mathbf{a}_i)}{\sqrt{\sum\limits_{\alpha=1}^{N} |\psi_\alpha(\mathbf{a}_i)|^2}} \ . \tag{33}$$

The $\mathbf{a}_i$ are points in real space called Fermi-orbital descriptors (FODs). The knowledge of these FODs is necessary for the construction of the Fermi orbitals.

To simplify notation, we express both the Fermi orbitals and the Kohn-Sham orbitals as vectors containing the actual orbitals. For N electrons, these vectors will contain N elements. The Kohn-Sham orbitals and Fermi orbitals, respectively, therefore read

$$\boldsymbol{\psi} = \left(|\psi_1\rangle, |\psi_2\rangle, ..., |\psi_N\rangle\right)^\dagger \ , \tag{34}$$

$$\mathbf{FO} = \left(|FO_1\rangle, |FO_2\rangle, ..., |FO_N\rangle\right)^\dagger \ , \tag{35}$$

and Eq. (33) can be expressed as

$$\mathbf{FO} = \mathbf{R}\boldsymbol{\psi} \ . \tag{36}$$

Some GTO codes use non-orthonormal basis sets, e.g., non-orthonormal linear combinations of atom-centered functions. When using orthonormal basis sets, the atomic overlap matrix $\mathbf{S}_{1e}$ of the atomic basis functions is simply the unit matrix $\mathbb{1}$, and we obtain

$$\boldsymbol{\psi}^\dagger \mathbf{S}_{1e} \boldsymbol{\psi} = \mathbb{1} \ . \tag{37}$$

Note that Fermi orbitals given by Eq. (36) generally do not satisfy Eq. (37), i.e.,

$$\mathbf{FO}^\dagger \mathbf{S}_{1\mathrm{e}} \mathbf{FO} = \mathbf{S} \neq \mathbb{1} \ , \tag{38}$$

introducing the overlap matrix $\mathbf{S}$. Therefore, to obtain an orthogonal set of localized orbitals, a symmetric Löwdin orthogonalization [121] is carried out. This can be achieved by solving the corresponding eigenvalue problem for the overlap matrix $\mathbf{S}$

$$\mathbf{S}\mathbf{T}_\alpha = Q_\alpha \mathbf{T}_\alpha \ , \tag{39}$$

with the eigenvectors $\mathbf{T}_\alpha$ and the eigenvalues Q_α. With these, one can transform the Fermi orbitals **FO** into Fermi-Löwdin orbitals ϕ by

$$\phi = \mathbf{T}\mathbf{Q}^{-1/2}\mathbf{T}^{\dagger}\mathbf{FO}\,. \tag{40}$$

Here, the matrix **T** is defined as the matrix of the eigenvectors, while $\mathbf{Q}^{-1/2}$ is

$$Q_{ij}^{-1/2} = \begin{cases} Q_i^{-1/2} & , i = j \\ 0 & , i \neq j\,. \end{cases} \tag{41}$$

The resulting Fermi-Löwdin orbitals ϕ now satisfy Eq. (37), i.e.,

$$\phi^{\dagger}\mathbf{S}_{1e}\phi = \mathbb{1}\,. \tag{42}$$

The complete transformation from Kohn-Sham to Fermi-Löwdin orbitals

$$\phi = \mathbf{T}\mathbf{Q}^{-1/2}\mathbf{T}^{\dagger}\mathbf{R}\psi \tag{43}$$

is unitary, leaving the density unchanged. The constructed Fermi-Löwdin orbitals can now be used to perform the self-interaction correction. The optimal set of FODs is obtained by moving the FOD positions in order to minimize the SIC energy [40, 41] in a variational way.

3.2 CLASSICAL FORCE FIELDS

There are problems (e.g., long timescale molecular dynamics) which are too large with respect to the system size to be investigated with DFT. Some of these problems are related to the materials studied within this thesis, i.e., MOFs and battery materials. Classical force fields provide a compromise between efficiency and appropriate results. Within classical force fields the energy of the system is parametrized using fixed functions depending on parameters like bond lengths, bond angles, torsion as well as functions describing long-range interactions. A general energy expression within force fields [8] reads

$$\begin{aligned} E_{\text{total}}(R_{ij}, \theta_{ijk}, \nu_{ijkl}, \kappa_{ijkl}) = &\sum_{i<j} E_{\text{stretching}}(R_{ij}) \\ &+ \sum_{ijk} E_{\text{bending}}(\theta_{ijk}) \\ &+ \sum_{ijkl} E_{\text{torsion}}(\nu_{ijkl}) \\ &+ \sum_{ijkl} E_{\text{out-of-plane}}(\kappa_{ijkl}) \\ &+ \sum_{i<j} E_{\text{coulomb}}(R_{ij}) \\ &+ \sum_{i<j} E_{\text{vdW}}(R_{ij}), \end{aligned} \tag{44}$$

with $E_{\text{stretching}}(R_{ij})$ being the energy of stretching a bond, $E_{\text{bending}}(\theta_{ijk})$ being the energy of bending the bond, $E_{\text{torsion}}(\nu_{ijkl})$ being the energy of the torque of a bond,

$E_{\text{out-of-plane}}(\kappa_{ijkl})$ describing improper out-of-plane bending interactions, $E_{\text{coulomb}}(R_{ij})$ being Coulomb interactions, and $E_{\text{vdW}}(R_{ij})$ being non-bonded van-der-Waals (vdW) interactions. In general, force field are developed for specific purposes or materials and commonly the fitting functions and the fitting procedure itself are physically motivated. The critical point of developing force fields is to find a force field description which is able to cover different aspects and properties of a system while being computationally efficient.

3.2.1 *Modified embedded atom method*

For the battery material class of lithium silicides, there exists a suitable force field formulation, within the so called modified embedded atom method (MEAM) formulation. This force field was used within this thesis for a large variety of properties of these systems. Therefore, the MEAM force field is shortly introduced. The MEAM total energy $E_{\text{tot}}^{\text{MEAM}}$ of a system of atoms [122, 123] can be written as

$$E_{\text{tot}}^{\text{MEAM}} = \sum_i E_{\text{tot},i}^{\text{MEAM}}, \tag{45}$$

where the energy of the i-th atom is defined as

$$E_{\text{tot},i}^{\text{MEAM}} = \underbrace{E_{\text{EB},i}(\mathbf{n}_i^{\text{MEAM}})}_{\text{embedding energy}} + \underbrace{\frac{1}{2}\sum_{i\neq j}\phi_{ij}(\mathbf{r}_{ij})}_{\text{pair potential term}} \quad . \tag{46}$$

The embedding energy $E_{\text{EB},i}$ is a function of the background electron density $\mathbf{n}_i^{\text{MEAM}}$ at the site of atom i whereas the pair potential $\phi_{ij}(\mathbf{r}_{ij})$ between atoms i and j depends on the distance $\mathbf{r}_{ij}$. The first energy is needed to insert an atom i at a site where the background electron density equals $\mathbf{n}_i^{\text{MEAM}}$. A detailed description of the method itself can be found in Gullet, Wagner, and Slepoy [122].

3.2.2 *Electron force field*

In the FLO-SIC method, the most time-consuming part is the optimization of the FODs. During this thesis, several methods to speed-up this process where studied. Commonly used classical force fields use parameters to capture the nuclei dynamics of a system. Force fields which additionally treat the dynamics of electrons of the system exist, for example in the form of the LEWIS [124, 125] or the LEWIS$^\bullet$ force fields [126]. Optimizing the positions of *semi-classically* treated nuclei and electrons would be just like a geometry optimization at $T = 0$ K. Therefore, it could be interesting to try using *semi-classically* optimized electron positions as FOD starting guesses. Unfortunately, the LEWIS [124, 125] or the LEWIS$^\bullet$ force fields [126] are limited to only a few chemical elements and there is no free implementation available. Another option is the so called electron force field (eFF) [47–49, 127]. The eFF delivered suitable results and was re-implemented during this thesis. The theory of the electron force field is shortly reviewed.

In eFF the nuclei are represented as point charges and the electrons as spherical Gaussians [128]

$$\psi_i = \exp((\mathbf{r} - \mathbf{x}_i)^2/s_i^2), \tag{47}$$

i.e., as a function of nuclear $\mathbf{r}$ and electron $\mathbf{x}_i$ positions and electron sizes s_i. The eFF total energy of the system is given by

$$E = E_{\text{ke}} + E_{\text{nuc,nuc}} + E_{\text{nuc,elec}} + E_{\text{elec,elec}} + E_{\text{Pauli}}, \tag{48}$$

with E_{ke} being the kinetic energy, $E_{\text{nuc,nuc}}$, $E_{\text{nuc,elec}}$ and $E_{\text{elec,elec}}$ being the Hartree electrostatic energies, and E_{Pauli} being the antisymmetrization (Pauli) correction. The kinetic energy is given by

$$E_{\text{ke}} = \frac{1}{2}\sum_i \int |\nabla \psi_i|^2 dV = \sum_i \frac{3}{2}\frac{1}{s_i^2}. \tag{49}$$

The nucleus-nucleus interaction energy can be expressed as

$$E_{\text{nuc,nuc}} = \sum_{I<J} \frac{Z_I Z_J}{R_{IJ}}, \tag{50}$$

with Z_I and Z_J being the charges of the nuclei and R_{IJ} the distance between them. The interaction between nuclei and electrons is described by

$$E_{\text{nuc,elec}} = -\sum_{I,j} \int Z_I \frac{|\psi_j|^2}{R_{Ij}} dV = -\sum_{I,j} \frac{Z_I}{R_{Ij}} \text{erf}\left(\frac{\sqrt{2}R_{Ij}}{s_j}\right), \tag{51}$$

where R_{Ij} is the nuclear-electron distance, and the electron-electron interaction is given by

$$E_{\text{elec,elec}} = \sum_{i<j} \int \frac{|\psi_i|^2 |\psi_j|^2}{r_{ij}} dV = \sum_{i<j} \frac{1}{r_{ij}} \text{erf}\left(\frac{\sqrt{2}r_{ij}}{\sqrt{s_i^2 + s_j^2}}\right), \tag{52}$$

with r_{ij} being the distance between the electrons. The Pauli correction energy is

$$E_{\text{Pauli}} = \sum_{\sigma_i = \sigma_j} E(\uparrow\uparrow)_{ij} + \sum_{\sigma_i \neq \sigma_j} E(\uparrow\downarrow)_{ij}, \tag{53}$$

where $E(\uparrow\uparrow)_{ij}$ and $E(\uparrow\downarrow)_{ij}$ are the Pauli potential functions, which are given by

$$E(\uparrow\uparrow)_{ij} = \left(\frac{S_{ij}^2}{1 - S_{ij}^2} + (1-\rho)\frac{S_{ij}^2}{1 + S_{ij}^2}\right) \Delta T_{ij} \tag{54}$$

and

$$E(\uparrow\downarrow)_{ij} = \frac{\rho S_{ij}^2}{1 + S_{ij}^2} \Delta T_{ij}, \tag{55}$$

where ΔT_{ij} is the measure of change in the kinetic energy of the electrons upon antisymmetrization

$$\Delta T_{ij} = \frac{3}{2}\left(\frac{1}{\bar{s}_1^2} + \frac{1}{\bar{s}_2^2}\right) - \frac{2(3(\bar{s}_1^2 + \bar{s}_2^2) - 2\bar{r}_{12}^2)}{(\bar{s}_1^2 + \bar{s}_2^2)^2}, \tag{56}$$

and

$$S_{ij} = \left(\frac{2\,\bar{s}_1 \bar{s}_2}{\bar{s}_1^2 + \bar{s}_2^2}\right)^{\frac{3}{2}} \exp\left(-\frac{\bar{r}_{12}^2}{\bar{s}_1^2 + \bar{s}_2^2}\right) \tag{57}$$

is the overlap between the two wave packets.

In the eFF each electron carries a spin ($+1/2$ or $-1/2$). One can calculate a C atom with $S = 2/2$ (4-up, 2-down electrons) and $S = 4/2$ (5-up, 1-down electrons) in the same way as it is done within FLO-SIC. The first eFF formulation (eFF1) [47–49] has three free parameters. The authors PYTHON implementation of eFF1, PYEFF, followed established conventions [47] and used $\rho = -0.2$, the scaled distance between the electrons $\bar{r}_{ij} = 1.125 \cdot r_{ij}$, and the scaled electron size $\bar{s}_i = 0.9 \cdot s_i$.

The eFF1 formulation may be called a quasi all-electron approximation, because all core and valence electrons are treated explicitly. The simple Gaussians used to represent electrons resemble s-orbitals. Therefore, it is not surprising that the force field becomes less accurate for atoms containing states with higher angular quantum number. In case of eFF1 only elements with $Z = 1 - 6$ are described well. The eFF2 [49] formulation tries to overcome this limitation, and has been tested for systems containing elements with $Z = 1 - 10$.

The standard eFF1 formulation is available in the EFF code [47] and in LAMMPS [129], but the eFF2 formulation is not yet available. The eFF1 formulation is already available in the PYEFF code, which was developed during this thesis. PYEFF is written in PYTHON and uses standard scientific PYTHON packages (e.g., NUMPY, SCIPY, SYMPY, ASE). It offers several input and output features to generate FOD input files for the FG-NRLMOL code [29–35] or our PYFLOSIC implementation [39]. A typical input for PYEFF is the nuclear geometry, the spin state and starting values for the electron sizes s_i. Thus, bonding information of the systems is not directly used to generate FOD starting guesses.

Besides the possibility of calculating different spin states, this force field formulation delivers a total energy expression and can therefore be used to describe bond dissociation. As will be shown later in the text, PYEFF can be used to calculate ionization potentials and electron affinities.

4

COMPUTATION OF THERMODYNAMIC PROPERTIES

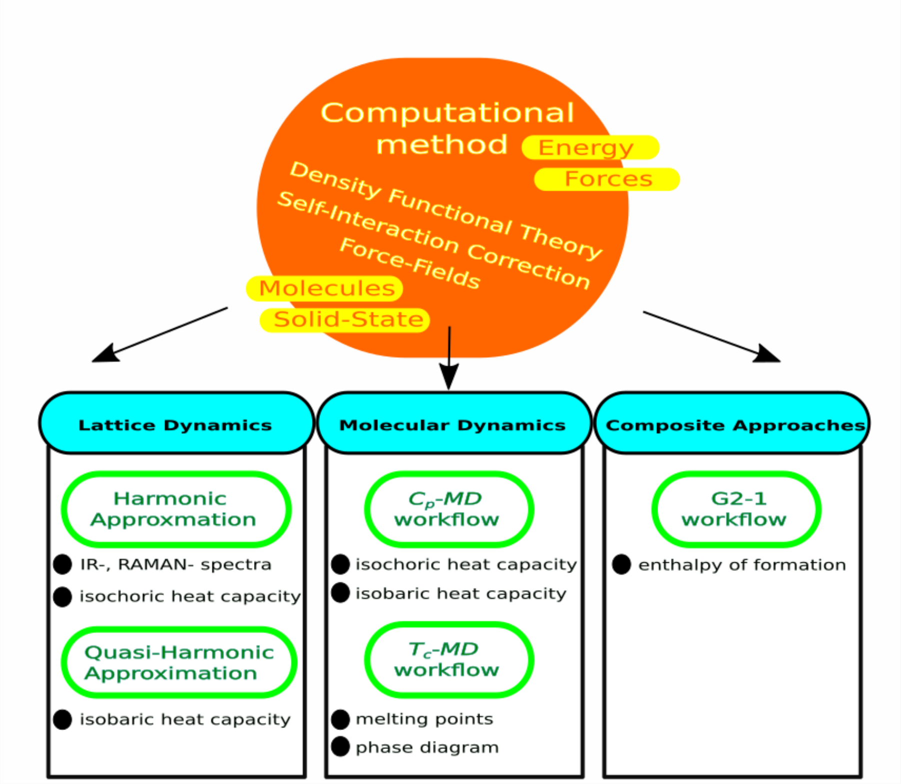

Figure 11: Determine a thermodynamic property (e.g., isochoric or isobaric heat capacity or enthalpy of formation) for specific systems (e.g., solid-state and molecules) using a computational method (e.g., density functional theory, self-interaction correction or force fields) with a certain numerical accuracy and respective numerical effort (see Fig. 2), within a specific thermodynamical approach (e.g., lattice dynamics or composite approach).

Thermodynamical properties are of general interest for molecules as well as for solid-state materials (see Fig. 11). While DFT and force fields deliver a description of energies and forces for the systems of interest, the calculation of thermodynamical properties needs further approximations, i.e., the theory of lattice dynamics (e.g., (quasi-) harmonic approximation) or composite approaches (e.g., G2-1 theory). More in detail, thermodynamical properties essentially depend on vibrational properties, which can be accessed for instance by displacements of non-equivalent atoms of the system, monitoring the energy as well as the force per atom as a function of these displacements. The essential approximations needed for all computational thermodynamic approximations used within this thesis are shortly reviewed.

4.1 EQUATION OF STATES

While molecules are calculated within vacuum, solid-state calculations are performed for a unit cell (spanned by the lattice constants **a**, **b** and **c**) which is repeat using periodic boundary conditions (pbcs) (see Fig. 12). The cell parameters defining the unit cell and with that the volume of the calculated solid-state system need to be optimized within the used level of theory. Within solid-state modelling using DFT it is common to calculate so called energy-volume curves. For a set of different volumes V of a given system the forces on the atoms are minimized and the total energy is calculated. An equation of state (EOS) [130], such as

1. Murnaghan [131] EOS

$$E_{\mathrm{M}}(V) = E_0 + B_0 V/B^{'}(((V_0/V)^{B^{'}}/(B^{'}-1)+1) - V_0 B_0/(B^{'}-1) \tag{58}$$

with the energies E_0 and volumes V of the references structures and the fitting parameter $B^{'} = dB/dp$ as the pressure derivative of the bulk modulus B,

2. Birch-Murnaghan [132] EOS

$$E_{\mathrm{BM}}(V) = E_0 + 9B_0V_0/16(\eta^2-1)^2(6+B^{'}(\eta^2-1)-4\eta^2) \tag{59}$$

with $\eta = (V_0/V)^{1/3}$,

3. Vinet [133, 134] EOS

$$E_{\mathrm{V}}(V) = E_0 + (9B_0V_0/(\eta_i^2)(1+(\eta_i(1-\eta)-1)\exp(\eta_i(1-\eta)))) \tag{60}$$

with $\eta_i = 3/2(B^{'}-1)$

and many more, can be used to produce a smooth fit of the data. Further, assuming constant temperature T and constant entropy S, the EOS can be used to access the bulk modulus B of a system (see Fig. 13) using

$$B_{\mathrm{EOS}}(V) = V\left(\frac{\partial^2 E_{\mathrm{EOS}}(V)}{\partial V^2}\right)_{T,S}. \tag{61}$$

It is possible to calculate molecules with approximations using pbcs, placing the molecule in the center of the unit cell and vary the lattice parameters such that the molecule

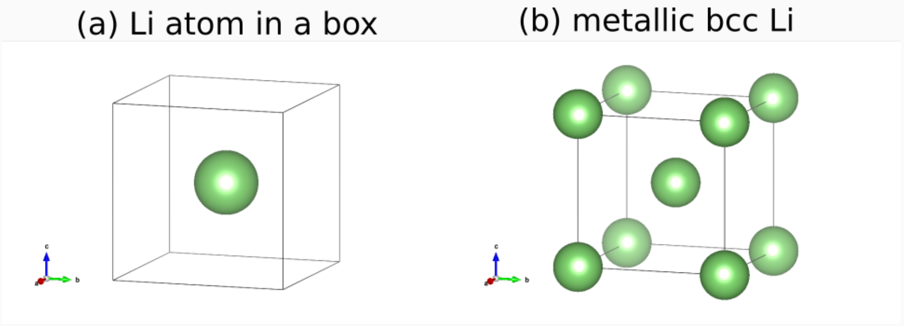

Figure 12: Introduction of periodic boundary conditions (pbcs) showing in (a) Li atom in a box and in (b) metallic body-centered cubic (bcc) Li with a lattice parameter a = 3.49 Å. The picture was produced by the author using Python with ASE, VESTA and Inkscape (see Appendix A).

cannot interact with its periodic images anymore (make the lattice parameters large enough). There are many libraries available which are able to perform this kind and various other kinds of calculations (e.g., for PYTHON there are the atomic simulation environment (ASE) [135], PYMATGEN [136], PWTOOLS [137], etc.).

For body centered cubic (bcc) lithium (Li) such EOS can be calculated using QUANTUM ESPRESSO (QE) and the ASE package for the EOS fitting procedure (see Fig. 13).

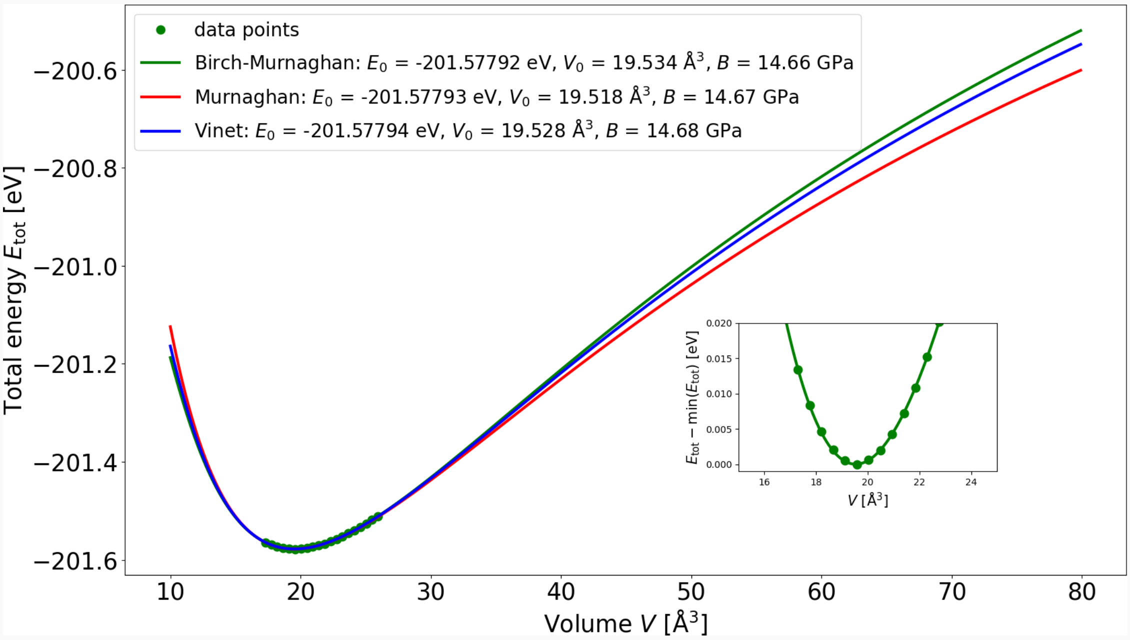

Figure 13: Example of equation of states for metallic bcc Li. For the calculation the QUANTUM ESPRESSO (QE) plane-wave pseudo-potential code was used. The inset provides a zoom around the equilibrium volume. Further, the LDA-PZ exchange-correlation functional, the PAW pseudo-potential `Li.pz-s-kjpaw_psl.0.2.1.UPF`, and a (24,24,24) k-grid were applied. From this simple calculation using the discussed EOS we get a bulk modulus $B_{\mathrm{M}} = 14.67$ GPa, $B_{\mathrm{BM}} = 14.66$ GPa and $B_{\mathrm{V}} = 14.68$ GPa which is in reasonable agreement with an experimental reference value of $B_{\mathrm{exp}} = 11.40$ GPa [138]. Similar results for the EOS and respective Bulk moduli can be computed using ase.eos and phonopy.qha.eos. The picture was produced by the author using QE and PYTHON with the MATPLOTLIB package (see Appendix A).

4.2 ELASTIC CONSTANTS

The aforementioned bulk modulus can be seen as a first elastic property. If a computational method is able to produce suitable results for elastic constants it can be assumed to deliver also suitable values for a phonon density of states (PDOS). Hooke's law connects the stresses σ_{ij} (stress tensor) and strains ε_{ij} (strain tensor) inside a material by the following linear relationship

$$\sigma_{ij} = \sum_{k,l}^{3} C_{ijkl}\varepsilon_{kl}, \tag{62}$$

where C_{ijkl} are elastic constants of the material.

It is convenient to describe elastic properties using Lagrangian theory of elasticity. Thus, the periodic system is treated as an anisotropic homogeneous elastic medium. [139]

Alternatively, the total energy of the system $E(\boldsymbol{\varepsilon})$ can be expressed in terms of a power series of the strain

$$E(\boldsymbol{\varepsilon}) = E_0 + V_0 \sum_{i,j}^{3} \sigma_{ij}\varepsilon_{ij} + \frac{V_0}{2!} \sum_{i,j,k,l}^{3} C_{ijkl}\varepsilon_{ij}\varepsilon_{kl} + ..., \tag{63}$$

with E_0 being the energy of the reference structure and V_0 being the volume of the reference structure. The physical stress tensor σ can be defined as

$$\sigma = \frac{1}{V}\frac{\partial E(\boldsymbol{\varepsilon})}{\partial \boldsymbol{\varepsilon}}. \tag{64}$$

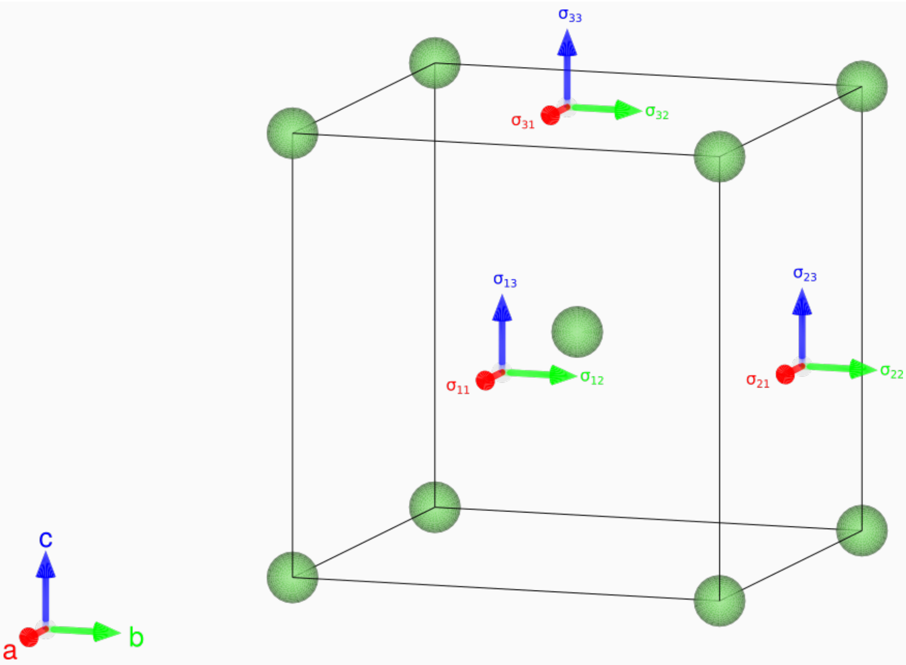

Figure 14: Visualization of the stress tensor using the unit cell of bcc Li. The picture was produced by the author using VESTA and INKSCAPE (see Appendix A).

The symmetric 3×3 stress tensor σ_{ij} (see Fig. 14) can be reduced

$$\sigma_{ij} = \begin{bmatrix} \sigma_{11} & \sigma_{12} & \sigma_{13} \\ \sigma_{21} & \sigma_{22} & \sigma_{23} \\ \sigma_{31} & \sigma_{32} & \sigma_{33} \end{bmatrix} \rightarrow \sigma_{\alpha} = \begin{bmatrix} \sigma_{11} \\ \sigma_{22} \\ \sigma_{33} \\ \sigma_{23} = \sigma_{32} \\ \sigma_{13} = \sigma_{31} \\ \sigma_{12} = \sigma_{21} \end{bmatrix} = \begin{bmatrix} \sigma_1 \\ \sigma_2 \\ \sigma_3 \\ \sigma_4 \\ \sigma_5 \\ \sigma_6 \end{bmatrix} \tag{65}$$

to a 6 dimensional vector σ using the Voigt notation. The symmetric 3×3 strain tensor ε_{ij} can be written similarly in the Voigt notation as

$$\varepsilon_{ij} = \begin{bmatrix} \varepsilon_{11} & \varepsilon_{12} & \varepsilon_{13} \\ \varepsilon_{21} & \varepsilon_{22} & \varepsilon_{23} \\ \varepsilon_{31} & \varepsilon_{32} & \varepsilon_{33} \end{bmatrix} \rightarrow \varepsilon_\alpha = \begin{bmatrix} \varepsilon_{11} \\ \varepsilon_{22} \\ \varepsilon_{33} \\ 2\varepsilon_{23} \\ 2\varepsilon_{13} \\ 2\varepsilon_{12} \end{bmatrix} = \begin{bmatrix} \varepsilon_1 \\ \varepsilon_2 \\ \varepsilon_3 \\ \varepsilon_4 \\ \varepsilon_5 \\ \varepsilon_6 \end{bmatrix}. \tag{66}$$

With that, Eq. (62) reduces to

$$\sigma_\alpha = \sum_{\alpha,\beta}^{6} C_{\alpha\beta}\varepsilon_\beta, \tag{67}$$

and Eq. (63) reduces to

$$E(\boldsymbol{\varepsilon}) = E_0 + V_0 \sum_{\alpha}^{6} \sigma_\alpha \varepsilon_\alpha + \frac{V_0}{2!} \sum_{\alpha,\beta}^{6} C_{\alpha\beta}\varepsilon_\alpha\varepsilon_\beta + ... \tag{68}$$

Typically one starts the calculation from a structure that has been optimized within the respective theory, i.e., having the optimal volume and minimal forces per atom. In such a situation the structure is stress-free $\sigma_\alpha = 0$, and the elastic constants can be calculated using the so called *stress approach*

$$C_{\alpha\beta} = \left.\frac{\partial \sigma_\alpha}{\partial \varepsilon_\beta}\right|_{\varepsilon=0} \tag{69}$$

or with the so called *energy approach*

$$C_{\alpha\beta} = \left.\frac{1}{V_0}\frac{\partial^2 E(\boldsymbol{\varepsilon})}{\partial \varepsilon_\alpha \partial \varepsilon_\beta}\right|_{\varepsilon=0}. \tag{70}$$

Born [140] formulated a condition for mechanical stability (elastic stability criterion) which is mathematically equivalent to the fact that all entries of the elastic matrix $C_{\alpha\beta}$ need to be positive and therefore $C_{\alpha\beta}$ is positive definite.

For the bulk modulus calculations, one isotropically contracts or expands the volume and calculate the respective energy. This is a first application of the energy approach. A more general expression for the bulk modulus B_{Voigt} depending on the elastic (stiffness) constants $C_{\alpha\beta}$ was given by Voigt [141]

$$B_{\text{Voigt}} = \frac{(C_{11} + C_{22} + C_{33}) + 2(C_{12} + C_{23} + C_{13})}{9}. \tag{71}$$

In the Voigt notation the 4th rang elastic tensor is a 6×6 matrix. For cubic lattice systems such a tensor is given by

$$C_{\alpha\beta} = \begin{bmatrix} C_{11} & C_{12} & C_{12} & 0 & 0 & 0 \\ C_{12} & C_{11} & C_{12} & 0 & 0 & 0 \\ C_{12} & C_{12} & C_{11} & 0 & 0 & 0 \\ 0 & 0 & 0 & C_{44} & 0 & 0 \\ 0 & 0 & 0 & 0 & C_{44} & 0 \\ 0 & 0 & 0 & 0 & 0 & C_{44} \end{bmatrix} \tag{72}$$

containing only three independent elastic constants. Calculating stress is implemented for instance in Quantum Espresso, thus one can use the stress approach to calculate elastic constants with this plane-wave code. The elastic code by Jochym and Badger [142] automatically performs the stress approach for codes providing stress for a given structure. A tool performing the stress as well as the energy approach is the ElaStic code by Golesorkhtabar et al. [139]. While the energy approach is in general applicable with any pbc code, one needs to evaluate the second energy derivative and, accordingly, one needs very high numerical accuracy.

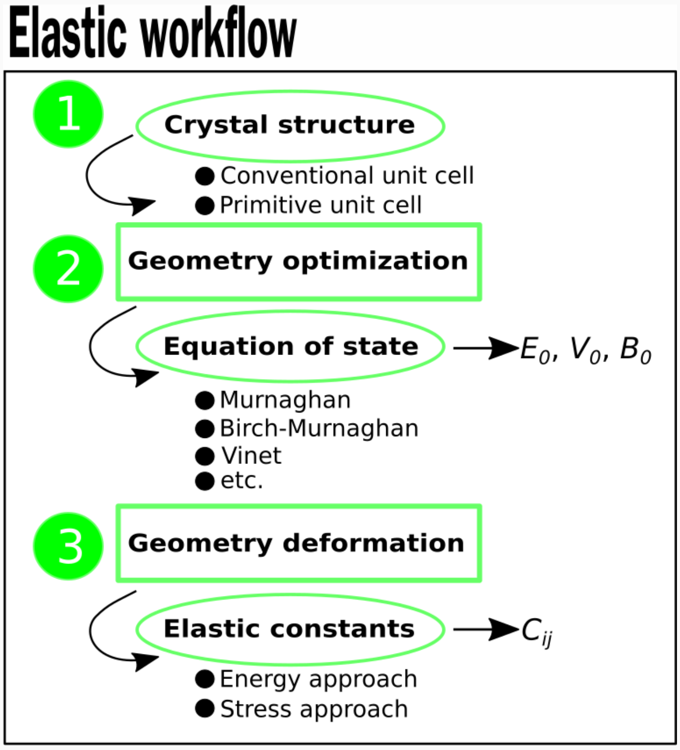

Figure 15: This Elastic workflow can be used to calculate elastic constants. It consists of three steps, (1) the analysis of the crystal structure, (2) the optimization of geometry and (3) the deformation of the optimized geometry. The picture was produced by the author using Inkscape (see Appendix A).

The author proposes the Elastic workflow (see Fig. 15), which is a three step procedure to calculate elastic constants. The first step is concerned with the analysis of the system of interest, e.g., determination of symmetry and whether a primitive or conventional unit cell should be used for the calculation. For the second step an equation of state is used to determine the optimal volume and the optimal lattice parameters for the system. With the third step the elastic constants are calculated using the energy- or stress approach. For the first step of the Elastic workflow it is important to determine the symmetry of the crystalline structure. Further, the choice whether the crystal should be calculated using the conventional or the primitive cell can be essential for post-processing analysis. For a bcc crystal this makes a difference for the volume $V_{\text{bcc}}^{\text{primitive}} = 1/2 V_{\text{bcc}}^{\text{conventional}}$, the respective lattice parameters and the number of atoms within the unit cell.

For bcc Lithium one can design and realize a Elastic workflow (*WF*) using Quantum Espresso (QE) and the THERMO_PW package *WF(THERMO-PW,ELASTIC)*, which automatically gives access to the elastic constants

$$C_{\alpha\beta} = \begin{bmatrix} 11.78 & 11.00 & 11.01 & 0 & 0 & 0 \\ 11.01 & 11.78 & 11.01 & 0 & 0 & 0 \\ 11.01 & 11.01 & 11.78 & 0 & 0 & 0 \\ 0 & 0 & 0 & 9.80 & 0 & 0 \\ 0 & 0 & 0 & 0 & 9.80 & 0 \\ 0 & 0 & 0 & 0 & 0 & 9.80 \end{bmatrix} \tag{73}$$

and the bulk moduli calculated from the EOS $B^{\mathrm{WF(QE,EOS\text{-}BM)}} = 14.66$ GPa and from the elastic constants $B^{\mathrm{WF(THERMO\text{-}PW,ELASTIC)}} = 11.27$ GPa. The `Li.pz-s-kjpaw_psl.0.2.1.UPF` pseudo-potential, the exchange-correlation functional LDA-PZ and a 24x2424 k-grid for the primitive unit cell was used for this calculation.

A similar Elastic workflow *WF(QE,ELASTIC)* can be designed using QE and an ASE QE calculator interface as well as the elastic ASE code [142]. This workflow can be adapted to any ASE calculator providing the stress tensor as output (e.g., GPAW using the plane-wave mode). The elastic constants calculated using these workflows for bcc lithium are summarized in Tab. 1.

The two proposed Elastic workflows produce nearly the same bulk moduli derived from EOS and elastic constants, while the elastic constants themselves slightly differ from each other (see Tab. 1). This is obvious as the calculated elastic constants are numerically very sensitive depending on the used maximal strain $\varepsilon_{\max}$ as well as the applied deformations. The standard deviation with respect to the usage of different k-points, plane-wave codes and different implementations of the elastic workflow is one order of magnitude higher than the respective standard deviation for the EOS workflow. A similar sensitivity of elastic constants to the used approaches (e.g., plane-wave pseudo-potential and all-electron) as well as other numerical parameters (e.g., k-points) were observed by Dal Corso [143] in case for hcp Be. For Li bcc the highest standard deviation are observed for the calculated C_{11} and C_{44} constants (see Tab. 1). Also, the standard deviation of experimental low temperature values for these elastic constants is higher than for the other elastic constants. The numerical differences between similar calculations is smaller for the conventional unit cell setting than for the respective primitive unit cell setting. The bulk modulus calculated from the EOS overestimates the experimental value by roughly 2 GPa, while the bulk modulus calculated from the Voigt equation using elastic constants underestimates the bulk modulus by roughly 2.6 GPa.

To show the general applicability of the proposed workflows, they are applied to study Si (diamond). The calculated bulk moduli and elastic constants are presented in Tab. 2. The magnitude of the bulk modulus and of the elastic constants with respect to each other is predicted correctly. The bulk modulus calculated from EOS show similar errors as determined for Li. The errors in the elastic constants and the bulk modulus calculated from these values are higher than the respective errors of Li.

A parameter workflow (see Fig. 16) is proposed to determine an optimal parameter set with respect to computational accuracy and effort. The parameter workflow is applied to Li (see Fig. 17) and Si (see Fig. 18). The objective defining the optimal value

Table 1: Numerical accuracy of elastic properties for Li (bcc) for conventional unit cell (CUC) as well as primitive unit cell (PUC) with respect to experimental values. Elastic constants derived from plane-wave pseudo-potential codes for an existing workflow (THERMO_PW) using QUANTUM ESPRESSO (QE), and our own workflows using QE (LDA-PZ) and GPAW (LDA-PW) are compared. All calculations of elastic constants are based on the stress approach. The numerical parameters were optimized with the parameter workflow (see Fig. 17, E_{cut} = 680.2849033 eV = 50 Ry and k-points = (12x12x12)). For each deformation 5 configurations were used for our workflows with a maximal relative strain $\varepsilon_{\max}$ = 0.0075. The THERMO_PW workflow with standard setup uses 4 configurations also with a maximal relative strain of a $\varepsilon_{\max}$ = 0.0075. The mean values $\overline{m}$ and the deviation σ of each property for CUC, PUC and low temperature (low-T) experiment are provided.

workflow	Parameters	$V_0^{\text{EOS-BM}}$ [Å^3]	$B^{\text{EOS-BM}}$ [GPa]	B^{Voigt} [GPa]	C_{11} [GPa]	C_{12} [GPa]	C_{44} [GPa]
CUC	$N_{k-\text{points}}$						
QE	(12x12x12)	19.52	14.70	11.77	13.35	10.98	10.69
QE	(24x24x24)	19.53	14.65	8.89	6.29	10.18	7.47
GPAW	(12x12x12)	19.16	15.11	10.28	11.60	9.63	8.32
GPAW	(24x24x24)	19.16	15.06	10.29	9.05	10.91	8.68
$\overline{m}$		19.34	14.88	10.31	10.07	10.43	8.79
σ		±0.18	±0.21	±1.02	±2.67	±0.56	±1.18
PUC	$N_{k-\text{points}}$						
THERMO_PW	(12x12x12)	19.57	15.36	11.18	11.06	11.24	14.21
THERMO_PW	(24x24x24)	19.56	14.69	11.27	11.78	11.01	9.80
QE	(12x12x12)	19.52	14.63	8.50	9.03	8.23	13.27
QE	(24x24x24)	19.53	14.66	9.93	8.65	10.57	9.73
GPAW	(12x12x12)	19.16	15.07	10.29	13.00	8.93	12.80
GPAW	(24x24x24)	19.17	15.07	10.30	9.44	10.73	8.39
$\overline{m}$		19.42	14.91	10.24	10.49	10.12	11.37
σ		±0.18	±0.27	±0.92	±1.58	±1.13	±2.15
Reference low-T	T [K]						
Exp. [144, 145]	low	-	13.3	13.3	13.5	11.4	8.8
Exp. [146]	78	-	12.90	12.90	14.44	12.11	10.94
Exp. [147]	78	-	13.30	13.30	14.81	12.48	10.77
$\overline{m}$		-	12.90	12.90	14.19	11.93	10.23
σ		-	±0.31	±0.31	±0.40	±0.33	±0.72
Reference high-T	T [K]						
Exp. [146]	110	-	12.80	12.80	14.29	12.03	10.63
Exp. [146]	150	-	12.60	12.60	14.10	11.80	10.26
Exp. [147]	155	-	12.50	12.50	14.01	11.79	9.97
Exp. [146]	190	-	12.40	12.40	13.92	11.72	9.89
Exp. [147]	195	-	12.00	12.00	13.42	11.25	9.60
Exp. [146]	298	-	12.00	12.00	13.42	11.30	8.89
Error analysis	max						
$\Delta\overline{m}$(EXP-CUC)	|4.12|		−1.98	2.59	4.12	1.51	1.44
σ	|3.07|		±0.52	±1.33	±3.07	±0.89	±1.90
$\Delta\overline{m}$(EXP-PUC)	|3.70|		−2.01	2.65	3.70	1.82	−1.14
σ	|2.87|		±0.58	±1.23	±1.98	±1.46	±2.87

depends on the specific task. For the elastic workflow error analysis this objective was to get a reasonable accuracy and converged k-points as well as a comparable parameter space for all codes used for this investigations. For the elastic workflow investigations of Li and Si, the numerical parameters were chosen to be slightly lower or higher compared to determined optimal values (cmp. Fig. 17 and Tab. 1, cmp. Fig. 17 and Tab. 2).

Table 2: Numerical accuracy of elastic properties for Si (diamond). Comparison of different elastic workflows for plane-wave pseudo-potential codes for an existing workflow (THERMO_PW) using QUANTUM ESPRESSO (QE), and our own workflows using QE and GPAW. All calculations of elastic constants are based on the stress approach. The numerical parameters were optimized with the parameter workflow (see Fig. 18, E_{cut} = 1088.4554419 eV = 80 Ry and k-points = (4x4x4)). For each deformation 5 configurations were used for our workflows with a maximal relative strain ε_{max} = 0.0075. The THERMO_PW workflow with standard setup uses 4 configurations also with a maximal relative strain of a ε_{max} = 0.0075. The mean values $\overline{m}$ and the deviation σ of each property for CUC, PUC and experiment are provided.

workflow	$N_{k-\text{points}}$	$V_0^{\text{EOS-BM}}$ [Å^3]	$B^{\text{EOS-BM}}$ [GPa]	B^{Voigt} [GPa]	C_{11} [GPa]	C_{12} [GPa]	C_{44} [GPa]
CUC	$N_{k-\text{points}}$						
GPAW	(4x4x4)	39.51	96.03	77.83	126.67	53.42	112.51
GPAW	(10x10x10)	39.51	95.83	91.62	152.55	61.15	97.14
QE	(4x4x4)	39.40	93.76	88.11	151.50	56.41	98.25
$\overline{m}$		39.47	95.21	85.85	143.57	56.99	102.63
σ		±0.05	±1.03	±5.85	±11.96	±3.18	±7.00
PUC							
THERMO_PW	(4x4x4)	39.40	94.32	94.51	160.10	61.71	80.08
THERMO_PW	(10x10x10)	39.40	94.19	94.36	159.87	61.61	77.94
QE	(4x4x4)	39.65	94.16	91.06	153.63	59.76	97.52
QE	(10x10x10)	39.41	93.68	88.63	151.51	57.19	97.94
QE	(20x20x20)	39.41	93.62	88.10	151.51	56.40	98.25
$\overline{m}$		39.45	93.99	91.33	155.32	59.33	90.35
σ		±0.10	±0.29	±2.72	±3.88	±2.20	±9.28
Reference	T [K]						
Exp. [148]	300	-	97.8	97.8	165.6	63.9	79.5
Exp. [149, 150]	300	-	97.9	97.9	165.7	63.9	79.6
Exp. [150, 151]	<100	-	99.2	99.2	167.7	65.0	80.4
$\overline{m}$		-	98.30	98.30	166.33	64.27	79.83
σ		-	±0.64	±0.64	±0.97	±0.52	±0.40
Error analysis	max						
$\Delta\overline{m}$(EXP-CUC)	$\lvert 22.80 \rvert$		3.09	12.45	22.76	7.27	-22.80
σ	$\lvert 12.93 \rvert$		±1.66	±6.49	±12.93	±3.70	±7.40
$\Delta\overline{m}$(EXP-PUC)	$\lvert 11.01 \rvert$		4.31	6.97	11.01	4.93	-10.51
σ	$\lvert 9.69 \rvert$		±0.92	±3.36	±4.85	±2.72	±9.69

This procedure allows to estimate the intrinsic errors of the elastic workflow. The elastic workflow using LSDA DFT to study Li and Si with different codes provided same magnitudes as well as correct trends comparing the elastic constants with experimental values. The absolute values will always have an error compared to experimental values, as experimental values themselves have errors. In general, a theory cannot entirely reproduce experimental data as this would include that the theory will also reproduce experimental errors.

Having workflows which provide the minimal volume, respective lattice parameters as well as an understanding of the elastic properties, one can go one step further and investigate the thermodynamic properties of the system.

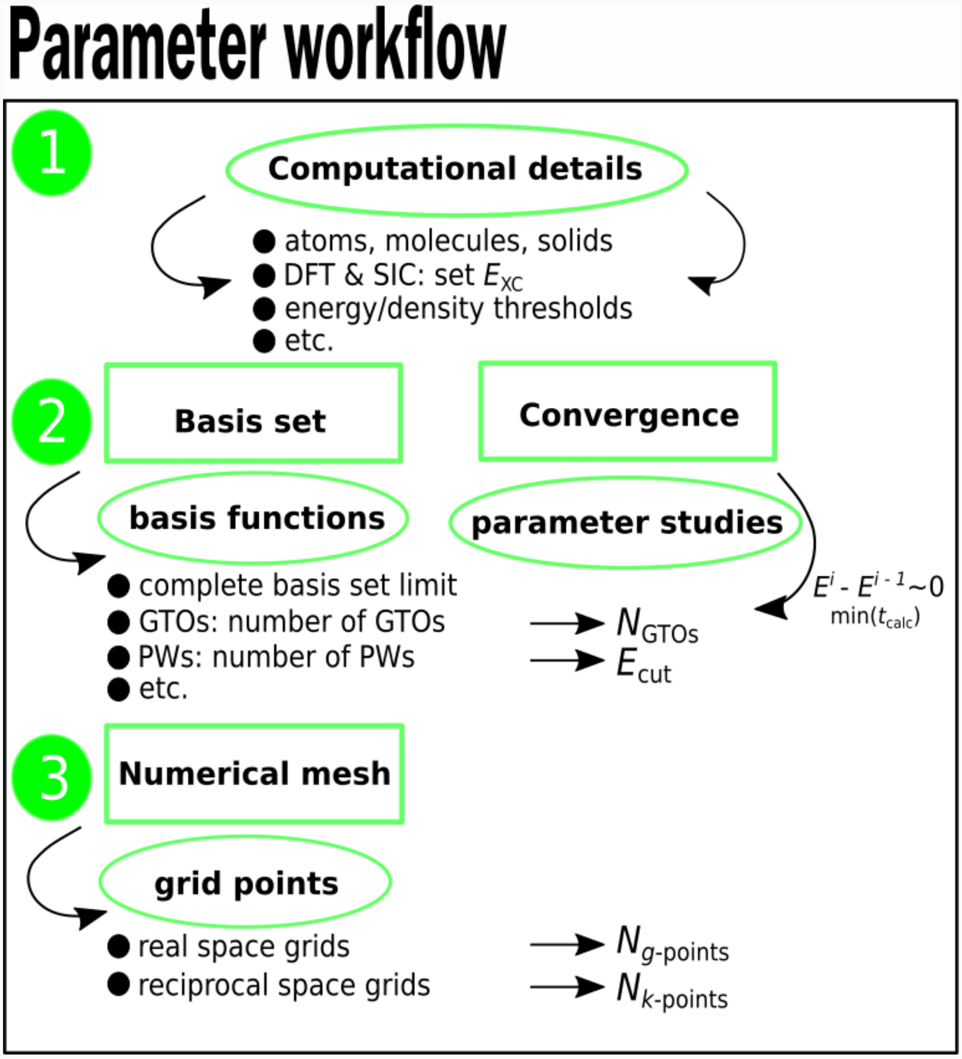

Figure 16: This Parameter workflow can be used to determine the optimal set of numerical parameters for a calculation. The picture was produced by the author using INKSCAPE (see Appendix A).

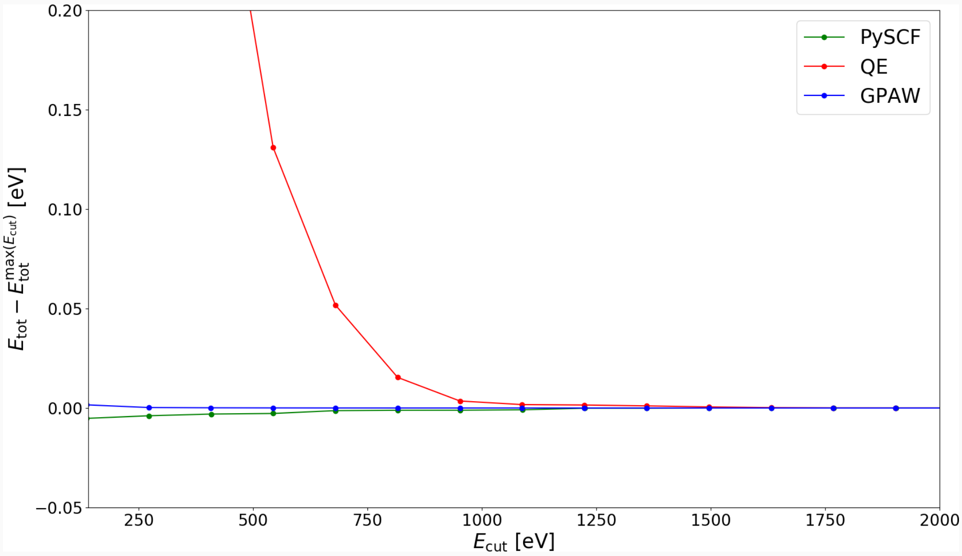

(a) E_{cut} convergence

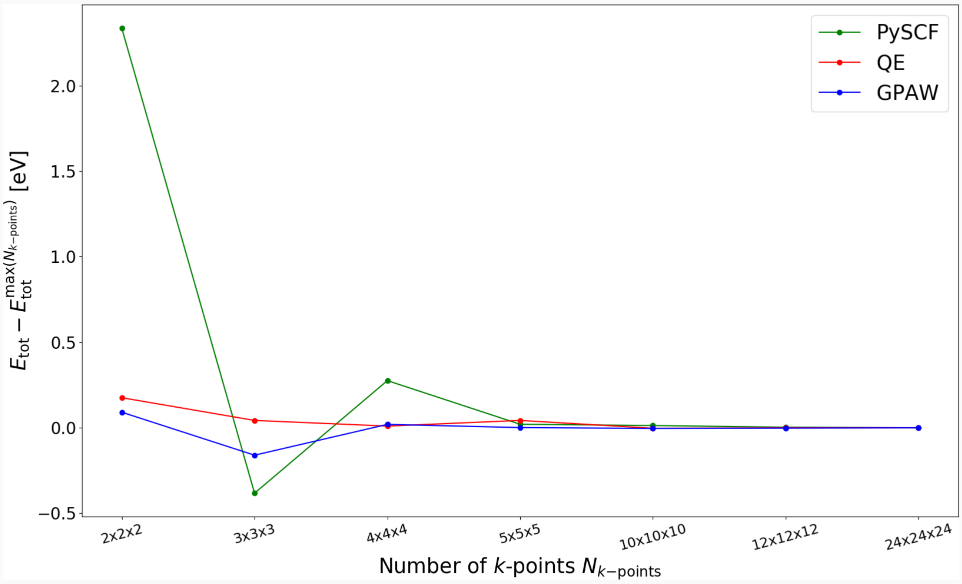

(b) k-points convergence

Figure 17: Parameter workflow for Li (bcc), (a) showing the convergence of E_{cut} for different DFT codes (PySCF, QE, GPAW) using a (12x12x12) k-points set, and (b) indicating an optimal set of k-points (12x12x12) using a fixed E_{cut} = 680.2849033 eV = 50 Ry = 25 Ha. The picture was produced by the author using Python with the Matplotlib package (see Appendix A).

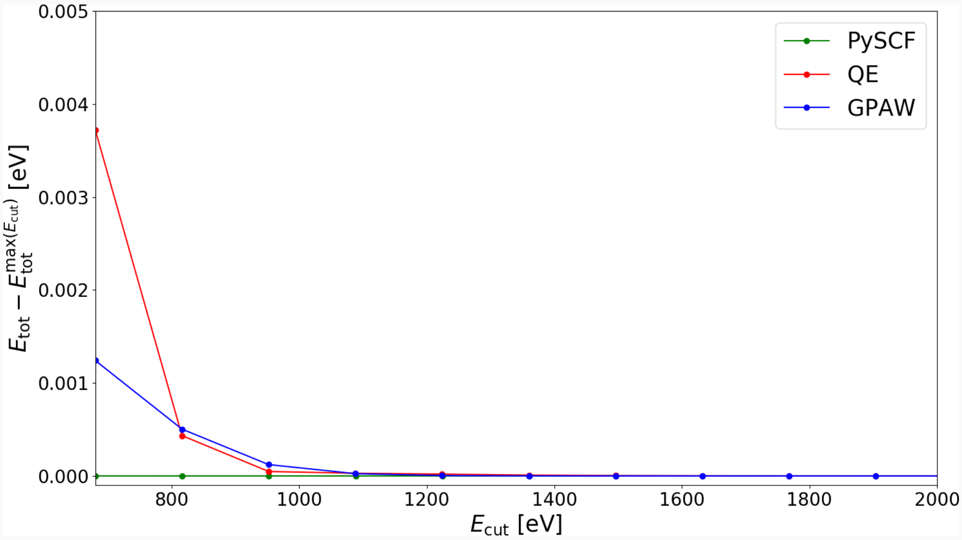

(a) E_{cut} convergence

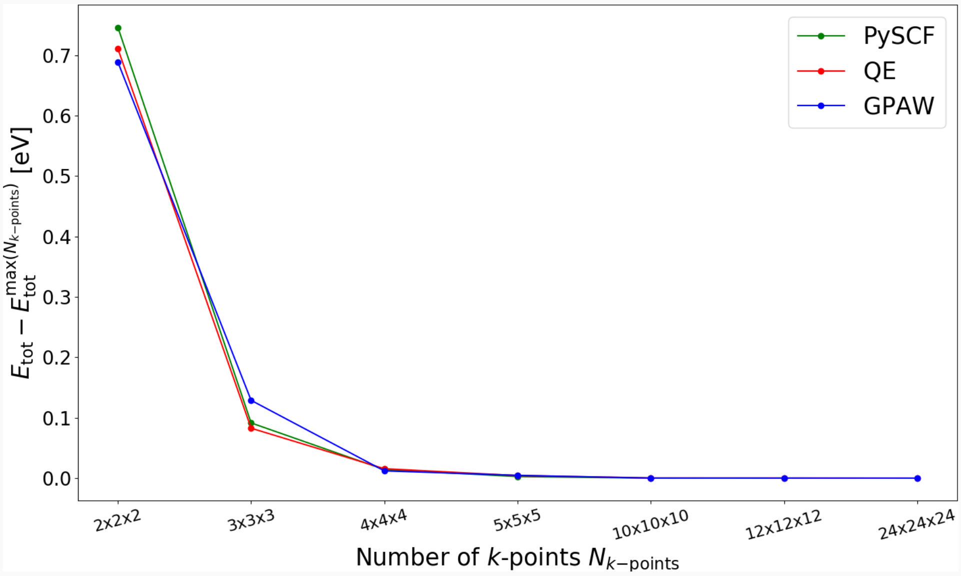

(b) k-points convergence

Figure 18: Parameter workflow for Si (diamond structure), (a) showing the convergence of E_{cut} for different DFT codes (PySCF, QE, GPAW) using a (10x10x10) k-points set, and (b) indicating an optimal set of k-points (4x4x4) using a fixed $E_{\text{cut}} = 680.2849033$ eV = 50 Ry = 25 Ha. The picture was produced by the author using Python with the Matplotlib package (see Appendix A).

4.3 HARMONIC APPROXIMATION

From a computational point of view thermodynamic properties for solids can be studied using lattice dynamics. The collective motion of the lattice, i.e., vibrations, are the subject of lattice dynamics. Displacing symmetry non-equivalent atoms within the unit cell leads to changes in the forces per atoms as well as the energy of the system.

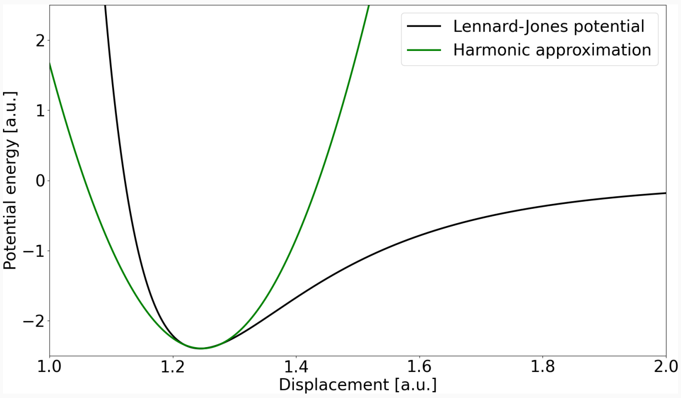

Figure 19: Harmonic approximation sketch using a simple Lennard-Jones potential [152] $V_{\mathrm{LJ}} = 4\varepsilon((\sigma/r)^{12}) - (\sigma/r)^{6})$ (ε is the potential well and σ the finite distance were the inter-particle potential is zero) and a quadratic fit of this potential around the equilibrium. Clearly, the latter approximation is only valid very close to this equilibrium. The Lennard-Jones potential is only used for this visualization purpose as this potential itself is limited in the application to real materials [153]. An alternative to the Lennard-Jones potential is the Buckingham potential [154] $V_{\mathrm{B}} = A \exp(-Br) - C/r^{6}$ (A, B, C are constants). A Lennard-Jones potential is used in the universal force field (UFF) [8, 155, 156] and the universal force field for MOFs (UFF4MOF) [8, 157] to model non-bonded van-der-Waals interactions. On the other hand, force fields like the BTW-FF [8, 9] and the VMOF [11] use a Buckingham potential to model the same kind of interactions.

The energy of the system can be expressed as a function of these displacements. Applying only small displacements with respect to inter-atomic spacing allows to write this energy as a quadratic function of displacements. Thus, the potential in which the particles can move can be expanded as a Taylor series around the equilibrium structure.

The ground state total energy in some configurations $\{u_n\}$ expanded as a Taylor expansion can be written as

$$\begin{aligned} U(\{u_n\}) = U_0 & \\ & + \frac{1}{1!}\sum_{n}\left(\frac{\partial U}{\partial u_n}\right)_{\{u_n\}=0} u_n \\ & + \frac{1}{2!}\sum_{nn'}\left(\frac{\partial^2 U}{\partial u_n \partial u_{n'}}\right)_{\{u_n\}=0} u_n u_{n'} \\ & + \frac{1}{3!}\sum_{nn'n''}\left(\frac{\partial^3 U}{\partial u_n \partial u_{n'} \partial u_{n''}}\right)_{\{u_n\}=0} u_n u_{n'} u_{n''} \\ & + \mathcal{O}\left(u_n^4\right) \end{aligned} \tag{74}$$

where all derivatives are evaluated at the equilibrium positions $\{u_n\} = 0$. The linear term vanishes, because the starting geometry is an equilibrium geometry and the forces (first-order derivative of the energy)

$$F_{n,\mathrm{eq}} = \left(-\frac{\partial U}{\partial\{u_n\}}\right)_{\mathrm{eq}} = 0 \tag{75}$$

vanish. This can be realized using an equation of states while relaxing the atoms for several volumes or a gradient based geometry optimization using further constraints for the unit cell. At equilibrium, the forces per atom and the unit cell stress are minimal. Assuming sufficiently small displacements, $U(\{u_n\})$ is truncated to quadratic terms (see Fig. 19) within the so called harmonic approximation (HA). All terms of higher order, i.e., anharmonic contributions are neglected. Therefore, Eq. (74) can be written as

$$U(\{u_n\}) = U_0 + E_{\mathrm{vib}} \tag{76}$$

where the equilibrium lattice energy U_0 can be calculated with DFT or sufficiently accurate force fields methods. For systems with high symmetry, even periodic coupled-cluster approaches [158] can be used to evaluate this energy.

In statistical physics, several physical quantities are derived from a so called partition function [159]

$$Z = e^{-U_0/(k_\mathrm{B}T)} \prod_{\boldsymbol{q},\nu} \frac{e^{-\hbar\omega(\boldsymbol{q},\nu)/(2k_\mathrm{B}T)}}{1 - e^{-\hbar\omega(\boldsymbol{q},\nu)/(k_\mathrm{B}T)}} \tag{77}$$

where $\boldsymbol{q}$ are the vibrational wave vectors, ν are the modes and k_B is the Boltzmann constant. The vibrational free energy can be obtained by

$$F_{\mathrm{vib}} = -k_\mathrm{B}T \ln Z \tag{78}$$

$$F_{\mathrm{vib}} = U_0 + \frac{1}{2}\sum_{\boldsymbol{q},\nu} \hbar\omega(\boldsymbol{q},\nu) + \sum_{\boldsymbol{q},\nu} \ln\left(1 - e^{-\hbar\omega(\boldsymbol{q},\nu)/(k_\mathrm{B}T)}\right) \tag{79}$$

$$F_{\mathrm{vib}} = U_0 + k_\mathrm{B}T \sum_{\boldsymbol{q},\nu} \ln\left[2\sinh\left(\frac{\hbar\omega(\boldsymbol{q},\nu)}{2k_\mathrm{B}T}\right)\right] \tag{80}$$

$$F_{\mathrm{vib}} = U_0 + E_{\mathrm{vib}} \tag{81}$$

where the summation over frequencies $\omega(\boldsymbol{q},\nu)$ in Eq. (80) can be replaced by an integral over the phonon density of states (PDOS) $g(\omega)$

$$F_{\mathrm{vib}} = U_0 + k_\mathrm{B}T \int \mathrm{d}\omega\, g(\omega) \ln\left[2\sinh\left(\frac{\hbar\omega(\boldsymbol{q},\nu)}{2k_\mathrm{B}T}\right)\right]. \tag{82}$$

The PDOS is normalized to the total number of modes

$$\int \mathrm{d}\omega\, g(\omega) = 3N \tag{83}$$

and can be calculated according to

$$g(\omega) = \int \mathrm{d}^3\boldsymbol{q}\,\delta(\omega - \omega(\boldsymbol{q})). \tag{84}$$

The PDOS is a central property. Therefore, reference data from methods like neutron scattering or other calculations like molecular dynamic calculations can be used for comparison. For molecules the harmonic approximation can be used to calculate the normal modes, giving access to IR- and Raman spectra. A detailed overview about lattice dynamics is given by [159, 160]. This section is based on articles written during this thesis [161, 162]. For solids the frozen phonon method (or sometimes called finite difference method) or linear response theory can be used to access the PDOS.

4.4 QUASI-HARMONIC APPROXIMATION

The free Gibbs energy G in the quasi-harmonic approximation (QHA) is determined by applying the harmonic approximation for a set of different volumes and searching for a unique minimum using the following transformation

$$G(T, p) = \min_{V}[F_{\text{vib}}(V, T) + pV]. \tag{85}$$

Thus, using the harmonic and the (quasi)-harmonic approximation, all other thermodynamic properties can be derived from the free energy $F(V, T)$ and the free Gibbs energy $G(T, p)$ using

$$C_V(T) = \left(\frac{\partial E(V,T)}{\partial T}\right)_V \tag{86}$$

$$C_p(T) = -T\left(\frac{\partial^2 G(T,p)}{\partial T^2}\right)_p \tag{87}$$

$$\alpha_V(T) = \frac{1}{V(T)}\left(\frac{\partial V(T)}{\partial T}\right)_p \tag{88}$$

$$B_T(V) = V\left(\frac{\partial^2 F(V,T)}{\partial V^2}\right)_T \tag{89}$$

$$\gamma = V\alpha_V B_T / C_V, \tag{90}$$

with $C_V(T)$ being the isochoric (constant volume) heat capacity, $C_p(T)$ being the isobaric (constant pressure) heat capacity, $\alpha_V(T)$ being the thermal expansion coefficient, $B_T(V)$ being the volume-dependent Bulk modulus, and γ being the dimensionless Grüneisen parameter.

In this chapter, mechanical properties like elastic constants $C_{\alpha\beta}$, bulk modulus B and PDOS as well as thermodynamic properties, i.e., used in QHA, such as the free Gibbs energy $G(T, p)$ have been introduced. It was shown that the results of numerical computations depend on the used numerical parameters. Workflows as conceptual guides were introduced. In detail, it was shown how the parameter workflow can be used to determine an optimal set of numerical parameters. In the next chapter, other workflows will be introduced to calculate thermodynamic properties efficiently.

Part II

THERMODYNAMICS OF SOLID STATE SYSTEMS

This part of the thesis describes a new method for the calculation of isobaric heat capacities of periodic systems and its application to battery materials. In addition, it introduces workflows enabling the usage of the quasi-harmonic approximation for various force-fields to calculate thermodynamical properties of metal-organic frameworks. For molecules and atoms the G2-1 workflow to calculate enthalpies of formation and ionization potentials is presented.

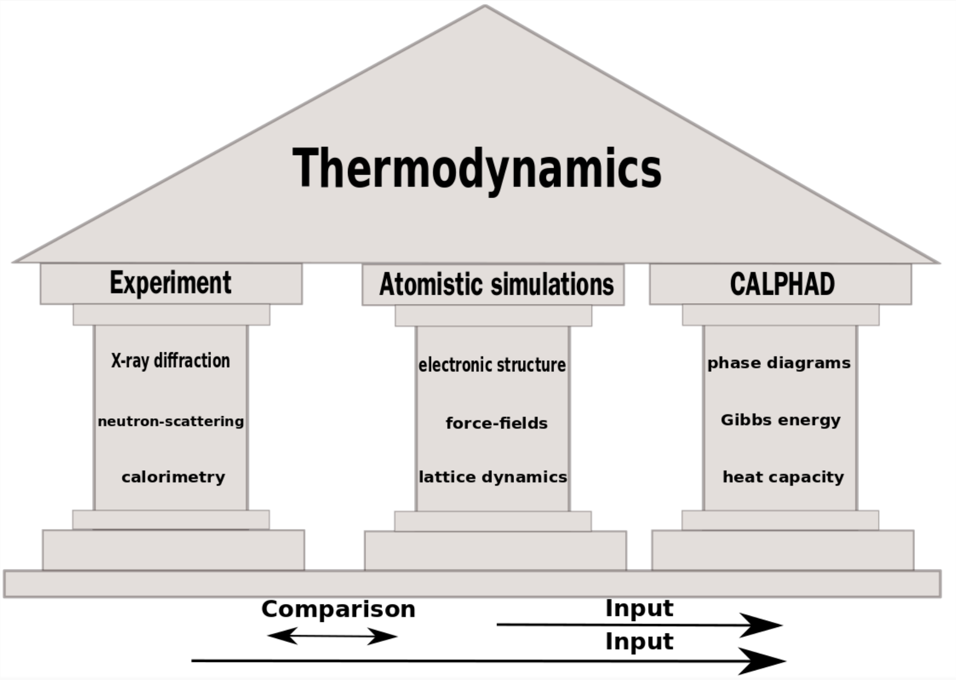

Figure 20: Thermodynamics of materials is a broad field, mainly built up by three major pillars, namely experiment, atomistic simulations and the CALPHAD method. Only a cooperation of all three of them allows for a detailed understanding of thermodynamics of materials.

5

METHODICAL DEVELOPMENTS

5.1 C_p-MD WORKFLOW

The understanding of thermodynamical material properties can be based on three pillars: experiment (e.g., X-ray diffraction (XRD), neutron-scattering, differential scanning calorimetry (DSC), etc.), atomistic simulations (e.g., electronic structure calculations), and the so called CALculation of PHAse Diagrams (CALPHAD) modelling [163]. Experimental methods can deliver structural information about battery materials, but often even neutron-scattering is not able to accurately determine lithium position in crystal structures. Many physical properties (e.g., phonon densities, free energies, heat capacities, etc.) depend on the crystal structure.

Electronic structure methods can often clarify structural uncertainties with the help of energy surface calculations, relaxation methods, or molecular dynamics. Computational methods can also be employed to calculate thermodynamic data from an experiment-independent point of view [164].

This data is useful to get insight in complex physical behaviors like diffusion effects [164] or phase transitions [165]. Additionally, theoretical investigations at these levels can provide thermodynamic data for structures which are not accessible by experiments (e.g., metastable phases).

The CALPHAD method can be based on input from both experiment as well as atomistic calculations to model phase diagrams for binary, ternary or even more complex systems.

This thesis focuses on computational aspects of thermodynamics (also called computational thermodynamics). Important physical properties are calculated from structural input quantities without any fit to experimental data. State-of-the-art computational thermodynamics is based on DFT and QHA, which is limited by the large computational cost. The advantage of DFT is the accuracy for total energies and forces. Thermodynamics based on molecular dynamics is limited by the given accuracy of the used force field approximation. The advantage of such methods is that configuration changes, diffusion effects or very large volume expansions or contractions can be calculated in an appropriate computational time. Additionally, force field methods offer the opportunity for long time molecular dynamics and thus reliable statistics. In this work, the author provides a pathway to combine the advantages of both methods to get a deeper understanding of lithium silicides Li_xSi_y. The focus of these investigations is on the crystalline structures of this battery material class. In this respect DFT [166] calculations are very accurate and deliver a good description of the electronic structure.

Lattice dynamics is a broad field and the most commonly used methods are based on HA and QHA. HA in the field of DFT is used to calculate IR- and RAMAN spectra for molecular systems while QHA is generally used to calculate thermodynamical properties of bulk systems. There are two common methods in DFT, the direct method (also called frozen phonon method) and the density functional perturbation theory (DFPT, also called linear response). Both methods allow to calculate the dynamical matrix, which is the Fourier transform of the force constant matrix. This dynamical matrix can be used to calculate the phonon dispersion relation or PDOS. In contrast to DFPT, where only unit cells are used, the direct method is based on supercells. Thus, the direct method may become computationally more demanding than DFPT. However, it is possible to extend the supercell approach to include anharmonic effects [167], while DFPT is restricted to harmonic effects. For large unit cells as in the case of $\mathrm{Li}_x\mathrm{Si}_y$ phases, both methods become computationally demanding.

In the field of classical molecular dynamics there are two basic methods to calculate the phonon density of states as well. Both methods are based on the fluctuation dissipation theorem. The first one uses the velocity autocorrelation function (VAF)

$$C_{\mathrm{VAF}}(t) = \langle \mathbf{v}(0)\mathbf{v}(t)\rangle \;/\; \langle \mathbf{v}(0)\mathbf{v}(0)\rangle \tag{91}$$

to calculate the vibrational density of states (VDOS, also called PDOS or power spectra) from the velocities $\mathbf{v}$ of the atoms (during a long MD run)

$$\mathrm{PDOS}(\omega) = \left| \frac{1}{\sqrt{2\pi}} \int_{-\infty}^{\infty} dt e^{i\omega t} C_{\mathrm{VAF}}(t) \right|^2 . \tag{92}$$

The isochoric heat capacity C_V can be calculated from this vibrational/phonon density of states using

$$C_V(T) = \left(\frac{\partial E_{\mathrm{vib}}}{\partial T}\right)_V \tag{93}$$

$$= k_{\mathrm{B}} \int \mathrm{PDOS}(\omega) \left(\frac{\hbar\omega}{2k_{\mathrm{B}}T}\right)^2 \frac{d\omega}{\sinh^2 \frac{\hbar\omega}{2k_{\mathrm{B}}T}} . \tag{94}$$

The second method is based on the fluctuations/displacements of atoms during a molecular dynamics simulation [168–170]. During the MD run the displacements of the atoms are recorded. Afterwards, Green's function coefficients are evaluated in reciprocal space, which are given by the ensemble average of the scalar product of the atomic displacements [168]. From these Green's function coefficients the force constants, the dynamical matrix, and with that $\mathrm{PDOS}(\omega)$ can be calculated.

The linear thermal expansion coefficient α_l can be determined according to

$$\alpha_l = \frac{1}{V}\left(\frac{\partial V}{\partial T}\right)_p . \tag{95}$$

For the evaluation of this expression it is necessary to perform a set of N molecular dynamics simulation with NPT ensembles for different temperatures T and fixed pressures p. From a specific MD run the mean volume $\langle V\rangle_{\mathrm{NPT},r}$ and for all MD runs the global minimum volume $\min_{\forall r} \langle V\rangle_{\mathrm{NPT},r}$ can be calculated. This leads to an expression of the linear thermal expansion coefficient

$$\alpha_l = \frac{1}{N} \sum_{r=1}^{N} \frac{\Delta \langle V' \rangle_{\mathrm{NPT},r}}{\Delta \langle T \rangle_{\mathrm{NPT},r}} , \tag{96}$$

with r indicating a specific MD run. The reduced volume $\langle V' \rangle_{\mathrm{NPT},r}$ is given by

$$\langle V' \rangle_{\mathrm{NPT},r} = \left(\frac{\langle V \rangle_{\mathrm{NPT},r}}{\min_{\forall r} \langle V \rangle_{\mathrm{NPT},r}} \right)_p . \tag{97}$$

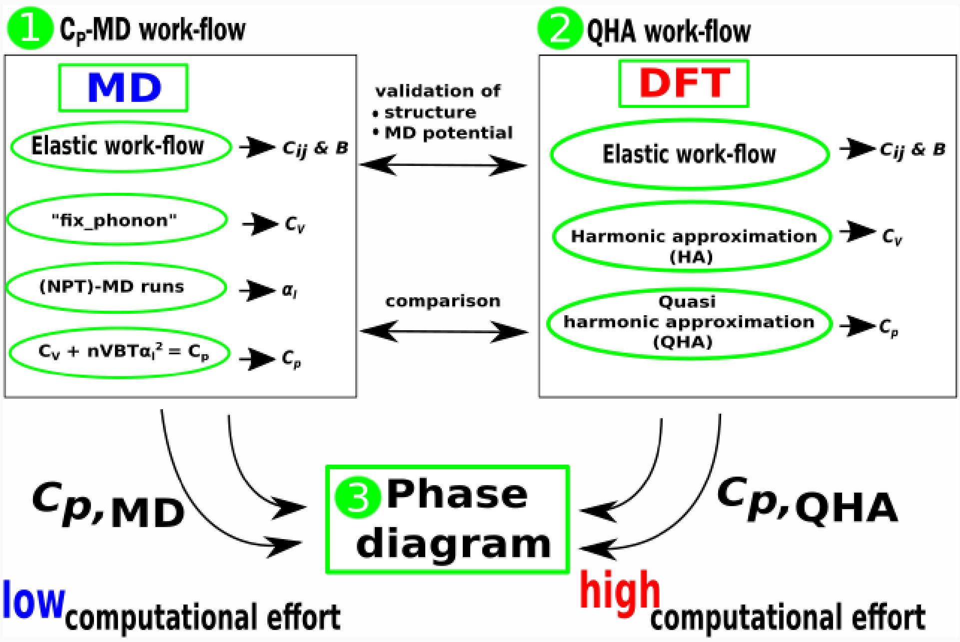

Figure 21: C_p-*MD* workflow as implemented in this work. The picture has been produced by the author using Inkscape (see Appendix A).

The isobaric heat capacity C_p can be computed with the knowledge of the bulk modulus B, the linear thermal expansion coefficient α_l and the isochoric heat capacity C_V

$$C_p - C_V = nVBT\alpha_l^2, \tag{98}$$

with n being the mole number. The evaluation of the equations using MD simulations are referred to as C_p-*MD* workflow (see Fig. 21). Sometimes the characteristics of structural changes in huge simulation cells during MD simulations are difficult to analyze.

The radial pair distribution function (RPDF) $g(r)$ can deliver additional information on changes in the coordination sphere of specified atoms at different temperatures. The RPDF is the average number of atoms in a shell $[r, r + dr]$ around an atom at $r = 0$. For each atom i = 1, ..., N the number of atoms j in the shell with the radius $r_{ij} = |\mathbf{R}_i - \mathbf{R}_j|$ $(r < r_{ij} \leq r + dr)$ are counted [171]

$$dN(r) = \rho 4\pi r^2 g(r) dr = n(r) dr, \tag{99}$$

where $\rho = N/V$ is the average density and the pair distribution function (PDF) $n(r)$ is given by

$$n(r) = \frac{1}{N} \langle \sum_{i \neq j = 1} \delta(r - |\mathbf{R}_i - \mathbf{R}_j|) \rangle \,. \tag{100}$$

Normalizing $dN(r)$ to the shell volume $dV(r) = 4\pi r^2 dr$ leads to the following expression for the RPDF,

$$g(r) = \frac{P_1}{P_2} = \frac{dN(r)/dV(r)}{N/V} = \frac{n(r)dr}{\rho 4\pi r^2 dr} \tag{101}$$

$$g(r) = \frac{V}{4\pi r^2 N^2} \langle \sum_{i \neq j = 1} \delta(r - |\mathbf{R}_i - \mathbf{R}_j|) \rangle \,, \tag{102}$$

where P_1 is the probability to find an atom in a volume $dV(r)$ at a distance r and P_2 is the probability to find an atom in a volume $dV(r)$ if the atoms where uniformly distributed [172]. Sharp features in the RPDF indicate crystallinity while broader and smeared out features indicate amporphous/liquid structure elements.

An explicit inclusion of anharmonicity in *ab initio* thermodynamics has been proposed by the group of Neugebauer, i.e., the upsampled thermodynamic integration using Langevin dynamics (UP-TILD) [173] approach. There, a set of different molecular dynamics runs is used to construct a force field, which reproduces the right temperature dependence. Furthermore, to mention some other important approaches here: there is one by the group of Monserrat, Drummond, and Needs [174], the stochastic self-consistent harmonic approximation by Errea, Calandra, and Mauri [175], and the temperature-dependent effective potential (TDEP) method by Hellman et al. [176] to include high-temperature anharmonicity. In the TDEP method, *ab initio* molecular dynamics are used to fit the temperature-dependent effective potential. All these approaches have in common that they try to represent the high-temperature anharmonicity by inclusion of the phonon-phonon coupling.

The C_p-MD workflow does not include phonon-phonon coupling directly. In principle, however, the performed MEAM MD runs are fully anharmonic, thus higher order anharmonic effects may be projected onto the harmonic force constants. Further investigations to include the phonon-phonon coupling directly within our method are planned for future work.

Advantages of the C_p-MD workflow are clearly based on the reduced numerical effort realized due to the used force fields as well as a reasonable accuracy for the tested systems.

Drawbacks of the C_p-MD workflow are based on the fact that one needs an appropriate force field description for the system of interest. If no suitable force field description is available it might be useful to fit force field using data produced by the QHA workflow using DFT.

In the next chapter, the *C_p-MD* workflow is applied to determine thermodynamical properties for lithium silicides. The results are compared to the standard QHA workflow based on DFT as well as experimental values.

5.2 FF-QHA WORKFLOWS

Two force field QHA workflows, FF-QHA, have been developed during this thesis. The idea is to use force field codes to calculate energy and forces, which are then utilized by applying the PHONOPY code [177] to calculate the PDOS as well as all QHA related thermodynamical properties. This would allow to combine the numerical efficiency of force field calculations with the accuracy of QHA calculations.

The first workflow GULP@FF-QHA is developed for the GULP force field code [46] (see Fig. 22). The second workflow LAMMPS@FF-QHA is designed for the usage with the LAMMPS code [45] (see Fig. 23). Both FF-QHA workflows have been designed to start from a cif file or similar crystal structure information. Typical structural inputs can be converted in other structural inputs using the ASE package [135]. In the next step an automatic molecular mechanics datatyes (MMtype, see Section 7.2) assignment is performed, which increase the usability and the user-friendliness of the proposed workflows. In case of GULP this is done by the AuToGRAFS code [178] and in case of LAMMPS this is done using the LAMMPS-INTERFACE [8]. Using core routines of the AuToGRAFS code allows to prepare GULP input files using a cif file as starting point and set up UFF or UFF4MOF force field calculations. The LAMMPS-INTERFACE also starts from a cif file and can assign the correct MMtypes for various force fields (i.e., UFF, UFF4MOF, BTW-FF, DREIDING and DWES) to generate LAMMPS input files. Given these initialization procedures, carrying out force field calculations is made very similar to perform electronic structure calculations.

The GULP code allows the direct combination with the PHONOPY code to perform QHA. Only the force constants need to be written by GULP in the correct format for the PHONOPY code, using the GULP output option to write SHENGBTE input files. For the LAMMPS code an additional application programming interfaces (API) called PHONOLAMMPS (see Appendix A) is used for the communication between LAMMPS and PHONOPY. In the case of the LAMMPS@FF-QHA workflow the calculation can completely run within PYTHON as all codes provide PYTHON APIs. It the future it might be possible to extend these workflows to calculate IR- or RAMAN spectra by using and extending the PHONOPY-SPECTROSCOPY PYTHON package [179]. Another future possibility is to use the calculated PDOS of various phases of a given material class to determine pressure-temperature phase diagrams using the PHASEGO package [180]. For further details of the mentioned packages and codes please see Appendix A.

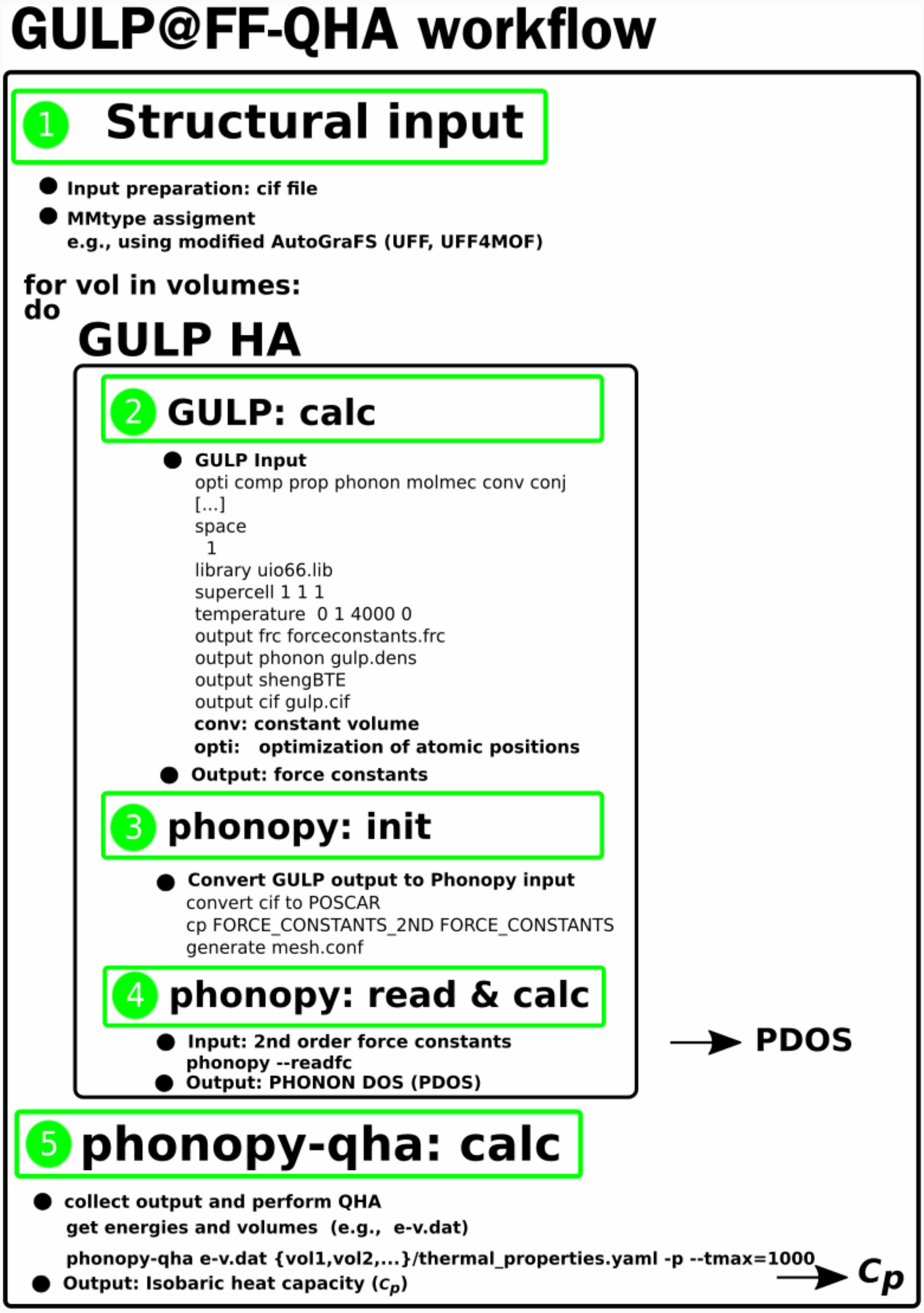

```
opti comp prop phonon molmec conv conj
[...]
space
  1
library uio66.lib
supercell 1 1 1
temperature  0 1 4000 0
output frc forceconstants.frc
output phonon gulp.dens
output shengBTE
output cif gulp.cif
```

```
convert cif to POSCAR
cp FORCE_CONSTANTS_2ND FORCE_CONSTANTS
generate mesh.conf
```

```
phonopy --readfc
```

```
phonopy-qha e-v.dat {vol1,vol2,...}/thermal_properties.yaml -p --tmax=1000
```

Figure 22: GULP@FF-QHA workflow for GULP to calculate PDOS as well as thermodynamical properties using QHA. The picture has been produced by the author using Inkscape (see Appendix A).

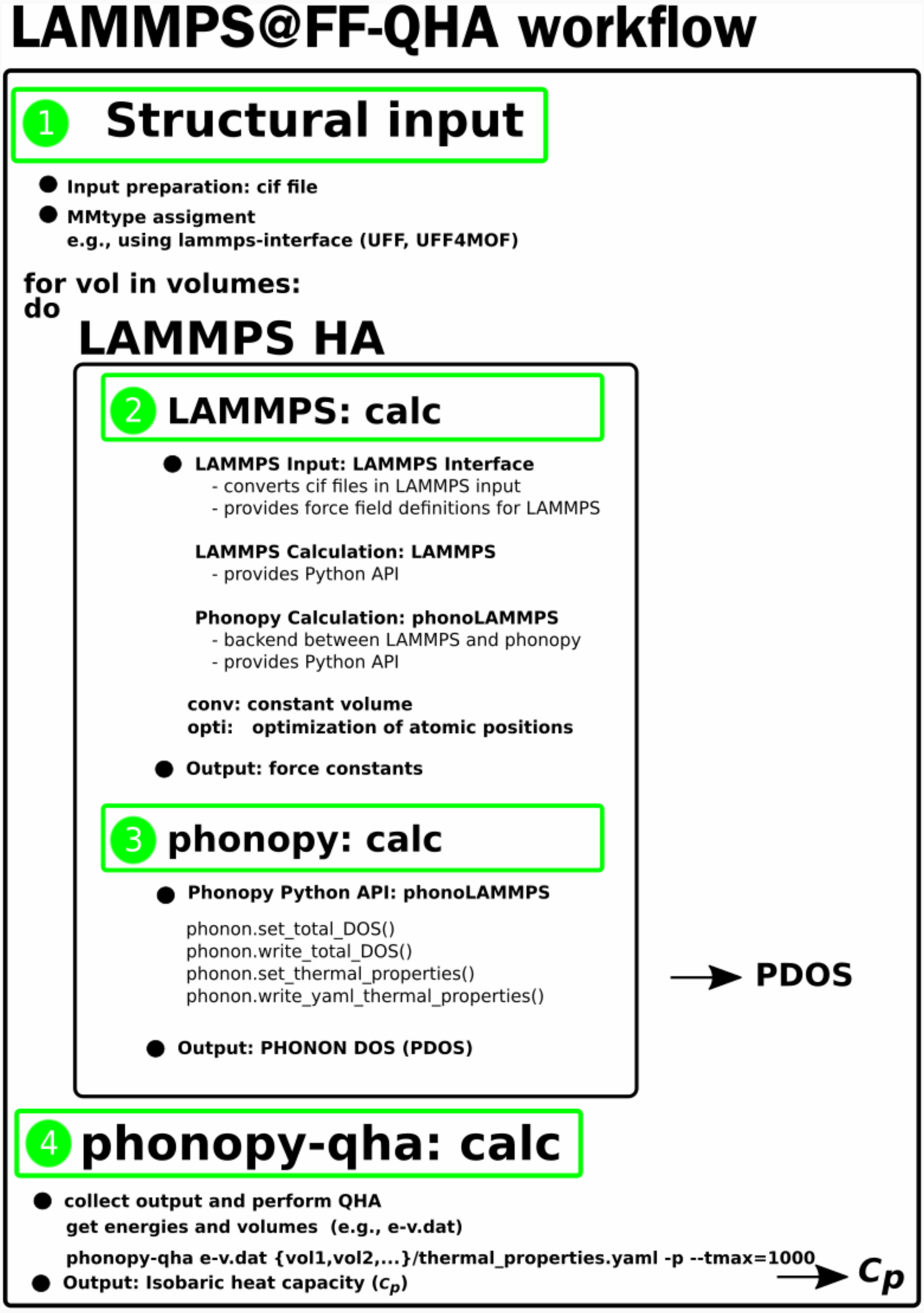

```
phonon.set_total_DOS()
phonon.write_total_DOS()
phonon.set_thermal_properties()
phonon.write_yaml_thermal_properties()
```

```
phonopy-qha e-v.dat {vol1,vol2,...}/thermal_properties.yaml -p --tmax=1000
```

Figure 23: LAMMPS@FF-QHA workflow for LAMMPS to calculate PDOS as well as thermodynamical properties using QHA. The picture has been produced by the author using Inkscape (see Appendix A).

5.3 G2-1 WORKFLOW

Composite methods [181, 182], also called thermochemical recipes, are computational methods which originated in quantum chemistry. These methods aim to achieve a high numerical accuracy by combining results and advantages of several calculations performed with different levels of theory using different quality basis sets. Primarily they are used to calculate thermodynamical properties (e.g., enthalpies of formation and ionization potentials) for a set consisting of several molecules and their atoms. The objective of these methods is to compute thermodynamical properties with chemical accuracy which is typically defined as 1 kcal/mol accuracy. Thus, a maximum overall error (e.g., mean absolute deviation (MAD) or mean unsigned deviation (MUD)) of 1 kcal/mol (1 kcal/mol = 4.184 kJ/mol = 0.0015936 Hartree) between calculations and experimental values is desired. [183]

The Gaussian-1 (G1) theory [184, 185] by John Pople was the first systematic realization of such a theory. Given their purpose for benchmarking a given theory, such test sets are commonly referred to as benchmark sets. The G1 evolved over the years to the Gaussian-2 (G2) [186], Gaussian-3 (G3) [187], and Gaussian-4 (G4) [188] theory and is still actively under development. One might refer to these collection of Gaussian theories as Gn theories. The Gn benchmark sets differ in the number of molecules as well as atoms which are used to perform the benchmark as well as the methods which are applied for the calculations. These benchmark sets developed over the years to benchmark suits such as the general main group thermochemistry, kinetics and non-covalent interactions (GMTKN) by Stefan Grimme and co-workers. The GMTKN benchmark suite developed over the time from GMTKN24 [189] over GMTKN30 [190] to the GMTKN55 [80] benchmark. These benchmark suits aim to test the quality of a given approximation (e.g., density functional approximation) for various calculated properties against high quality reference data. There also exist smaller benchmark sets, for example, the AE6 benchmark [191] is a test set of six atomization energies (AE), while the BH6 benchmark [191] consists of six barrier heights (BH). Any benchmark should be used with care and not as an absolute indicator for the performance of an investigated theory, as each benchmark has its own strengths and weaknesses [192, 193].

Within this thesis the G2-1 theory, which is available in the GAUSSIAN code and a sub-benchmark of the GMTKN benchmark set, was implemented as pre- and post-processing tool for the usage of any DFT code. The framework is called PYG21 and is written in PYTHON. For each of these benchmark sets one has a given set of structures where properties, such as the total energy and ionization potential, need to be calculated with the given geometry using the approximation which needs to be benchmarked. Thus, one needs to prepare the input files for the used DFT code and collect the properties one needs to evaluate the benchmark objectives (e.g., enthalpies of formation). These procedure has been summarized for the G2-1 theory as the G2-1 workflow (see Fig. 24). The G2-1 workflow can be seen as a prototype for a general benchmark workflow, were one needs to adjust the reference structures, the input preparation for the calculation of the properties needed as well as the post-processing steps for a given benchmark set. Further numerical details can be found in the work Schwalbe et al. [94].

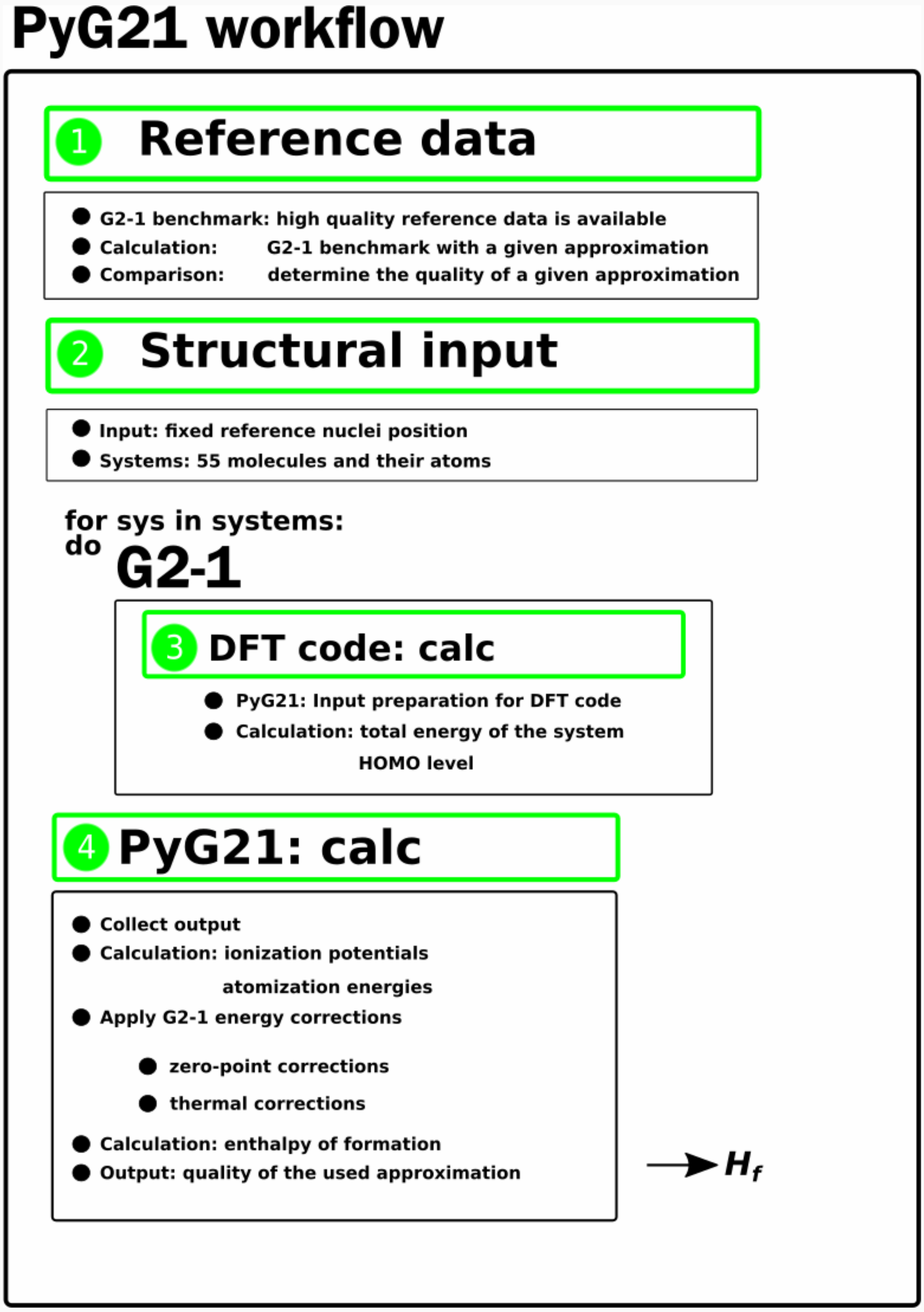

Figure 24: G2-1 workflow to calculate enthalpies of formation for G2-1 theory. The picture has been produced by the author using Inkscape (see Appendix A).

6

LITHIUM SILICIDES

List of own publications related to this chapter.

- S. Schwalbe, T. Gruber, K. Trepte, F. Taubert, F. Mertens and J. Kortus
  Mechanical, elastic and thermodynamic properties of crystalline lithium silicides
  Computational Materials Science, 134, 48 - 57, 2017
- F. Taubert, S. Schwalbe, J. Seidel, R. Hüttl, T. Gruber, R. Janot,
  M. Bobnar, R. Gumeniuk, F. Mertens and J. Kortus
  Thermodynamic characterization of lithium monosilicide (LiSi)
  by means of calorimetry and DFT-calculations
  International Journal of Materials Research, 108, 11, 2017

Crystalline and thermodynamically stable lithium silicides phases (Li_xSi_y) are investigated with density functional theory (DFT, see Section 3.1.4) and a force field method based on modified embedded atoms (MEAM, see Section 3.2.1). All results are compared with experimental data. The objective is to provide a fast method for theoretical thermodynamical calculations besides the standard quasi-harmonic approximation (QHA, see Section 4.4) utilizing DFT for large unit cells. For this purpose, the C_p-*MD* workflow (see Section 5.1) to calculate thermodynamical properties with MEAM based on molecular dynamics (MD) is presented, obtaining appropriate accuracy while significantly reducing computational cost. Mechanical properties like the bulk modulus and the elastic constants were evaluated in addition to thermodynamic properties including the phonon density of states, the vibrational free energy and the isochoric/isobaric specific heat capacity for Li, $Li_{12}Si_7$, Li_7Si_3, $Li_{13}Si_4$, $Li_{15}Si_4$, $Li_{21}Si_5$, $Li_{17}Si_4$, $Li_{22}Si_5$ and Si. For a selected phase ($Li_{13}Si_4$) the effect of a temperature-dependent phonon density of states and its effect on the isobaric heat capacity was studied. In addition, diffusion coefficients for the Li_xSi_y structures were calculated using MEAM based MD calculations and compared to experimental values. A second workflow called T_c-*MD* is presented, which allows to calculate critical temperatures, fitting exponents as well as melting points based on the intrinsic behaviour of temperature-dependent diffusion coefficients. This workflow allows to calculate the melting points for the Li_xSi_y structures, which are then used to present a purely theoretical phase diagram.

Investigations of this topic are motivated by the rapid growth of new technologies (e.g., portable devices like smart-phones and tablets, electro-mobility or hybrid-cars etc.), demanding new and efficient energy storage systems. The development of a new improved energy storage system requires a material which has a higher specific energy density, current density and charge/discharge cycling stability. To address these challenges a thorough scientific understanding of these materials is required.
One important physical property for characterizing lithium ion batteries is the so called specific storage capacity C_s. The leading graphite anode material is limited due to a low Li storage capacity $C_s \approx 372$ mAh/g [194]. Lithium silicides (Li_xSi_y) are discussed as an new kind of lithium ion battery materials due to their high lithium storage ca-

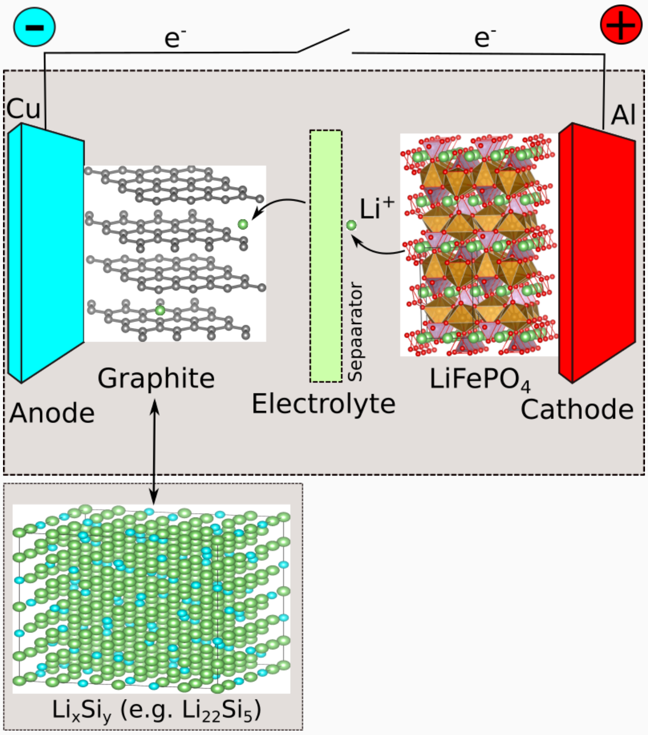

Figure 25: A sketch of a Li-ion battery highlighting the role of Li_xSi_y structures. The picture was produced by the author using VESTA and INKSCAPE (see Appendix A).

pacity ($C_s \approx 4200$ mAh/g for $Li_{22}Si_5$, see Tab. 3) [195]. Several experimental and *ab initio* investigations were carried out in the last years to determine the specific heat capacity and related properties to construct the phase diagram of Li_xSi_y [164, 196–198]. On the one hand experiments need highly accurate sample preparation and measurements and with that an appropriate time span for the evaluation of thermodynamical data. Furthermore, some of the phases (e.g., $Li_{17}Si_4$, $Li_{21}Si_5$, $Li_{22}Si_5$) have a very similar Li mass content, which makes a phase-pure sample preparation and thermodynamic measurements (e.g., DSC) very difficult. Theory can provide detailed information for a structure with a given Li mass content and can help to complete the understanding of the Li_xSi_y phase diagram. On the other hand some of the Li_xSi_y phases have large unit cells with hundreds of atoms, resulting in a high computational effort to describe such systems theoretically.

Cui et al. [198] started to create Li_xSi_y modified embedded atom potentials and calculated elastic and dynamic properties of Li_xSi_y amorphous phases. Their main focus was on the crystalline structures of the thermodynamically stable Li_xSi_y phases. The author with his co-authors investigated elastic properties like the bulk modulus and elastic constants as well as thermodynamic properties like the vibrational free energy and phonon density of states in the framework of DFT and the force field method of modified embedded atoms.

The C_p-*MD* workflow is applied and compared to DFT+QHA calculations. For Li_xSi_y it turns out that the C_p-*MD* workflow is a computationally fast alternative to the standard DFT+QHA with appropriate accuracy. Also, it presents a temperature-dependent phonon density of states calculated from molecular dynamics simulations. All computational results are compared to available experimental data [197].

The specific storage capacity C_s have been calculated for all Li_xSi_y crystal structures (see Tab. 3) using

$$C_s = x \cdot F/(y \cdot m_{Si}), \tag{103}$$

where $F = 96485.33$ C mol^{-1} is the Faraday constant and $m_{Si} = 28.08$ g mol^{-1} is the molar mass of silicon. With increasing lithium content, C_s also increases from 1636 to 4200 mAh g^{-1}. In accordance with this observation, the phases with similar Li to Si ratio ($Li_{21}Si_5$, $Li_{22}Si_5$ and $Li_{17}Si_4$) only slightly differ in their respective absolute value.

Table 3: Theoretical specific lithium storage capacity C_s of Li_xSi_y crystal structures.

Structure	Li mass content [%]	C_s [mAh g^{-1}]
Si	0	0
LiSi	19.8	954
$Li_{12}Si_7$	29.8	1636
Li_7Si_3	36.6	2227
$Li_{13}Si_4$	44.5	3102
$Li_{15}Si_4$	48.1	3579
$Li_{21}Si_5$	50.9	4009
$Li_{17}Si_4$	51.2	4056
$Li_{22}Si_5$	52.1	4200
Li	100	—

6.1 structural considerations

Lithium silicides consist of small alkali-metal lithium atoms and bigger half-metal silicon atoms. The silicon atoms are not always isolated from each other. In fact, in some phases they tend to build rigid Si-Si clusters (e.g., dimers, rings, etc.). There is an ongoing discussion whether or not lithium silicides can be classified with the well known Zintl concept [199] (see Refs. Nesper and Schnering [200], Nesper [201] and Chevrier, Zwanziger, and Dahn [196]). Zintl phases consist of one alkaline/alkaline earth metal and one element of the 3rd or 5th period. Zintl phases show both ionic and covalent bonding parts. These conceptional aspects are important with respect to the goal to describe the class of lithium silicides with only one force field. If some Li_xSi_y phases follow the Zintl concept and some do not, one force field may not be sufficient to treat all Li_xSi_y phases.

The structural parameters for each phase are given in Tab. 4. It should be noted that all phases have been transformed in an orthogonal setup, which was necessary to obtain consistent results for all phases considering the ELASTIC module within LAMMPS. The $Li_{21}Si_5$, the $Li_{22}Si_5$ phase, and the $Li_{17}Si_4$ phase show a very similar lithium content (see Tab. 4) and their lattice parameters are only slightly different. These structures are very hard to distinguish with experimental methods (e.g., X-ray diffraction or neutron-scattering). In case of $Li_{13}Si_4$ there exist diverse structural settings, but we will exclusively focus on the structure found by Schnering et al. [202], labeled $Li_{13}Si_4$ ICSD, and the structure found by the evolution algorithm EVO [203] by Gruber, Bahmann, and Kortus [164], labeled $Li_{13}Si_4$ EVO.

Within simulations one uses the given structures, thus one can explicitly calculate each of these phases. These investigations may provide further information regarding the stability of these phases.

Table 4: Crystal structure overview of all calculated Li_xSi_y phases. The lattice parameters are given by a, b and c (all angles $\alpha = \beta = \gamma = 90°$). In addition, SG is the spacegroup, w_{Li} the Lithium mass content and N_{atoms} the number of atoms per unit cell with and without symmetry. Notes: a) Original cell is transformed in an orthogonal setting and values given for DFT optimized structure. b) Same cell as $Li_{21}Si_5$ with one additional Wykoff Li position.

Structure		Ref.	SG	w_{Li} [%]	a [Å]	b [Å]	c [Å]	N_{atoms}
Si		[204]	227	0	5.43	5.43	5.43	1 (8)
$Li_{12}Si_7$		[205]	62	29.8	8.60	19.76	14.34	22 (152)
Li_7Si_3	a	[202]	1	36.6	7.42	4.29	17.69	40
$Li_{13}Si_4$ EVO	a	[164]	55	44.5	7.75	14.56	4.34	9 (34)
$Li_{13}Si_4$ ICSD		[206]	55	44.5	7.99	15.21	4.43	9 (34)
$Li_{15}Si_4$		[207]	220	48.1	10.60	10.60	10.60	3 (76)
$Li_{21}Si_5$		[200]	216	50.9	18.71	18.71	18.71	16 (416)
$Li_{17}Si_4$	b	[200]	216	51.2	18.71	18.71	18.71	17 (420)
$Li_{22}Si_5$		[208]	216	52.1	18.75	18.75	18.75	20 (432)
Li		[209]	229	100	3.51	3.51	3.51	1 (2)

6.2 ELASTIC PROPERTIES

For the C_p-MD workflow it is necessary to validate the force fields which should be used for the computation of the isobaric heat capacity. The elastic constants describe the interplay of the resulting forces acting on different atoms by applying external deformation of the systems. The right elastic behavior is the key property for any phonon calculation. The elastic properties for Li_xSi_y phases have been calculated with MEAM MD and compared to DFT results (see Tab. 5). In the MEAM MD calculations the energy volume relation was obtained using different structurally relaxed volumes.

The geometry optimization was performed with a conjugate gradient (cg) minimizer. Different volumes have been calculated for each phase and the resulting $E(V)$ curve was evaluated with a Birch-Murnaghan equation of state [132] (see Section 4.1) to access the bulk modulus B_{EOS}. All phases besides silicon are calculated with the same M1 MEAM potential. For silicon the M2 MEAM potential was used, because it describes the Si-Si bond better.

One remarkable result is that the obtained elastic constants of the crystalline Li_xSi_y phases are in good agreement with those calculated by Cui et al. [198] for the amorphous phases. In conclusion, this potential allows the description of the Li_xSi_y system with amorphous and crystalline structures. Generally, the DFT and M1/M2 values deliver similar values for each elastic property and the trends within the elastic constants are the same. The M1 calculations for the $Li_{13}Si_4$ EVO (M1 a, Ref. [164]) and $Li_{13}Si_4$ ICSD (M1 b, Ref. [206]) structures (see Tab. 5) give the same magnitude and only slightly differ in the total value. The performed DFT and M1 MEAM calculations show a similarity of the $Li_{21}Si_5$ and the $Li_{22}Si_5$ phase in all elastic properties, whereas the $Li_{17}Si_4$ phase differs more from these stoichiometrically similar phases. In summary, the used MEAM potential M1 is able to describe the elastic properties of the Li_xSi_y

phases properly and is suitable to be used for the proposed C_p-*MD* workflow. The calculated entries of the elastic matrix for each phase are positive (see Tab. 5). With that, one can conclude that all investigated phases are mechanically stable by fulfilling the elastic stability criterion.

6.3 SPECIFIC HEAT CAPACITIES

6.3.1 *Specific heat capacities of lithium and silicon*

The experimental reference data for the isobaric heat capacity was obtained by Thomas et al. [197]. Initial calculations were carried out on the pure Li and Si systems to ensure that the MD results agree with the ones obtained by DFT and with the experimental data. This comparison is the first evaluation of the MEAM potentials for the calculation of thermodynamic properties within the C_p-*MD* workflow.

One core property for a good description of the heat capacities is the phonon density of states. The PDOS has been calculated for pure silicon with DFT using Quantum Espresso and from MD using LAMMPS with the "fix_phonon" option. The results of these calculations are visualized in Fig. 26. The resulting DFT and MD PDOS are in good agreement, because the main features appear in both density of states. Based on this result DFT (in the framework of the quasi-harmonic approximation) and the C_p-*MD* workflow are used to calculate the isobaric heat capacity C_p for silicon and lithium.

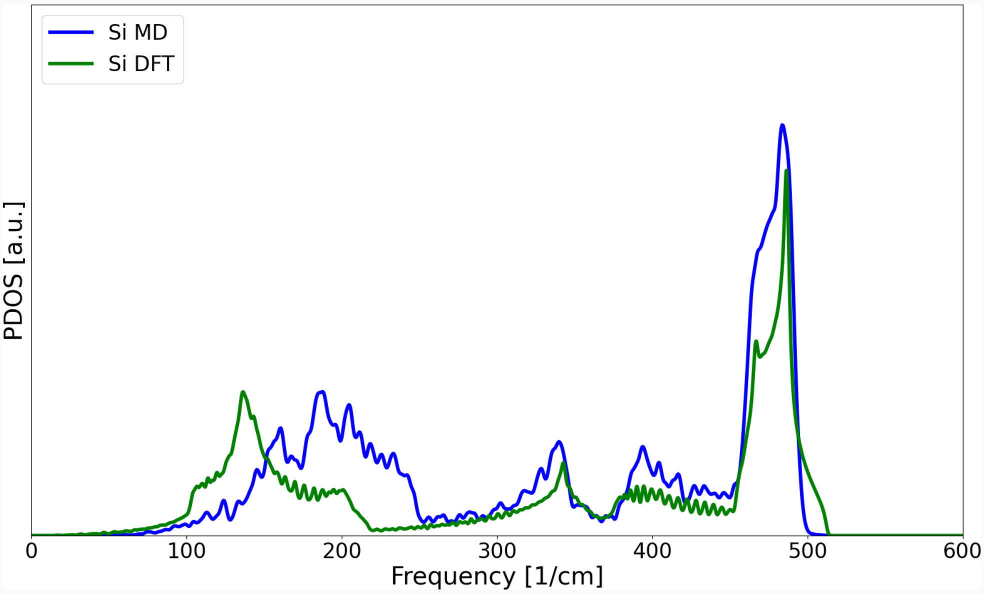

Figure 26: Phonon density of states of silicon.

In Fig. 27 (b) and 28 (b) the isobaric heat capacities for pure silicon and lithium are plotted versus temperature. In case of silicon (see Fig. 27 (b)), the values of the MD calculations agree with the DFT and experimental values over a wide range of temperatures. Fig. 27 (a) shows the RPDF of pure Si. The crystallinity of this system can be clearly seen, even at rather high temperatures. This indicates that Si itself is

Table 5: Elastic properties of Li_xSi_y phases. Here M1 and M2 are the labels for the MEAM calculations, DFT is the label for the QUANTUM ESPRESSO LDA DFT calculation and Ref is the reference value (first row MEAM reference and second row *ab initio* reference). The M2 setup was only used for the pure Si structure. Furthermore, the subscripts a stands for the $Li_{13}Si_4$ EVO, whereas b stands for the $Li_{13}Si_4$ ICSD structure. All values are given in GPa.

	Li		$Li_{12}Si_7$				Li_7Si_3	$Li_{13}Si_4$					$Li_{15}Si_4$				$Li_{21}Si_5$		$Li_{17}Si_4$		$Li_{22}Si_5$				Si	
	M1	DFT	M1	DFT	Ref [198]		M1	$M1_a$	$M1_b$	DFT_a	Ref [198]		M1	DFT	Ref [198]		M1	DFT	M1	DFT	M1	DFT	Ref [198]		M2	DFT
B_{EOS}	11.8	15.0	60.6	39.8			30.4	43.3	42.2	35.8			37.8	33.5			36.0	34.4	40.4	35.2	35.8	34.3			94.9	94.3
B_{Voigt}	12.8	15.3	55.8	40.5			47.7	43.3	40.7	36.7			37.9	33.9			36.4	34.9	36.6	35.5	35.8	35.1			95.3	96.2
C_{11}	16.4	16.3	87.3	100.3	87.0	92.0	99.3	84.7	75.2	87.6	75.0	74.0	47.7	50.3	48.0	47.0	56.5	65.5	64.8	60.4	51.6	55.0	52.0	46.0	122.9	161.3
C_{22}	16.4	16.3	79.5	106.5	78.0	97.0	99.3	72.7	69.9	80.4	70.0	61.0	47.7	50.3	48.0	47.0	56.5	65.5	66.2	60.4	51.6	55.0	52.0	46.0	122.9	161.3
C_{33}	16.4	16.3	86.9	101.5	85.0	90.0	92.3	78.5	74.1	95.2	74.0	77.0	47.7	50.3	48.0	47.0	56.5	65.5	67.6	60.4	51.6	55.0	52.0	46.0	122.9	161.3
C_{12}	11.0	14.8	44.0	5.7	45.0	5.0	36.9	24.7	21.7	18.6	22.0	17.0	32.9	25.7	33.0	21.0	26.3	19.7	23.3	23.1	27.9	25.1	28.0	23.0	81.4	63.6
C_{13}	11.0	14.8	40.6	13.5	42.0	11.0	16.1	22.5	23.7	7.2	24.0	11.0	32.9	25.7	33.0	21.0	26.3	19.7	21.1	23.1	27.9	25.1	28.0	23.0	81.4	63.6
C_{23}	11.0	14.8	39.7	8.7	39.0	8.0	16.1	29.7	28.0	7.6	28.0	10.0	32.9	25.7	33.0	21.0	26.3	19.7	20.9	23.1	27.9	25.1	28.0	23.0	81.4	63.6
C_{44}	11.1	14.5	17.1	31.2	17.0	28.0	21.5	20.8	20.3	25.5	20.0	23.0	22.7	34.4	23.0	28.0	21.7	33.0	17.6	38.0	29.6	41.7	30.0	35.0	81.3	76.7
C_{55}	11.1	14.5	18.8	32.0	20.0	26.0	21.5	18.1	13.6	28.0	14.0	24.0	22.7	34.4	23.0	28.0	21.7	33.0	17.5	38.0	29.6	41.7	30.0	35.0	81.3	76.7
C_{66}	11.1	14.5	12.4	27.1	15.0	24.0	31.2	16.7	13.6	32.1	14.0	28.0	22.7	34.4	23.0	28.0	21.7	33.0	18.9	38.0	29.6	41.7	30.0	35.0	81.3	76.7

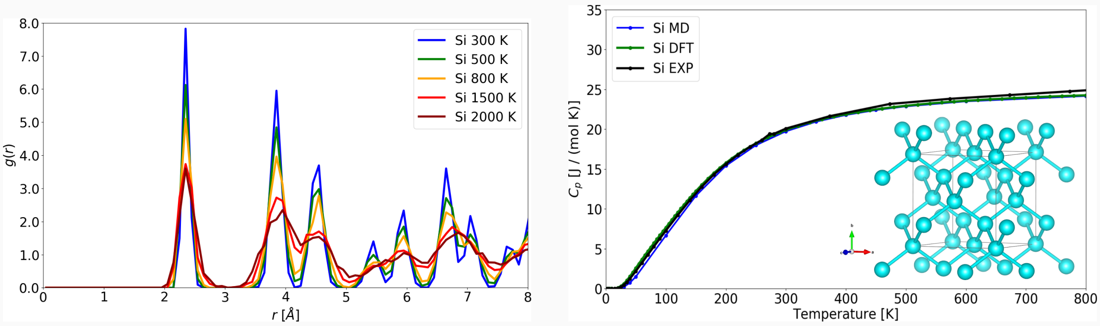

(a) $g(r)$ (b) C_p

Figure 27: (a) Radial pair distribution function $g(r)$ and (b) specific heat capacity C_p of silicon. The inset shows the crystalline structure with Si-Si bonds visualizing Si-structure elements (Si-tetrahedron). The experimental C_p data is extracted from Flubacher, Leadbetter, and Morrison [210] for $T < 300$ K and from Shanks et al. [211] for $T \geq 300$ K. The pictures were produced by the author using MATPLOTLIB (see Appendix A).

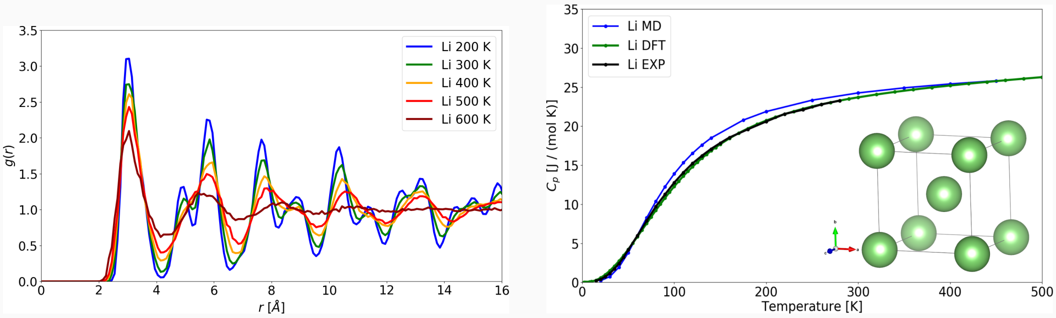

(a) $g(r)$ (b) C_p

Figure 28: (a) Radial pair distribution function $g(r)$ and (b) specific heat capacity C_p of lithium. The inset shows the crystalline structure. The experimental C_p data is extracted from Douglas et al. [212] (original published by Simon and Swain [213]). The pictures were produced by the author using MATPLOTLIB (see Appendix A).

thermally very stable. However, from 1500 K on the features at larger distances smear out, indicating a decrease in crystallinity at such temperatures.

It should be noted here that the isobaric specific heat capacity for lithium slighlty differs in the temperature region from 100 to 200 K from the DFT values, which could lead to small systematic errors for the Li_xSi_y phases in those temperature regions due to the given MEAM potential. However, there is a general agreement of our MD results with those obtained by DFT and the experiment for pure lithium in the entire temperature range. As can be seen in Fig. 28 (a), the crystallinity of lithium is preserved up to a temperature of ca. 500 K. Clearly at higher temperatures ($>$ 600 K) the RPDF shows liquid behavior and the crystalline features become absent, indicating a melting process appearing at around 500 K. Based on these preliminary results, the C_p-*MD* workflow should allow to calculate the specific heat capacity for the Li_xSi_y phases.

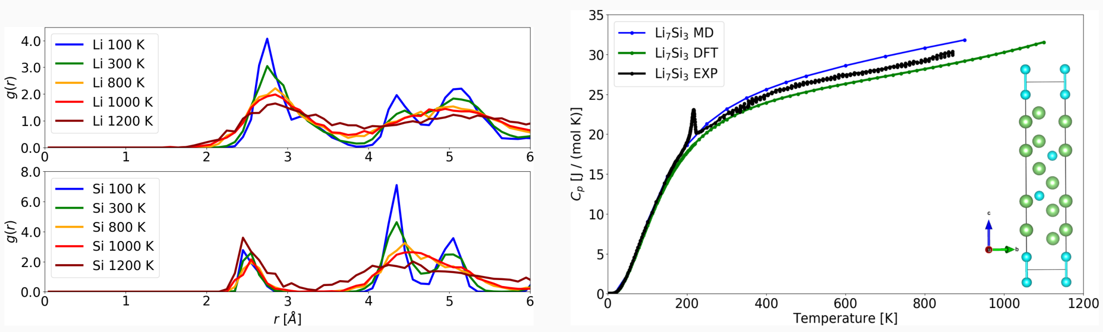

(a) $g(r)$ (b) C_p

Figure 29: (a) Radial pair distribution function $g(r)$ and (b) specific heat capacity C_p of Li_7Si_3. The inset shows the crystalline structure with Si-Si bonds visualizing Si-structure elements (Si-dimers). The experimental C_p data is extracted from Thomas et al. [197]. The pictures were produced by the author using MATPLOTLIB (see Appendix A).

6.3.2 *Specific heat capacity of lithium silicides*

None of the calculated phonon densities of states (PDOS) for the investigated Li_xSi_y structures show noticeable imaginary frequencies. Therefore, one can conclude that all calculated structures are dynamically stable (see supplementary material [161]). Further, the formation energy ($T = 0$ K) as a function of the Li mass content has a known trend, e.g., that Li_7Si_3 seems to be thermodynamical most stable phase (see supplementary material [161]). In general all calculated *ab initio* isobaric heat capacity curves for the Li_xSi_y phases are in good agreement with experimental curves over the entire temperature range. Only for $Li_{12}Si_7$ and $Li_{13}Si_4$ the DFT values differ from the experimental values in the high temperature region, which indicates that for these phases high-temperature effects may play a role. As already mentioned earlier these effects cannot be described by the quasi-harmonic approximation and therefore cannot be treated within this framework. For these phases the proposed C_p-*MD* workflow seems to give a better description of the high-temperature limit. For Li_7Si_3, as seen in Fig. 29 (b), the heat capacity calculated with the MEAM potentials is in good agreement with experimental and DFT results. There is a slight overestimation at higher temperatures, but the trend is preserved for both methods. A possible explanation could be that silicon forms stable dimers [196] in Li_7Si_3, which show local order even at higher temperatures.

In Fig. 29 (a) the RPDF of Li and Si within Li_7Si_3 is displayed. For lithium a very similar trend as in pure lithium is observed, that is the *double peak* at approximately 4-5 Å, which smears out at higher temperatures. The general features for small distances are preserved as well. At $T > 1000$ K the RPDF for Li shows liquid features, while the crystalline ones are reduced. This fact indicates a melting process at this temperature. For Si, the RPDF remains qualitatively unchanged over the investigated temperature range, indicating the high stability of the Si structure within the phase.

For $Li_{12}Si_7$ in Fig. 30 (b) it is possible to identify two different $V(T)$ dependencies, one occurring at lower temperatures (up to approximately 400 K) leading to a specific $\alpha_{\mathrm{low}-T}$ and one occurring at higher temperatures, which results in a different $\alpha_{\mathrm{high}-T}$

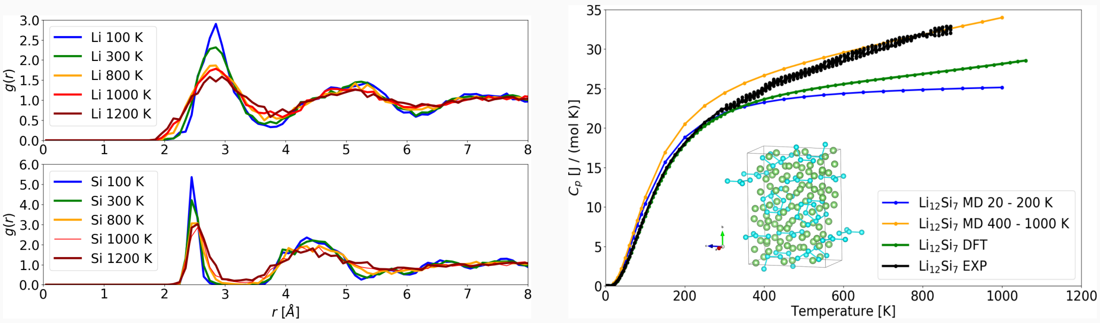

(a) $g(r)$ (b) C_p

Figure 30: (a) Radial pair distribution function $g(r)$ and (b) specific heat capacity C_p of $Li_{12}Si_7$. The inset shows the crystalline structure with Si-Si bonds visualizing Si-structure elements (Si-pentagon-ring, Si-star). The experimental C_p data is extracted from Thomas et al. [197]. The pictures were produced by the author using MATPLOTLIB (see Appendix A).

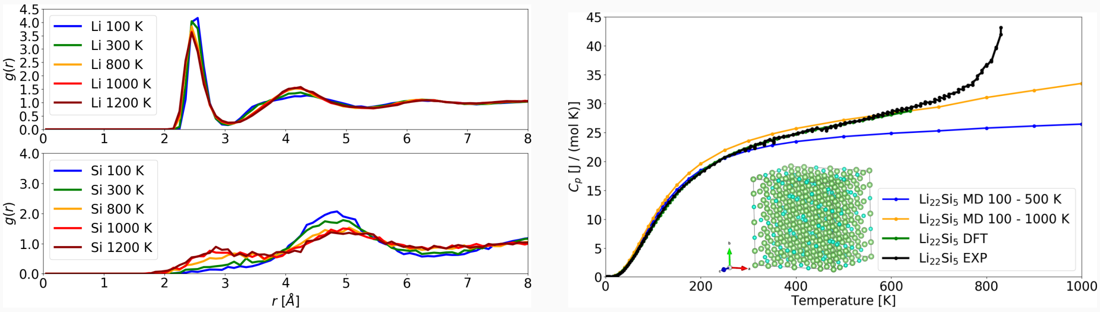

(a) $g(r)$ (b) C_p

Figure 31: (a) Radial pair distribution function $g(r)$ and (b) specific heat capacity C_p of $Li_{22}Si_5$. The inset shows the crystalline structure with Si-structure elements (Si-atoms). The experimental C_p data is extracted from Thomas et al. [197]. The pictures were produced by the author using MATPLOTLIB (see Appendix A).

(see Tab. 6). Based on the Li RPDF (see Fig. 30 (a)), which indicates structural changes at temperatures $T > 300$ K, two temperature regions are separated. There is one from 20 - 200 K leading to $\alpha_{\text{low}-T}$ and another from 400 - 1000 K leading to $\alpha_{\text{high}-T}$. This difference may be caused by anharmonic contributions or diffusion effects which take place at higher temperatures, giving rise to a different expansion behavior. The two distinguishable values of α lead to different C_p values, see Eq. (98). It is not possible to describe phase transitions with the standard quasi-harmonic approximation, which delivers a possible explanation why the DFT data are in good agreement with experiments in the low temperature region but not in the high temperature region. In the $Li_{12}Si_7$ phase the silicon atoms form Si_5 rings with a lithium atom inside. These Si_5 rings are stacked between two Li_5 rings. Concerning this situation, it is not necessary to break a bond to disturb the structure, as the Li_5 rings can slide between the Si_5, and the crystalline structure may transform into another one or becomes amorphous.

Fig. 30 (a) displays the RPDF of Li and Si within $Li_{12}Si_7$. For lithium a somewhat different behavior in comparison to pure Li is found, as there is only one peak at a distance

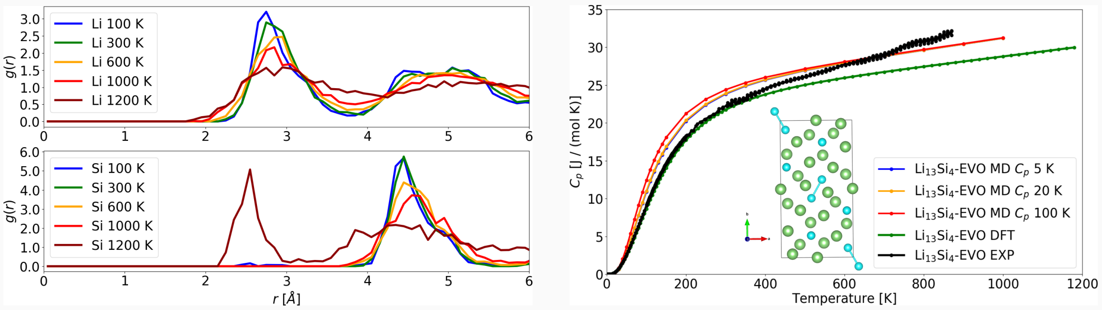

(a) $g(r)$ (b) C_p

Figure 32: (a) Radial pair distribution function $g(r)$ and (b) specific heat capacity C_p of Li$_{13}$Si$_4$. The inset shows the crystalline structure with Si-Si bonds visualizing Si-structure elements (Si-atoms, Si-dimers). The MD calculations have been performed for different low temperatures. The DFT values were already published in [164]. The experimental C_p data is extracted from Thomas et al. [197]. The pictures were produced by the author using MATPLOTLIB (see Appendix A).

of 4-5 Å. Starting from ca. 1000 K, the features in the RPDF become more liquid-like. The shape and position of Si peaks (single peak at about 2.5 Å, smeared out peak at 4-5 Å) are largely temperature independent up to high temperatures, showing again high stability of the Si structures.

Table 6: Thermal expansion coefficients for Li$_x$Si$_y$ crystal structures. If more than one value is present, the temperature regime is given.

Li$_x$Si$_y$	$\alpha_{l,\text{low}-T}$ [10^{-6} K^{-1}]	$\alpha_{l,\text{high}-T}$ [10^{-6} K^{-1}]	$\alpha_{l,\text{ref}}$ [214] [10^{-6} K^{-1}]
Si	5.6	5.6	2.6–3
Li$_{12}$Si$_7$	4.4 (20-200 K)	18.7 (400-1000 K)	—
Li$_7$Si$_3$	26.5	26.5	—
Li$_{13}$Si$_4$	58.6	58.6	—
Li$_{22}$Si$_5$	33.9 (100-500 K)	72.6 (100-1000 K)	—
Li	54.7	54.7	56

For Li$_{22}$Si$_5$ in Fig. 31 (b) a similar behavior like for Li$_{12}$Si$_7$ has been found. Again, there are two different α values describing the resulting heat capacity at different temperature regimes. One major difference is that the Li RPDF (see Fig. 31 (a)) indicates no structural changes at higher temperatures, thus both linear α values were evaluated with the same starting temperature $T = 100$ K, and were chosen until 500 K for $\alpha_{\text{low}-T}$ and until 1000 K for $\alpha_{\text{high}-T}$. Here, the agreement of the two different plots to the other values is more obvious.

Fig. 31 (a) displays the RPDF of Li and Si within Li$_{22}$Si$_5$. The Li RPDF is somewhat different from those of the other phases. In detail, the initial sharp peak around 2.5 Å looks crystalline, while no other crystalline features are present. Thus, the Li atoms prefer a specific Li-Li distance, which is constant over the investigated temperature range. In addition, the other features have characteristics of a liquid (declining sinusoidal-like behavior). This indicates that even at low temperatures a permanent Li diffusion in the phase takes place. Experimental crystal structure determination methods like XRD or neutron scattering are therefore only able to measure snapshots of the structure at a specific time, at which the diffusive Li atoms are quasi-frozen for the moment of the measurement. In addition, the liquid-like behavior will make it very difficult to distinguish between $Li_{22}Si_5$, $Li_{21}Si_5$, and $Li_{17}Si_4$ as all of them have a high and very similar Li content. For Si on the other hand there is a very broad peak at around 5 Å at low temperatures, indicating that the Si atoms within this phase are only ordered to a certain degree. Once the temperature is increased, the peak strongly smears out, thus the Si atoms become disordered. This is obvious, as within this phase Si is not present in clusters, but only as single atoms. These atoms are surrounded by a large amount of diffusive Li. With that, the Si atoms cannot form any ordered structures.

For $Li_{13}Si_4$ in Fig. 32 (b) a temperature-dependent PDOS was calculated (5 K, 20 K, 100 K). Here the agreement with experiment and DFT C_p results for a low temperature PDOS is better. This might be caused by suppressed diffusion processes [164] within the phase at low temperature, which are certainly more important for higher temperatures. Thus, the description of the systems becomes better at low temperatures because the diffusion process is frozen out. In Fig. 32 (a) the RPDF of Li and Si within $Li_{13}Si_4$ is shown. The first peak for Li shows similarities to $Li_{12}Si_7$ and Li_7Si_3. However, in contrast to Li_7Si_3 and in correspondence to $Li_{12}Si_7$, there is a single, broad second peak at around 4.5 Å. The RPDF for Si indicates that initially more single atoms than single dimers are present, which can be seen from the broad peak at approximately 4.5 Å and from the crystal structure itself. However, at a temperature of 1200 K, this peak is strongly smeared out and an additional peak at about 2.5 Å appears, again resembling the features seen in all other phases. At this temperature the first nearest neighbors peak in the Si RPDF increases significantly, which indicates structural changes concerning the Si atoms with increasing temperature.

6.3.3 *Temperature-dependent phonon density of states*

Elastic constants and bulk modulus have been calculated for another $\mathrm{Li}_x\mathrm{Si}_y$ phase, i.e., LiSi, with DFT and MEAM force field MD (see Tab. 7). This LiSi phase is discussed separately, as it experimentally forms only at high pressures and high temperatures [162]. Again it is necessary to validate the MEAM potential for further investigations as accurate elastic constants will deliver the right phonon density of states and with that thermodynamic data with appropriate accuracy. The calculated elastic properties are in good agreement for DFT as well as for the MEAM values with literature values. The relationships determined by DFT among the elastic constants are reproduced well by the MEAM calculations indicating that the used MEAM potential can be regarded as accurate enough for further investigations using the C_p-*MD* workflow.

In a next step, a set of NPT calculations have been performed and the value of linear thermal expansion coefficient α_l of LiSi is determined to be $13.6 \cdot 10^{-6}\ \mathrm{K}^{-1}$. Further, the effect of temperature on the PDOS of LiSi is analyzed (see Fig. 33 (a)). This information allows to calculate different C_p curves based on different phonon density of states corresponding to different temperatures. Comparing the different PDOS for 300 K, 400 K, and 1000 K, a shift of the PDOS to lower frequencies with increasing temperature is observed. At this point all properties have been calculated (see Eq. (98)) which are needed to determine the isobaric heat capacity of LiSi based on molecular dynamics. The corresponding MEAM C_p curves are shown in Fig. 33 (d), where all C_p curves for different temperatures are shown together with our DFT QHA C_p curve.

One can see that the agreement between DFT and MD is better at high temperatures. While the structure is fixed and does not have the freedom to change freely as a function of temperature in the QHA DFT, the structure is free to change in the NPT MD runs. These changes can be visualized by evaluating the radial pair distribution function for some specific NPT MD runs (see Fig. 33 (c)). The Li projected RPDF shows crystalline features at low temperatures (100 K - 300 K). At higher temperature these features smear out, indicating an amorphous/liquid like behavior of the Li atoms. Similar trends also appear in the Si projected RPDF. This indicates that, there is a possible melting of the structure at $T \leq 1000$ K. The accumulated computational time for the final C_p-*MD* workflow is 62.19 CPUh, whereas the DFT QHA C_p computational time amounts to 2190 CPUh. Given these values, the C_p-*MD* workflow is about 35 times faster than the DFT QHA procedure with comparable accuracy.

Table 7: Elastic properties of LiSi. Here MEAM is the label for the LAMMPS MEAM force field calculation, DFT is the label for the QUANTUM ESPRESSO LDA DFT calculation and Ref is the reference value (first row MEAM reference and second row *ab initio* reference).

		This work		Reference[198]	
		MEAM	DFT	MEAM	DFT
B_{EOS}	[GPa]	81.7	56.8	-	-
B_{Voigt}	[GPa]	80.2	56.8	-	-
C_{11}	[GPa]	111.9	110.5	112.0	101.0
C_{22}	[GPa]	111.9	110.5	112.0	101.0
C_{33}	[GPa]	93.9	79.0	94.0	77.0
C_{12}	[GPa]	57.9	23.7	58.0	19.0
C_{13}	[GPa]	72.1	41.0	72.0	37.0
C_{23}	[GPa]	72.1	41.0	72.0	37.0
C_{44}	[GPa]	41.4	47.0	42.0	45.0
C_{55}	[GPa]	41.4	47.0	42.0	45.0
C_{66}	[GPa]	25.7	37.9	26.0	37.0

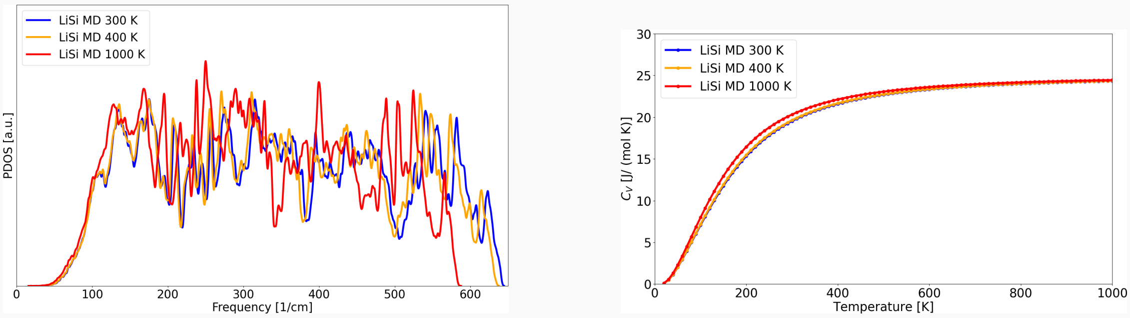

(a) PDOS of LiSi

(b) C_V of LiSi

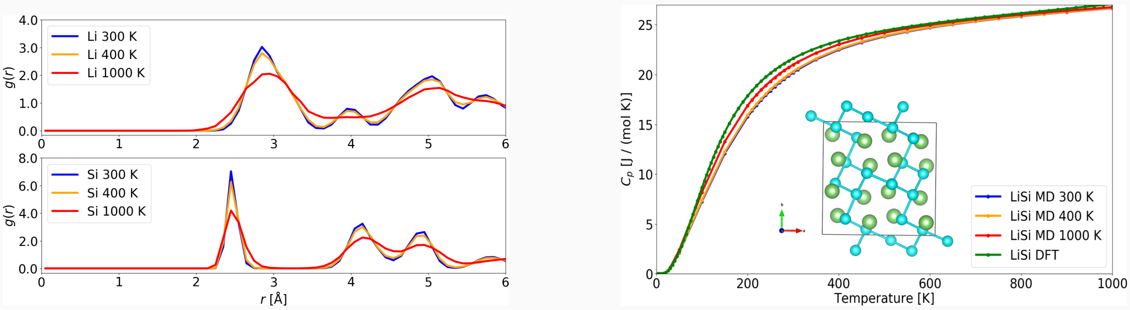

(c) RPDF of LiSi

(d) C_p of LiSi

Figure 33: Temperature-dependent phonon density of states in (a), the respective isochoric specific heat capacity C_V in (b) and the radial pair distribution function $g(r)$ in (c) and the isobaric heat capacity in (d) of LiSi. The inset in (d) shows the crystalline structure (Li: green, Si: blue) with Si-Si bonds visualizing Si-structure elements (Si-network). The MD calculations have been performed for different temperatures. The pictures were produced by the author using MATPLOTLIB (see Appendix A).

6.4 T_c-*MD* WORKFLOW

6.4.1 *Diffusion*

Molecular dynamic simulations can be used to identify structural changes due to the influence of temperature. For simulations cells including many atoms (e.g., battery materials) during long MD runs the so called mean squared displacement (MSD) is given by

$$\mathrm{MSD} := \langle r^2(t) \rangle := \lim_{N \to \infty} \frac{1}{N} \sum_{n=1}^{N} (R_n(t) - R_n(0))^2, \tag{104}$$

and can be used to analyze structural changes driven by diffusion processes. There is a connection between the MSD and the diffusion coefficient D, given by the following Einstein equation (for three dimensional systems)

$$D = \frac{\langle r^2(t) \rangle}{6t} = \frac{\mathrm{MSD}(t)}{6t}. \tag{105}$$

Considering battery materials (e.g., $\mathrm{Li}_x\mathrm{Si}_y$) it is import to analyze lithium transport properties in order to understand the mobility of lithium-ions within the system. For these materials the knowledge of diffusion, especially diffusion coefficients, is relevant.

The diffusion coefficients for Si, $\mathrm{Li}_{12}\mathrm{Si}_7$, $\mathrm{Li}_7\mathrm{Si}_3$, $\mathrm{Li}_{13}\mathrm{Si}_4$ and $\mathrm{Li}_{22}\mathrm{Si}_5$ have been calculated using NPT ensemble MD runs using LAMMPS applying the MEAM force field (see Tab. 8) and compared to experimental reference values. As reference values are available for T = 688 K [215], the NPT MD calculations have been performed at this temperature. The MD calculations predict similar magnitudes as well as similar relative orderings. For example, $\mathrm{Li}_{13}\mathrm{Si}_4$ shows the highest lithium diffusion and $\mathrm{Li}_{12}\mathrm{Si}_7$ has the lowest lithium diffusion of the investigated $\mathrm{Li}_x\mathrm{Si}_y$ structures.

Table 8: $\mathrm{Li}_x\mathrm{Si}_y$: Calculated diffusion coefficients at T = 688 K. The calculations were performed using LAMMPS NPT runs applying the MEAM force field.

System	D_{MD} [m^2/s]	$D_{\mathrm{Li,exp}}$ [m^2/s][215]
Si	$3.10\ 10^{-12}$	$1.67\text{-}6.56\ 10^{-12}$
$\mathrm{Li}_{12}\mathrm{Si}_7$	$6.72\ 10^{-11}$	$4.85\text{-}5.44\ 10^{-11}$
$\mathrm{Li}_7\mathrm{Si}_3$	$3.16\ 10^{-11}$	$4.16\text{-}4.96\ 10^{-11}$
$\mathrm{Li}_{13}\mathrm{Si}_4$	$3.71\ 10^{-10}$	$2.88\text{-}5.01\ 10^{-11}$
$\mathrm{Li}_{22}\mathrm{Si}_5$	$6.89\ 10^{-11}$	$2.99\text{-}3.45\ 10^{-11}$

6.4.2 *Melting points*

The melting point is related to the temperature T_{melt} where a structure switches from a solid to a liquid state. Directly at the melting point solid and liquid phase are considered to co-exist in equilibrium. As shown in the previous sections (see Section 6.3), the behaviour of the Li_xSi_y changes with temperatures (e.g., different temperatures regimes for C_p and α), thus the knowledge of the melting points may help to understand these findings. In the next section different methods to calculate melting points are discussed and applied to study Li_xSi_y phases.

One-phase approach

In the one-phase approach [216, 217] (or hysteresis method) NVT ensemble molecular dynamics simulations are performed using a given heating-/cooling rate define as

$$Q_s = \frac{\Delta T}{N_{\text{steps}} t_{\text{step}}}, \tag{106}$$

with ΔT being the temperature difference between starting and end temperature, N_{steps} being the number of MD steps and t_{step} being the timestep of the MD run. The NVT ensemble is also known as canonical ensemble where N the number of particles, V the volume of the system and T the temperature of the systems are held constant during the MD simulation. For this approach one needs to perform a MD run heating the system with a given heating rate. At some point on this heating curve the system starts to melt. After finishing the heating run, one needs to cool the system with the same rate, which is then considered as a cooling rate. Starting at the last structure from the heating curve the system slowly cools down and at some point on this cooling curve a solidification starts. Visualizing the total energy of the system against the temperature for both runs determines the super-heating critical temperature T_p and the super-cooling critical temperature T_m (see Fig. 34). The magnitude of the super-heating point is determined on the heating curve where the phase transitions stops, whereas the magnitude of the super-cooling point is determined on the cooling curve where the phase transitions stops.

Melting temperature T_{melt} can be calculated from the aforementioned critical temperatures (i.e., T_p and T_m) using the following equation

$$T_{\text{melt}} = T_p + T_m - \sqrt{(T_p \cdot T_m)}. \tag{107}$$

The one-phase approach is applied to lithium (see Fig. 34). The calculated critical temperature as well as melting points depend on how super-heating- and super-cooling temperatures are determined.

The advantage of the one-phase approach is that one can access the tempered structures at any point of the heating or cooling process. This allows to visualize and further analyze the structures using, e.g., (radial) pair-distribution functions.

The disadvantage of the one-phase approach is that the determination of T_p and T_m is not unique. Besides, there might be problems if the system does not completely solidify back to the starting structure.

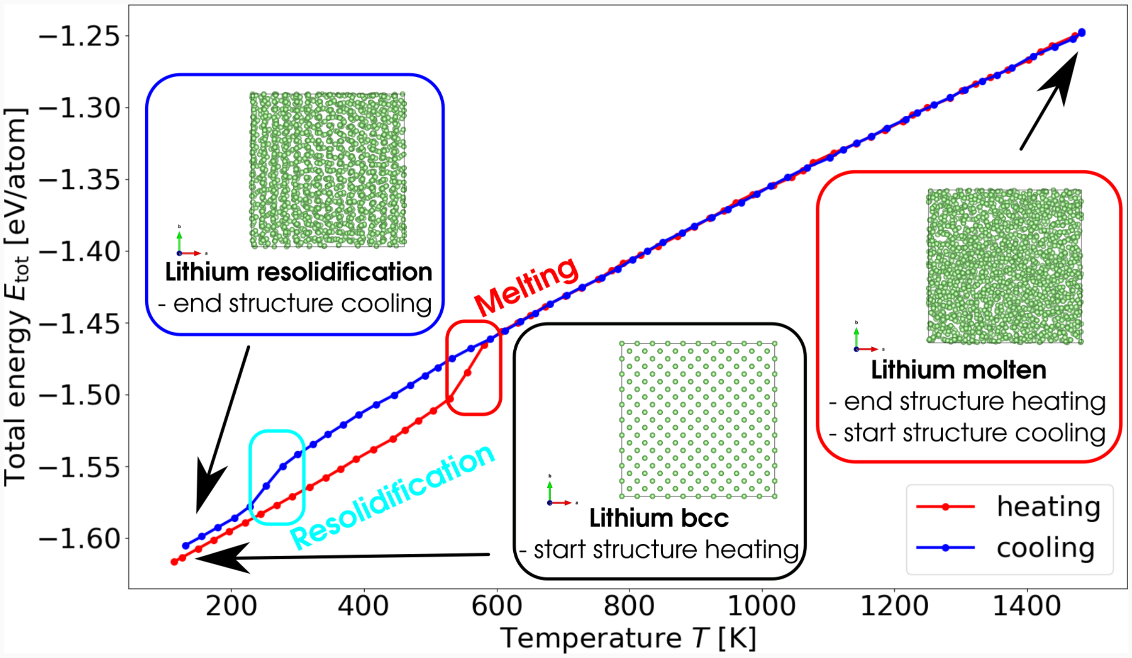

Figure 34: Determination of critical temperatures T_c for Li using the one-phase approach applying MD simulations using LAMMPS and the MEAM force field. The insets show the crystalline starting structure, the final molten structure of the heating run as well as the final solidified structure of the cooling run. The picture was produced by the author using VESTA, MATPLOTLIB and INKSCAPE (see Appendix A).

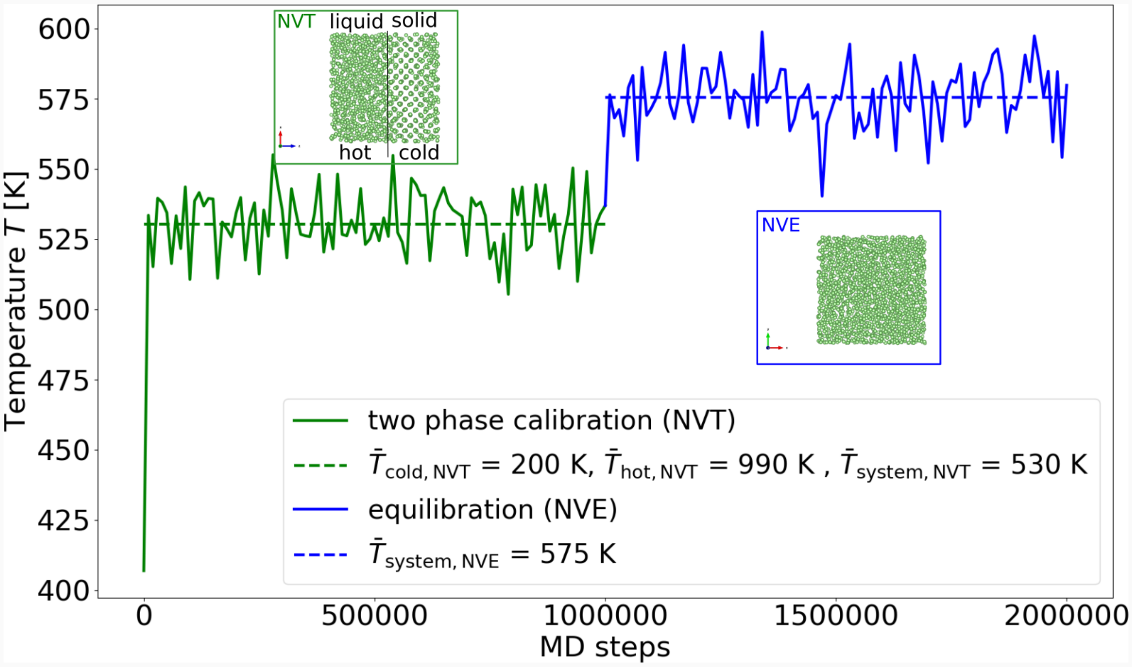

Figure 35: Determination of critical temperatures T_c for Li using the two-phase approach applying MD simulations using LAMMPS and the MEAM force field. The insets show the snapshot of the structure of the cold and hot region of the NVT MD run as well as a snapshot of the global structure of the NVE MD run. The picture was produced by the author using VESTA, MATPLOTLIB and INKSCAPE (see Appendix A)

Two-phase approach

An alternative approach to the one-phase approach is the two-phase approach [216, 217]. The two-phase approach is also known as coexistence method [218]. Within the two-phase approach one needs to divide a given crystal structure into two regions. The first region approaches a temperature T_{cold} where the structure stays crystalline. This region is referred to as cold region. The second region needs to approach a temperature T_{hot} where the structure represents a molten/ liquid structure. The temperature regions are equilibrated simultaneous with NVT ensemble MD runs. For the first run one can calculate the average temperature for the cold region $T_{\text{cold,NVT}}$, the hot region $T_{\text{hot,NVT}}$ as well as the global NVT ensemble $T_{\text{c,NVT}}$. Another critical temperature $T_{\text{c,NVE}}$ can be determined while running a global NVE run after the NVT run and calculating the average NVE temperature (see Fig. 35).

The melting temperature can be obtained from the solid-liquid coexistence, where the free energies of solid and liquid states are equal. [217] One can compare the critical temperatures from both NVT and NVE run and approximate these values as melting temperature.

The advantage of the two-phase approach is that the melting temperature calculated match exactly the definition of the temperature for the coexistence of a solid and a liquid phase in equilibrium.

The disadvantage of the two-phase approach is that one needs to know optimal temperatures for the cold and the hot region. Optimal values for the cold and the hot region might only be a few Kelvin below or above the meting temperature, which is the unknown to be determined with this procedure. For lithium the two phase approach is applied with different values for the cold and the hot region (see Tab. 9). The values for the critical temperatures vary with different starting values (see Tab. 9) for the cold and hot region.

Table 9: Li: T_c results using two-phase approach. All values were calculated using LAMMPS applying the MEAM force field.

$T_{\text{cold,NVT}}$ [K]	$T_{\text{hot,NVT}}$ [K]	$T_{\text{c,NVT}}$ [K]	$T_{\text{c,NVE}}$ [K]
314	793	521	554
200	990	530	575
253	889	523	566
261	1190	646	701
192	693	407	441
144	840	435	471
141	642	352	384
401	499	445	451

T_c-MD workflow

The author proposes a different approach to calculate critical temperatures. Within previous calculations the diffusion coefficient D at different temperatures T has been determined (see Section 6.4.1). By analyzing the diffusion behavior (see Fig. 37), the temperature-dependent diffusion coefficients $D(T)$ show a similar behavior as determined by the one-phase approach. In detail, a $D(T)$ curve changes its behavior at critical temperatures. These critical temperatures might be identified as super-heating and super-cooling points similar to the ones introduced in the one-phase approach. Thus, melting points might be evaluated from the respective super-heating temperature T_p and super-cooling temperature T_m using Eq. (107). The values of $D(T)$ within a critical temperature region can be evaluated with a T_c fitting function developed for this purpose

$$log(D) = \Re(A((T - T_\mathrm{c})^\alpha - (T_\mathrm{c} - T)^\alpha + y_\mathrm{s})), \tag{108}$$

which is designed to evaluate the critical temperature T_c as well as the fitting exponent α. One can think of other fittings functions for this purpose as well as, but the focus of this work is to show that using a certain fitting function helps to determine critical temperatures in a more reproducible fashion as currently used procedures. As used in the Einstein relation D is the diffusion coefficient, $\Re$ denotes the real part, A is the amplitude of the fit function, T is the temperature and y_s is the offset of the fit function. Conceptionally, critical exponents describe the behaviour of physical properties close to the occurrence of phase transitions. It is believed that such exponents are to some degree *universal*, thus they only depend on general features and not on specific details of the investigated system. [219, 220] Such critical exponents as well as respective physical laws can be found for various physical quantities (i.e., magnetization, magnetic susceptibility and specific heat capacities). [221] In the context of critical temperatures, the fitting exponent α might help to determine groups of $\mathrm{Li}_x\mathrm{Si}_y$ phases showing similar behaviours. However, the relation of the used fitting exponents to critical exponents needs to be determined by further research. The proposed fitting procedure is applied for a set of temperatures T and corresponding $D(T)$ which show a distinct change (e.g., jump or step). Thus, one only needs to identify temperature regions showing such behaviours, everything else is uniquely determined within the accuracy of the performed fit, including the calculation of the critical temperatures. The overall procedure to determine the critical temperatures as well as fitting exponents is referred to as T_c-*MD* workflow (see Fig. 36).

The advantage of the T_c-MD workflow is that one only nees to determine the critical temperature regions and unique critical temperatures for these regions are obtained from the proposed fit.

The disadvantage of the T_c-MD workflow might be the limitation to systems showing significant changes in the diffusion behaviour.

To test and verify the T_c-*MD* workflow it is applied to calculate the critical temperatures for $\mathrm{Li}_x\mathrm{Si}_y$ systems. In addition, it will be shown that the proposed T_c-*MD* workflow indeed is able to calculate melting temperatures for investigated battery material. On the next pages the results for the T_c-*MD* workflow applied to $\mathrm{Li}_x\mathrm{Si}_y$ phases are presented, summarized and discussed in detail.

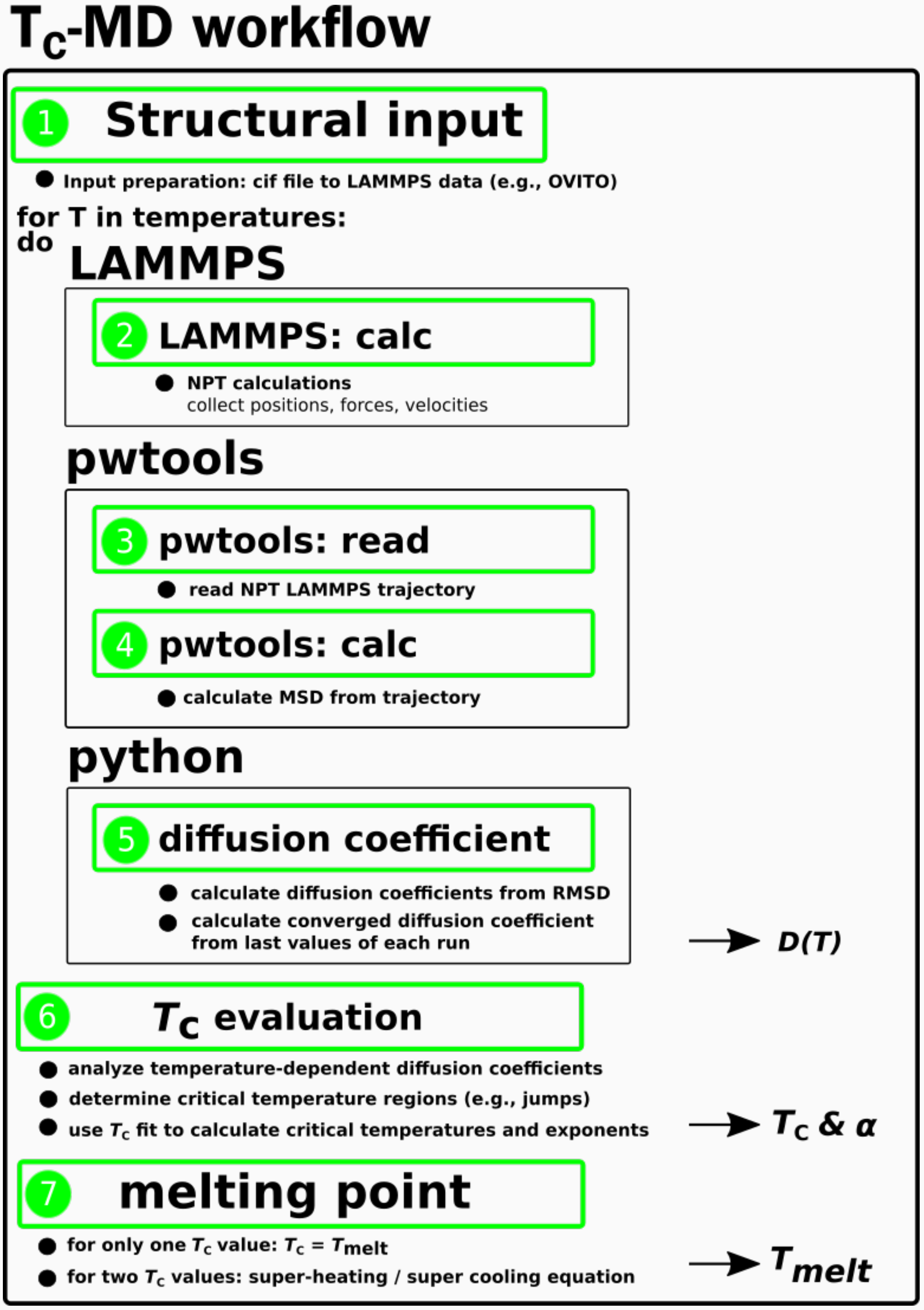

Figure 36: T_c-*MD* workflow as implemented in this work. The picture was produced by the author using INKSCAPE (see Appendix A).

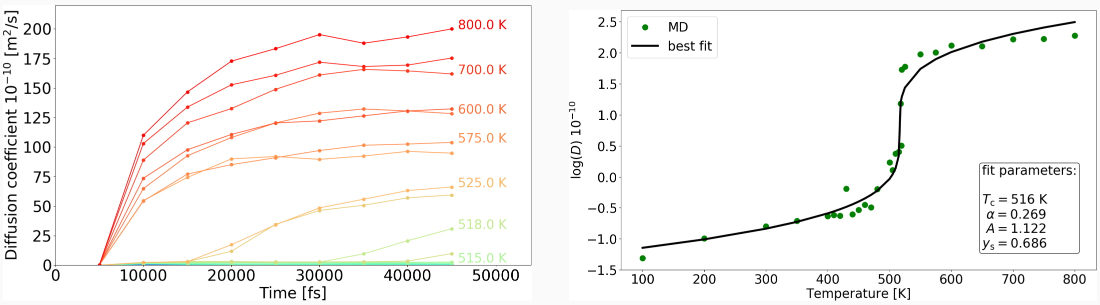

(a) Diffusion coefficients

(b) T_c-*MD* workflow

Figure 37: Li: Performed NPT MD runs enable the calculation of (a) temperature-dependent diffusion coefficients $D(T)$. Only selected curves are labeled with the respective temperatures of the MD run at the end of the curve to avoid overlapping of labels. The calculated $D(T)$ relation further allows (b) the determination of critical temperatures T_c using the T_c-*MD* workflow. For the T_c-*MD* workflow fitting procedure the lmfit Python packages was used. The obtained fitting parameters are provided as inset of subfigure (b). The calculations were performed with the LAMMPS code using NPT MD runs applying the MEAM force field. The pictures were produced by the author using Matplotlib (see Appendix A).

For Li, the diffusion coefficients are calculated from NPT ensemble MD calculations using LAMMPS with the MEAM force field for various temperatures (see Fig. 37 (a)). After a certain amount of timesteps the diffusion coefficients converged to a certain value for each run. The actual value is determined as the average of the last values of the run. The visualization of these converged diffusion coefficients for the respective temperatures shows, in case of Li, one distinct jump (see Fig. 37 (b)). This jump can further be analyzed using the proposed fitting procedure (see Fig. 37 (b)). For Li (see Tab. 10) the calculated $T_c = 516$ K agrees reasonably well with the experimental melting point of $T_{\mathrm{melt,exp}} = 453.15$ K [222].

Table 10: Li_xSi_y: Critical temperatures T_c, fitting exponents α and melting temperatures $T_{\mathrm{melt,calc}}$ calculated using the T_c-*MD* workflow.

Li_xSi_y	$T_{\mathrm{c,low}}$ [K]	α_{low}	$T_{\mathrm{c,high}}$ [K]	α_{high}	$T_{\mathrm{melt,calc}}$ [K]	$T_{\mathrm{melt,exp}}$ [K]
Li	-	-	516	0.269	516	453 [222]
Li_7Si_3	800	0.352	1199	0.266	1020	1027 [223]
$Li_{12}Si_7$	595	0.703	1049	0.483	854	921 [223]
$Li_{13}Si_4$	606	0.693	1162	0.531	929	995 [223]
$Li_{22}Si_5$	716	1.232	1081	0.822	917	901 [223]
LiSi	-	-	673	0.881	673	743 [223]
Si	-	-	2208	1.835	2208	1684 [224]

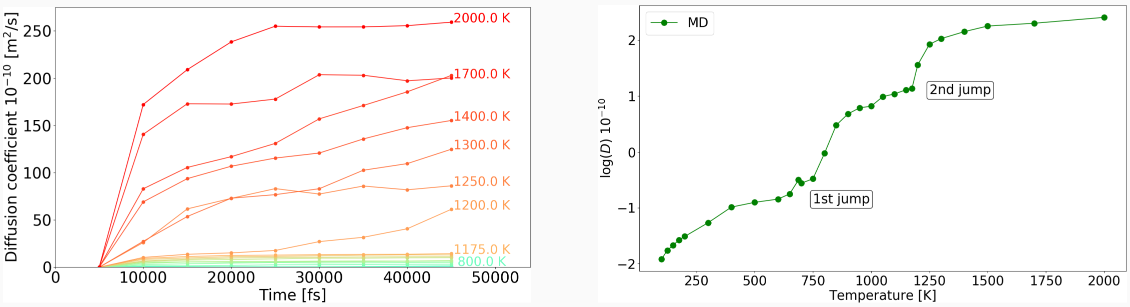

(a) Diffusion coefficients convergence (b) Converged diffusion coefficients

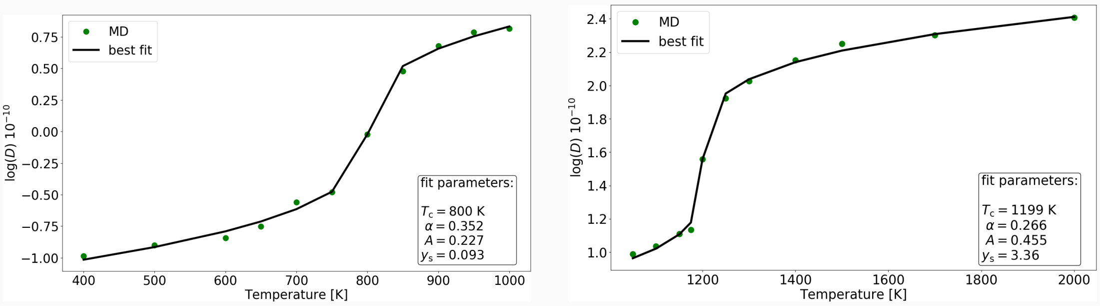

(c) T_c low temperature (d) T_c high temperature

Figure 38: Li_7Si_3: Performed NPT MD runs enable the calculation of (a) temperature-dependent diffusion coefficients $D(T)$. Only selected curves are labeled with the respective temperatures of the MD run at the end the curve to avoid overlapping of labels. The calculated $D(T)$ relation further allows (b) the determination of critical temperatures T_c using the T_c-*MD* workflow. The two critical regions determined within subfigure (b) are analyzed in the low temperature region in (c) and in the high temperature region in (d). For the T_c-*MD* workflow fitting procedure the LMFIT PYTHON packages was used. The obtained fitting parameters are provided as inset of subfigure (c) and (d). The calculations were performed with the LAMMPS code using NPT MD runs applying the MEAM force field. The pictures were produced by the author using MATPLOTLIB (see Appendix A).

The same procedure is also applied to the other systems of interest. For Li_7Si_3 (see Fig. 38) two critical temperature regions are observed, one for low temperatures and one for high temperatures. Thus, one can calculate two fitting exponents, one for each critical temperature region. The fitting exponents of the second one is very similar to the one of Li (see Tab. 10). Using the formula given for the one-phase approach (see Eq. (107)) for the two determined critical regions allows to calculate the melting point for Li_7Si_3 $T_{\text{melt,calc}} = 1020$ K, which is in excellent agreement with the experimental value of $T_{\text{melt,exp}} = 1027$ K [223].

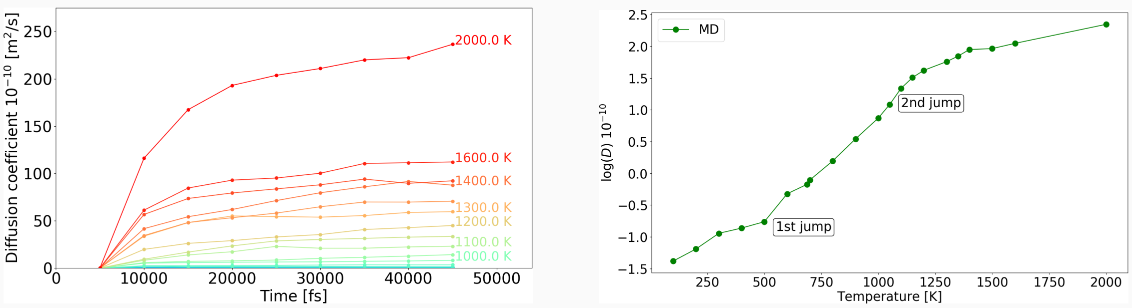

(a) Diffusion coefficients convergence

(b) Converged diffusion coefficients

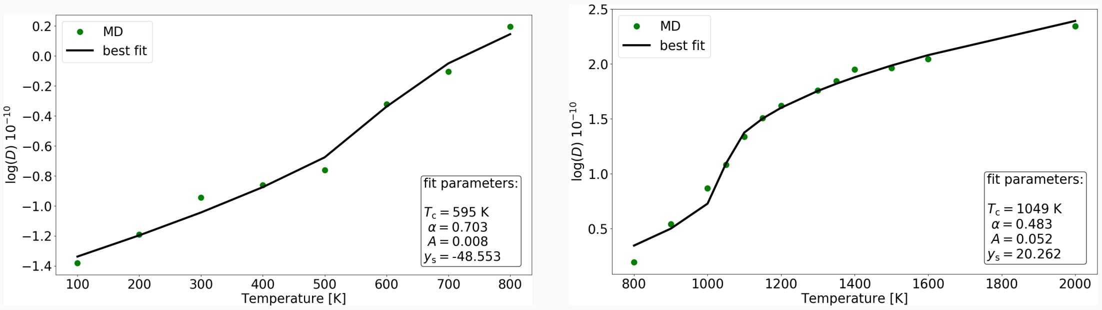

(c) T_c low temperature

(d) T_c high temperature

Figure 39: $Li_{12}Si_7$: Performed NPT MD runs enable the calculation of (a) temperature-dependent diffusion coefficients $D(T)$. Only selected curves are labeled with the respective temperatures of the MD run at the end the curve to avoid overlapping of labels. The calculated $D(T)$ relation further allows (b) the determination of critical temperatures T_c using the T_c-*MD* workflow. The two critical regions determined within subfigure (b) are analyzed in the low temperature region in (c) and in the high temperature region in (d). For the T_c-*MD* workflow fitting procedure the LMFIT PYTHON packages was used. The obtained fitting parameters are provided as inset of subfigure (c) and (d). The calculations were performed with the LAMMPS code using NPT MD runs applying the MEAM force field. The pictures were produced by the author using MATPLOTLIB (see Appendix A).

As for Li_7Si_3, also $Li_{12}Si_7$ shows two temperature regions (see Fig. 39 (c) and (d)), were distinct changes of the diffusion behavior can be determined (see Fig. 39 (b)). The melting point calculated from the two critical temperatures belonging to that temperature regions $T_{\text{melt,calc}} = 854$ K is in good agreement with the experimental melting point of $T_{\text{melt,exp}} = 921$ K [223]. The two fitting exponents are different from the values found for Li and Li_7Si_3 (see Tab. 10).

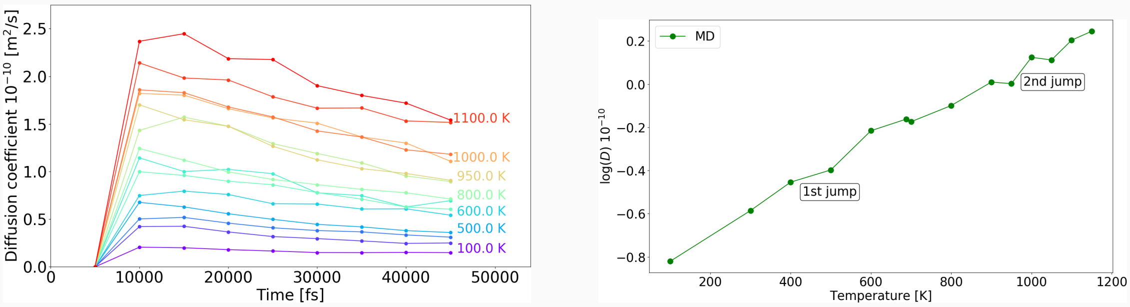

(a) Diffusion coefficients convergence (b) Converged diffusion coefficients

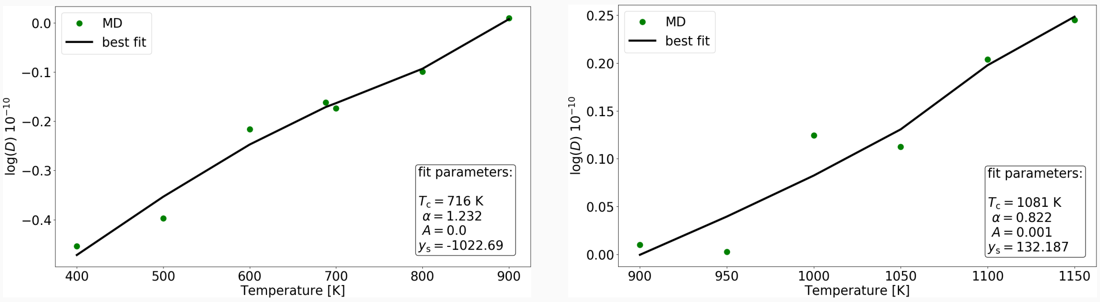

(c) T_c low temperature (d) T_c high temperature

Figure 40: $Li_{22}Si_5$: Performed NPT MD runs enable the calculation of (a) temperature-dependent diffusion coefficients $D(T)$. Only selected curves are labeled with the respective temperatures of the MD run at the end the curve to avoid overlapping of labels. The calculated $D(T)$ relation further allows (b) the determination of critical temperatures T_c using the T_c-*MD* workflow. The two critical regions determined within subfigure (b) are analyzed in the low temperature region in (c) and in the high temperature region in (d). For the T_c-*MD* workflow fitting procedure the LMFIT PYTHON packages was used. The obtained fitting parameters are provided as inset of subfigure (c) and (d). The calculations were performed with the LAMMPS code using NPT MD runs applying the MEAM force field. The pictures were produced by the author using MATPLOTLIB (see Appendix A).

$Li_{22}Si_5$ shows two temperature regions (see Fig. 40 (c) and (d)), were distinct changes of the diffusion behavior can be determined (see Fig. 40 (b)). The melting point calculated from the two critical temperatures belonging to that temperature regions $T_{\mathrm{melt,calc}}$ = 917 K is in good agreement with the experimental melting point of $T_{\mathrm{melt,exp}}$ = 901 K [223]. The two fitting exponents are different from the values found for Li, Li_7Si_3, and $Li_{12}Si_7$ (see Tab. 10).

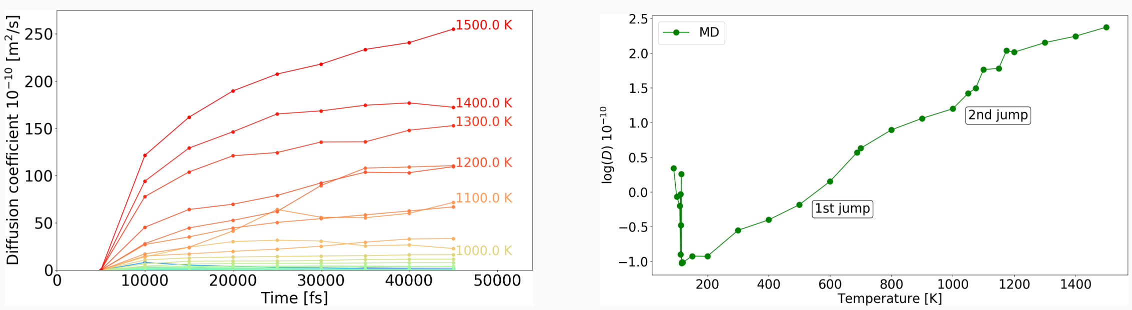

(a) Diffusion coefficients convergence

(b) Converged diffusion coefficients

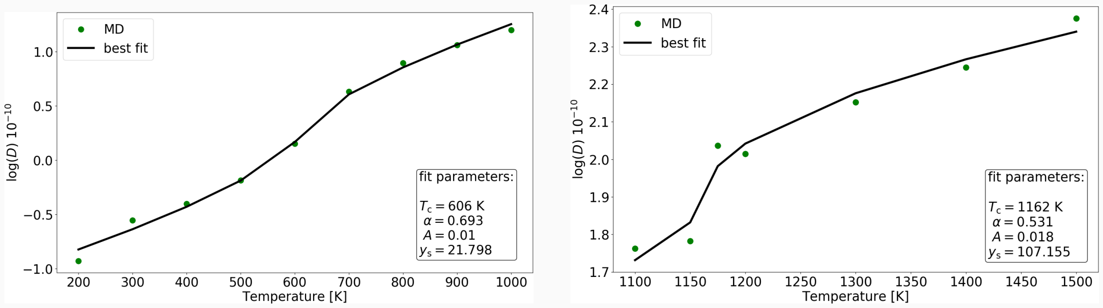

(c) T_c low temperature

(d) T_c high temperature

Figure 41: $Li_{13}Si_4$: Performed NPT MD runs enable the calculation of (a) temperature-dependent diffusion coefficients $D(T)$. Only selected curves are labeled with the respective temperatures of the MD run at the end the curve to avoid overlapping of labels. The calculated $D(T)$ relation further allows (b) the determination of critical temperatures T_c using the T_c-*MD* workflow. The two critical regions determined within subfigure (b) are analyzed in the low temperature region in (c) and in the high temperature region in (d). For the T_c-*MD* workflow fitting procedure the lmfit Python packages was used. The obtained fitting parameters are provided as inset of subfigure (c) and (d). The calculations were performed with the LAMMPS code using NPT MD runs applying the MEAM force field. The pictures were produced by the author using Matplotlib (see Appendix A).

$Li_{13}Si_4$ shows two temperature regions (see Fig. 41 (c) and (d)), were distinct changes of the diffusion behavior can be determined (see Fig. 41 (b)). The melting point calculated from the two critical temperatures belonging to that temperature regions $T_{\text{melt,calc}}$ = 929 K is in good agreement with the experimental melting point of $T_{\text{melt,exp}}$ = 995 K [223]. The fitting exponent is similar to the one in the high temperature region determined for $Li_{12}Si_7$ (see Tab. 10).

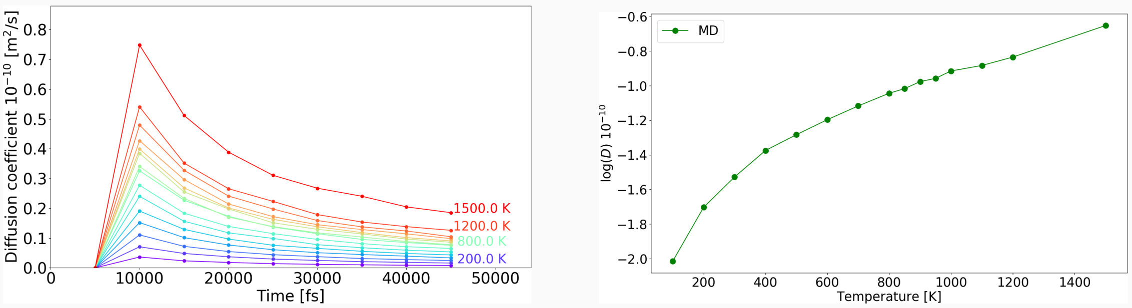

(a) Diffusion coefficients convergence

(b) Converged diffusion coefficients

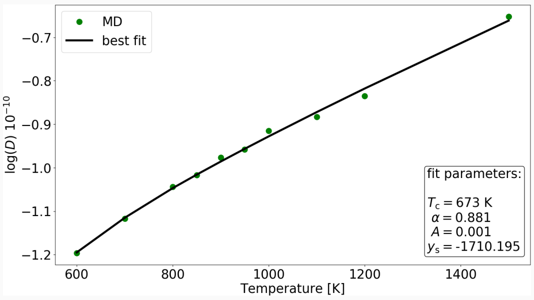

(c) T_c high temperature

Figure 42: LiSi: Performed NPT MD runs enable the calculation of (a) temperature-dependent diffusion coefficients $D(T)$. Only selected curves are labeled with the respective temperatures of the MD run at the end the curve to avoid overlapping of labels. The calculated $D(T)$ relation further allows (b) the determination of critical temperatures T_c using the T_c-*MD* workflow. One critical region was determined shown in subfigure (c). For the T_c-*MD* workflow fitting procedure the LMFIT PYTHON packages was used. The obtained fitting parameters are provided as inset of subfigure (c). The calculations were performed with the LAMMPS code using NPT MD runs applying the MEAM force field. The pictures were produced by the author using MATPLOTLIB (see Appendix A).

As in case of Li also for LiSi only one critical temperature region has been identified (see Fig. 42 (c)), were distinct changes of the diffusion behavior are observed. The critical temperature T_c is in this case identical to the melting point $T_{\mathrm{melt,calc}}$. The calculated melting point $T_{\mathrm{melt,calc}} = 673$ K is in good agreement with the experimental melting point of $T_{\mathrm{melt,exp}} = 743$ K [223]. The determined fitting exponent is similar to the one in the high temperature region for $Li_{22}Si_5$ (see Tab. 10).

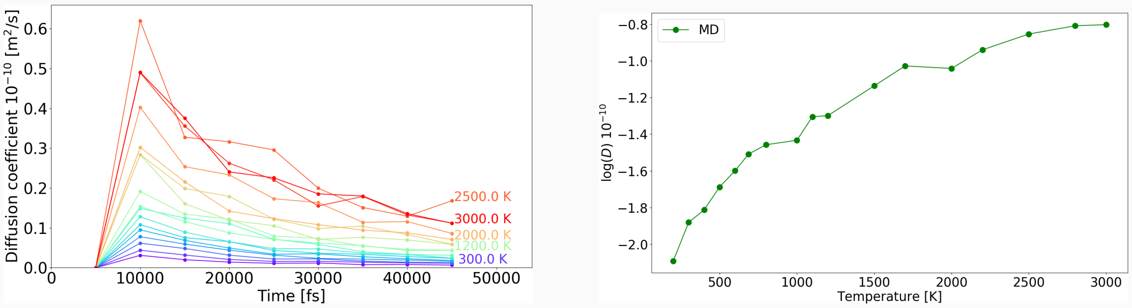

(a) Diffusion coefficients convergence

(b) Converged diffusion coefficients

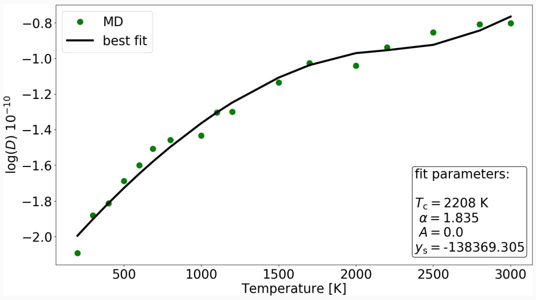

(c) T_c high temperature

Figure 43: Si: Performed NPT MD runs enable the calculation of (a) temperature-dependent diffusion coefficients $D(T)$. Only selected curves are labeled with the respective temperatures of the MD run at the end the curve to avoid overlapping of labels. The calculated $D(T)$ relation further allows (b) the determination of critical temperatures T_c using the T_c-*MD* workflow. One critical region was determined shown in subfigure (c). For the T_c-*MD* workflow fitting procedure the LMFIT PYTHON packages was used. The obtained fitting parameters are provided as inset of subfigure (c). The calculations were performed with the LAMMPS code using NPT MD runs applying the MEAM force field. The pictures were produced by the author using MATPLOTLIB (see Appendix A).

As in case of Li and LiSi, also for Si only one critical temperature region has been identified (see Fig. 43 (c)), which corresponds to the global temperature region. Also for Si the calculated critical temperature T_c is identical to $T_{\mathrm{melt,calc}}$. The calculated melting point $T_{\mathrm{melt,calc}} = 2208$ K overestimates the experimental melting point of $T_{\mathrm{melt,exp}} = 1684$ K [223]. The determined fitting exponent has the highest value from all investigated systems.

In summary, for $Li_{12}Si_7$, and $Li_{13}Si_4$ (see Fig. 39 and 41) two critical regions are observed, where each of the fitting exponents are quite similar ($\alpha_{\text{low}} = 0.7$, $\alpha_{\text{high}} = 0.5$), but are different from the ones observed for Li and Li_7Si_3 ($\alpha_{\text{high}} = 0.3$). On the other hand, the fitting exponents of Li and Li_7Si_3 are quite similar. The systems Li, LiSi and Si showing only one critical temperature region and the highest fitting exponents ($\alpha_{\text{high}} = [0.8, 0.9, 1.8]$).

Thus, one can group the investigated systems using the second order fitting exponents. The first group g_1 (lithium like phases, high lithium diffusion) having the fitting exponent $\alpha = 0.3$ and the member $\{Li, Li_7Si_3\} \in g_1$. The second group g_2 (confined lithium diffusion) showing up the fitting exponent $\alpha = 0.5$ with the members $\{Li_{12}Si_7, Li_{13}Si_4\} \in g_2$. And the third group g_3 (silicon like phases, lower lithium diffusion) with the fitting exponents $\alpha = [0.8, 0.9, 1.8]$ and the members $\{Li_{22}Si_5, LiSi, Si\} \in g_3$. A phase group diagram visualizes these findings (see Fig. 6.4.2). For all systems showing only one critical temperature, this value is approximated as the melting temperature. For systems showing up more than one critical temperature, these temperatures are approximated as super-cooling and super-heating critical temperatures. The melting point for these systems is calculated as it is done in the one-phase approach.

The calculated melting points are in good agreement with experimental reference values (see Tab. 10). Given these results, the T_c-MD workflow delivers suitable results for Li_xSi_y.

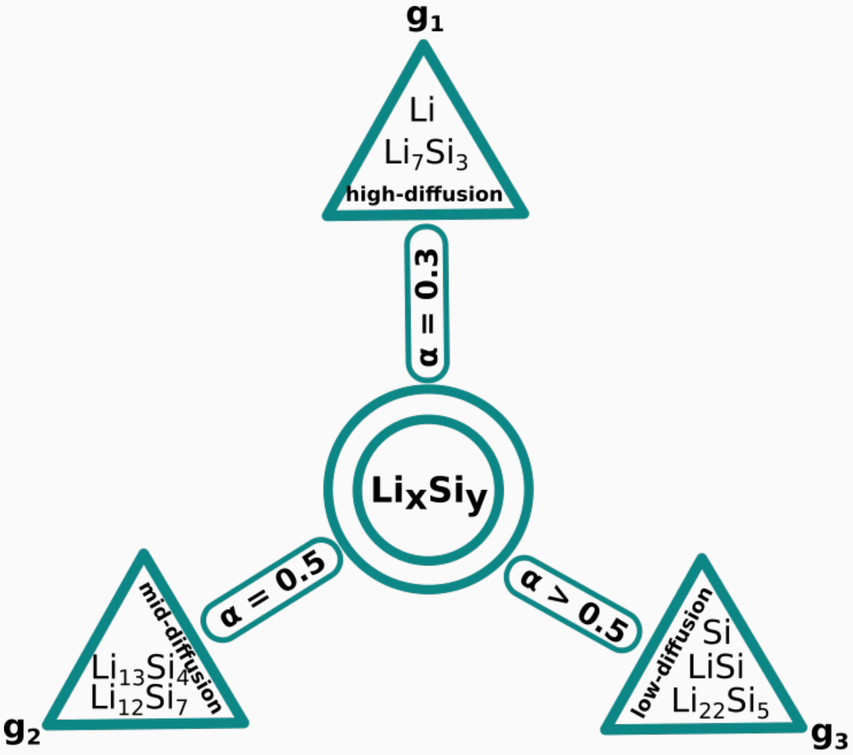

Figure 44: Phase group diagram for Li_xSi_y binary system evaluated with fitting exponents α calculated with the T_c-MD workflow. The picture has been produced by the author using MATPLOTLIB (see Appendix A).

6.5 CALCULATED PHASE DIAGRAM

Having calculated the critical temperatures and melting points for the Li_xSi_y systems allows a theoretical assessment of a phase diagram for the investigated Li_xSi_y phases (see Fig. 6.5). There exist a variety of thermodynamics assessments using the CALPHAD methodology to evaluate the phase diagram for the Li-Si binary system [225–230]. These phase diagrams show similarities as well as differences comparing all of them. The major difference might be the actual set of Li-Si structures included in the phase diagram. The objective is not to compare the calculated phase diagram with the ones available, the goal is to show that one can access the phase diagram for selected structures purely theoretically. As discussed previously, some of the discussed Li-Si structures only differ by one lithium atom in the given crystal structure (e.g., $Li_{21}Si_5$ and $Li_{22}Si_5$). For a theoretical phase diagram the diffusion coefficients have been evaluated, which show very high values for selected phases. Thus, at a given temperature there might be not one fixed structure, as lithium tends to move within the system. Instead, as shown in the previous section there might be groups of Li_xSi_y structures showing very similar diffusion effects. Concluding, future investigations or assessments of the Li-Si system might need to switch the perspective from a fixed set of possible crystal structures to a global dynamical system dominated by diffusion.

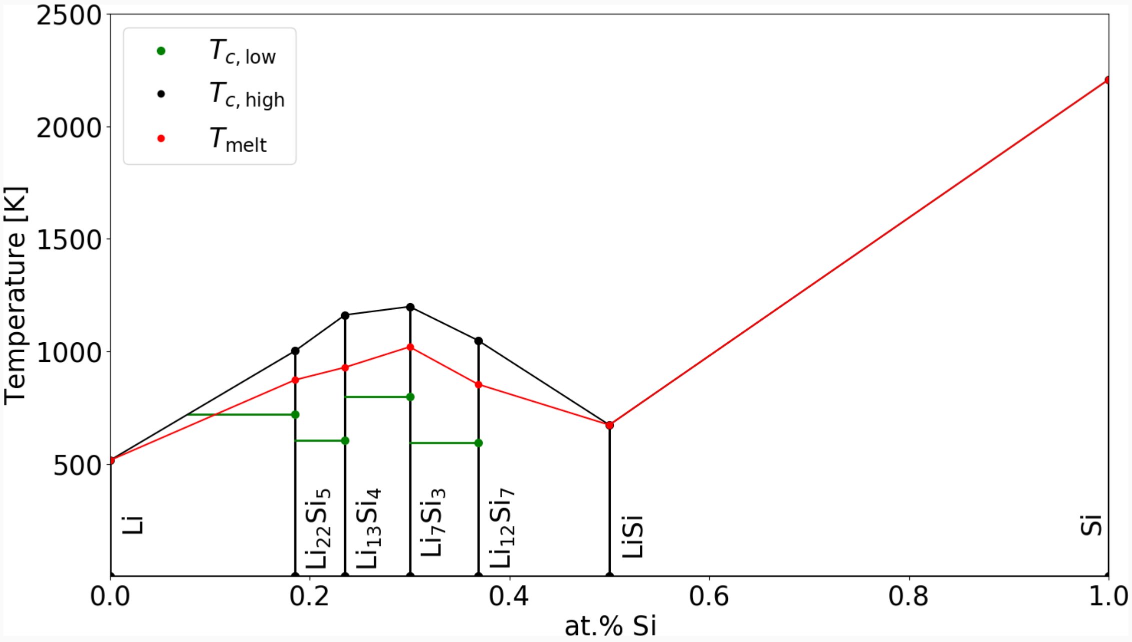

Figure 45: Calculated phase diagram for Li_xSi_y binary system evaluated with critical temperatures calculated with the T_c-*MD* workflow. The picture has been produced by the author using MATPLOTLIB (see Appendix A).

6.6 COMPUTATIONAL TIME ANALYSIS

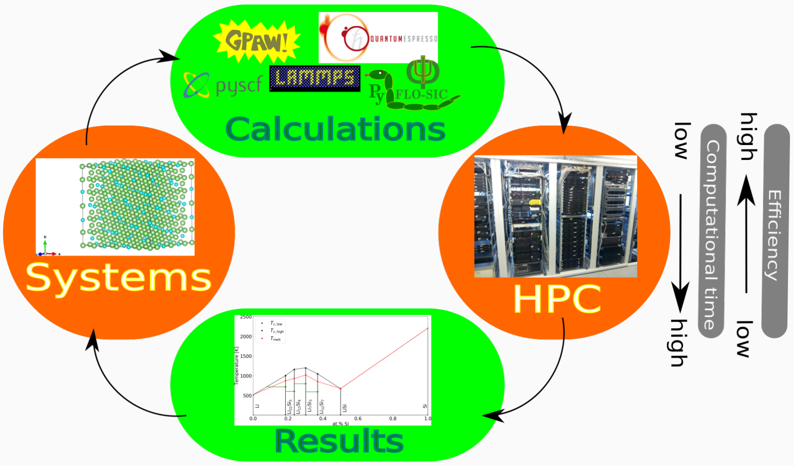

Figure 46: Visualization of computational resources needed to perform computations with high numerical effort. The system visualized is $Li_{22}Si_5$, the code logos are freely available at the respective code homepages (see Appendix A), the picture of the HPC was made by the author and the phase diagram presented is the computed one of the last section. The picture was produced by the author using INKSCAPE (see Appendix A).

To perform computational investigations, especially the ones with high numerical effort (e.g., QHA using DFT), one needs a certain amount of computational time on a high performance computing (HPC, see Fig. 46). Computational time is the amount of wall time which is required to perform a specific computational task. The process time or central processing unit (CPU) time can be measured in CPUh (CPU hours). This time is a measure for the amount of time a CPU was used to process instructions of a computer program or operating system. Many theoretical or computational institutes host local cluster were the computational time might not be limited, but the performance is limited by the facilities. Thus, one typically needs to apply for computational time on an external HPC. An essential part of this work was calculated on the ZIH Dresden (mainly on the Taurus HPC cluster). The author has applied as co-author for several millions of CPUh during this thesis. In this section the numerical effort of the standard QHA workflow using DFT is compared to the C_p-*MD* workflow.

Computational thermodynamics based on DFT is able to deliver accurate specific heat capacity values in low temperature regime (0 - 300 K). Such calculations become numerically demanding if the system has no symmetry or a high number of atoms in the unit cell (see Tab. 11). To calculate thermodynamical properties using QHA applying DFT for the Li_xSi_y phases, approximately 8.2×10^6 CPUh were used. This high amount of CPU time is due to the fact that each symmetry non-equivalent atom needs to be shifted out of its equilibrium position and the resulting forces have to be calculated. As shown in the previous sections, the C_p-*MD* workflow can calculate thermodynamical properties with a suitable accuracy compared to the standard approach of QHA using DFT. Besides this, the C_p-*MD* workflow is orders of magnitudes faster than the standard procedure (see Tab. 12). Using the C_p-*MD* workflow to determine the same set of thermodynamical properties for the Li_xSi_y phases requires only 672 CPUh. This is an significant improvement as calculations need to use resources such as energy required to perform the calculations in a most efficient and ecologically sustainable way.

Table 11: CPU time for *ab initio* computational thermodynamics. The time of self-consistent-field calculation is t_{SCF}, the number of cores used for the SCF calculation is $N_{\mathrm{cores}}^{\mathrm{SCF}}$, the time for one displacement is t_{disp}, the number of cores used for the displacement calculations is $N_{\mathrm{cores}}^{\mathrm{disp}}$, the number of calculated volumes is N_{vol}, the number of displacements is N_{disp}, the time for one quasi-harmonic approximation (QHA) run per structure is t_{QHA}, the error factors (e.g., k-point/-supercell convergence, structural considerations and numerical artifacts which lead to a rerun of the whole QHA calculation for this structure) are e and the total time for a whole *ab initio* thermodynamical calculation for one structure is t_{total}.

Li_xSi_y: CPU time for *ab initio* computational thermodynamics

System	t_{SCF} [CPUh]	$N_{\mathrm{cores}}^{\mathrm{SCF}}$	t_{disp} [CPUh]	$N_{\mathrm{cores}}^{\mathrm{disp}}$	N_{vol}	N_{disp}	t_{QHA} [CPUh]	e	t_{total} [CPUh]
Li	0.1	3	3	3	5	2	91.5	1	92
$Li_{12}Si_7$	0.2	216	2	288	5	120	345816	1	345816
Li_7Si_3	0.1	16	5	12	5	20	6008	3	18008
$Li_{13}Si_4$	0.2	60	9	72	5	36	116700	36	4199100
$Li_{15}Si_4$	0.2	24	4	60	5	10	12024	1	12024
$Li_{17}Si_4$	0.2	64	14	184	5	42	541024	2	1081984
$Li_{22}Si_5$	4.0	24	7	300	5	48	504480	5	2520480
Si	0.1	4	0.1	2	5	2	4	1	4
Total time									**8.2×10^6 CPUh**

Table 12: CPU time using MD computational thermodynamics for the Li-Si binary system. The time of a bulk modulus calculation is t_B, the number of performed NPT calculations is N_{NPT}, the number of used cores for each NPT calculations is $N_{\mathrm{cores}}^{\mathrm{NPT}}$, the time of a α calculations is t_α, the time of a PDOS calculation is t_{PDOS}, the number of cores used for each PDOS calculation is $N_{\mathrm{cores}}^{\mathrm{PDOS}}$, the error factors are e, the time for one complete MD C_p calculation is t_{MD} and the total time for a whole MD C_p thermodynamical calculation for one structure is t_{total}.

Li_xSi_y: CPU time for MD computational thermodynamics

System	t_B [CPUh]	N_{NPT}	$N_{\mathrm{cores}}^{\mathrm{NPT}}$	t_α [CPUh]	t_{PDOS} [CPUh]	$N_{\mathrm{cores}}^{\mathrm{PDOS}}$	e	t_{MD} [CPUh]	t_{total} [CPUh]
Li	0	27	40	0.12	8	200	15	11.24	168.6
$Li_{12}Si_7$	0.26	35	22	0.17	9.77	22	3	15.98	47.94
Li_7Si_3	0	15	22	0.14	11.69	22	1	13.79	13.79
$Li_{13}Si_4$	0.02	29	16	0.24	24.01	100	6	31.00	185.94
$Li_{22}Si_5$	0.06	26	40	0.57	46.56	100	3	61.44	184.32
Si	0.05	24	1	0.03	3.7	1	16	4.47	71.52
Total time									**672 CPUh**

6.7 CONCLUSION

In this chapter it was shown that for the complex material class of lithium silicides, it is possible to calculate properties, such as elastic constants and bulk moduli, with comparable accuracy to DFT using one MEAM force field (see Tab. 5). Thermodynamical properties based on a phonon density of states have been calculated using DFT as well as MEAM FF. In addition, it was shown that the C_p-*MD* workflow is able to calculate the isobaric heat capacity numerically efficient (cp. Tab. 11 and Tab. 12) and accurate compared to experimental or *ab initio* data.

The C_p-MD workflow also allows structural screening and the inclusion of diffusive effects, which was not possible using the standard methods. A further advantage of this approach is that the estimate in the high temperature regime of specific heat becomes more accurate than the standard method. This observation is based on the fact that the MD method allows for structural changes due to the effect of temperature. For $Li_{12}Si_7$ and $Li_{22}Si_5$, two extended temperature ranges with almost constant but different linear expansion coefficients for both structures have been identified using this method. One of this expansion coefficients describes the low temperature region, whereas the other one describes the high temperature region.

A temperature-dependent phonon density of states was presented, which in case of $Li_{13}Si_4$ shows a better agreement between the C_p-*MD* workflow and the obtained *ab initio* data by freezing out the diffusion process using a low temperature phonon density of states. In general the *ab initio* thermodynamical calculations are in excellent agreement with experimental data in the low temperature region (0 - 300 K), while the C_p-*MD* workflow based thermodynamical data can deliver a faster description in good agreement with experimental data, especially in the high temperature limit ($T > 300$ K). Other groups showed that an explicit treatment of anharmonic effects is necessary to overcome the limitations of the quasi-harmonic approximation [174–176]. The C_p-*MD* workflow is able to describe the high temperature limit better by using a temperature-dependent phonon density of states (see Fig. 32). Additionally, linear expansion coefficients were determined by performing a set of NPT-ensemble MD runs (see Fig. 30 and Fig. 31).

The essential advantage of the C_p-MD workflow is that it is capable to describe the structural change due to the effect of temperature (e.g., see radial distribution function (RPDF) Fig. 28 (a) and Fig. 30 (a)). Thus, the C_p-*MD* workflow allows to describe diffusion effects as well as melting behavior of the treated system. Based on these essentials of the C_p-*MD* workflow, it was observed that Li atoms in the $Li_{22}Si_5$ phase show amorphous/liquid-like behavior (e.g., RPDF Fig. 31 (a)). If this behavior is correct it may also explain why it is difficult to distinguish between $Li_{22}Si_5$, $Li_{21}Si_5$ and $Li_{17}Si_4$ experimentally, as all of them have a high and very similar Li content.

The T_c-MD workflow has been proposed for the calculation of critical temperatures, exponents and melting temperatures. The calculated melting points using the T_c-*MD* workflow are in good agreement with experimental values (see Tab. 10). The analysis of the fitting exponents showed that there may be groups of Li_xSi_y showing a similar diffusion behavior (see Fig. 6.4.2). This might further explain why it is difficult for experiments to distinguish some phases. Finally, a purely theoretical phase diagram for the Li_xSi_y system was presented (see Fig. 6.5).

7

METAL-ORGANIC FRAMEWORKS

7.1 STRUCTURAL CONSIDERATION

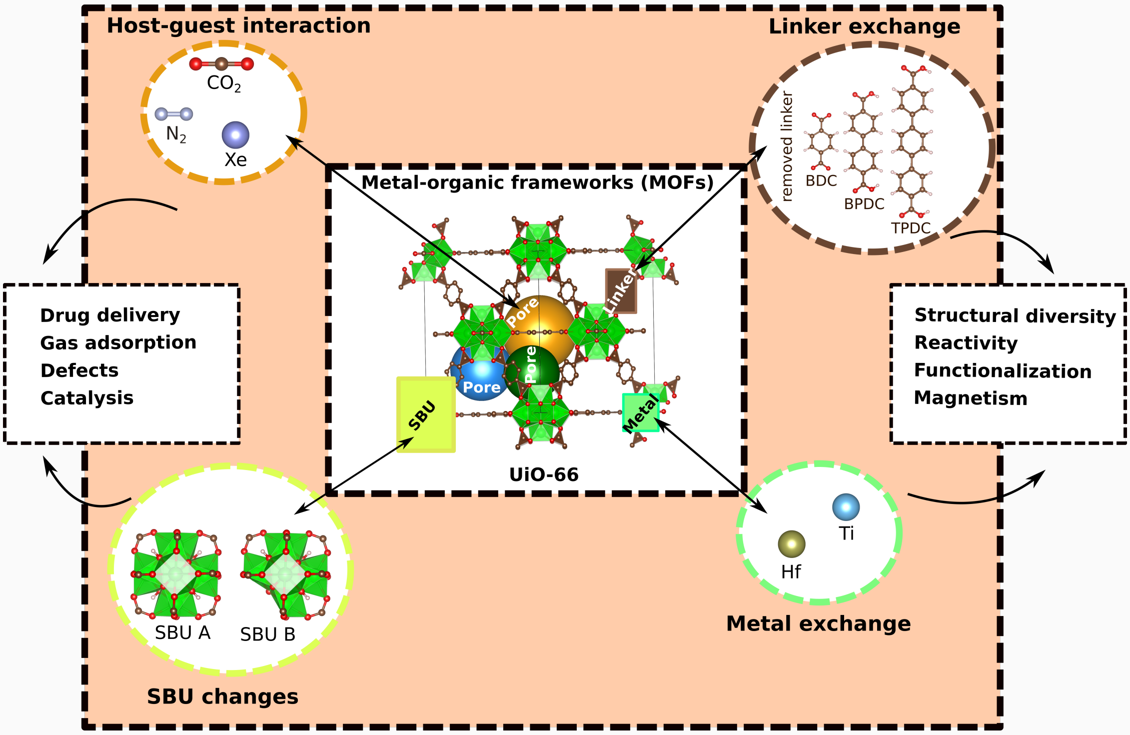

Figure 47: General overview of metal-organic frameworks (MOFs). MOFs can be build up by connecting secondary building units (SBUs) with organic linkers. Both SBU (e.g., SBU changes, metal exchange [231]) and linkers (e.g., missing linkers [232, 233]) can have defects, which can change the properties of a MOF. In addition, MOFs have empty space referred to as pores [234]. Guest atoms or molecules can be adsorbed within these pores if respective pore windows are big enough. This may lead to host-guest interactions. These structural properties of MOFs allow possible applications for gas adsorption, drug delivery or catalysis.

Metal-organic frameworks (MOFs) consist of a central unit containing metal centers, called secondary build unit *SBU*, which are connected through organic molecules called *linkers* (see Fig. 47). SBUs are sometimes referred to as bricks or nodes. As the linker connect the SBUs, there can be empty space between these linkers called a *pore*. The number of different pores as well as the pore diameters vary between different MOFs. Given these pores, MOFs might offer various application (e.g., gas adsorber, drug delivery, catalysis) based on the adsorption of species like simple atoms (e.g., Xe) or molecules (e.g., N_2, CO_2) and storing them in the empty pores.

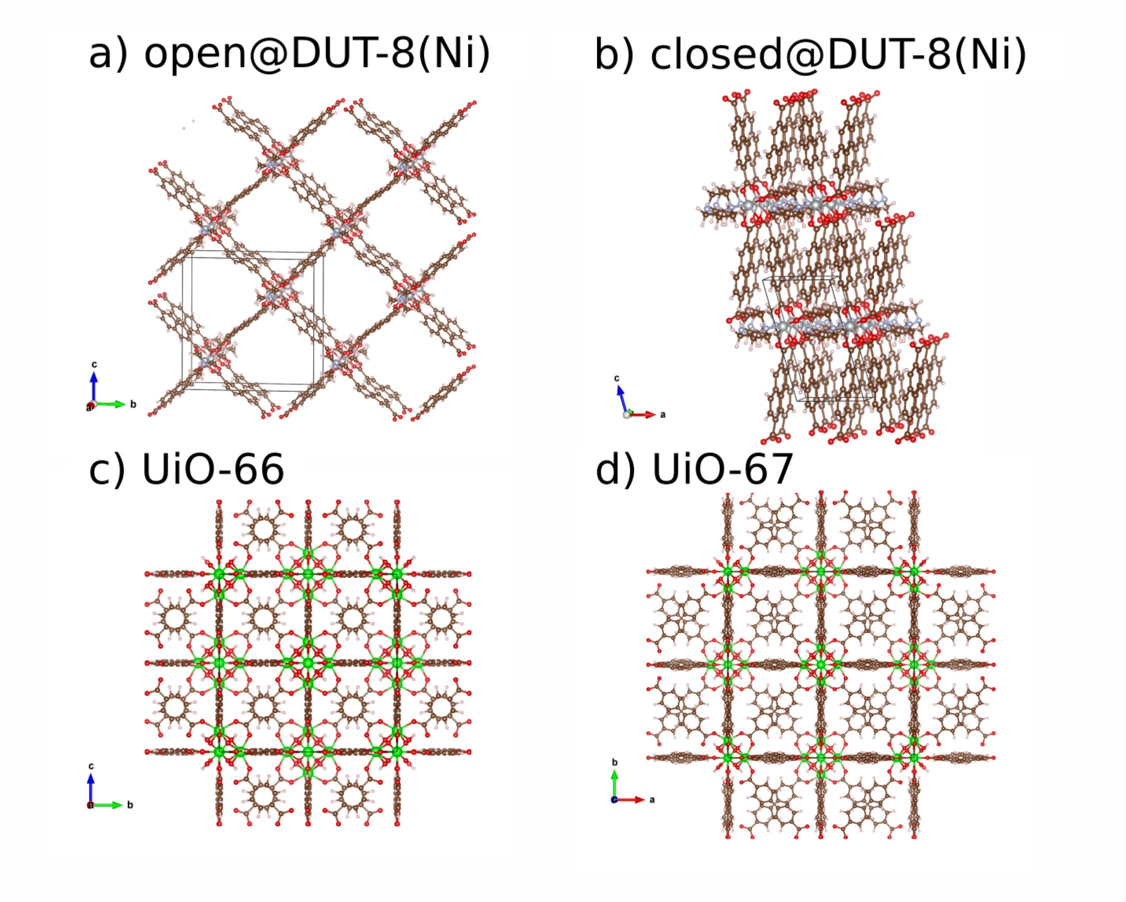

Figure 48: Metal-organic frameworks (MOFs) typically have high porosity by exhibiting large pores like for (a) open@DUT-8(Ni). Some MOFs are flexible (e.g., DUT-8(Ni)) and besides the open structure also the closed structure shown in (b) closed@DUT-8(Ni) can exist. Other MOFs even show up in families (e.g., the UiO family with (c) UiO-66 and (d) UiO-67). The picture was produced by the author using VESTA and INKSCAPE (see Appendix A).

HKUST-1 (HKUST - *Hong Kong University of Science and Technology*) is one of the best-known representatives of the MOF class. A lot of reference data is available for HKUST-1, which offers the possibility to use this MOF for proof-of-principles calculations.

MOFs can exist in families, i.e., the UiO (UiO - *Universitetet i Oslo*) family consisting of UiO-66, UiO-67, UiO-68 and others. The different UiOs differ in the respective linker size going from smaller to larger linkers from UiO-66 to UiO-68.

DUT-8(Ni) (DUT - *Dresden University of Technology*) is a flexible MOF existing in an open and a closed state. The number of atoms per unit cell may differ with each sample of a MOF. In reality, MOFs might not be entirely empty, linkers might be broken or SBUs disordered. A synthesized MOF may include some adsorbate molecules in the respective pores.

The symmetry of the mentioned MOFs are initially determined with a self-written program utilizing the SPGLIB [235] PYTHON library. Given a cif file, the code allows for an analysis of the symmetry, especially the space group, and provides the primitive and the conventional setting of the unit cell.

Table 13: Symmetry, metal centers in the SBUs and linker of MOFs (benzene-1,3,5-tricarboxylic acid (BTC) , biphenyl-4,4′-dicarboxylate (BPDC), benzene-1,4-dicarboxylate (BDC), p-terphenyl-4,4″-dicarboxylate (TPDC), 2,6-naphthalenedicarboxylate (NDC), 1,4-diazabicyclo[2.2.2]octane (DABCO)).

MOF	reference	space group		metal center	ligand
HKUST-1	[238]	225	$Fm\bar{3}m$	Cu^{2+}	BTC
IRMOF-10	[239]	225	$Fm\bar{3}m$	Zn^{2+}	BPDC
UiO-66	[236]	216	$F\bar{4}3m$	Zr^{4+}	BDC
UiO-67	[236]	196	$F23$	Zr^{4+}	BPDC
UiO-68	[236]	216	$F\bar{4}3m$	Zr^{4+}	TPDC
open@DUT-8(Ni)	[240]	11	$P21m$	Ni^{2+}	NDC DABCO
closed@DUT-8(Ni)	[240]	1	$P1$	Ni^{2+}	NDC DABCO

Table 14: Structural parameters of the investigated MOFs. The cell parameters a, b and c are given Å and the angles α, β and γ are given in °.

MOF	unit cell	a	b	c	α	β	γ	N_{atoms}
HKUST-1	CUC	26.303	26.303	26.303	90	90	90	672
HKUST-1	PUC	18.599	18.599	18.599	60	60	60	168
IRMOF-10	CUC	34.281	34.281	34.281	90	90	90	664
IRMOF-10	PUC	24.240	24.240	24.240	60	60	60	166
UiO-66	CUC	20.978	20.978	20.978	90	90	90	456
UiO-66	PUC	14.834	14.834	14.834	60	60	60	114
UiO-67	CUC	27.094	27.094	27.094	90	90	90	696
UiO-67	PUC	19.158	19.158	19.158	60	60	60	174
UiO-68	CUC	33.331	33.331	33.331	90	90	90	936
UiO-68	PUC	23.569	23.569	23.569	60	60	60	234
open@DUT-8(Ni)	PUC	18.431	18.431	9.391	90	90	90	132
closed@DUT-8(Ni)	PUC	6.947	8.181	12.172	91.1	103.9	104.5	66

The symmetries (see Tab. 13) and structural parameters (see Tab. 14) of the investigated MOFs for the conventional unit cell (CUC) for UiO-66, UiO-67, and UiO-68 are in excellent agreement with the values reported by [236]. Such a pre-processing step can save computational time, because the determined primitive unit cell (PUC) of each MOF reduces the number of atoms by a factor of 4. While the space group for UiO-66 agrees with [9] ($F\bar{4}3m$), the one for UiO-67 is different ($F23$ compared to $F\bar{4}3m$). Rogge et al. [237] analyzed the effect of pressure on MOFs of the UiO family and reported distinct space groups for different volumes of UiO-66 ($Pnnm$ to $Fm\bar{3}m$), UiO-67 ($Pa\bar{3}$ to $Fm\bar{3}m$), and UiO-68 ($Pa\bar{3}$ to $Fm\bar{3}m$).

7.2 PREPARATION OF CALCULATIONS

In DFT one only needs the structural information (e.g., nuclei positions and cell information). For force field or molecular mechanics (MM) modelling one further needs information about the coordination of a respective atom. Many force fields can have several species for one element with different local chemical environments. Such species may be called molecular mechanics datatyes (MMtypes). For simple molecules or structures, the assignment of these datatypes is straightforward. For complex or large unit cell as for MOFs the correct assignment might be complicated. For MOFs there exist two codes LAMMPS-INTERFACE [8] and AuToGraFS [178] which enable an automatic assessment of MMtypes for structural inputs (e.g., cif files). While LAMMPS-INTERFACE produces input for the LAMMPS code, AuToGraFS produces input files for the GULP code.

7.3 PROPERTIES AND SYMMETRY

The different space group assignments for UiO-66 and UiO-67 motivated the author to investigate these systems in more detail.

The electronic structure of the systems was studied with LSDA GPAW in the LCAO mode with a grid refinement factor $h = 0.1$ and the dzp basis set. A developer branch of the GPAW code by Aleksei Ivanov was used, which allows the usage of a direct minimization LCAO eigensolver (see Appendix A) guaranteeing that the total energy converges variationally. The energy volume curve has been calculated, while the atomic positions are relaxed (with a BFGS algorithm using ASE with a force criteria of $f_{\max} = 0.001$ eV/Å) for each volume. The relaxation is important as the calculated bulk modulus indicates the material as a soft material. Thus, small changes by, e.g., an external pressure might lead to a significant response of the system.

The porosity was analyzed with poreE mainly developed by Kai Trepte. The author co-developed poreE [241] with the focus of increasing user-friendliness, providing a Python GUI allowing the usage of poreE Fortran routines as shared libraries within Python to enable calculations, called PyPORE. The poreE code is able to calculated porosities with the Helium approach, with the overlapping sphere or a grid based approach. The grid approach is able to separate void and accessible volume. In addition to that, poreE can calculate pore size distributions (PSD) as well as pore windows.

The symmetry of the system was analyzed with various symmetry tools (Spglib [235], PLATON [242], FINDSYM [243] and AFLOW-SYM [244]). The usage of various symmetry tools was essential to resolve the symmetry problem.

The SBUs and linkers of the relaxed minima structures were prepared for the usage with AuToGraFS (version 2.3.2) to validate the topology of the determined structures. For AuToGraFS one needs to define the coupling points between SBU and linker. Having such prepared SBUs and linkers and a given topology allows AuToGraFS to automatically build periodic MOFs structures.

7.3.1 *UiO-66*

As the initial and essential step for these investigations, the energy volume curve for UiO-66 has been calculated with LSDA GPAW and is visualized in Fig. 49. Using the LAMMPS-INTERFACE with the universal force field (UFF) [155, 156] allowed for a larger screening of volumes and thus helped to determine stable EOS fit regions for the LSDA GPAW calculations. Besides the properties of the energy, this interface also provides pressures for each volume, thus one can apply the EOS relation directly to the pressure-volume pV curve and compare these results with the pressure-volume relation gained from the energy-volume fit for the LSDA GPAW results (see Fig. 50). Within a region around the experimental determined ground state volume, three distinct configurations of UiO-66 are observed, called hereafter C_1@UiO-66, C_2@UiO-66 and C_3@UiO-66

Table 15: UiO-66 configurations: Electronic and mechanical properties. The calculation were performed with LSDA using GPAW. The bulk modulus was calculated for Murnaghan equation of state for C_1, C_2 and C_3 in the volume ranges of (V_{min}= 1991 Å^3,V_{max}= 2060 Å^3), (V_{min}= 2070 Å^3,V_{max}= 2132 Å^3), (V_{min}= 2140 Å^3,V_{max}= 2400 Å^3)). The porosities Φ were evaluated with the grid approach with PorE using a 100 x 100 x 100 grid.

Configuration	V	E_{tot}	E_{g}	B	Φ void	Φ accessible
	[Å^3]	[eV]	[eV]	[GPa]	[%]	[%]
C_1@UiO-66	2056.97	-889.32562	2.670	42.41	55.51	48.36
C_2@UiO-66	2131.38	-890.16659	2.723	39.33	56.81	49.81
C_3@UiO-66	2199.21	-890.59438	2.776	40.23	57.72	50.77

Table 16: UiO-66 configurations: symmetry analysis. The tag min represents the symmetry detected at the chosen minimal tolerance setup for the respective code, whereas max indicates the symmetry for the maximal tolerance value. The detailed tolerance benchmarks of each code can be found in the Appendix (see Section A.3).

Configuration	Spglib		PLATON		FINDSYM		AFLOW-SYM	
	$\varepsilon_{\mathrm{min}}$	$\varepsilon_{\mathrm{max}}$	$\varepsilon_{\mathrm{min}}$	$\varepsilon_{\mathrm{max}}$	$\varepsilon_{\mathrm{min}}$	$\varepsilon_{\mathrm{max}}$	$\varepsilon_{\mathrm{min}}$	$\varepsilon_{\mathrm{max}}$
C_1@UiO-66	$P1$	$F\bar{4}3m$	$P1$	$F\bar{4}3m$	$P1$	$F\bar{4}3m$	$P1$	$F\bar{4}3m$
C_2@UiO-66	$P1$	$F\bar{4}3m$	$P1$	$F\bar{4}3m$	$P1$	$F\bar{4}3m$	$P1$	$F\bar{4}3m$
C_3@UiO-66	$P1$	$F\bar{4}3m$	$P1$	$F\bar{4}3m$	$P1$	$F\bar{4}3m$	$P1$	$F\bar{4}3m$

(see Tab. 15). The energy volume curve can be fitted for each configuration separately, leading to three different bulk moduli (see Tab. 15). The lowest energy structure is represented by configuration C_3@UiO-66 with a bulk modulus of 40.23 GPa. Configuration C_2@UiO-66 has a higher energy and a slightly lower band gap, and a bulk modulus of 39.33 GPa. Configuration C_1@UiO-66 has the highest energy, the largest bulk modulus as well as the smallest void and accessible porosity of all three conformations. Given the EOS pV fits obtained from LSDA GPAW calculations, there is a transition from C_3@UiO-66 to C_2@UiO-66 at 1.14 to 1.28 GPa, corresponding to the jump around 2134 Å^3 in the energy-volume curve. The LAMMPS-INTERFACE UFF pV calculation shows a transition at 1.65 - 1.79 GPa (2038 - 2030 Å^3) and at 2.35 - 2.77 GPa (1992 - 1903 Å^3). The knowledge of the second transition helped to divide the LSDA GPAW energy-volume curve into three regions, thus EOS fits produce suitable results. With that, there is an additional transition given by the LSDA GPAW values from C_2@UiO-66 to C_1@UiO-66 at about 2.12 - 2.98 GPa (2079 - 2057 Å^3).

The symmetry for each configuration was analyzed with different symmetry tools (Spglib [235], PLATON [242], FINDSYM [243] and AFLOW-SYM [244]). Each code has different options to set up tolerances. These tolerances determine whether a symmetry is applicable or not. The main results are summarized in Tab. 16.

After a detailed benchmark of symmetry tolerances ε used in each of the tested symmetry codes, the lowest reasonable symmetry tolerance $\varepsilon_{\mathrm{min}}$ and the highest reasonable tolerance $\varepsilon_{\mathrm{max}}$ was used to analyze the three configurations of UiO-66 (see Tab. 16). All used symmetry codes predict the same space groups for $\varepsilon_{\mathrm{min}}$ and $\varepsilon_{\mathrm{max}}$. The lowest determined symmetry in any case is $P1$, while the highest determined symmetry is $F\bar{4}3m$. The tolerances to determine the higher symmetry are largest for C_1, smaller for C_2, and smallest for C_3. The space group of $Fm\bar{3}m$ found in literature can only be determined with very loose tolerances using PLATON. The standard values in PLATON typically

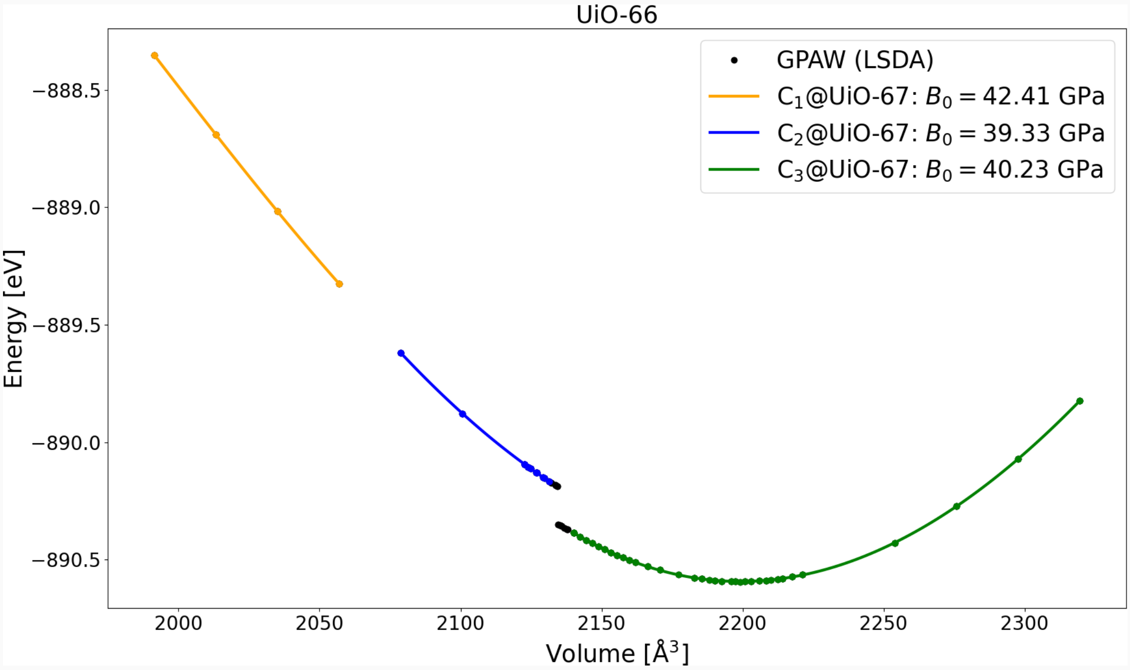

(a) GPAW

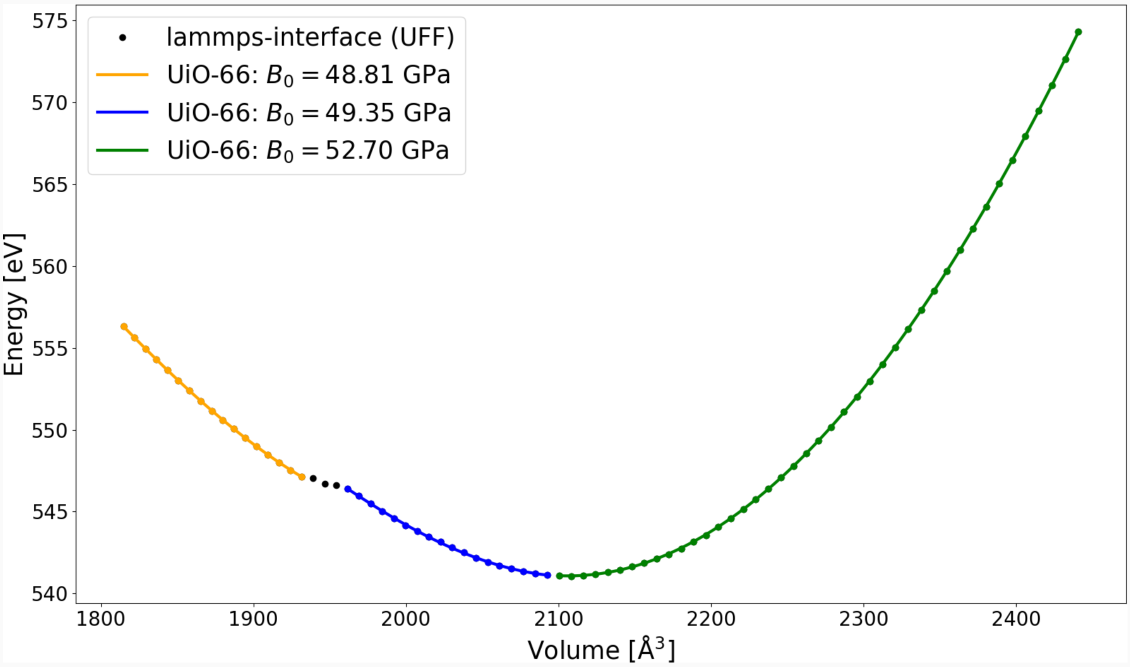

(b) LAMMPS-INTERFACE

Figure 49: UiO-66: Energy-volume curve and bulk modulus using a) LSDA DFT applying GPAW and b) UFF applying LAMMPS-INTERFACE. There are three different UiO-66 configurations, which exist in volume regimes corresponding to different volume expansions or compression states. The volume regions are marked with different colors. The picture was produced by the author using MATPLOTLIB (see Appendix A).

represent maximum values in other symmetry codes. Thus, the author would recom-

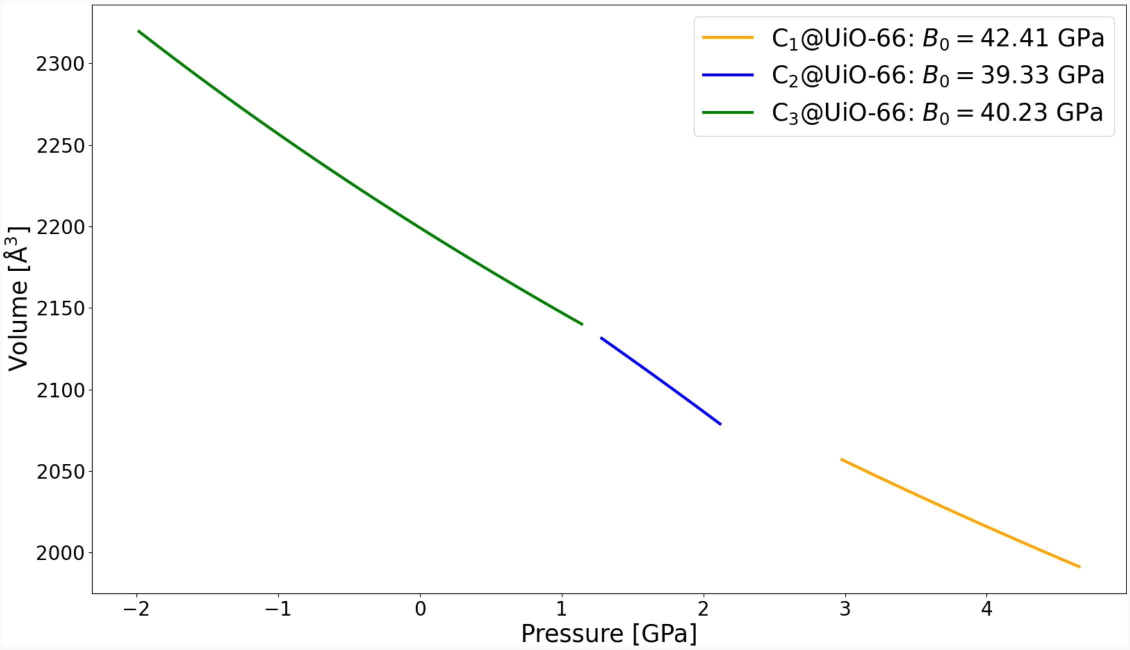

(a) GPAW

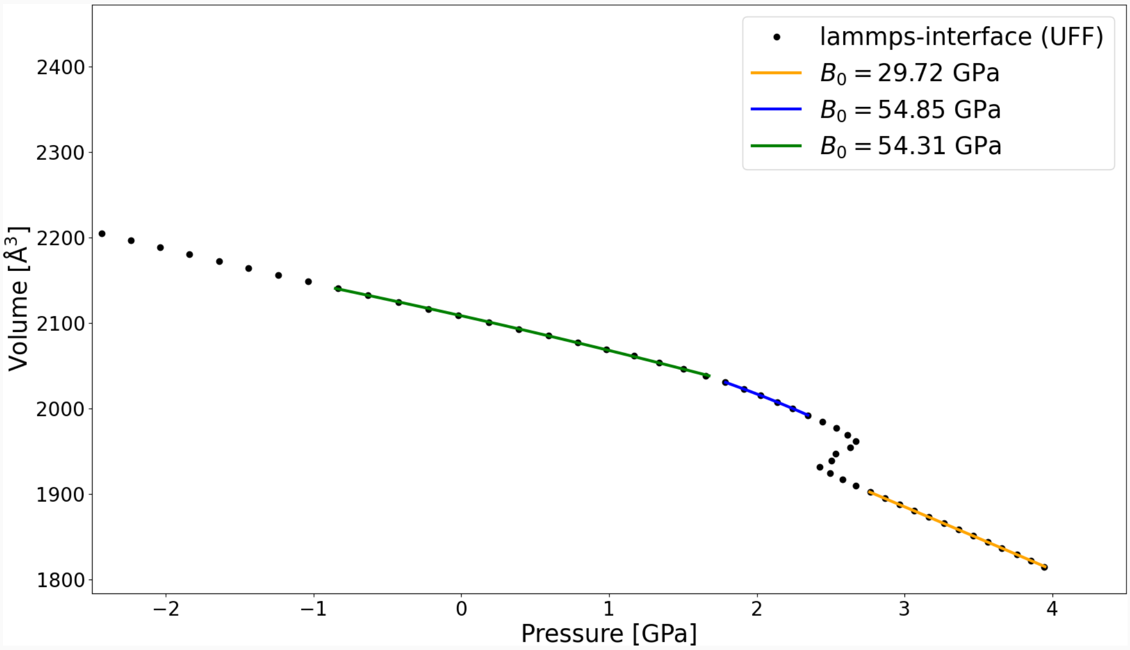

(b) LAMMPS-INTERFACE

Figure 50: UiO-66: Pressure-volume pV curve and bulk modulus using a) LSDA DFT applying GPAW and b) UFF applying LAMMPS-INTERFACE. There are three different UiO-66 configurations, which exist in volume regimes corresponding to different volume expansions or compression states. The volume regions are marked with different colors. The picture was produced by the author using MATPLOTLIB (see Appendix A).

mend to use PLATON with more strict tolerances as the standard tolerances. Further, the author would recommend in each case to use PLATON with the *exact* option.

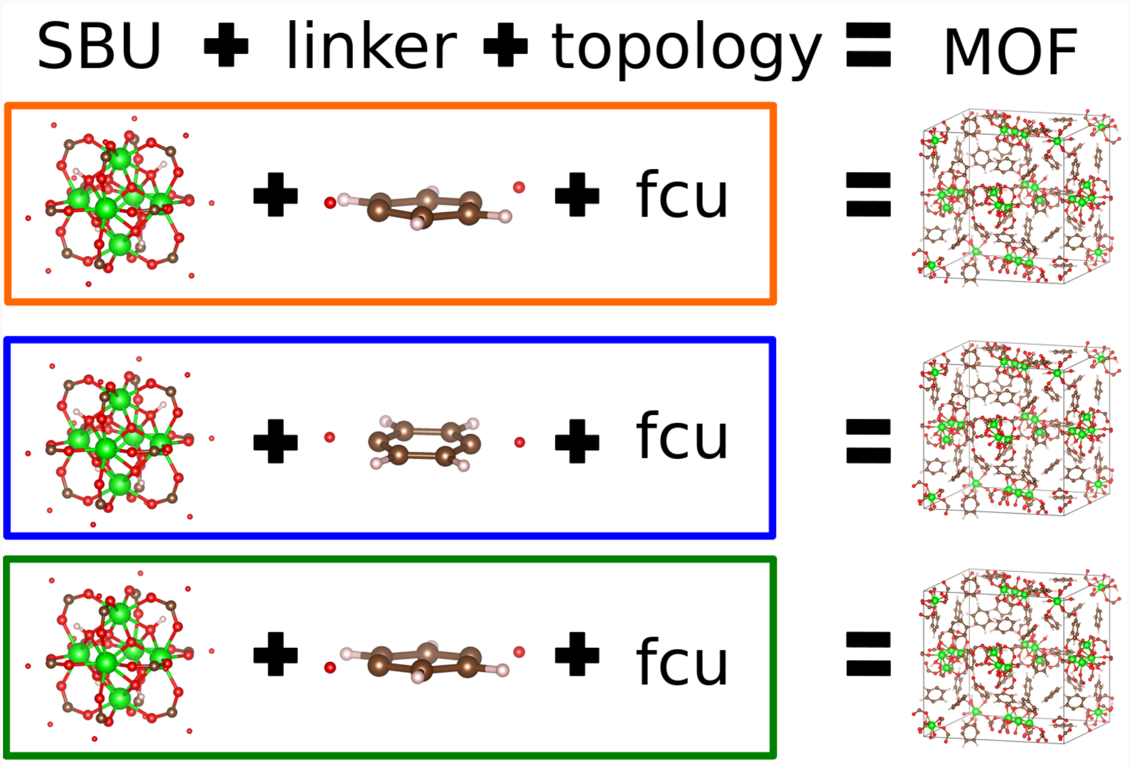

Figure 51: UiO-66: Topology analysis of the three UiO-66 configurations. Color code: C_1@UiO-66 (orange), C_2@UiO-66 (blue), C_3@UiO-66 (green). The picture was produced by the author using VESTA and INKSCAPE (see Appendix A).

In addition to the symmetry, the topology of the three determined conformations have been analyzed. For each conformer the respective SBU and the respective linker have been cut from the LSDA GPAW relaxed structures. The SBU of UiO-66 is 12 times coordinated and the next nearest atom to the coordination points are C atoms of the linkers. For the linkers the coordination points are the C atoms of the SBUs. Using the three conformer sets of SBUs and linkers given the fcu (face-centered unit) topology, AUTOGRAFS is able to produce UiO-66 structures for each conformer setting (see Fig. 51). While the coordination points for C_2@UiO-66 are within the molecular plane of the linkers, for the other two conformations the coordination points are outside the molecular plane.

The theoretical claim of an existence of different conformations of UiO-66 aims for an experimental verification. For this purpose, two experimental data sets [245, 246] for UiO-66 have been evaluated (see Fig. 52). For low pressures an experimental bulk modulus of 38.45 GPa can be determined, which is in good agreement with the calculated bulk modulus of conformation C_3@UiO-66 with a value of 40.23 GPa. In addition to that, the experimental data also show two transitions. One at approximated 0.34 GPa and the other around 4.16 GPa, which might be a first evidence of a possible existence of different UiO-66 conformations at different pressures.

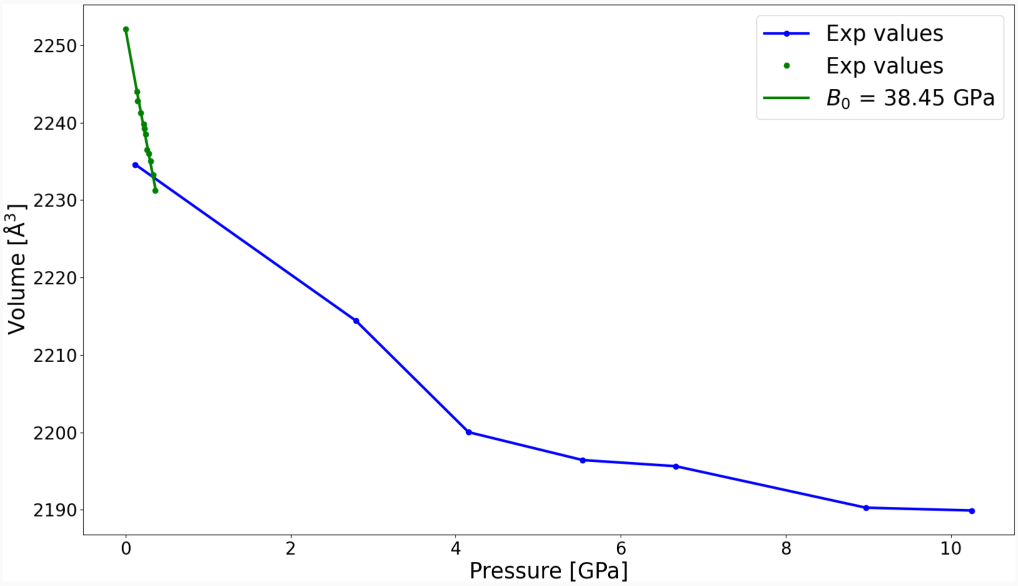

Figure 52: UiO-66: Experimental pressure-volume pV curve and bulk modulus. Two sets of experimental data have been plotted together and highlighted in blue [245] and green [246]. The volume regions are marked with different colors. The green experimental values are provided in the supplemental material of Redfern et al. [246]. The *engauge-digitizer* [247] has been used to extract the blue experimental data from a visualized picture [245]. The green experimental pressures and volumes have been fitted using the Birch-Murnaghan [132] EOS for the global data set. This fit results in a bulk modulus of 38.45 GPa. For the blue experimental data, no reasonable EOS fit was found. There is a transition between the green and the blue experimental data at approximated 0.34 GPa. In addition to that, the blue data switches its trend around 4.16 GPa. The picture was produced by the author using MATPLOTLIB (see Appendix A).

7.3.2 *UiO-67*

After studying the smallest member of the UiO family, UiO-66, the next bigger member UiO-67 is analyzed. In analogy to UiO-66, for UiO-67 the energy volume curve is calculated with LSDA GPAW and visualized in Fig. 53. Within a region around the experimental determined ground state volume, once again three distinct different configurations are observed. The conformations are called hereafter C_1@UiO-67, C_2@UiO-67 and C_3@UiO-67 (see Tab. 17). The LSDA GPAW energy volume curve can be fitted for each configuration separately leading to three different bulk moduli (see Tab. 17). The lowest energy structure is C_3@UiO-67 with a bulk modulus of 18.95 GPa. Configuration C_2@UiO-67 has a slightly higher energy and a slightly lower band gap but a larger bulk modulus of 23.92 GPa. The third configuration C_1@UiO-67 has the highest energy, a similar band gap as C_3@UiO-67 but the largest bulk modulus of 25.00 GPa. Configuration C_3@UiO-67 has the highest void and accessible porosity.

The symmetry analysis is repeated for these three UiO-67 conformations. The main results are summarized in Tab. 18.

The benchmark of symmetry tolerances again provides a lowest reasonable symmetry tolerance ε_{min} and a highest reasonable tolerance ε_{max} for each code and each of the three determined configurations of UiO-67 (see Tab. 18). The symmetry codes SPGLIB,

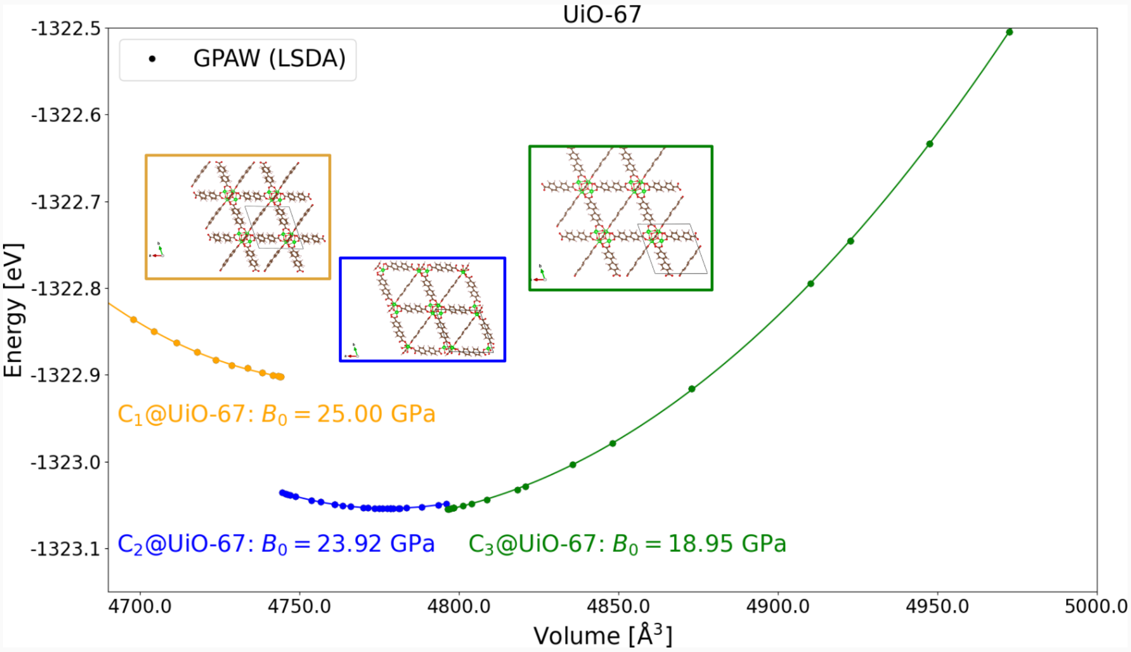

Figure 53: UiO-67: Energy-volume curve and bulk modulus using LSDA DFT. There are three different UiO-67 configurations, which exist in volume regimes corresponding to different volume expansions or compression states. The volume regions are marked with different colors. The insets show the respective unit cells. The picture was produced by the author using VESTA (see Appendix A).

PLATON and FINDSYM predict the same symmetries for all configurations. Only AFLOW-SYM does not allow to use the needed loose tolerances, thus the predicted space groups for C_2 and C_3 are different from the other codes. The lowest symmetry in any case is $R3$, while the highest determined symmetry differs between the different configurations. For configuration C_1 all codes predict $F23$, for C_2 and C_3 SPGLIB, PLATON and FINDSYM predict $F\bar{4}3$ while AFLOW-SYM still predicts $F23$.

A detailed inspection of the linkers of the three configurations shows that they are twisted in C_1, whereas they are aligned in C_2 and C_3 (see insets of Fig. 54). Twisted linkers might reduce the symmetry of the system, thus $F23$ seems like a reasonable space group for configuration C_1, while a higher symmetry as $F\bar{4}3$ seems reasonable for configurations C_2 and C_3. Accordingly, there is a clear distinction between configuration C_1

Table 17: UiO-67 configurations: Electronic and mechanical properties. The calculation were performed with LSDA using GPAW. The bulk modulus was calculated for Murnaghan equation of state for C_1,C_2 and C_3 in the volume ranges of (V_{min}= 4680 Å^3,V_{max}= 4744.5 Å^3), (V_{min}= 4744.6 Å^3,V_{max}= 4796 Å^3), (V_{min}= 4796 Å^3,V_{max}= 5000 Å^3). The porosities Φ were evaluated with the grid approach with poreE [241] using a 100 x 100 x 100 grid.

Configuration	V [Å^3]	E_{tot} [eV]	E_g [eV]	B [GPa]	Φ void [%]	Φ accessible [%]
C_1@UiO-67	4686.51	-1322.80793	2.597	25.00	71.14	66.41
C_2@UiO-67	4777.51	-1323.05404	2.583	23.92	71.60	67.14
C_3@UiO-67	4796.41	-1323.05503	2.605	18.95	71.66	67.29

Table 18: UiO-67 configurations: Symmetry analysis. The tag min represents the symmetry detected at the chosen minimal tolerance setup for the respective code, whereas max indicates the symmetry for the maximal tolerance value. The detailed tolerance benchmarks of each code can be found in the Appendix (see Section A.3).

Configuration	Spglib		PLATON		FINDSYM		AFLOW-SYM	
	ε_{min}	ε_{max}	ε_{min}	ε_{max}	ε_{min}	ε_{max}	ε_{min}	ε_{max}
C_1@UiO-67	$R3$	$F23$	$R3$	$F23$	$R3$	$F23$	$R3$	$F23$
C_2@UiO-67	$R3$	$F\bar{4}3m$	$R3$	$F\bar{4}3m$	$R3$	$F\bar{4}3m$	$R3$	$F23$
C_3@UiO-67	$R3$	$F\bar{4}3m$	$R3$	$F\bar{4}3m$	$R3$	$F\bar{4}3m$	$R3$	$F23$

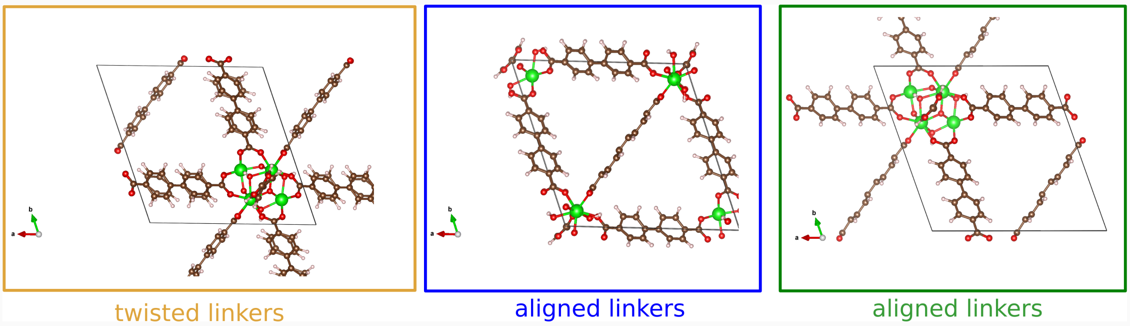

twisted linkers

aligned linkers

aligned linkers

Figure 54: UiO-67: Linkers of the three determined UiO-67 configurations. Color code: C_1@UiO-67 (orange), C_2@UiO-67 (blue), C_3@UiO-67 (green). The picture was produced by the author using VESTA (see Appendix A).

and configurations C_2 and C_3. The configurations C_2 and C_3 cannot be distinguished by means of symmetry. One can conclude that at this level of theory, UiO-67 can form a low symmetry configuration C_1 at a compressed volume state and a higher symmetry configuration at the ground state is represented by both configurations C_2 as well as C_3.

In the work of Rogge et al. [237] the authors used PLATON as symmetry analyzing tool considering standard values for the tolerances and determined the space group of $Fm\bar{3}m$ for UiO-67. As shown in the Appendix (see Section A.3) one can reproduce this result only for the calculation mode *CALC ADDSYM* while the mode within PLATON itself recommends the usage of *CALC ADDSYM EXACT*. The *exact* option delivers results of lower space groups, which is in agreement with our results (see Tab. 18). The same conclusion as for UiO-66 can be drawn, i.e., in comparison to the other used symmetry tools (Spglib, FINDSYM and AFLOW-SYM) the standard tolerances within PLATON appear very high. For instance similar tolerance values cannot be set up within AFLOW-SYM, as AFLOW-SYM determines this value as too large (improper).

The topology analysis is repeated for the three UiO-67 conformations.

As the SBUs are the same for UiO-66 and UiO-67, also the SBU of UiO-67 is 12 times coordinated and the next nearest atom to the coordination points are C atoms of the linkers. Also in the case of UiO-67, for the linkers the coordination points are identified as the C atoms connecting to the SBUs. Using the three conformer sets of SBUs and linkers given a fcu (face-centered cubic lattice) topology, AuToGraFS is able to produce UiO-67 structures for each conformer setting (see Fig. 55). For configuration C_3@UiO-67 the resulting MOF is distorted, while the other structures are not distorted within the given numerical accuracy.

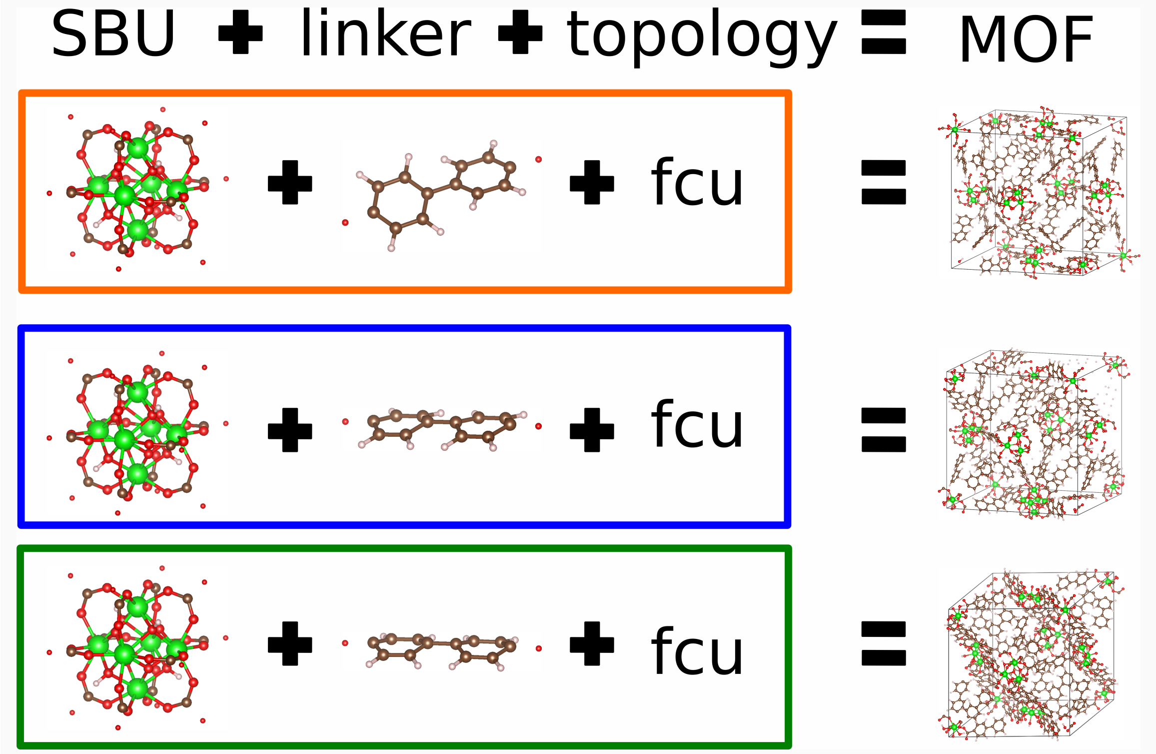

Figure 55: UiO-67: Topology analysis of the three UiO-67 configurations. Color code: C_1@UiO-67 (orange), C_2@UiO-67 (blue), C_3@UiO-67 (green). The picture was produced by the author using VESTA and Inkscape (see Appendix A).

Having all these theoretical predictions aims from some kind of experimental verification. For widely studied MOFs there exist various studies discussing mechanical properties using DFT or FF, but actual experimental values are rarely available. For UiO-67 one can find the following experimental references [246, 248]. The main discussions of the second reference are concerned with actual experimental results, while the main discussions in the first reference are DFT results. The results of Redfern et al. [246] are provided as supplemental material, thus one can easily use the same fitting procedure of the Birch-Murnaghan [132] EOS as used for the GPAW results to evaluate the bulk modulus. For the global set of experimental data, a bulk modulus of 22.05 GPa is evaluated, which is in good agreement with the value of 21.26 GPa evaluated by the authors themselves. For the experimental data it is obvious that there exist not a single linear trend, but instead there are several nearly linear regions (see Fig. 56). The bulk modulus has been evaluated for these nearly linear regions as well. It turns out that these nearly linear regions coincide with the regions spanned by the determined UiO-67 conformers. Clearly, the transition of conformation C_1@UiO-67 (highlighted in orange) and C_2@UiO-67 (highlighted in blue) occurs in a pressure range of 0.075 GPa to 0.1 GPa (see Fig. 56). One can determine a similar transition within the experimental data highlighted with the same colors at about 0.13 GPa between (see Fig. 56). This might be interpreted as evidence that different UiO-67 conformers exist experimentally. In addition, using the LAMMPS-INTERFACE with UFF allows to calculate a broader range of volumes (see Fig. 57) for a more detailed analysis. A small distinct change around 0 - 0.09 GPa appears in the LAMMPS calculations, while a more global change between

0 - 0.5 GPa appears. Such a global transition appears also in the experimental pV data of Hobday et al. [248] from 0.33 - 1.15 GPa. In the work of Redfern et al. [246] also the possibility of a pressure-dependent change of linker coordination within Zr-MOFs is discussed, which is in agreement with the observations of this part of this thesis.

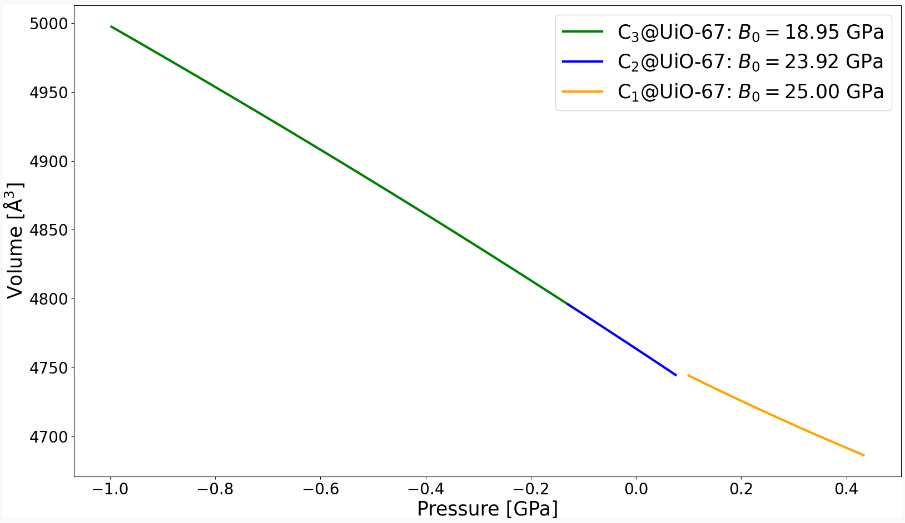

(a) pV-curve GPAW

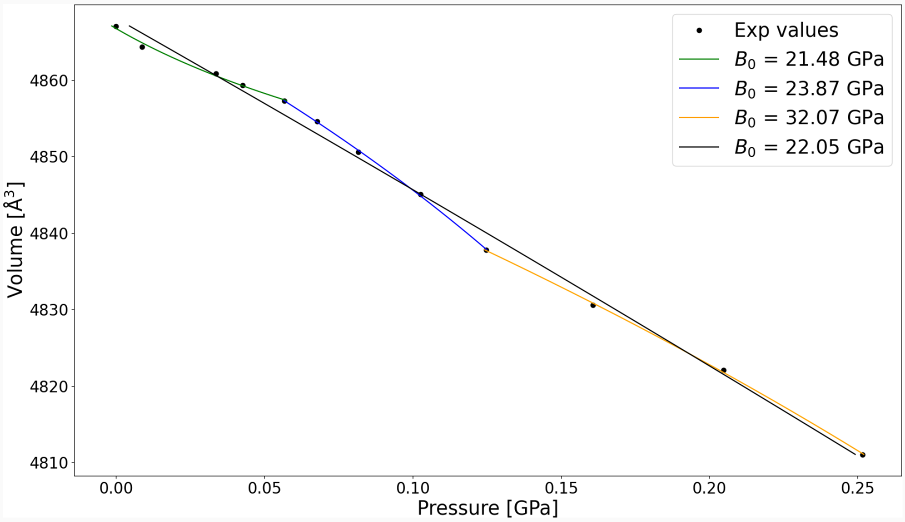

(b) pV-curve experiment

Figure 56: UiO-67: Pressure-volume pV curve and bulk modulus using LSDA DFT. There are three different UiO-67 configurations, which exist in volume regimes corresponding to different volume expansions or compression states. The volume regions are marked with different colors. The experimental values are provided in the supplemental material of Redfern et al. [246]. Experimental pressures and volumes have been fitted using the Birch-Murnaghan [132] EOS for the global data set as well as linear parts. The transition between conformation C$_1$@UiO-67 (orange) and C$_2$@UiO-67 (blue) occurs in a pressure range of 0.075 GPa to 0.1 GPa. In the experiment data one can determine a similar transition at about 0.13 GPa between. Further, the experimental bulk moduli for the linear parts (orange, blue, green) in (b) exhibit a similar change from highest to lowest bulk moduli as given by the three conformation using the same colors in (a). The picture was produced by the author using MATPLOTLIB (see Appendix A).

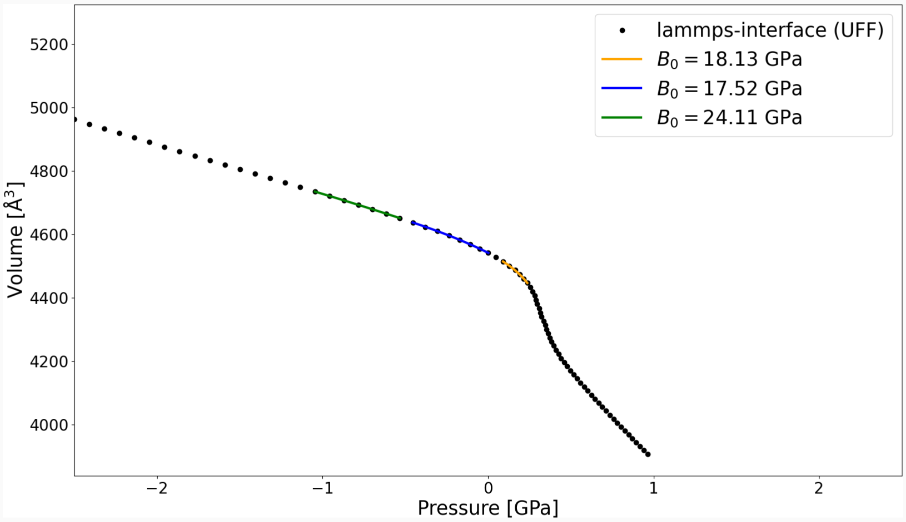

(a) pV-curve LAMMPS-INTERFACE

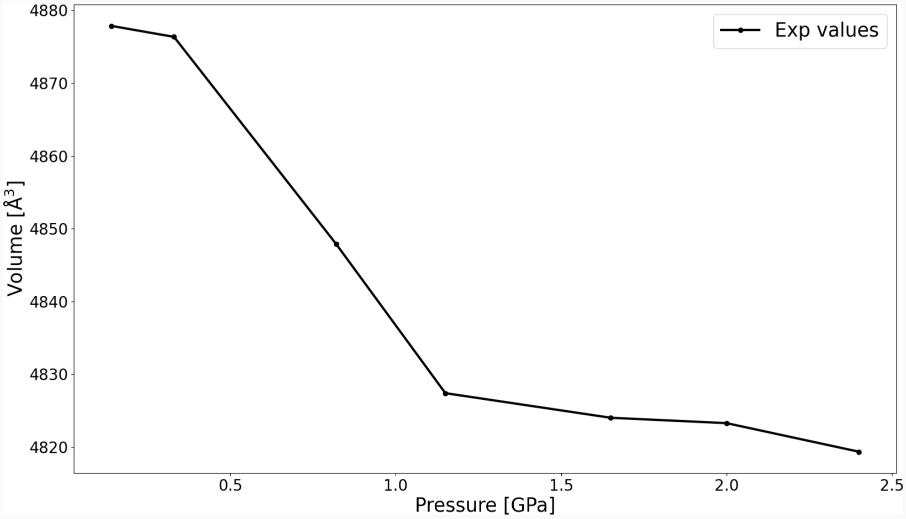

(b) pV-curve experiment

Figure 57: UiO-67: Extended pressure-volume pV curve and bulk modulus using LAMMPS-INTERFACE with UFF. There are three different UiO-67 configurations, which exist in volume regimes corresponding to different volume expansions or compression states. The volume regions are marked with different colors. The experimental values are provided in the supplemental material of Hobday et al. [248]. The calculated pressures and volumes have been fitted using the Birch-Murnaghan [132] EOS for linear parts. No reasonable EOS fit for the experimental values were found. The picture was produced by the author using MATPLOTLIB (see Appendix A).

Table 19: Bulk moduli for MOFs calculated with LAMMPS-INTERFACE using UFF and UFF4MOF force fields within the elastic workflow. All values are given in GPa.

MOF	UFF		UFF4MOF	
	B_{EOS}	B_{Voigt}	B_{EOS}	B_{Voigt}
HKUST-1	23.41	24.16	27.02	27.32
IRMOF-10	4.59	8.92	4.69	3.50
UiO-66	43.94	48.53	24.12	27.75
UiO-67	15.51	27.97	9.72	8.67
UiO-68	4.01	18.22	3.53	4.10
exp@open@DUT-8(Ni)	17.45	22.48	17.10	12.19
dft@open@DUT-8(Ni)	29.31	31.60	30.58	29.62

Screening of bulk moduli for MOFs As shown in the previous section, force field calculations can help to understand properties in a computationally efficient way. For this purpose the bulk modulus is calculated for a test set consisting of the MOFs HKUST-1, IRMOF-10, UiO-66, UiO-67, UiO-68 and open@DUT-8(Ni). The LAMMPS-INTERFACE is used with the UFF and the universal force field for MOFs (UFF4MOF) [157] to calculate bulk moduli using the elastic workflow (see Section 4.2). To calculate the bulk modulus using the Voigt definition, the elastic module provided by LAMMPS has been implemented in a PYTHON module to enable the usage with the force fields provided by the LAMMPS-INTERFACE. The elastic procedure has a parameter describing the finite deformation size used for the calculations. Until now there is no automatic procedure to determine the best value of this parameter. For the values presented this value was chosen such that small changes do not change the results significantly. The error associated with this procedure is in the same magnitude as using a different volume region for the EOS fit.

Experimental values for the bulk modulus of HKUST-1 are available in literature (e.g., B_0 = 30.7 GPa [249]). For HKUST-1 one finds literature values calculated with BTW-FF (B_0 = 25.05 GPa [9]), and even DFT values calculated with QUANTUM ESPRESSO using PBE (B_0 = 24.53 GPa [250]). Another widely known MOF is IRMOF-10. For this MOF one finds BTW-FF data (B_0 = 8.25 GPa [9]), VMOF data (B_0 = 5.1 GPa [11]) as well as DFT data using PBEsol with D3 dispersion correction (B_0 = 8.6 GPa [11]).

For the UiO family there exist QuickFF [237] force field values for the bulk moduli (UiO-66: B_0 = 22.2 GPa, UiO-67: B_0 = 13.3 GPa, UiO-68: B_0 = 8.1 GPa). Additional literature values for the BTW-FF [9] (UiO-66: B_0 = 27.15 GPa, UiO-67: B_0 = 19.15 GPa) and the more advanced VMOF [11] (UiO-66: B_0 = 19.0 GPa, UiO-67: B_0 = 11.7 GPa) force fields are available. There are also DFT values calculated with the VASP code using the PBE functional [251] (UiO-66: B_0 = 36.6 GPa, UiO-67: B_0 = 22.1 GPa, UiO-68: B_0 = 14.8 GPa), and the PBEsol functional using D3 dispersion correction [11] (UiO-66 B_0 = 40.4 GPa, UiO-67 B_0 = 21.9 GPa)

To the best of the authors knowledge, no reference values for the bulk modulus of DUT-8(Ni) are available. With that, one can use the other MOFs as a benchmark for the accuracy of the proposed workflow. Then, the bulk modulus of an unknown MOF can be studied.

The calculated bulk moduli of HKUST-1 (see Tab. 19) are in good agreement with reference values. While UFF resembles DFT and FF results, the UFF4MOF results agree slightly better with the experimental values. The calculated IRMOF-10 values are in good agreement with reference VMOF calculations. For the UiO family the presented force field calculations reproduce the same trend found in literature (see Tab. 19). One finds that UiO-66 has the largest, UiO-67 the second largest and UiO-68 the smallest bulk modulus. For this investigation the experimental DUT-8(Ni) structure exp@open@DUT-8(Ni) appears to have a lower bulk modulus than the DFT optimized DUT-8(Ni) structure dft@open@DUT-8(Ni).

Conclusion In summary, the author has shown the possible existence of conformers for UiO-66 and UiO-67, using both DFT and FF. These conformers might exist in small pressure regions and can be classified by small changes in the organic linkers as well as a decrease or an increase in symmetry. The changes in the small pressure regimes might cause problems for calculating elastic and thermodynamic properties (e.g., using QHA) as such calculations critically depend on the fact that the structure is not changing. The fact that small changes in the linkers can lead to significant changes in the observables like the bulk modulus motivated the author to study local properties of linkers (see Chapter 8), SBUs (see Section 7.6), and pores of MOFs (see Section 7.5) in more detail.

7.4 THERMODYNAMIC PROPERTIES

7.4.1 *HKUST-1*

As the previous investigations have shown, the bulk modulus of HKUST-1 can be predicted with reasonable accuracy using the UFF force field applying the LAMMPS-INTERFACE. This indicates that this force field can be used also for thermodynamical calculations using the FF-QHA workflow (see Section 5.2). The LAMMPS@FF-QHA workflow using the UFF and UFF4MOF force field is applied to calculate thermodynamical properties of HKUST-1. For slightly expanded volumes around the equilibrium volume the calculated phonon density of states (PDOS) do not show significant imaginary contributions (see Fig. 58).

Having non-imaginary contributions in the PDOS for volumes around the equilibrium volume verifies the usage of QHA for UFF (see Fig. 58 (a)) and for UFF4MOF (see Fig. 58 (b)). Based on this, the thermal expansion coefficient α, the Grüneisen parameter, the temperature-dependent bulk modulus B_0 as well as the isobaric heat capacity C_p have been calculated using both UFF and UFF4MOF force field with the LAMMPS@FF-QHA workflow (see Fig. 59). The $T = 0$ K value of the temperature-dependent bulk modulus is in the correct magnitude of the previously calculated values. This is a first evidence that the proposed workflow works as expected. As mentioned in the previous sections, HKUST-1 is a well studied MOF. Thus, one can find some experimental isobaric heat capacity values in literature [252, 253]. The primitive cell of HKUST-1 has the chemical formula of $C_{72}H_{24}Cu_{12}O_{60}$ with a molar mass of $M_{\text{HKUST-1}} = 2611.48$ g/mol. Having this, one can convert the calculated isobaric heat capacity at $T = 320$ K from $C_{p,\text{UFF}}(T = 320\text{ K}) = 2023$ J/(molK) to $C_{p,\text{UFF}}(T = 320\text{ K}) = 0.775$ J/(gK). The calculated isobaric heat capacity value is in good agreement with the experimental one of $C_{p,\text{exp}}(T = 323\text{ K}) = 0.780$ J/(gK) [253]. The respective value for UFF4MOF calculations $C_{p,\text{UFF4MOF}}(T = 320\text{ K}) = 1945$ J/(molK) $= 0.745$ J/(gK) has the same magnitude as the UFF value, but differs slightly more from the experimental value. Both force fields give similar trends for the investigated thermodynamical properties (see Fig. 59). Having verified the FF-QHA workflow allows to study other systems, like the thermodynamical properties of the UiO family.

7.4.2 *UiO-66*

With the knowledge of the previous investigations, the volume range around the approximated ground state structure of UiO-66 is known, using the LAMMPS-INTERFACE with UFF. Thus, QHA can be applied to UiO-66. For these calculations the LAMMPS-@FF-QHA workflow is applied. In addition, the GULP@FF-QHA workflow using the VMOF force field is used for reference calculations.

Given UFF results, within the volume range 2132 - 2544 Å^3 no significant imaginary modes are found in the PDOS (see Fig. 60 (a)). Compression of UiO-66 leads to significant imaginary contributions in the PDOS. The general features of the PDOS agree with literature values produced using the VMOF force field in GULP [11].

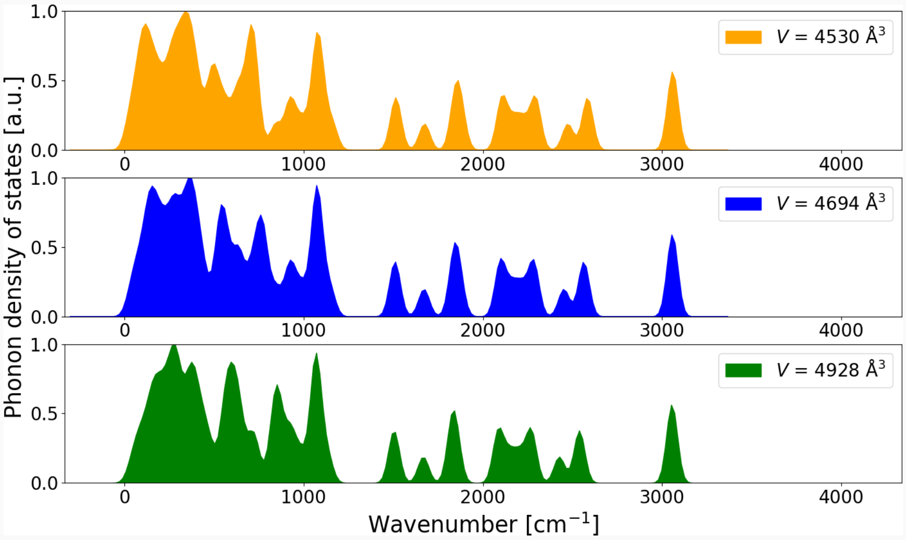

(a) UFF

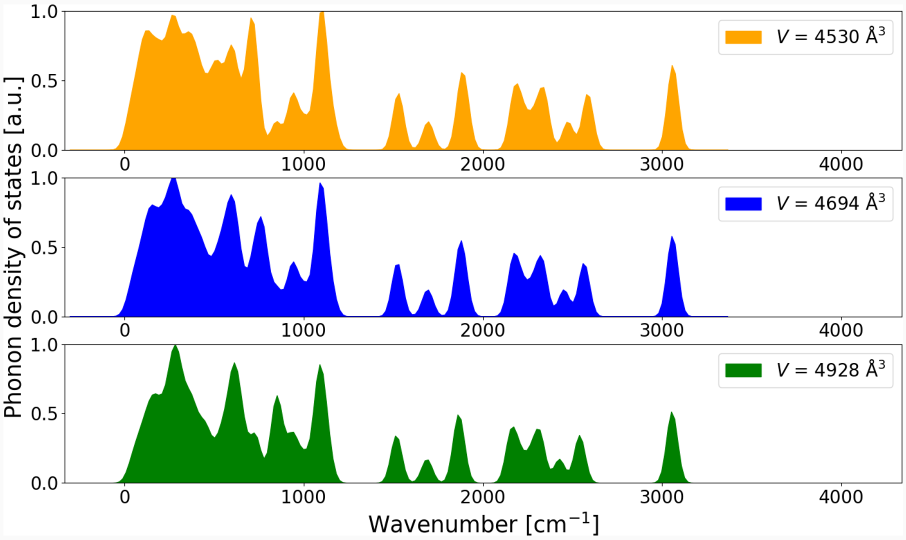

(b) UFF4MOF

Figure 58: HKUST-1: PDOS calculated using the LAMMPS@FF-QHA workflow with (a) UFF and (b) UFF4MOF for selected volumes of HKUST-1. For PHONOPY a 32x32x32 grid was used. The picture was produced by the author using MATPLOTLIB (see Appendix A).

The set of volumes having non-imaginary contributions in the PDOS have been used to calculate thermodynamical properties using QHA (see Fig. 62). The value of the bulk modulus at $T = 0$ K has a similar magnitude as calculated within the previous section.

All calculations have been repeated using the UFF4MOF force field for a volume range of 2302 - 2537 Å^3. Note that different force fields may not predict identical ground state volumes, thus the investigated volumes ranges change accordingly. In contrast to UFF, UFF4MOF results show significant imaginary contribution (see Fig. 60 (b)). Besides this the overall features in the UFF4MOF PDOS are very similar to ones which can be found in the UFF PDOS. Nevertheless, applying PHONOPY using QHA produces stable fits for these volumes (see Fig. 62). The trends for the thermal expansion coeffi-

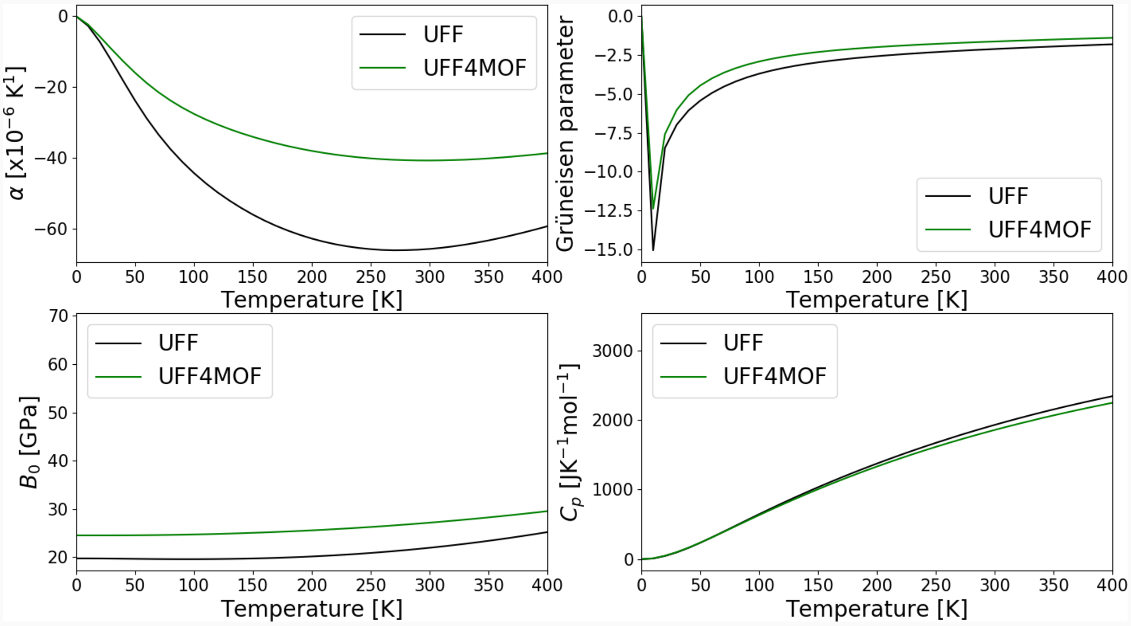

Figure 59: HKUST-1: QHA for HKUST-1 using UFF and UFF4MOF applying the LAMMPS@FF-QHA workflow. A variation of the maximum value for the temperature T_{max} used for the QHA does not change the results significant. The picture was produced by the author using Matplotlib (see Appendix A).

cient, the Grüneisen Parameter (see Section 4.4) as well as the temperature dependence of the bulk modulus are in better agreement with reference calculations done with the VMOF force field in GULP [11]. However, comparing UFF with UFF4MOF results, the resulting isobaric heat capacities within a temperature range of 0 - 400 K are nearly identical for UiO-66.

Using input files provided within the supplemental material of Bristow et al. [11], VMOF calculations have been done using the provided GULP input files for the given volumes of Bristow et al. [11]. An automatic assignment of the MMtypes for the VMOF force field was not available. Further, the VMOF potential include charge corrections, thus the results are different from the ones of UFF and UFF4MOF where no charge corrections were applied. The reason for not including charges corrections [8] (e.g., charge equilibration (QEq) method, Repeating Electrostatic Potential Extracted ATomic (REPEAT) charge method or Density Derived Electrostatic and Chemical (DDEC) method) for these investigations was to keep the calculations as simple as possible with the highest degree of automation. In general, the LAMMPS-INTERFACE [8] allows to include such charge corrections. Thus, the effect of charge treatment can be studied in future investigations. Like UFF, the VMOF force field result shows no significant imaginary contributions within the PDOS (see Fig. 61). Thus, the GULP@FF-QHA workflow (see Section 5.2) was applied to calculate thermodynamical properties (see Fig. 62).

The calculated VMOF PDOS values are different from the UFF and UFF4MOF PDOS values between 1000 - 2500 cm^{-1}. The features found in the UFF and UFF4MOF calculations are spread over these wavenumbers whereas they are shifted to lower wavenumbers in the VMOF calculations. The general features of the calculated VMOF PDOS are in agreement with literature values for this force field [11]. The two features found at wavenumbers above 2500 cm^{-1} are consistent within all three force fields. In addition to

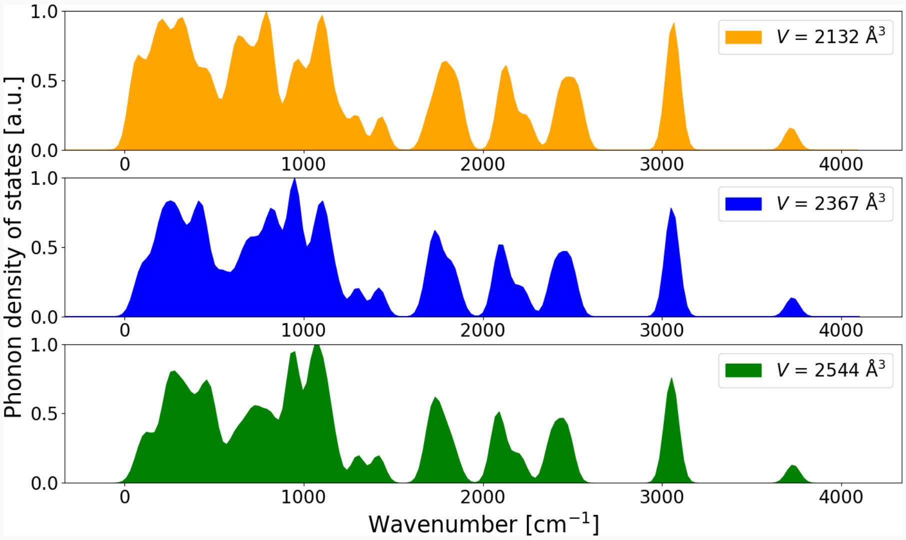

(a) UFF

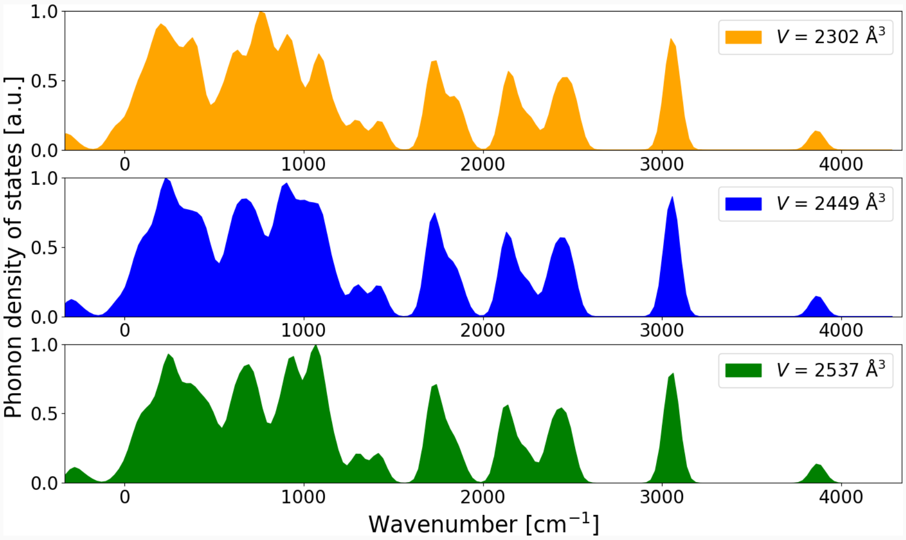

(b) UFF4MOF

Figure 60: UiO-66: PDOS calculated using the LAMMPS@FF-QHA workflow with (a) UFF and (b) UFF4MOF for selected volumes of UiO-66. For PHONOPY a 32x32x32 grid was used. The picture was produced by the author using MATPLOTLIB (see Appendix A).

that, all three force fields indicate a similar negative feature in the Grüneisen parameter at low temperatures. VMOF calculations predict overall higher values for the isobaric heat capacity for the investigated temperature range 0 - 400 K. In general for UiO-66, the calculated thermodynamical properties using the VMOF force field are consistent with the values published in literature [11]. This indicates that the GULP@FF-QHA workflow works as expected.

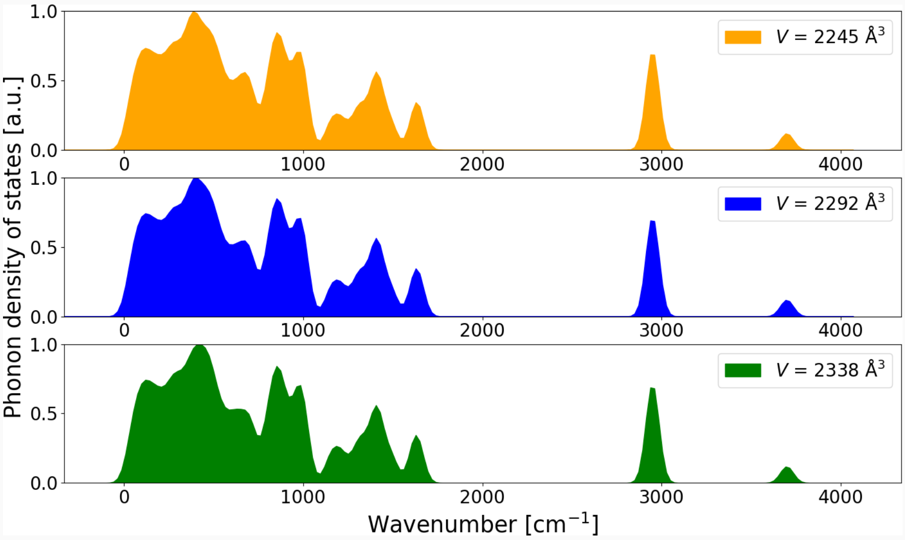

Figure 61: UiO-66: PDOS of UiO-66 calculated using the GULP@FF-QHA framework selected volumes of UiO-66. For Phonopy a 33x32x32 grid was used. The picture was produced by the author using Matplotlib (see Appendix A).

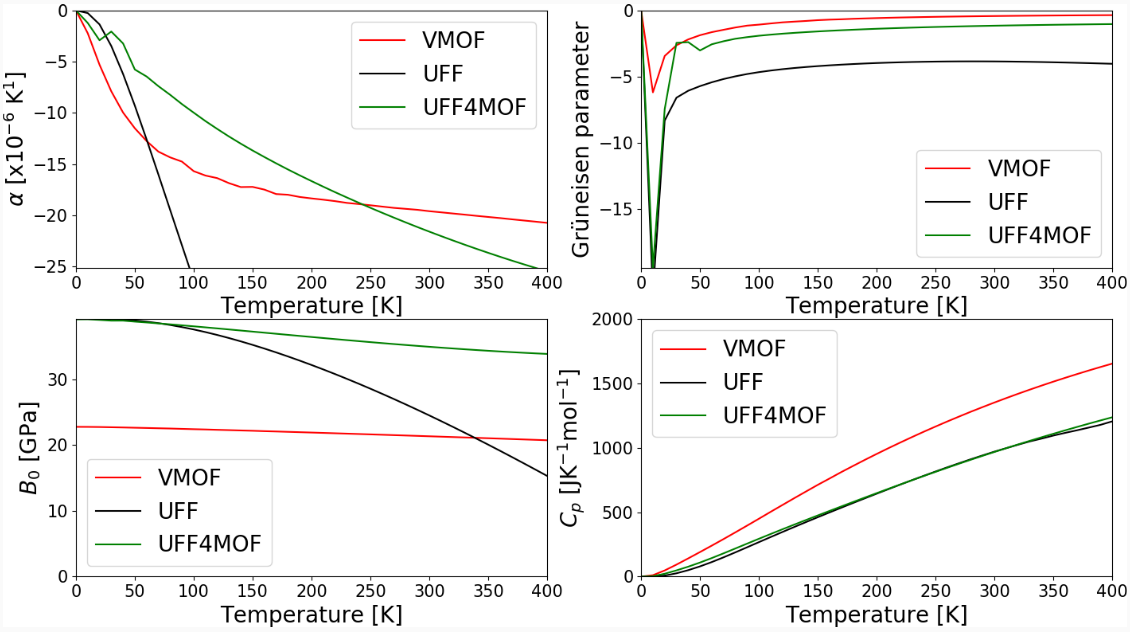

Figure 62: UiO-66: QHA for UiO-66 applying UFF and UFF4MOF using the LAMMPS@FF-QHA workflow and VMOF using the GULP@FF-QHA workflow. For the Phonopy QHA a maximum value for the temperature $T_{\max}$ = 400 K was used. Increasing the temperature deliver non-stable fits for the isobaric heat capacity C_p. The picture was produced by the author using Matplotlib (see Appendix A).

7.4.3 *UiO-67*

UFF and UFF4MOF calculations performed with the lammps-interface using phonoLAMMPS show that for compressed volumes of UiO-67 there is a significant imaginary mode, which gets smaller for more expanded volumes and disappears for even more expanded volumes (see Fig. 63). These imaginary modes are more dominant in the UFF4MOF calculations than in the UFF calculations. These imaginary modes are also present in the PDOS calculated with the VMOF force field using the GULP@FF-QHA workflow (see Fig. 64).

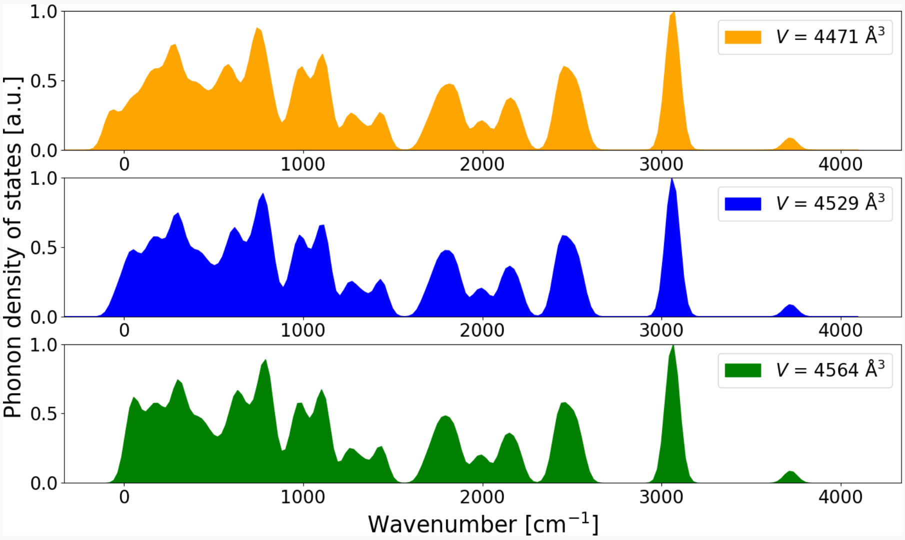

(a) UFF

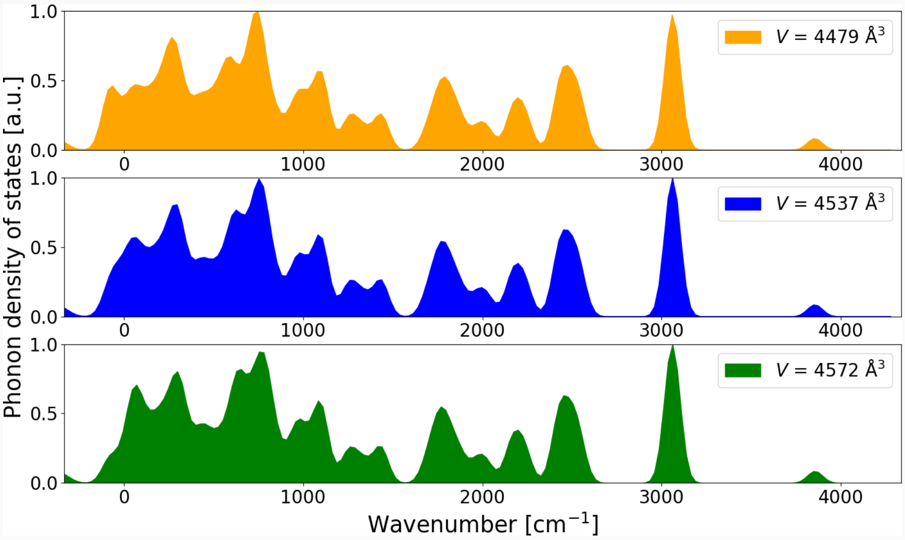

(b) UFF4MOF

Figure 63: UiO-67: PDOS calculated using the LAMMPS@FF-QHA workflow with (a) UFF and (b) UFF4MOF for selected volumes of UiO-67. For Phonopy a 32x32x32 grid was used. The picture was produced by the author using Matplotlib (see Appendix A).

The QHA approximation still produces only stable fits including some compressed volumes showing up small imaginary parts in the respective PDOS (see Fig. 65 (a)).

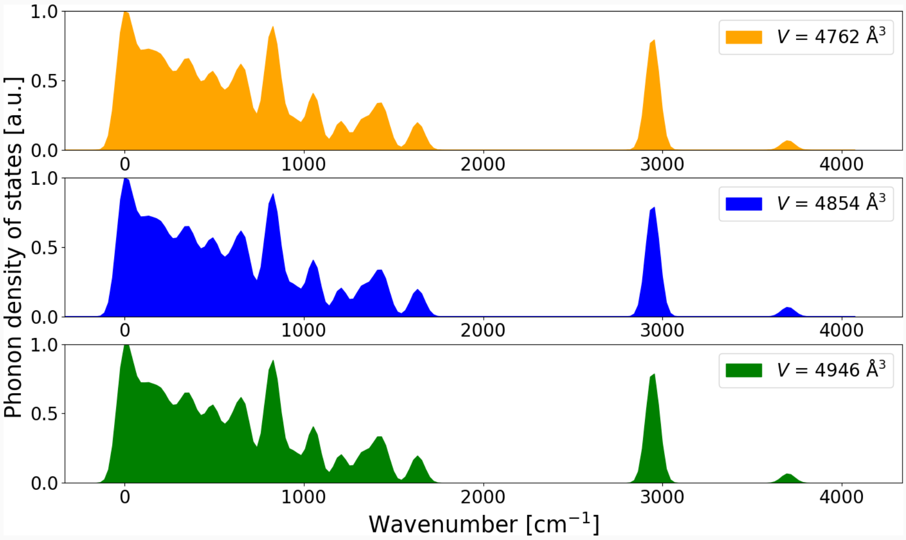

Figure 64: UiO-67: PDOS of UiO-67 calculated using the GULP@FF-QHA framework selected volumes of UiO-67. For PHONOPY a 33x32x32 grid was used. The picture was produced by the author using MATPLOTLIB (see Appendix A).

The presented results are stable with respect to changing the maximal temperature T_{max} as well as changing the EOS fits used for the QHA. A value of $T_{\mathrm{max}} = 400$ K and the Vinet [133, 134] EOS was used for the visualization. There is a distinct change in the temperature-volume curve around 20 K, which is also present in thermal expansion coefficient, the Grüneisen parameter as well as the isobaric heat capacity. The respective volume for UFF of approximate 4510 Å^3 coincides with the global change within the respective pressure-volume curve (see Fig. 57) within the same volume range and a pressure range of 0 - 0.5 GPa. For the VMOF calculations the pressure was varied within the QHA (see Fig. 65 (b)) and the feature around 20 K is sensitive to this pressure change. While the overall isobaric heat capacity from 0 to 400 K is not distinguishable, the calculated thermal expansion and Grüneisen parameter change significantly for different pressures. Thus, the thermodynamical calculations in the framework of the QHA for UiO-67 show a thermodynamical instability around 20 K, which is consistent with the jump at low pressures (0 - 0.5 GPa) within the previously calculated pV curves. This might be an additional hint for the existence of different UiO-67 conformers.

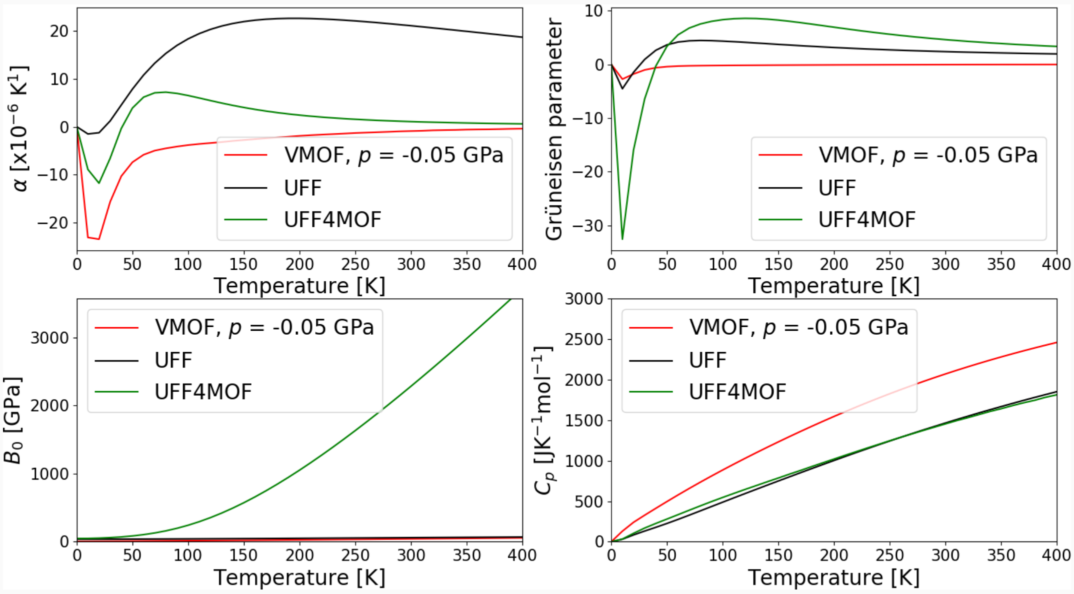

(a) QHA

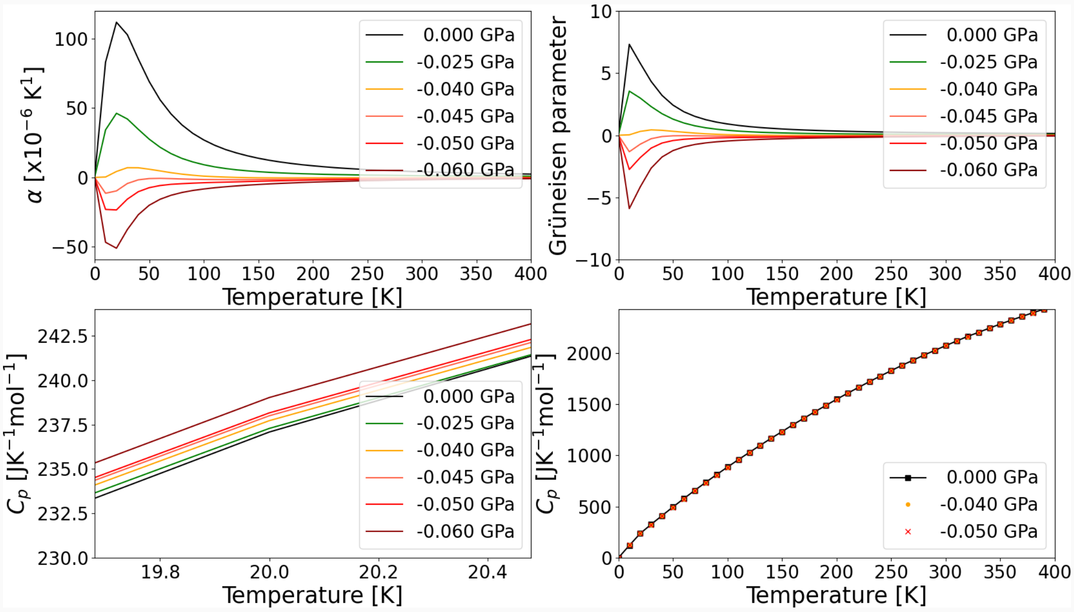

(b) Instability

Figure 65: UiO-67: QHA of UiO-67 using lammps-interface with UFF and UFF4MOF coupled with phonoLAMMPS as well as the VMOF force field using the GULP@FF-QHA workflow. For the given set the fits are stable with respect to $T_{\max}$. For the VMOF calculations in (a) a pressure $p =$ -0.05 GPa was applied within the QHA procedure. For the GULP@FF-QHA workflow, in (b) p has varied for the QHA calculations. While the isobaric heat capacity from 0 to 400 K is nearly identical, an inset in the temperature range from 19.7 to 20.4 K shows a feature around 20 K. This feature changes drastically for different pressures as can be seen in the behaviour of the thermal expansion coefficient as well as the Grüneisen parameter. For C_p the pure values instead of the fit are plotted. The picture was produced by the author using Matplotlib (see Appendix A).

7.4.4 *UiO-68*

Having found the instability for UiO-67 opens the question whether this is an intrinsic feature of UiO-67 or something which can also found in other MOFs. Thus, UiO-68 has been studied as the next bigger member of the UiO family. The LAMMPS@FF-QHA workflow has been applied using the UFF and UFF4MOF force field to calculate thermodynamical properties of UiO-68.

Similar to UiO-66 and UiO-67, the UFF calculations (see Fig. 66 (a)) show non-significant imaginary modes which can be found to be dominant for UFF4MOF calculations (see Fig. 66 (b)).

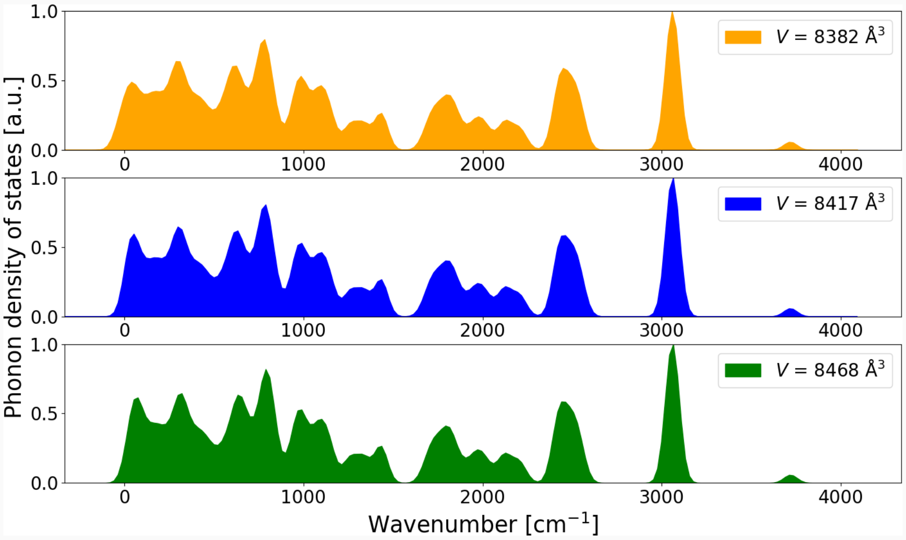

(a) UFF

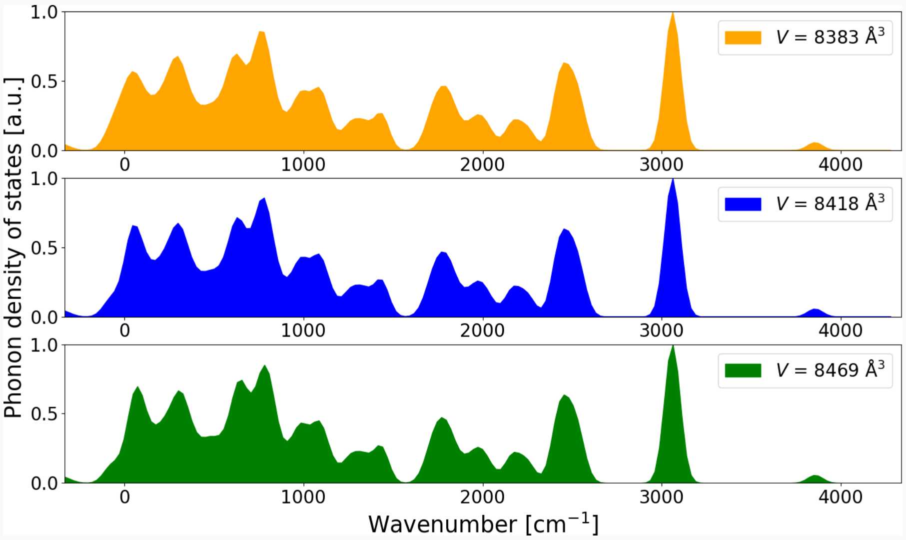

(b) UFF4MOF

Figure 66: UiO-68: PDOS calculated using the LAMMPS@FF-QHA workflow with (a) UFF and (b) UFF4MOF for selected volumes of UiO-68. For PHONOPY a 32x32x32 grid was used. The picture was produced by the author using MATPLOTLIB (see Appendix A).

Applying a pressure of -0.5 GPa for QHA calculations based on UFF result in an overall agreement with the UFF4MOF investigations (see Fig. 67 (a)). Both UFF and UFF4MOF calculations show also for UiO-68 a similar behavior. In contrast to UiO-67, instabilities can clearly be found using UFF in the isobaric heat capacity at low temperatures (see Fig. 67 (b)). One instability is visual in the range of 20 to 40 K and another in the range of 80 to 100 K. At higher temperatures, i.e., above 200 K, the calculated isobaric heat capacities for the different pressures become indistinguishable.

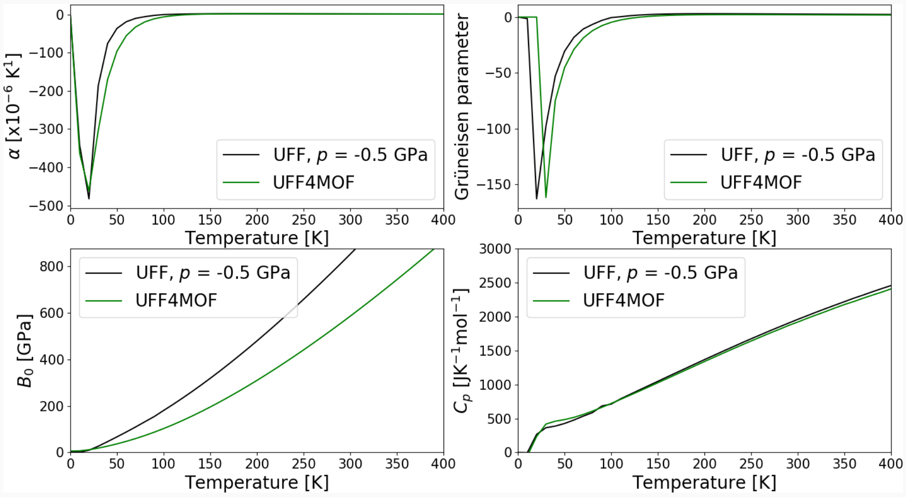

(a) QHA

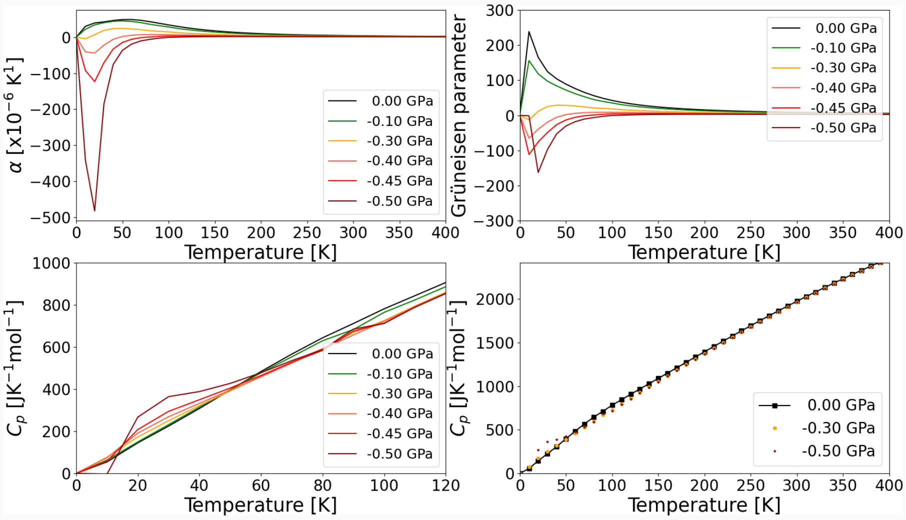

(b) Instability

Figure 67: UiO-68: QHA of UiO-68 using LAMMPS-INTERFACE with UFF and UFF4MOF coupled with PHONOLAMMPS. For the given set the fits are stable with respect to T_{max}. For the UFF calculations in (a) a pressure $p = -0.5$ GPa was used for the QHA. For the LAMMPS@FF-QHA workflow using UFF in (b) p has varied for the QHA calculations. The isobaric heat capacity from 200 to 400 K is nearly identical for all pressures used. An inset in the lower temperature range of the isobaric heat capacity shows two features. These features change drastically for different pressures as can be seen in the behavior of the thermal expansion coefficient as well as within the Grüneisen parameter. For C_p the pure values instead of the fit are plotted. The picture was produced by the author using MATPLOTLIB (see Appendix A).

7.4.5 *open@DUT-8(Ni)*

As a last example the thermodynamical properties of open@DUT-8(Ni) are calculated using the LAMMPS@FF-QHA workflow applied both the UFF and UFF4MOF force field. For all investigations the DFT optimized structure dft@open@DUT-8(Ni) was used as starting structure. Consistent with the other calculations also for this MOF UFF only shows non-significant imaginary modes (see Fig. 68 (a)), which are more dominant in the UFF4MOF calculations (see Fig. 68 (b)).

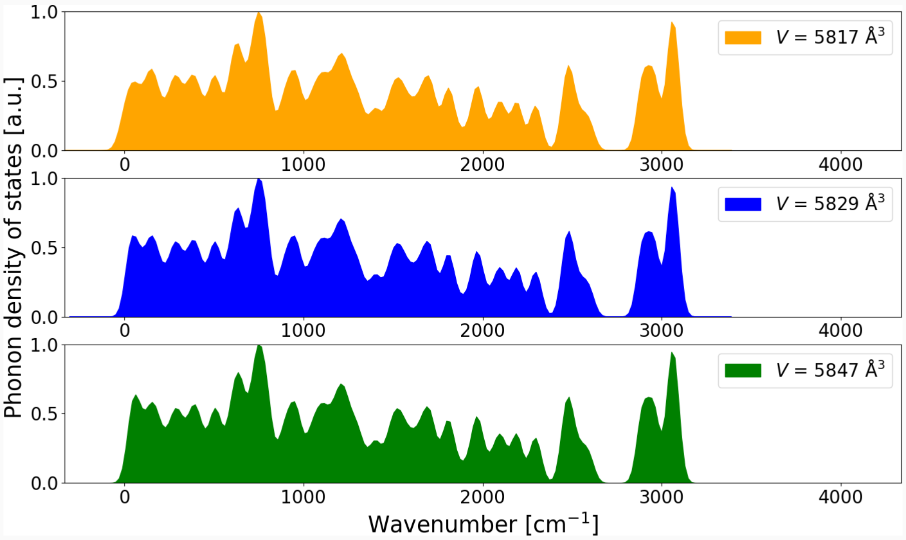

(a) UFF

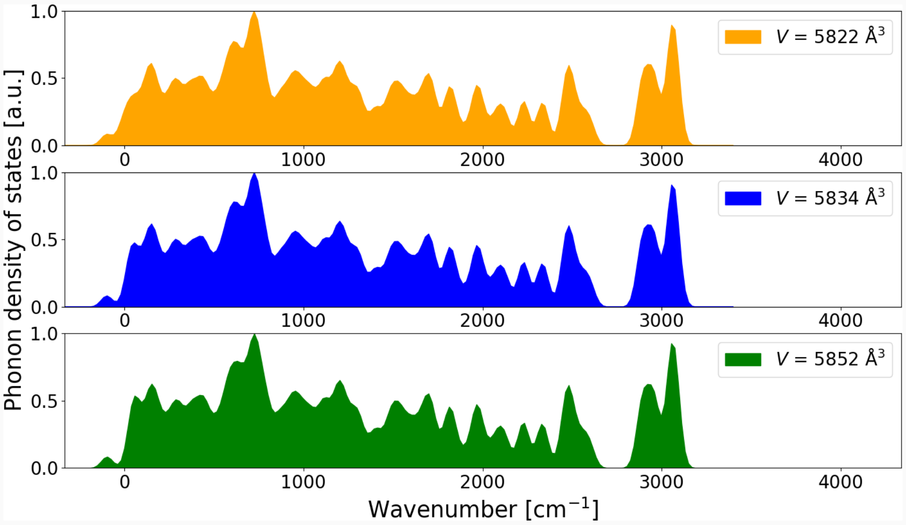

(b) UFF4MOF

Figure 68: open@DUT-8(Ni): PDOS calculated using the LAMMPS@FF-QHA workflow with (a) UFF and (b) UFF4MOF for selected volumes of open@DUT-8(Ni). For PHONOPY a 32x32x32 grid was used. The picture was produced by the author using MATPLOTLIB (see Appendix A).

Applying the QHA procedure for different pressures one can find a good agreement between UFF with a pressure p = -0.4 GPa and UFF4MOF with a pressure p = 0.22 GPa (see Fig. 69 (a)). At these pressures values the temperature-dependent bulk modulus at $T = 0$ K shows the correct magnitude as calculated in the previous section. The choice of the pressures for the QHA does not change the calculated thermodynamical properties from 200 - 400 K. As observed for UiO-67 and UiO-68, also open@DUT-8(Ni) shows a thermodynamical instability at low temperatures (see Fig. 69 (b)).

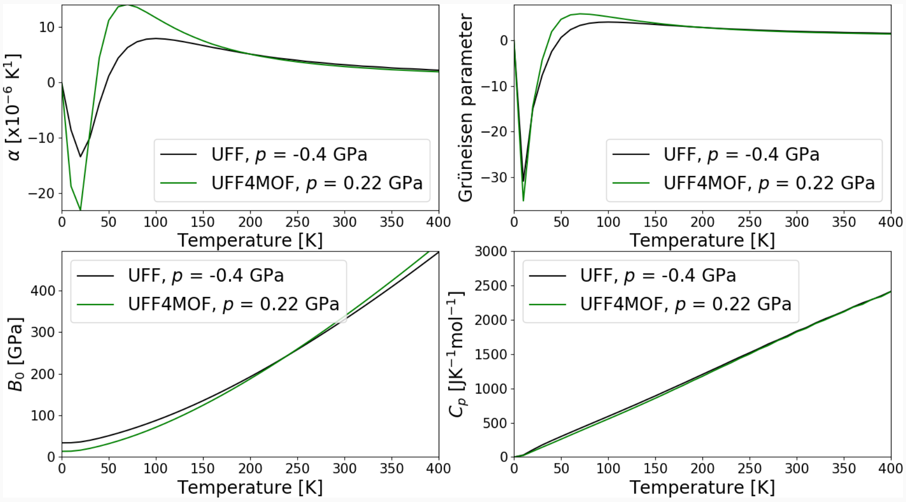

(a) QHA

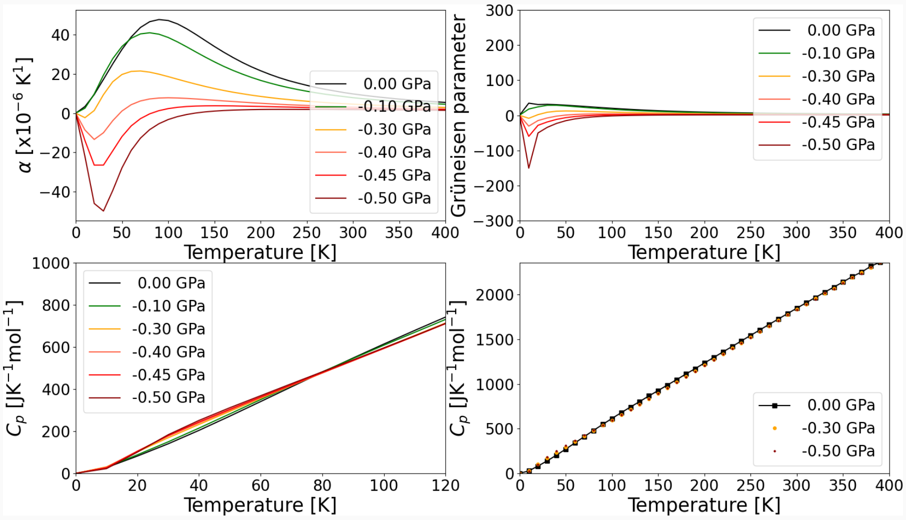

(b) Instability

Figure 69: open@DUT-8(Ni): QHA of open@DUT-8(Ni) using LAMMPS-INTERFACE with UFF and UFF4MOF coupled with PHONOLAMMPS. For the given set the fits are stable with respect to T_{max}. For the UFF calculations in (a) a pressure p = -0.4 GPa and for UFF4MOF p = 0.22 GPa was used for the QHA. For UFF in (b) p has varied for the QHA calculations. The isobaric heat capacity from 200 to 400 K is nearly identical for all pressures used. The lower temperature range of the isobaric heat capacity shows two features. These features change drastically for different pressures as can be seen in the behavior of the thermal expansion coefficient as well as within the Grüneisen parameter. For C_p the pure values instead of the fit are plotted. The picture was produced by the author using MATPLOTLIB (see Appendix A).

7.4.6 *Conclusion*

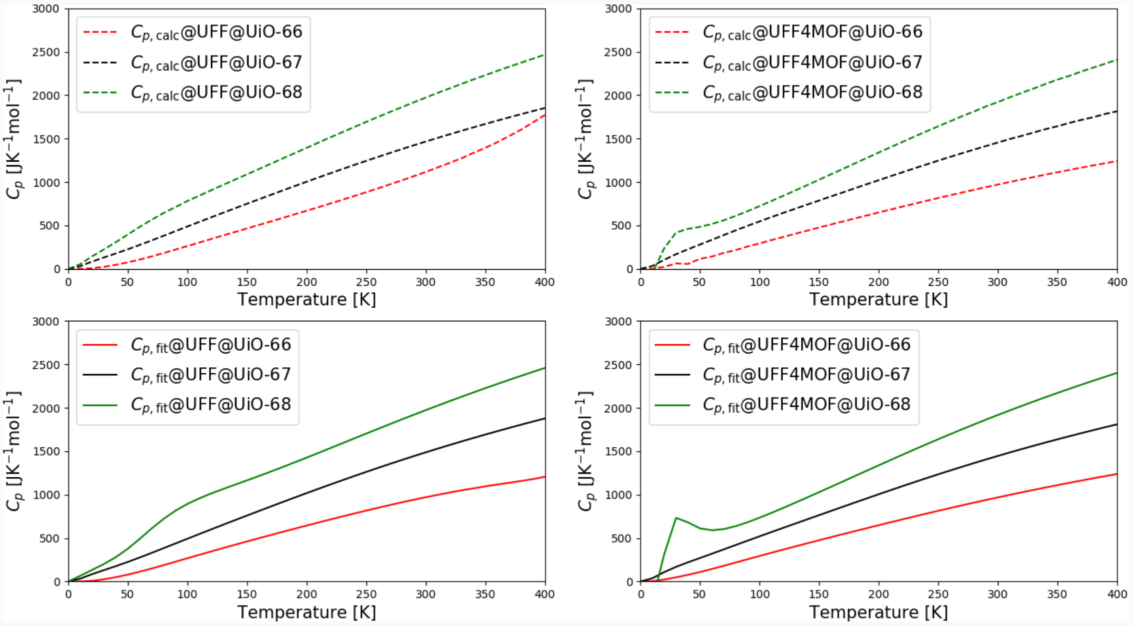

Figure 70: UiO-family: Isobaric heat capacities for UiO-66, UiO-67, and UiO-68 using LAMMPS-INTERFACE with UFF and UFF4MOF coupled with PHONOLAMMPS. The difference between the calculated and fitted isobaric heat capacities is presented. Overall, UiO-66 has the lowest, UiO-67 the second lowest, and UiO-68 the highest isobaric heat capacity. In the low temperature region, thermodynamical instabilities can be identified, while in the high temperature region all results are very similar (with the outlier of $C_{p,\mathrm{calc}}$@UFF@UiO-66). The picture was produced by the author using MATPLOTLIB (see Appendix A).

The proposed FF-QHA workflows (see Section 5.2) can be applied to calculate thermodynamical properties within the quasi-harmonic approximation using different force field codes (GULP and LAMMPS) as well as various force field definitions (e.g., UFF, UFF4MOF and VMOF). While absolute values for the temperature-dependent bulk modulus, the thermal expansion coefficient, the Grüneisen parameter or the isobaric heat capacity may change with the given force field definition, overall trends can be studied in a computationally efficient way. Thus, systematic comparisons of various materials, like the UiO family (see Fig. 70), using the same force field definition and the proposed workflows may help to provide further insights into thermodynamics of MOFs in the future. The thermodynamical calculations for UiO-67 and UiO-68 showed clear thermodynamical instabilities at low temperatures. Variation of pressure within the QHA approximation showed that these instabilities are sensible to the applied pressure. For UiO-67 the respective instability is consistent with the jump in the pV curve at low pressures. This further indicates the existence of UiO-67 conformers. Over the investigated temperature range UiO-68 showed the highest isobaric heat capacity and UiO-66 the lowest one. UFF and UFF4MOF provide consistent trends for the analyzed thermodynamical properties. In case of open@DUT-8(Ni) a similar low temperature thermodynamical instability as found in UiO-67 and UiO-68 was determined.

7.5 VOID AND ACCESSIBLE POROSITIES

List of own publications related to this chapter.

- K. Trepte and S. Schwalbe
  porE: A code for deterministic and systematic analyses of porosities
  Journal of Computational Chemistry, 42, 630-643, 2021

Accurate numerical calculations of porosities and related properties are of importance when analyzing MOFs. This is because porosities are one of the key properties to characterize and differentiate MOFs. The porE code [241] (see Appendix A), co-developed by the author, is applied to compute such properties. The results are systematically compared to various other codes. Three different approaches are implemented to calculate porosities. Besides porosities porE is able to calculate pore size distributions (PSDs) as well as pore windows. To be able to compare calculated values to reference values, a clear differentiation between void and accessible porosities is done.

The pore sizes in MOFs can be varied by enforcing an external pressure on a given MOF [254]. Many applications of MOFs are based on the porous nature of these materials, as MOFs typically exhibit several pores. These pores usually have different sizes. With that, an accurate determination of the porosity and the pore sizes is important [255]. In general, the porosity Φ is defined as the empty volume V_{empty} within a given total volume V_{total} (e.g., the unit cell of a MOF)

$$\Phi = \frac{V_{\text{empty}}}{V_{\text{total}}}. \tag{109}$$

The total volume for crystal structures is always well defined, which is generally not the case for the empty volume. One major aim of this investigation is to define and clearly separate two different empty volumes, namely the void volume V_{void} and the accessible volume V_{acc}. The void volume is the space that is not occupied by any atom in the unit cell. This volume can easily be analyzed given the sizes of the atoms, e.g., their respective van der Waals (vdW) radii [256]. With this volume, the void porosity Φ_{void} can be obtained, which serves as a first descriptor of a porous material. However, it has to be considered that a void porosity does not necessarily reflect the volume/porosity which can be accessed by adsorbed species. Such a porosity strictly depends on the size of that species. With that, another volume occurs, i.e., the accessible volume. Accordingly, the accessible porosity Φ_{acc} can be defined. This porosity, in contrast to Φ_{void}, depends on a probe radius r_{probe} which varies for different species. One has to be careful when analyzing the porosity in a material, as the porosity of interest is usually Φ_{acc}. When reporting this quantity, one needs to provide the respective probe radius, such as the vdW radius of H $r_{\text{probe}} = 1.20$ Å or Xe $r_{\text{probe}} = 2.16$ Å.

Choosing different probe radii significantly impacts the evaluated porosity. A systematic analysis of the probe radius dependence allows to evaluate the porosity for any adsorbed species, i.e., any atom or molecule with an effective probe radius.

The porE code can calculate porosities with different approaches, namely the Helium approach (HEA), the overlapping spheres approach (OSA) and the grid point approach (GPA). The HEA approach invented by the author is based on an cell list approach to predict He-fraction-like porosities, making it numerically efficient. A given unit cell is divided into smaller sub-cells. These sub-cells have the same orientation as the unit cell vectors of the original cell, and therefore conserve lattice symmetries. The sub-cells are calculated to give the best He-He spacing based on the vdW radius of He. Having this set of sub-cells, one can calculate the center of mass (COM) of each sub-cell and place a He atom at these positions. The overlap of all inserted He positions with the framework positions is then calculated; all He positions showing an overlap with the framework are excluded.

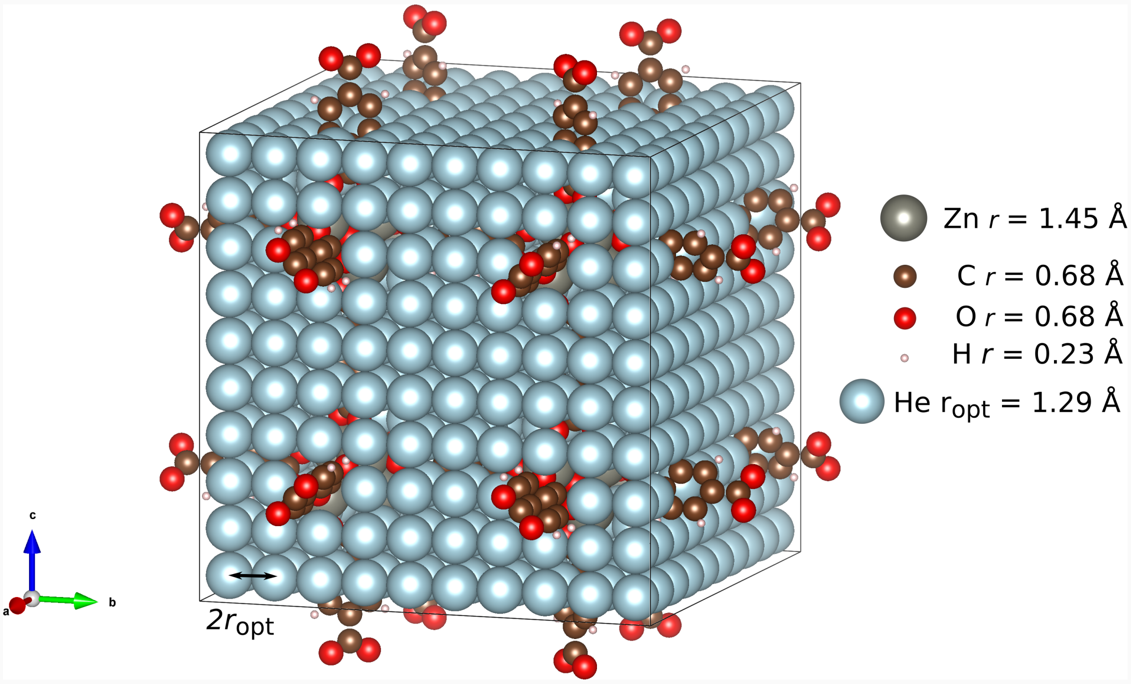

Figure 71: HEA applied to MOF-5 with a resulting porosity of $\Phi_{\text{HEA}} = 77\%$ and a packing factor of $f_{\text{HEA}} = 0.52$. The individual pictures are generated with VESTA with an effective radius equal to the radii in HEA (with r_{opt} for He). The entire picture was generated using the Inkscape program.

In OSA, a hard sphere model is used. The overlap of atomic spheres is evaluated and consequently subtracted from the total volume of all spheres/atoms. While this approach is computational very efficient, only void porosities can be calculated. An alternative approach to calculate the porosity is based on a numerical grid inside the unit cell. This procedure requires the explicit treatment of each grid point. Any grid point is either close to an atom (inside its vdW sphere) and can be considered occupied. If no such occupation is found, the grid point is considered unoccupied. Using further classifications, a clear differentiation between accessible and void porosities can be made. The core routines of porE have been designed by Kai Trepte using Fortran. One needs to provide as input the unit cell parameters and the coordinates of the atoms. The input is similar to alternative implementations [242, 257–260]. The author increased the user-friendliness of the code and wrote a graphical-user-interface (GUI) and a Python application programming interface (API) called PyPORE (see Appendix A). For more details about the implementation as well as further results the interested reader is referred to Trepte and Schwalbe [241]. Various reference calculations have been performed by the author. In this section, major results regarding the importance of the probe radius dependence with respect to the accessible porosity are discussed.

A systematic study of porosities for the MOFs UiO-66 [261–263], UiO-67 [236, 262, 263], open@DUT-8(Ni) [240, 264, 265], closed@DUT-8(Ni) [240], IRMOF-10 [239], MOF-5 [266], HKUST-1 [267–269] and MOF-210 [270] have been performed. For illustration, the different pore centers of various MOFs determined using porE are plotted as spheres within the investigated structure (see Fig. 72). While HKUST-1, UiO-66, and UiO-67 have three distinct pores, MOF-5 has two characteristic pores, and open@DUT-8(Ni) and IRMOF-10 only have one pore, which is repeated within the periodic structure. This illustrates that the knowledge of the pores of MOF is, next to its SBUs and linkers, an essential characteristics.

To validate porE, several reference calculations were performed. For this, the codes RASPA2 [258, 259], poreblazer [257], PLATON [242] and Zeo++ [260, 271–274] were used.

Table 20: porE8: Comparison of calculated porosities between reference codes (RASPA2 [258, 259] (π), poreblazer 3.0.2 [257] (ρ), PLATON [242] (γ), Zeo++ [260, 271–274] (ξ)), literature values and the presented approaches (HEA (η), OSA (α), GPA(void) (ω_{void}), and GPA(acc) (ω_{acc})). For the GPA, $r_{\text{probe}} = 1.20$ Å using the largest possible grids; for MOF-210 we used $\overline{n} = 5$ points/Å). All porosities are given in %. The literature values (REF) are: DUT-8(Ni)[240], UiO-66 and UiO-67[275], IRMOF-10[239], MOF5 and MOF-210[270], HKUST-1[255, 276].

MOF	π	ρ	γ	ξ	η	α	ω_{void}	ω_{acc}	Φ_{REF}
open@DUT-8(Ni)	70	68	66	68	70	61	70	67	67
closed@DUT-8(Ni)	0	0	0	0	25	−1	27	1	0
UiO-66	52	51	53	55	63	49	59	54	53
UiO-67	72	72	69	70	68	68	72	69	68
IRMOF-10	91	90	86	87	85	88	88	87	87
MOF-5	81	81	76	79	77	77	80	79	79
HKUST-1	73	72	69	69	72	68	71	69	68
MOF-210	93	—	—	88	87	90	90	89	89

The void porosities calculated with porE applying the GPA agree well with the results of the RASPA2 and the poreblazer code (see Tab. 20). The accessible porosities applying porE with the GPA for the set of MOFs is in excellent agreement with the results calculated with the PLATON and the Zeo++ codes (see Tab. 20 and Fig. 73). Further, a comparison to literature values is carried out. Here, one essential point is that literature values are accessible porosities, while the corresponding probe radius is usually not provided. Clearly, the void porosities do not accurately reflect the porous nature of the MOFs. This is especially true for systems with more complex pore structures. There, the probe radius plays an even more crucial role (compare, e.g., UiO-66 and MOF-5). In MOFs with large, open pores the void porosity will already reflect the porous nature of the MOF fairly accurately. If a pore would be entirely spherical, i.e., the pore would have a spherical symmetry, the calculated porosity would be independent of the probe radius (unless $r_{\text{probe}} \geq r_{\text{pore}}$). Using any probe radius smaller than the pore radius would sample the pore entirely, as there are no areas/volumes which are inaccessible. With that, the porosity is independent of the probe radius and the void porosity is already a good quantity. However, if the pores are different from the spherical symmetry, e.g., having tetrahedral or octahedral symmetries as in the UiOs, the probe radius dependence is significantly larger. In such a case, a sphere is not a suitable approxi-

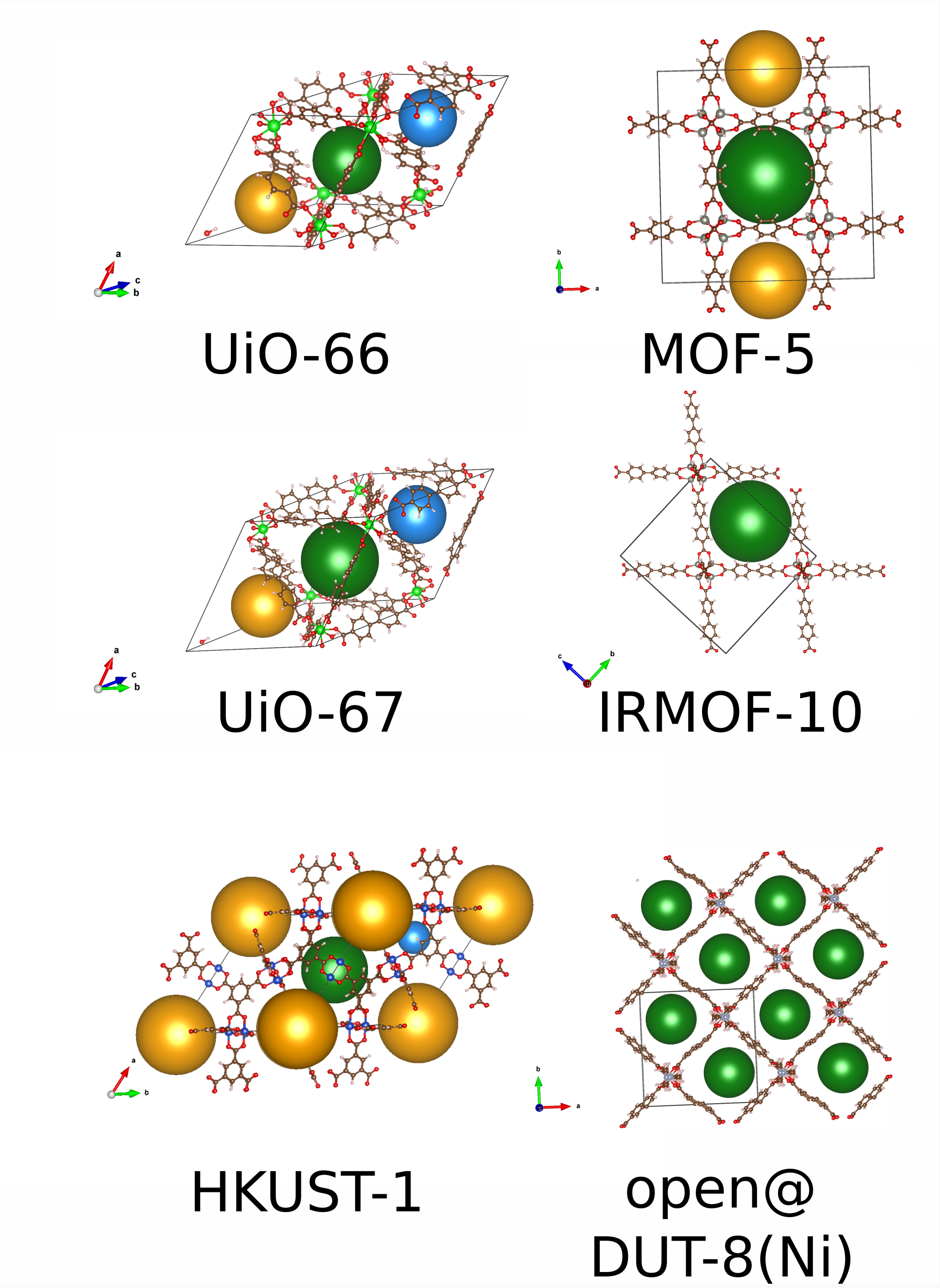

Figure 72: Visualization of pores in MOFs. HKUST-1, UiO-66, and UiO-67 have three distinct pores. MOF-5 has two characteristic pores, while open@DUT-8(Ni) and IRMOF-10 only have one pore, which is repeated within the periodic structure. The individual pictures are generated with VESTA using the calculated pore centers as additional species with an effective radius equal to the determined pore size. The entire picture was generated using the Inkscape program (see Appendix A).

mation for the pores (see Fig. 72 for UiO-66 and UiO-67). Quantitatively, this can be seen for UiO-66 (see Tab. 20), where the void and the accessible porosities are quite different (59 % and 54 %). This is true even at a fairly small probe radius of 1.20 Å.

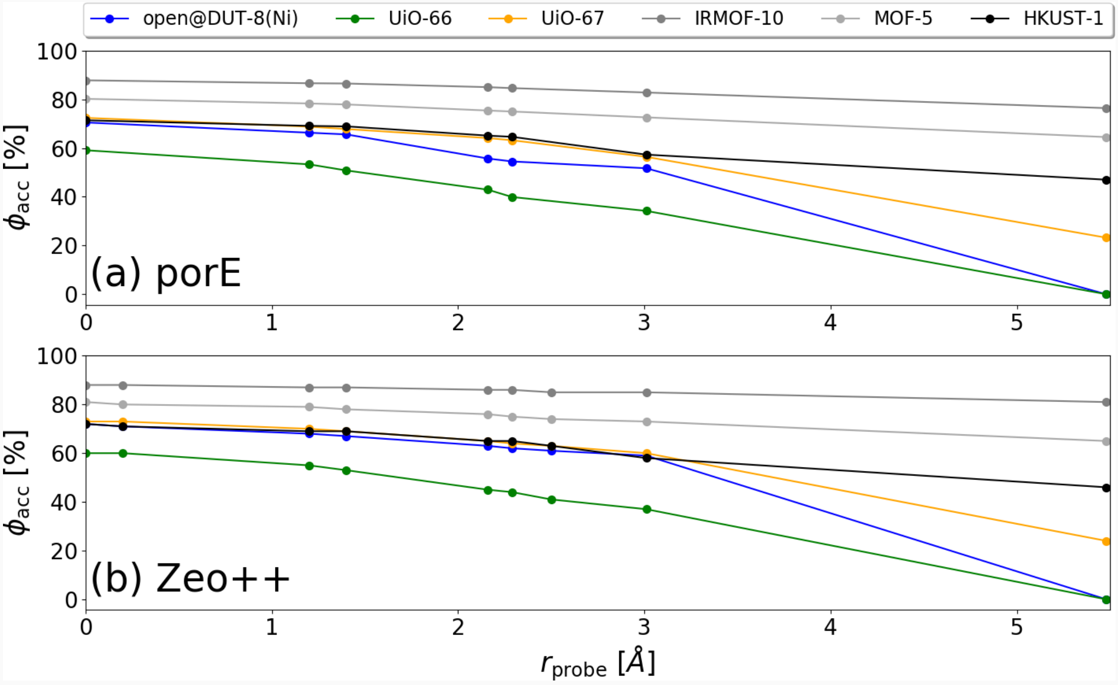

Figure 73: Probe radius dependence of the accessible porosity for various MOFs using porE and Zeo++. Both codes produce nearly identical probe radius dependencies for the investigated MOFs.

The dependence becomes clearer the larger the probe radius becomes. Further, this explains the rather small dependence of the accessible porosity for $r_{\text{probe}} = 1.20$ Å in the MOFs IRMOF-10, MOF-5 and HKUST-1 [241], as for these three MOFs spheres are a fair approximation to describe the respective pores.

In summary, HEA is based on a cell list approach to efficiently compute the porosities based on He. The accessible porosities from the GPA are in excellent agreement with literature values, reassuring a proper implementation of porE. Considering its limitations, even the OSA provides reasonable results. Further, the crucial importance of a clear differentiation between accessible and void porosity for the correct description of porosities in MOFs was demonstrated. For the accessible porosity, it was shown that a correct treatment of the probe radius is essential for reliable results. Thus, this dependence must be considered in any case. A comparison to reference calculations and literature values confirms that both approaches work as intended, and that the GPA gives very accurate results.

7.6 ELECTRONIC AND MAGNETIC PROPERTIES

List of own publications related to this section are given below.

- K. Trepte, S. Schwalbe and G. Seifert
  Electronic and magnetic properties of DUT-8(Ni)
  Physical Chemistry Chemical Physics, 17, 17122 - 17129, 2015
- S. Schwalbe, K. Trepte, G. Seifert and J. Kortus
  Screening for high-spin metal organic frameworks (MOFs):
  density functional theory study on DUT-8(M1,M2) (with Mi = V,...,Cu)
  Physical Chemistry Chemical Physics, 18, 8075 - 8080, 2016

Magnetism is important, as nowadays technologies are needed for the development of smart devices for data-/signal-transfer, -manipulation and -storage and many of these devices are based on magnetic materials. The general trend goes to smaller and smaller devices, but the downsizing and miniaturization in magnetic storage devices is physically limited. Below a critical domain size (superparamagnetic limit) thermal excitations can flip the spin orientation and data loss is the result. The author and his co-authors [265] showed how one can realize a promising concept for solving this problem by integrating the so called single-molecule magnets (SMMs) into the crystalline nature of MOFs. This section summaries the main findings of Schwalbe et al. [265].

Studies of magnetism within solids and molecules, especially SMMs, have been done experimentally as well theoretically for various systems. In contrast, such studies for MOFs are not common. Thus, the author and his co-authors started to investigate magnetism in MOFs using the framework of DFT. In detail, the electronic and magnetic properties of closed and open DUT-8(Ni) were studied with DFT [264]. The energetically favored magnetic ordering of both DUT-8(Ni) forms has been identified to be a low-spin spin-state with the total spin-state $S_{\text{tot}} = 0$ [264] and the local spin-state $S_{\text{center}} = 1$ [264]. Further, the electronic and magnetic properties of the MOF itself was analyzed to be dominated by the local electronic and magnetic properties of the SBU. Additional calculations (e.g., molecular test systems) showed that changes in local chemical environment may introduce a change in the magnetic ordering, i.e., switching from low-spin (LS) to high-spin (HS) ordering. Given this, the author and his co-authors set up to screen for stable HS configurations of SBUs. Such screening strategies can help to identity promising candidate structures fulfilling the screening objective.

SMMs are metal-organic compounds that show magnetic behavior below a critical temperature (blocking temperature). Magnetism in such compounds is localized and no long-range order occurs. MOFs consist of SBUs containing metal-centers and organic-building blocks, which are repeated due to their crystalline nature. Thus, SBUs of MOFs may be structurally considered as SMMs. A SMM building unit for a MOF combines the advantages of both the local magnetism and the periodic boundary conditions, which would allow to arrange local magnetic sites in a distinct three-dimensional order. The screening is performed on the flexible MOF DUT-8(Ni) [240, 277, 278], in detail on a special model system identified by Trepte, Schwalbe, and Seifert [264] hereafter referred to as M1 (see Fig. 74).

The M1 model system contains Ni atoms, which are bipyramidally coordinated with four O and one N each. The interatomic Ni-Ni distance is about 2.8 Å and the metal centers A and B have slightly different chemical environments. Given the interest in the influence of the metal centers on the coupling constant J in the given geometry, no geometry optimizations were carried out. This ensures that the changes in J come solely from the different transition metals and not from an alteration in the geometry. The two metal centers in the M1 model were varied to determine the influence on the magnetic ground state and with that on the coupling constant. The magnetization in each system has been chosen to be either the sum or the difference of unpaired electrons per atom in the HS and LS case. The Ni atoms at centers A and B are replaced with every combination of 3d-elements, where Zn as a closed shell system would not contribute to the magnetism and is therefore excluded from the screening. Furthermore any HS solutions for Sc systems should be disregarded, as Sc tends to be in a non-magnetic state and usually does not form any HS solution [265]. Thus, Sc systems are not further investigated. For Ti system a similar behavior was found and the found HS solution was neglected for the same reason. With that, only the elements from V to Cu are taken into account for further discussion. The denominator Ω_S for the calculation of J with

$$J = \left(E_{\mathrm{LS}} - E_{\mathrm{HS}}\right) / \left(\langle \vec{S}^{\,2} \rangle_{\mathrm{HS}} - \langle \vec{S}^{\,2} \rangle_{\mathrm{LS}}\right)_{\mathrm{ideal}} = \Delta E / \Omega_S, \tag{110}$$

for different pairs of 3d metals is given in Tab. 21.

Table 21: Denominator Ω_S for different pairs of 3d metals. This picture have been published [265]. The picture has been produced by the author using the tikz package within LaTeX.

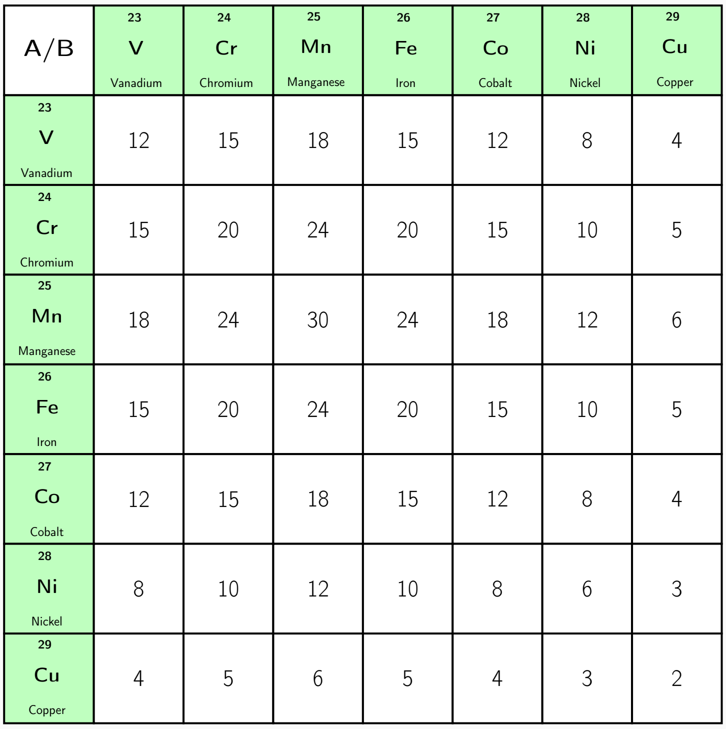

A/B	23 V Vanadium	24 Cr Chromium	25 Mn Manganese	26 Fe Iron	27 Co Cobalt	28 Ni Nickel	29 Cu Copper
23 V Vanadium	12	15	18	15	12	8	4
24 Cr Chromium	15	20	24	20	15	10	5
25 Mn Manganese	18	24	30	24	18	12	6
26 Fe Iron	15	20	24	20	15	10	5
27 Co Cobalt	12	15	18	15	12	8	4
28 Ni Nickel	8	10	12	10	8	6	3
29 Cu Copper	4	5	6	5	4	3	2

The objective for the screening was to find a HS solution for the magnetic coupling of the metal centers of this MOF. In other words the goal was to search for a MOF with stable local HS magnetic ordering which could results in a stable ferromagnetic MOF. This may be interesting for a possible application in spintronics or a molecular switchable gas-sensor. It was analyzed how the magnetic properties of MOFs behave by changing the 3d metal centers.

DFT has limited accuracy due to several systematic shortcomings like self-interaction-error (see Section 3.1.5) and the problem of spin-contamination [279]. However, it is a widely used and well established theory for the calculation of ground state energies. To determine exchange coupling constants, DFT is used for the calculation of the energy difference between LS and HS states, which should give qualitatively accurate results. Those energy differences are used as parameters for the calculation of the coupling constant J as given in a model Heisenberg Hamiltonian.

All calculations were performed in the framework of DFT all-electron codes (NRLMOL [29–35], FPLO [280], ORCA [36]) and were systematically compared to plane wave codes (Quantum Espresso [26], GPAW [27]). For the computational details the interested reader is referred to Trepte, Schwalbe, and Seifert [264] and Schwalbe et al. [265]. The usage of several codes ensures the reduction of methodological errors, which may occur in every implementation of DFT. Another reason is the comparison between all-electron and pseudo-potential codes, as it becomes unfeasible to use all-electron codes for larger systems like MOFs. Thus, it has to be proven that pseudo-potential implementations reproduce all-electron results. This is important for further investigations, where the model systems can be used as SBUs for new MOFs.

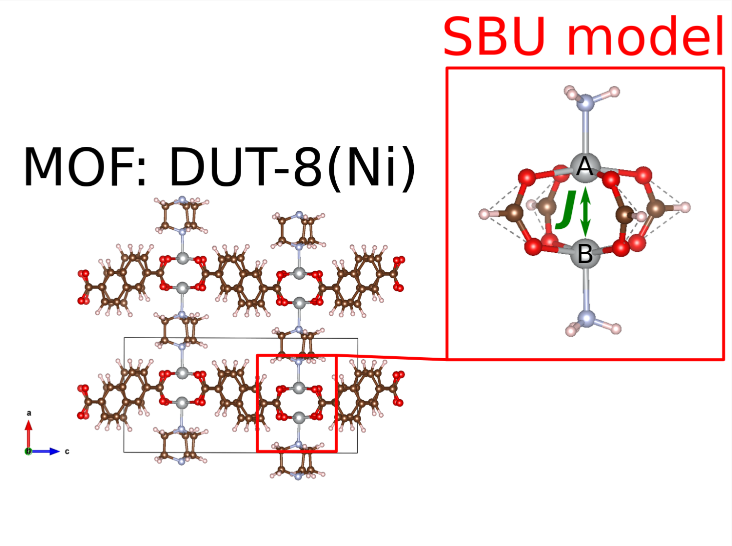

Figure 74: DUT-8(Ni) and SBU model structure M1, where the metal centers changed for the screening are highlighted with A and B. Color code: transition metal (gray), oxygen (red), carbon (brown), nitrogen (light blue) and hydrogen (pink).

Magnetism as well as the exchange coupling constant can be described by the coupling of local spins at distinguishable magnetic centers (e.g., i and j). A possible description is given by the so called Heisenberg-Dirac-Van Vleck (HDVV) Hamiltonian [281–283]

$$\hat{H}_{\mathrm{HDVV}} = -2\sum_{i>j} J_{ij}\, \vec{S}_i \cdot \vec{S}_j \tag{111}$$

where J_{ij} is the coupling constant between neighboring spins and $\vec{S}_i/\vec{S}_j$ are spin operators. A high-spin state (parallel aligned spins, ferromagnetic coupling) is indicated by a positive sign of the coupling constant J_{ij} while a negative sign refers to a low-spin state (anti-parallel spins, anti-ferromagnetic coupling). For dimers ($i = 1$ and $j = 2$)

the coupling can be expressed with the total energies of these two different magnetic orderings [284, 285]

$$J_a = \left(E_{\mathrm{LS}} - E_{\mathrm{HS}}\right) \Big/ \left(\langle \vec{S}^{\,2} \rangle_{\mathrm{HS}} - \langle \vec{S}^{\,2} \rangle_{\mathrm{LS}} \right), \tag{112}$$

which can be derived directly from Eq. (111). The total energies E_{LS} and E_{HS} can be taken from spin-polarized DFT calculations. The total magnetizations for the HS and LS state were taken to evaluate the corresponding spins and with that the values of the expectation values $\langle \vec{S}^{\,2} \rangle_{\mathrm{HS}}$ and $\langle \vec{S}^{\,2} \rangle_{\mathrm{LS}}$. The denominator in Eq. (112) changes with the metal centers as shown in Tab. 21. In literature there are different equations discussed for the exchange coupling constant J_b [286–288] and J_c [289, 290]

$$J_b = \left(E_{\mathrm{LS}} - E_{\mathrm{HS}}\right) \Big/ \left(S_{\mathrm{HS}}^2\right) \tag{113}$$

$$J_c = \left(E_{\mathrm{LS}} - E_{\mathrm{HS}}\right) \Big/ \left(S_{\mathrm{HS}}(S_{\mathrm{HS}} + 1)\right). \tag{114}$$

For dimers which include the same metal centers or metal centers with the same number of unpaired electrons, Eq. (112) reduces to Eq. (114), because $\langle \vec{S}^{\,2} \rangle_{\mathrm{LS}}$ becomes 0. Thus, Eq. (114) is only valid for those cases and not usable for other kinds of mixed dimers. Further approximation can be done by assuming that $S_{\mathrm{HS}}^2 \gg S_{\mathrm{HS}}$, which transforms Eq. (114) into Eq. (113). This is not suitable for our study, as this assumption is not valid in all systems. With that, all calculated coupling constants were derived from Eq. (112). A more detailed discussion about the used calculations scheme, i.e., restricted open shell Kohn-Sham (ROKS for NRLMOL, FPLO and QE) and unrestricted Kohn-Sham (UKS for ORCA) as well as a detailed discussion about the broken symmetry method is given in the supplementary material of Schwalbe et al. [265] or the excellent review paper of Neese [279].

Table 22: Coupling constant: Influence of exchange-correlation and accuracy of DFT. Results have been published [265].

code	method/basis sets	functional	J [cm^{-1}]
ORCA	UKS def2-TZVP[291]	PBE	-264.1
ORCA	UKS def2-TZVP[291]	B3LYP	-204.8
NRLMOL	optimized Gaussian basis[35]	PBE	-261.5
FPLO	local-orbital minimum-basis[280, 292]	PBE	-274.8
GPAW	LCAO DZP	PBE	-222.3
QE	PW PAW	PBE	-272.2

In preliminary calculations the coupling constant of the original model system M1 [264] containing Ni has been investigated using various DFT codes with different implementations and levels of precision (see Tab. 22). The dependence of the calculated coupling constants on the choice of the exchange-correlation functional has been studied by comparing results obtained with PBE and B3LYP. The value of the coupling constant changes, but the sign and the magnitude are retained (see ORCA PBE/B3LYP results Tab. 22). Thus, the PBE functional was used for the HS screening. It should be considered that only in the UKS formalism spin-contamination is explicitly calculated. Given this reason Eq. (113) is used for the evaluation of the results from ORCA to make those accurate ORCA values comparable with all other results. This corresponds to the ideal spin operator expectation values in the LS and HS state. All performed calculations of the coupling constant with the PBE functional give the same sign and a very similar absolute value, besides GPAW where the basis set might be too small. Additionally, the QE results are comparable with the all-electron calculations (see Tab. 22). Due to reasons of reproducibility NRLMOL and FPLO have been applied to have independent all-electron codes for the calculation of J considering the variation of metal centers. For comparison of two different implementations of DFT (all-electron and pseudo-potentials) and because of the demonstration of the preliminary results, the screening was additionally performed with QE.

Table 23: Resulting coupling constant J [cm^{-1}] for the implementation of the range of 3d metals into the M1 model system as obtained with NRLMOL, FPLO and QE. The resulting high-spin solutions are marked green. For non-converged calculations the tag **n.c.** is given. Results have been published [265].

NRLMOL

A/B	V	Cr	Mn	Fe	Co	Ni	Cu
V	+149.8	-80.8	-96.2	-396.2	-480.3	-667.6	-1208.2
Cr	-83.3	-275.3	-180.9	-239.8	-331.3	-633.1	-715.3
Mn	-94.7	-180.0	-105.2	-97.8	-124.6	-263.9	-547.4
Fe	-388.6	-213.6	-105.6	+115.6	+40.1	+151.1	+150.9
Co	-483.4	-328.0	-128.4	+39.6	-169.6	-190.4	-211.9
Ni	-664.4	-629.4	-261.8	+227.8	-192.2	-261.5	-251.6
Cu	-1171.4	-702.2	-538.3	+158.7	-194.8	-246.4	-520.4

FPLO

A/B	V	Cr	Mn	Fe	Co	Ni	Cu
V	+191.4	-85.4	-99.9	-405.7	-385.9	-669.9	-1215.2
Cr	-88.1	-287.6	-191.2	-245.7	-280.9	-635.9	-728.9
Mn	-98.3	-190.3	-112.3	-115.6	-153.1	-272.2	-546.5
Fe	-402.1	-232.7	-81.6	+109.8	+84.7	+153.9	+144.1
Co	-377.5	-279.7	-132.9	+69.8	-195.3	-206.9	-158.8
Ni	-667.2	-631.9	-269.9	+156.2	-196.5	-274.8	-243.6
Cu	-1177.4	-716.7	-537.4	+185.2	-166.8	-237.7	-496.4

QE

A/B	V	Cr	Mn	Fe	Co	Ni	Cu
V	+197.6	-88.3	-99.2	-397.9	-353.5	-679.1	-1208.3
Cr	-90.6	-285.9	-187.3	-231.9	-314.9	-631.2	-714.1
Mn	-97.6	-186.4	-110.2	-115.1	-129.5	-270.6	-554.2
Fe	-394.8	-214.9	-115.0	+106.8	+66.9	+154.1	+207.3
Co	-363.5	-314.5	-141.5	**n.c.**	-197.7	-92.9	**n.c.**
Ni	-677.5	-627.5	-268.5	+155.9	-70.9	-272.2	-248.1
Cu	-1171.7	-702.7	-545.4	+197.2	-182.2	-242.7	-517.8

The results obtained from the two all-electron calculations (see Tab. 23) are for most models in excellent agreement with each other regarding the prediction of the J trends as well as the absolute value of the coupling constants. In addition, it was found that the kinetic exchange term is converging fast with basis set, similar to the observation made by Park and Pederson [293] in case of the more complex Fe_4Mn_8 and Mn_{12} clusters. These calculations showed that the pseudo-potential calculations are in good agreement with the results from the all-electron calculations (see Tab. 23). Furthermore, the screening was performed with ORCA within the UKS scheme. For those calculations the influence of several different definitions of J was investigated [265]. Comparing the results from different numerical codes clearly demonstrated that the identified ferromagnetic building blocks are not an artifact of the way the calculation has been carried out (ROKS or UKS). Additionally, the determined coupling constant trends are independent of the definition of J. Based on the results of the DFT calculations (see Fig. 75), the following promising HS candidates were identified: M1-[V,V], M1-[Fe,Fe], M1-[Fe,Co], M1-[Fe,Ni] and M1-[Fe,Cu]. M1-[element1,element2] describes the model system M1 for both substitutions with those elements, e.g., M1-[Fe,Ni] stands for M1-FeNi and M1-NiFe. All those systems show a HS coupling. These model systems may be used to construct a new kind of MOF using the corresponding HS SBU. V and Fe in MOFs usually form chains and no paddle wheels, especially not the kind which is found in DUT-8(Ni). Ni, Co and Cu on the other hand are able to form such paddle wheel structures. This might lead to a stable crystalline structure by doping the DUT-8(Ni) with e.g. Fe. Another possibility is to use the proposed model systems as SBUs for a new kind of MOF, in which the magnetic characteristics of the model system are retained.

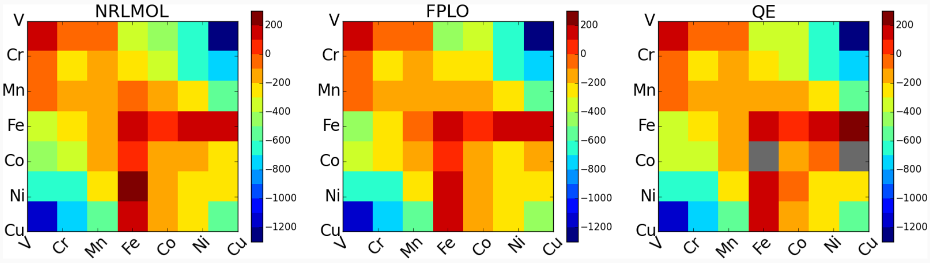

Figure 75: Colormap of coupling constants J. All HS solutions are marked red. The colors for the LS solutions are scaled from the smallest J (orange) to the largest J (blue). Derived from all-electron (NRLMOL & FPLO) and PAW (QE) calculations. Results have been published [265]. Note: The two calculations which did not converged in QE are marked gray.

In summary, a parameter free screening for the determination of HS solutions for the DUT-8(Ni) model system M1 has been performed using DFT. A comparison between different exchange-correlation functionals showed that PBE is sufficient for the calculation of the exchange coupling constant J. Further investigations were carried out for the following *HS candidates: M1-[V,V], M1-[Fe,Fe], M1-[Fe,Co], M1-[Fe,Ni] and M1-[Fe,Cu].*

All used DFT codes agree qualitatively as well as quantitatively. Thus, it is possible to use the plane wave method for further investigations. Based on the results of this analysis it should be considered to insert the obtained HS SBUs into the crystalline structure of DUT-8(Ni), either as a complete replacement of the original SBUs to gain a fully ferromagnetic MOF or as a "magnetic doping" by replacing individual SBUs with some HS SBUs to introduce local HS sites.

7.7 CONCLUSION

In this chapter mechanical, elastic, electronic, magnetic and thermodynamical properties of MOFs have been discussed. It was shown that MOFs are soft materials, were a small external pressure might change intrinsic properties of MOFs (e.g., space group or orientation of linkers). The possibility of the existence of conformers at different pressure regimes of UiO-66 and UiO-67 has been discussed. Both DFT and FF showed similar trends.

The previously introduced elastic workflow has been used to calculate the bulk moduli for various MOFs. The force field (i.e., UFF and UFF4MOF) results are in reasonable agreement with reference values. This is a first evidence that such force fields might be accurate enough to study thermodynamical properties of MOFs.

Pores as intrinsic parts of MOFs have been systematically studied with a co-developed code called poreE for a set of MOFs. The results of the poreE are in excellent agreement with reference calculations. A clear differentiation between void and accessible volume has been outlined. In addition to that it was shown that calculated accessible porosities critically depend on the probe radius.

SBUs as another intrinsic part of MOFs were studied. In detail, the idea of SBUs interpreted as SMMs in periodic structures has been investigated. The goal of this investigations was to determine stable ferromagnetic build units. A screening for these was performed for the model system M1 for the MOF DUT-8(Ni). This SBU originally consists of two Ni centers. For this study these centers were exchange with various transition metals. Overall reproducible DFT calculations (see Fig. 75) predicted promising ferromagnetic SBU candidates: M1-[V,V], M1-[Fe,Fe], M1-[Fe,Co], M1-[Fe,Ni] and M1-[Fe,Cu].

QHA force field workflows (LAMMPS@FF-QHA and GULP@FF-QHA) developed during this thesis were applied to get insights in thermodynamical properties of MOFs. It was shown that force fields are able to produce phonon density of states for various MOFs without showing significant imaginary frequencies. For the QHA calculations the pressure-dependent change of a given MOF lead to instabilities in the calculated thermodynamical properties. This might be an additional hint for the existence of conformers for MOFs like UiO-67. Similar instabilities have been found for UiO-68 as well as open@DUT-8(Ni).

The knowledge of MMtypes as shown within this chapter enables fast force field calculations with reasonable accuracy. In the AuToGraFS code, coordination points are needed to connect SBUs and linkers within a given topology to MOFs. Having these points the code automatically assigns the MMtypes for example for the UFF or UFF4-MOF force field. This allows a user-friendly usage of modern and accurate force fields for more complex calculations such as phonon calculations enabling QHA investigations. The logical next step would be an automatic assignment of such coordination points. On the other hand a more detailed insight in the electronic structure of SBUs and linker might aim for more accurate methods than force fields or standard DFT, as the accuracy of DFT is limited by problems like the self-interaction error. Further, there is no intrinsic way within DFT to allow for an *ab initio* bond characterization as Kohn-Sham wavefunctions have no physical meaning.

The Fermi-Löwdin orbital self-interaction correction (FLO-SIC) might offer a solution for both problems. Within FLO-SIC the Fermi-orbital descriptors (FODs) form a so called electronic geometry. In a simplified view FODs can be interpreted as semi-classical electron positions. Interpreting the FODs as electron positions would allow for an automatic generation of coordination points for tools like AuToGraFS, which itself can be used for the automatic assignment of MMtypes for force fields. Further, FLO-SIC aims to cure problems of standard DFT. The numerical accuracy of FLO-SIC might be helpful to study and understand electronic and magnetic effects of SBUs and linkers with respect to bonding and the switching between different conformations of MOFs. In the next chapter, the FLO-SIC method is analyzed and applied to provide insights whether these are useful assumptions or not.

Part III

THERMODYNAMICS OF NUCLEI AND ELECTRONS

In the third part of this thesis, thermodynamical properties of smaller building units like atoms and molecules are analyzed with force fields as well as pure and self-interaction-corrected density functional theory. The main focus of this part is to answer the question whether an explicit treatment of electrons is needed to understand thermodynamical properties.

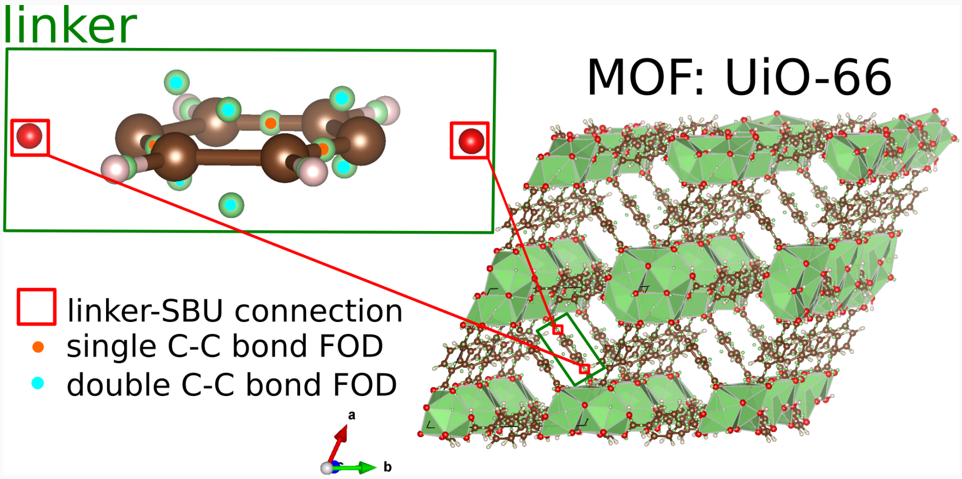

Figure 76: Thermodynamics may not only requires knowledge of nuclei related properties. Electron related properties may increase the understanding of thermodynamical processes. Local chemical environments might be described by semi-classical electron positions, which might be approximated with Fermi-orbital descriptors (FODs). The pictures shows the MOF UiO-66 with nuclei and FOD positions. The FODs were introduced using the fodMC. The inset shows the linker with a Lewis-like bonding situation, having single and double C-C bonds, and highlights the FODs connecting SBU and linker. The picture were produced by the author using VESTA and Inkscape (see Appendix A).

8

ELECTRONS AND BONDING INFORMATION

8.1 EXPLICIT TREATMENT OF SEMI-CLASSICAL ELECTRONS

List of own publications related to this section.

- S. Schwalbe, K. Trepte, L. Fiedler, A. I. Johnson, J. Kraus, T. Hahn, J. E. Peralta, K. A. Jackson, J. Kortus
  Interpretation and Automatic Generation of Fermi-Orbital Descriptors
  Journal of Computational Chemistry, 40, 2843-2857, 2019

The analysis of MOFs introduced several questions (see Section 7.7). One of these questions was concerned with whether the knowledge of semi-classical electron positions can help to automatically assign MMtypes for force fields like UFF, UFF4MOF or VMOF to increase the automation capability of such force field formulations. A possible way to answer this question is to remove MMtypes from a force field definition and include an explicit treatment of electrons within the force field itself. As introduced in Section 3.2.2, the electron force field (eFF) explicitly treats semi-classical electrons and the nuclei. The first formulation of eFF was originally implemented in the EFF code [47–49]. Within this thesis the eFF was implemented in PYTHON. The code is called PYEFF and available under Apache License 2.0. The examples calculated in Tab. 24 show that the PYEFF code works as expected.

Table 24: PYEFF: Energy benchmark against EFF code.

System	EFF code E_{tot} $[E_{\mathrm{h}}]$	PYEFF code E_{tot} $[E_{\mathrm{h}}]$
H	-0.424413	-0.424413
He	-2.300987	-2.300987
H_2	-0.955935	-0.955935
CH_4	-34.074464	-34.074464
LiH	-6.593373	-6.593373

As eFF explicitly treats electrons it is possible to calculate different spin configurations using eFF. Besides this, the total energy expression delivered by eFF can be used to describe bond dissociation. This is a first hint that this force field formulation includes bonding information as represented by MMtypes in other force field formulations. Exemplary this is shown for the H_2 dissociation curve. The PYEFF results are compared to the results to LSDA and FLO-SIC LSDA results (see Fig. 77). It is known that DFT is not able to reproduce the correct dissociation limit (e.g., for the H_2^+ molecule) in contrast to FLO-SIC as shown in the work of [94]. The PYEFF H_2 bond dissociation curve shows a qualitatively correct description of bond breaking in the stretched-bond region, in analogy to FLO-SIC LSDA. However, the energy in the current formulation of the eFF is not sufficient to reach FLO-SIC LSDA accuracy. Having these results, it is interesting to consider how physical the results are, in view of the fact that the optimal semi-classical electron positions suggested by PYEFF are used as guesses for FOD positions, which themselves can be loosely thought of as semi-classical electronic positions. Therefore,

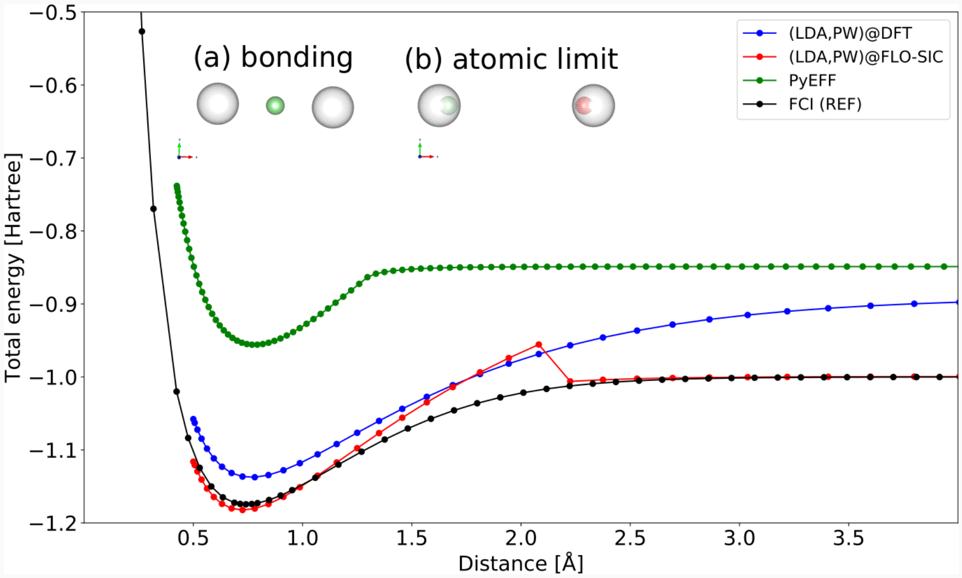

Figure 77: H_2 bond dissociation curve calculated variationally using PyEFF, DFT LSDA as well as FLO-SIC LSDA (PyFLOSIC code). The insets show the corresponding H nuclei (white) and the "semi-classical electron positions" (green and red). Inset (a) shows the electronic geometry using PyEFF at the equilibrium structure (up and down "semi-classical electrons" are at the same position) and inset (b) the electronic geometry at $r_{\text{H-H}}$ = 1.34 Å (each H atom has one "semi-classical electron"). The typical DFT error, i.e., orbitals delocalizing over the whole molecule, does not occur for PyEFF because the "semi-classical electron positions" are clearly localized at the H atoms. The FLO-SIC LSDA values using FLO-SIC optimized FODs are in excellent agreement with the exact values (full configuration interaction (FCI)) extracted from Kołos, Szalewicz, and Monkhorst [294]. PyEFF is able to deliver a qualitatively correct description of the H_2 bond dissociation. The cc-pVQZ basis set and a high quality numerical mesh (PySCF grids.level = 9) were used for the DFT and FLO-SIC calculations.

further calculations are performed, e.g., using the PyEFF code to calculate ionization potentials and electron affinities from total energy differences. The optimized PyEFF electron positions can then be used as fixed FODs to perform FLO-SIC calculations. For this purpose, ionization potentials (IPs) are calculated with PyEFF for atoms from H to C using the well established Δ-SCF method, given by

$$\mathrm{IP} = E(N-1) - E(N), \tag{115}$$

where $E(N)$ and $E(N-1)$ are the total energies of the system with N or $N-1$ electrons. In DFT and FLO-SIC, the IPs can be approximated as

$$\mathrm{IP} = -\varepsilon_{\text{HOMO}}. \tag{116}$$

The optimized PyEFF guesses for H to C are used within the FLO-SIC LSDA methodology as input (see Fig. 78). FLO-SIC LSDA using PyEFF guesses delivers atomic IPs with a remarkable accuracy, while saving significant amounts of computational time in comparison to fully optimized FOD positions.

In addition to the treatment of atoms and molecules, PyEFF is also applicable to simple solids (e.g., solid face-centered cubic (fcc) Li). The EOS of solid fcc Li has been calculated using the eFF and the PyEFF code (see Fig. 79). The initial guess for the

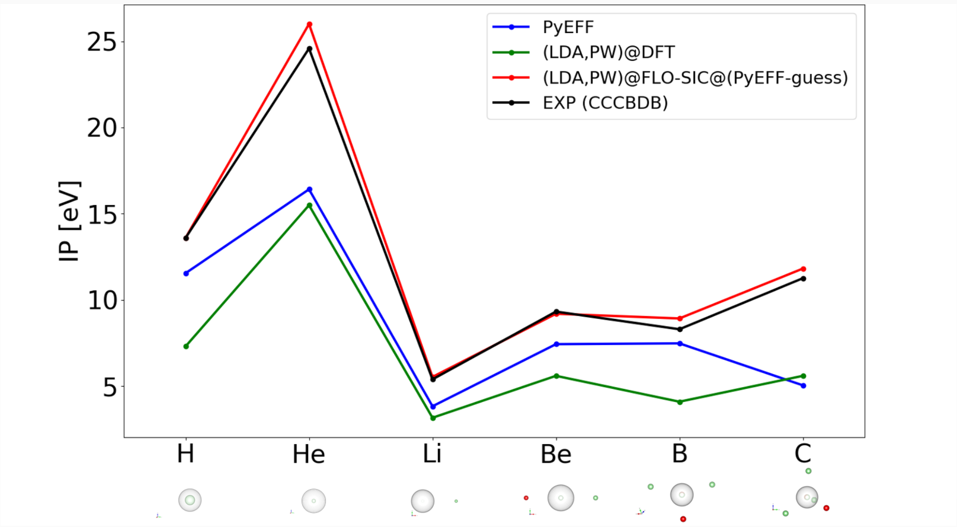

Figure 78: Ionization potentials (IPs) for atoms calculated with PyEFF, DFT LSDA and FLO-SIC LSDA using the PyEFF optimized guesses. The FLO-SIC LSDA values are in good agreement with experimental values, while the optimized PyEFF guesses deliver an enormous speed-up in comparison to fully optimized FOD positions. Experimental reference values are from the CCCBDB database [295]. The insets show the respective nuclei (white) as well as "semi-classical electron" positions (up in green and down in red). The valence electrons resemble Linnett double-quartet structures proposed by Luder [296, 297]. The cc-pVQZ basis set and a high quality numerical mesh (PySCF grids.level = 9) were used for our DFT and FLO-SIC calculations.

structures were produced using a script included in the eFF code. Both codes (i.e., the eFF and the PyEFF code) are in remarkable agreement. In detail, both codes give a bulk modulus for fcc Li of 11.8 GPa which is in reasonable agreement with experimental values (e.g., 10.43 to 13.5 GPa [298]).

Thus, for simple solids PyEFF may provide suitable FOD guesses for a future periodic FLO-SIC implementation.

The explicit treatment of electrons besides nuclei within the eFF showed promising results, as the eFF within its limitations can treat bond dissociation qualitative correctly. This indicates that bonding information is described as it is done within MMtype force fields. The usage of eFF optimized semi-classical electron positions as FOD guesses for FLO-SIC calculations delivered promising accuracy for the calculated ionization potentials. In addition to molecules, also simple solids as Li can be calculated using eFF. The results are in reasonable agreement with experimental reference values. Thus, eFF might be able to deliver suitable FOD guesses for simple solids for a periodic FLO-SIC implementation. As the scope of eFF is currently limited, in the next section the FLO-SIC method is used for further investigations. Especially the promising accuracy of ionziation potentials for fixed PyEFF optimized semi-classical electron positions used within FLO-SIC indicate that FLO-SIC can be used to calculate high quality thermodynamical data. In future, other electron force field formulations will be included in the PyEFF code, with parameters optimized using FLO-SIC reference data.

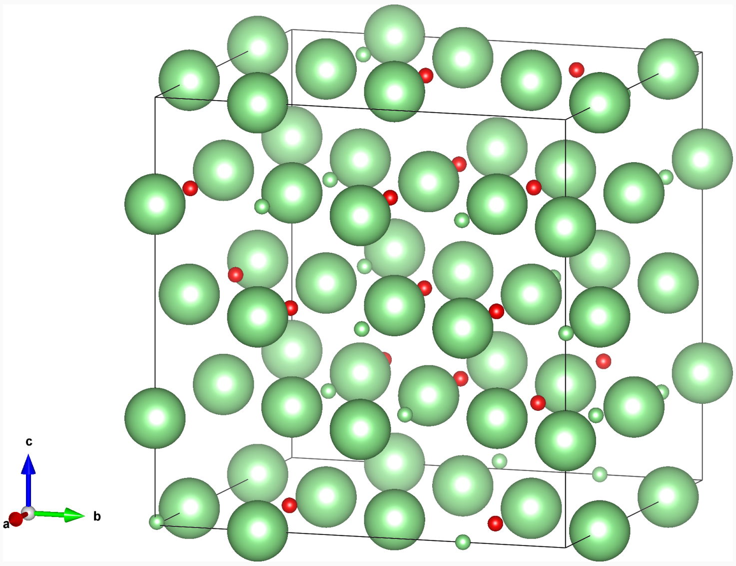

(a) Solid lithium: nuclei and electrons

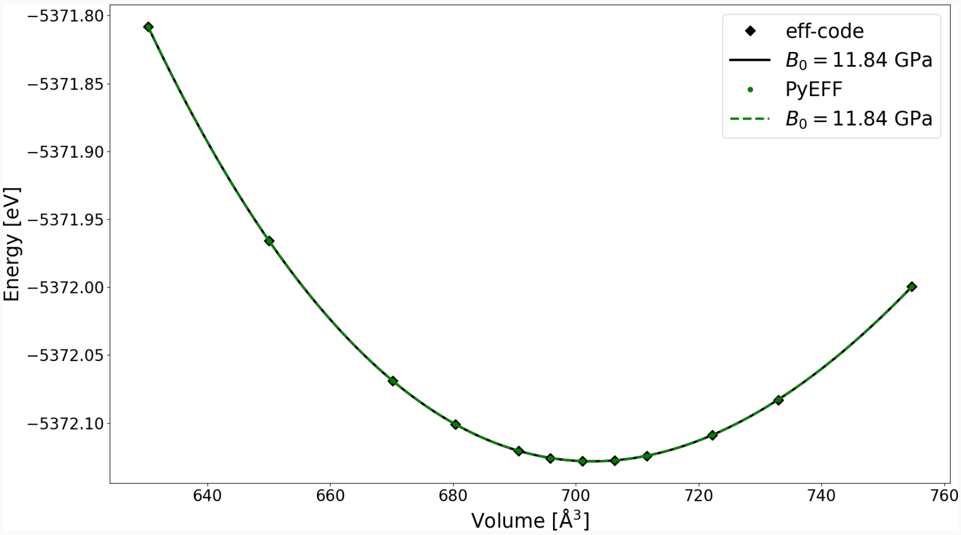

(b) EOS

Figure 79: Solid Li (fcc) nuclei and electrons is calculated with a 2x2x2 supercell, using the eFF code and PyEFF code. In both codes periodic boundary conditions (pbc) are applied. In (a) an example Li configuration (V = 701 Å^3) with nuclei (big green spheres) and electrons (small red and green spheres) is shown. In (b) the calculated values were fitted with a Vinet [133, 134] EOS. Both codes agree remarkably.

8.2 fermi-orbital descriptors: interpretation

List of own publications related to this section.

- S. Schwalbe, K. Trepte, L. Fiedler, A. I. Johnson, J. Kraus,
  T. Hahn, J. E. Peralta, K. A. Jackson, J. Kortus
  Interpretation and Automatic Generation of Fermi-Orbital Descriptors
  Journal of Computational Chemistry, 40, 2843-2857, 2019

Fermi-orbital descriptors (FODs) need to be optimized within FLO-SIC similar to nuclei positions which need to be optimized in standard DFT calculations to determine the lowest energy of the system. The number of FODs is equal to the number of electrons in the system. The set of optimized FODs for a given nuclei configuration is referred to as electronic geometry. In a general sense, FODs arrange in typical structural motifs (see Fig. 80). A simple related mathematical problem is how a fixed number of points arrange on a sphere (see Fig. 80 (a)). Such a sphere can be interpreted as a shell around a nucleus. FODs corresponding to s-like orbitals are located close to the respective nucleus. Further, 2s2p FODs arrange as tetrahedra around the nucleus on a sphere (see Fig. 80 (b)). For molecules the valence FODs show typical bonding pattern (see Fig. 80 (c)). There exist two sets of FODs corresponding each to the number of electrons in the up and down spin channel. For two nuclei forming a single bond, there exist two FODs, one of each spin channel, located at the bonding axis between the two nuclei. In the previous chapter, semi-classical electron positions optimized with PyEFF have been used within FLO-SIC to calculate ionization potentials with remarkable accuracy. The semi-classical electron positions within eFF have been identified to describe bonding information similar to MMtypes within other force fields (e.g., UFF, UFF4MOF, VMOF). Thus, in this chapter it is analyzed if FODs themselves carry similar information.

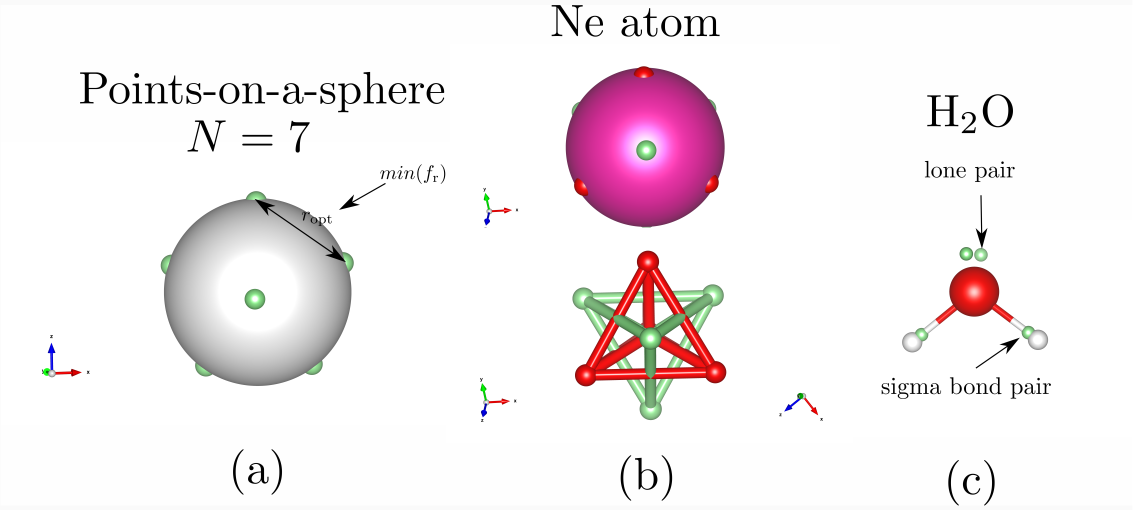

Figure 80: FOD motifs examples for (a) the model system points-on-a-sphere ($N = 7$), (b) the Ne atom (to visualize the structural motif of tetrahedra) and (c) the H_2O molecule generated with fodMC. Note: The FODs for the H_2O molecule are symmetric, therefore only one channel (green) is visible. (color code: sphere - gray, O - red, Ne - purple, H - white, up FODs - green, down FODs - red). The picture has been published as supplemental material [299].

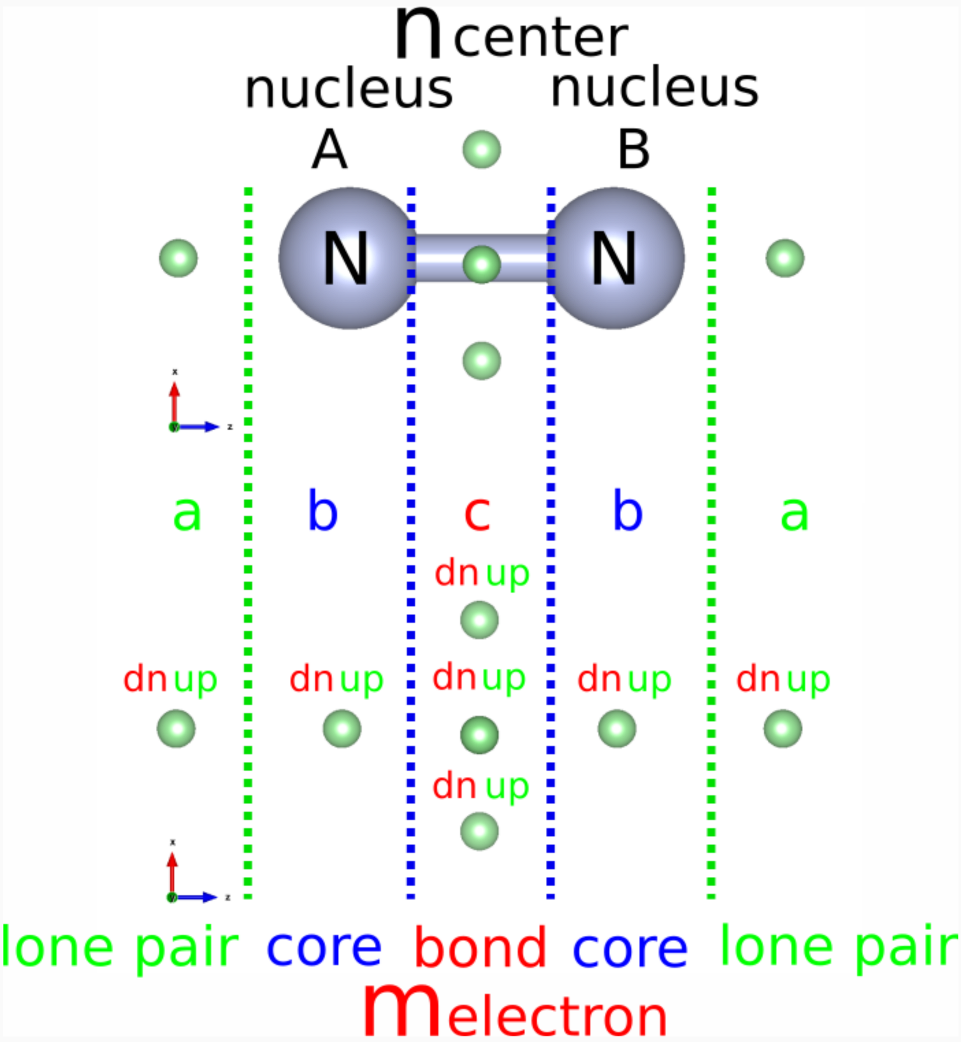

Figure 81: FOD bond order BO_{FOD} explanation. The N_2 molecule is used as an example consisting of the nuclear centers (A, B) with their respective FODs (shown as small spheres). Region **a** describes where lone pair FODs are located. These FODs are associated with one center, but are not spatially close to the nucleus. Region **b** describes the core FODs. Core FODs are spatially very close to one center, in contrast to valence FODs. Here, spatially close means that the distance of the core FODs is much smaller than the covalent radius of the corresponding atom. Region **c** describes the bond region, which contains the valence FODs of connected centers (in this case A and B). Counting all m FODs (up, down) in region **c** for a specific n center arrangement gives the FOD bond order (see Eq. (117)). For the N_2 example one counts 2 centers ($n = 2$) as well as 3 up FODs and 3 down FODs in region **c** ($m = 6$). The resulting FOD bond order is $m/n = 6/2 = 3$, which is interpreted as a triple bond. The three bond FODs form an equiliteral triangle around the bond axis. All lone pair and bond FODs form the set of valence FODs (color code: nuclei (blue), up FODs (green), down FODs (red)). Note: There are cases where up and down FODs are located at the same position, thus the resulting FODs are overlapping and only one color is seen. In the lower part of the figure, the atoms have been omitted to show the entire electronic geometry, including the core FODs. The picture has been published [299].

In the chemistry community, it is common practice to use the concept of bond order [300, 301]. Localized orbitals (e.g., NBO [302]) and other concepts [303, 304] can be used to determine bond orders in a post-processing fashion. In FLO-SIC, one can define a simple FOD bond order ($\mathrm{BO}_{\mathrm{FOD}}$) as

$$\mathrm{BO}_{\mathrm{FOD}} = m_{\mathrm{electrons}} / n_{\mathrm{centers}}, \tag{117}$$

where m is the number of electrons involved in the bond and n is the number of atoms which belong to this bond. In this context, one FOD is attributed to one electron. The $\mathrm{BO}_{\mathrm{FOD}}$ is based on counting the FODs between bonded nuclear centers. A detailed example of the FOD bond order for N_2 is given in Fig. 81. A $\mathrm{BO}_{\mathrm{FOD}}$ of 1 represents a single bond, 2 represents a double bond and 3 represents a triple bond (see Fig. 82).

A systematic analysis of recently published FLO-SIC results for the G2-1 benchmark set [94] allows to determine the FOD bond order for all molecules of this set. FLO-SIC provides essentially the same bond order as is provided by Lewis structures for systems with straightforward bonding (51 molecules in total). Exemplary, the systems ethane, ethene and ethyne are used to illustrate the agreement with the FOD bond order and common chemical bond order expectations (see Fig. 82). For four systems in the G2-1 benchmark, literature references give conflicting bond order values. All of these systems can be described as radicals, i.e., with a structure containing at least one unpaired electron. In such cases, the Lewis structure is not clear, and different sources (e.g., CCCBDB [295], PubChem [305], ChemSpider [306]) give different structures and hence different bond orders. In view of this, it is unclear which reference value should be taken for comparison. For further details the interested reader is refered to the work [299]. While FLO-SIC predicts, in agreement with Lewis theory, a bond order of 2 for the O_2 molecule, the FLO-SIC electronic geometry is different from the conventional Lewis structure. FLO-SIC predicts a double bond consisting of 3 electrons of one spin channel and one electron of the other spin channel.

Linnett double-quartet (LDQ) theory [307–310] is a nearly forgotten theory, which is recalled for this example. Whereas Lewis never included the spin in his famous model, it plays a critical role in Linnett theory. For Linnett, the octet consists of two quartets, each only containing electrons of the same spin, giving the theory its name. LDQ does not contradict Lewis theory, but rather delivers additional insights where Lewis theory fails. According to Linnett, the spatial distribution of electrons is determined by two different correlation effects [296, 308, 309]. One of them is the Pauli exclusion principle, which leads to the tendency of electrons having parallel spins to keep apart, and favors the spatial proximity of electrons with antiparallel spins [296, 308, 309]. The second correlation effect is that all electrons carry the same negative charge and therefore aim to keep apart from each other because of Coulomb repulsion. Consequently, four electrons of the same spin experience negative charge correlation on top of negative spin correlation. These electrons try to arrange themselves in a way that maximizes their distance from each other [296, 308, 309]. Geometrically, this is achieved by occupying the corners of a regular tetrahedron (i.e., 4 sp^3 orbitals) [296, 308, 309]. The overall correlation between the two spin quartets is assumed to be small, as the positive spin correlation partly cancels the negative charge correlation. Therefore, the quartets and their tetrahedra keep a certain degree of independence from each other concerning their orientations around the nuclei [296, 308, 309]. Linnett implicitly argues that a relatively

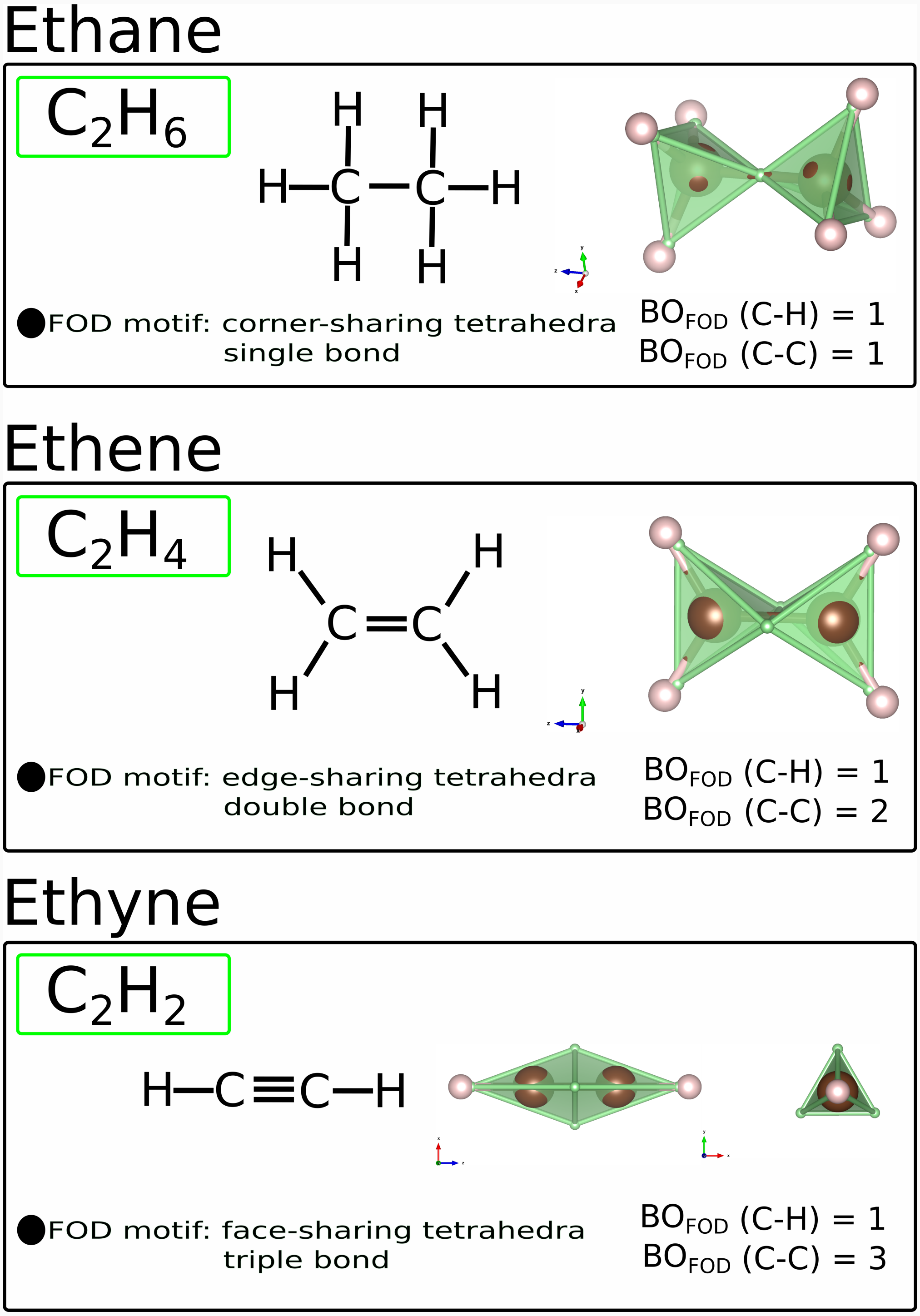

Figure 82: FOD bond order BO_{FOD} for ethane (C_2H_6), ethene (C_2H_4) and ethyne (C_2H_2). Chemical structural formula and the respective FOD configurations with the nuclear positions are shown. FOD motifs corresponding to different bonding situations are illustrated. The VESTA and the INKSCAPE programs were used for the generation of this figure (color code: C - brown, H - purple, FOD up - green, FOD down - red). Note: There are cases where up and down FODs are located at the same position, thus the resulting FODs are overlapping and only one color is seen.

small deviation from the strictly regular tetrahedra might be energetically favorable in certain cases [308, 309].

In general, LDQ structures are constructed by arranging the electron tetrahedra in a way that minimizes inter-electronic repulsion by spin and charge, while still maintaining the octet rule [296, 308, 309]. Linnett structures can be written similarly to their Lewis counterparts. In contrast to Lewis, however, each simplified Linnett structure assigns every single electron to either a dot or a cross, depending on its spin [296, 308, 309]. Linnett and Lewis structures are expected to be the same in straightforward cases like CH_4 [310], where the bonding arrangement dictates that the up and down spin quartets should be arranged in the same way. Various details and additional aspects are discussed in the bachelor thesis of J. Kraus [301].

In the following, we will call attention to analogies between Linnett's semi-classical electron positions and the arrangements of optimized FOD positions. The discussion will be qualitative in nature, with a focus on general structural motifs. Linnett proposed a LDQ structure for the O_2 molecule which is in excellent agreement with the FLO-SIC electronic geometry. For benzene and the linker of UiO-66 one can find a Lewis and a Linnett arrangement of FODs (see Fig. 83). While the local bond order of each C-C bond is different the global bond order for the aromatic ring is the same for both cases. The UiO-66 linker also has free FODs in both cases, which can be interpreted as connection points between the linker and the SBU. This is similar to the points needed by the AuToGraFS tool, but here these points represented by FODs intrinsically carry bonding information of the linker and are not chosen by hand. The theoretical foundation of these observations is discussed next.

The exchange-correlation hole is a central object in quantum chemistry or DFT related methods. The adiabatic connection formula [166] relates the exchange-correlation energy to a coupling-constant integrated exchange-correlation hole. The exchange-correlation hole visualizes electron correlation in an inhomogeneous material by measuring the change in density from its mean value at each point in a system with respect to a particular reference point. The exchange-correlation energy per particle can be interpreted as the interaction energy of the particle with its exchange-correlation hole. The exchange hole refers to a noninteracting ground state and contains only correlation due to the Pauli principle. It is often the dominant part of the total exchange-correlation hole [311]. In the case of covalent bonds, the exchange hole is not very dependent on the reference position and can be approximated by localized orbitals near the bond center [311]. This connection between chemical bonding and the exchange-correlation hole has also been discussed by Giesbertz, Leeuwen, and Barth [312]. The FODs are used to construct the Fermi orbitals, whose squares can be used to approximate the exchange-correlation hole [116, 313, 314]. This indicates that the optimized positions of the FODs in FLO-SIC may carry bonding information.

The bonding information gained from FODs might be used for an automatic assignment of MMtypes or enable the development of a universal electron force field. Having verified that FODs within FLO-SIC carry bonding information answers one of the questions raised within the MOF chapter (see Section 7.7). Another question was about whether FLO-SIC may also delivers a higher accuracy for thermodynamical properties. This question should be answered in the next section.

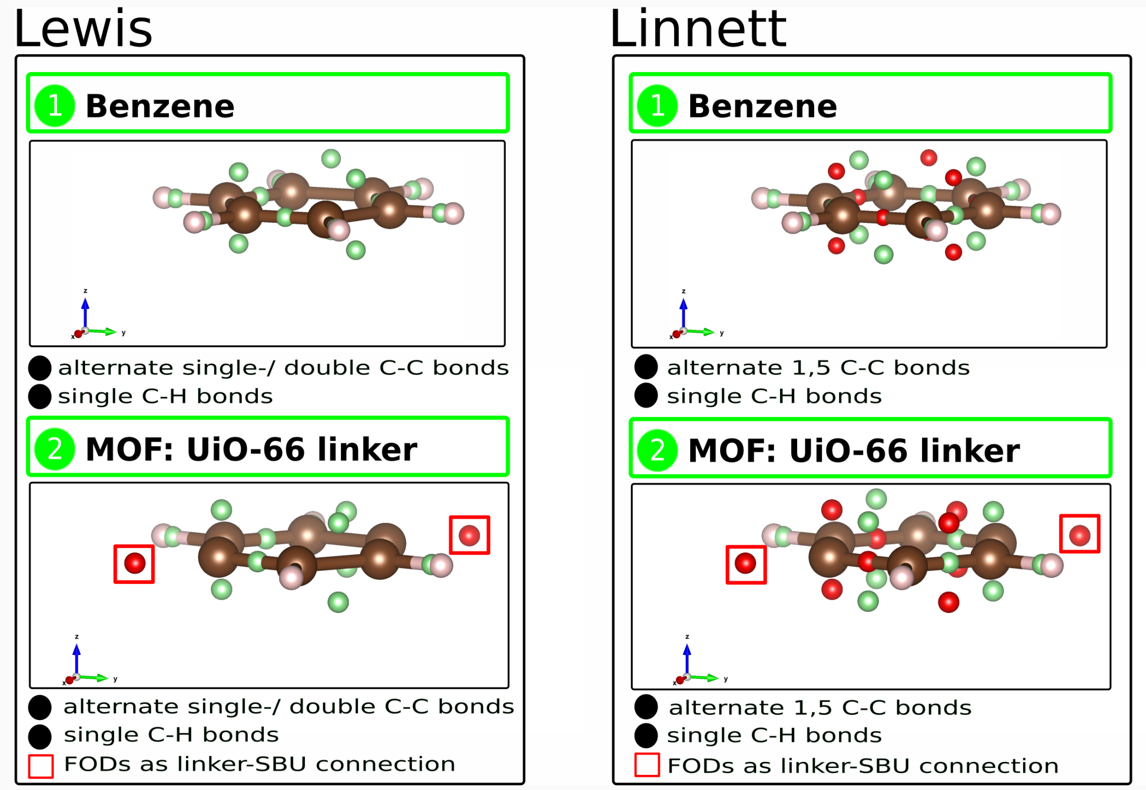

Figure 83: Comparison between FODs in benzene and the UiO-66 linker regarding Lewis theory (alternating single (up,down) and double (up,down,up,down) bonds) and Linnett theory (alternating (up,up,down) and (down,down,up) bonds). The respective FOD configurations as well the nuclear positions are shown. The VESTA and the Inkscape programs were used for the generation of this figure (color code: C - brown, H - purple, FOD up - green, FOD down - red). Note: up- and down FODs can be identically. Then, only one FOD channel (green) is visible.

9

THERMODYNAMIC PROPERTIES

9.1 IONIZATION POTENTIALS AND ENTHALPIES OF FORMATION

List of own publications related to this section.

- T. Hahn, S. Schwalbe, J. Kortus and M. R. Pederson
  Symmetry Breaking within Fermi-Löwdin Orbital Self-Interaction Corrected Density Functional Theory
  Journal of Chemical Theory and Computation, 13, 5823 - 5828, 2017
- S. Schwalbe, T. Hahn, S. Liebing, K. Trepte and J. Kortus
  Fermi-Löwdin orbital self-interaction corrected density functional theory:
  Ionization potentials and enthalpies of formation
  Journal of Computational Chemistry, 39, 2463 - 2471, 2018

The FLO-SIC method is currently only available for atoms, molecules and clusters. Thus, thermodynamical properties are calculated for the G2-1 benchmark set containing 55 molecules and respective atoms applying the G2-1 workflow (see Section 5.3). While for solids the Gibbs energy and the isobaric heat capacity are characteristic thermodynamical properties, for molecular systems ionization potentials and enthalpies of formation are essential. The G2-1 workflow was applied using the pure DFT exchange-correlation functionals without FLO-SIC and the pure DFT functionals using FLO-SIC ontop of it to calculate these properties.

The first FLO-SIC implementation was done in the NRLMOL code by Mark R. Pederson. For the first investigations a developer version of the NRLMOL code called FG-NRLMOL (here FG indicates the city Freiberg) maintained by Torsten Hahn and Mark R. Pederson was used. The G2-1 benchmark set using the G2-1 workflow (see Section 5.3) was calculated and the FLO-SIC results are compared to other SIC implementations. In detail, enthalpies of formation as well as ionization potentials have been calculated using LSDA FLO-SIC as well as PBE FLO-SIC. The results are summarized in the work of [94]. Essentially, the LSDA FLO-SIC and PBE FLO-SIC results give the same trends as other real valued SIC implementations (e.g., RSIC in ERKALE). The slight differences can be attributed to different numerical standards used in NRLMOL (e.g., density functional optimized (DFO) basis set, variational mesh). The thermochemical performance for the calculation of enthalpies of formations is only improved using LSDA. FLO-SIC and other SIC implementations applied ontop of PBE worsen the thermodynamical performance of the pure PBE functional. Ionization potentials are consistently improved while applying FLO-SIC ontop of LSDA or PBE compared to the pure functionals.

PyFLOSIC is a new implementation co-developed by the author during this thesis. PyFLOSIC is using the core functionality of the PySCF electronic structure code. Both codes (i.e., PySCF and PyFLOSIC) are available under Apache License 2.0. The development of the PyFLOSIC code started with core routines developed during the master thesis of Lenz Fiedler. The FOD optimization can be done using one of the geometry optimizers (e.g., conjugate gradient, L-BFGS [315–319] , FIRE [320], etc.) provided by ASE. The idea of this implementation was to enable FLO-SIC calculations ontop of any standard exchange-correlation functional available in the Libxc [82] library as well as to enable the usage of numerical standards used in various GTO codes (e.g., Gaussian [20], ERKALE [37], ORCA [36] etc.).

The G2-1 workflow was used with the STO3G basis set applying LSDA and PBE with FG-NRLMOL as well as PyFLOSIC to verify the new implementation. While the standard G2-1 set is designed from the objective of calculating enthalpies of formation, in many codes the energy levels are standard output. Using the negative of the highest occupied molecular orbital (HOMO) energy as approximation for the ionization potential can also be considered for comparisons. As one can see in Fig. 84, the pure DFT values as well as the FLO-SIC values are in excellent agreement for ionization potentials as well as enthalpies of formation.

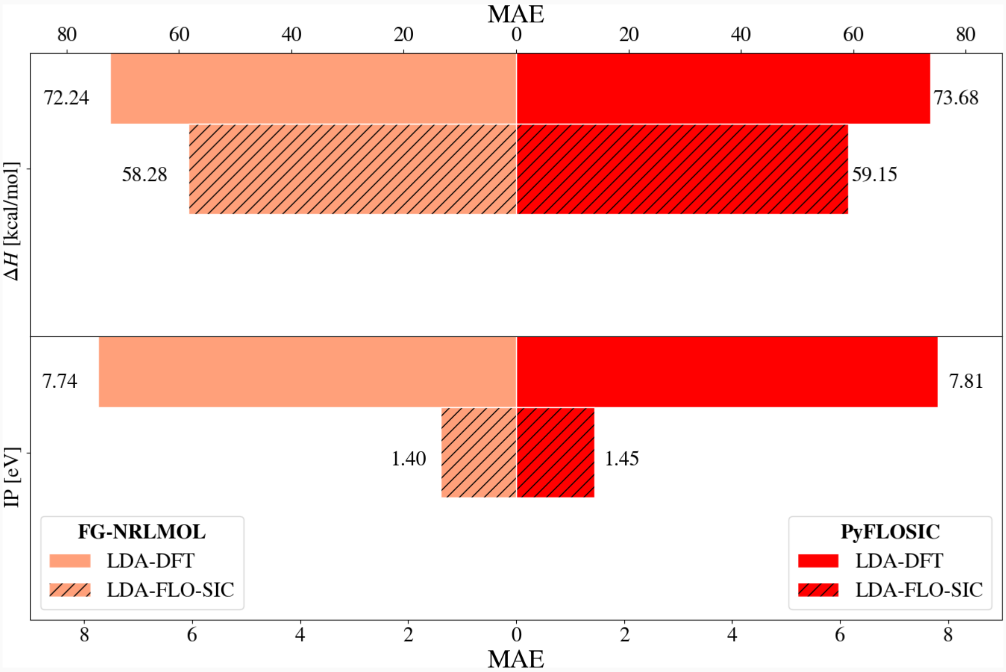

Figure 84: Mean absolute errors (MAE) for the G2-1 set using the STO3G basis set for FLO-SIC applied to the LSDA functional (labeled with LDA).

Using PyFLOSIC enables to apply FLO-SIC ontop of modern types of exchange-correlation functionals, which can be easily accessed using the Libxc library. The strongly-constrained and appropriately-normed (SCAN) functional [78] was considered for further investigations. As already mentioned earlier (see Section 3.1.4) SCAN fulfills 17 currently known constraints [78] for a semi-local functional, thus it would be interesting to see how the good thermochemical performance of this functional changes when applying FLO-SIC ontop of it. The G2-1 workflow has been performed with the density functional optimized (DFO) [35] basis set for LSDA, PBE and SCAN using PyFLOSIC (see Fig. 85). While the LSDA and PBE results can be compared to FG-NRLMOL results, SCAN results are only reliably available within PyFLOSIC. The LSDA and PBE results are in excellent agreement between both codes. FLO-SIC only improves the thermochemical performance of the LSDA functional, while decreasing the good performance of the pure PBE and SCAN functional. In contrast, FLO-SIC ontop of LSDA, PBE and SCAN clearly improves the calculated ionization potentials.

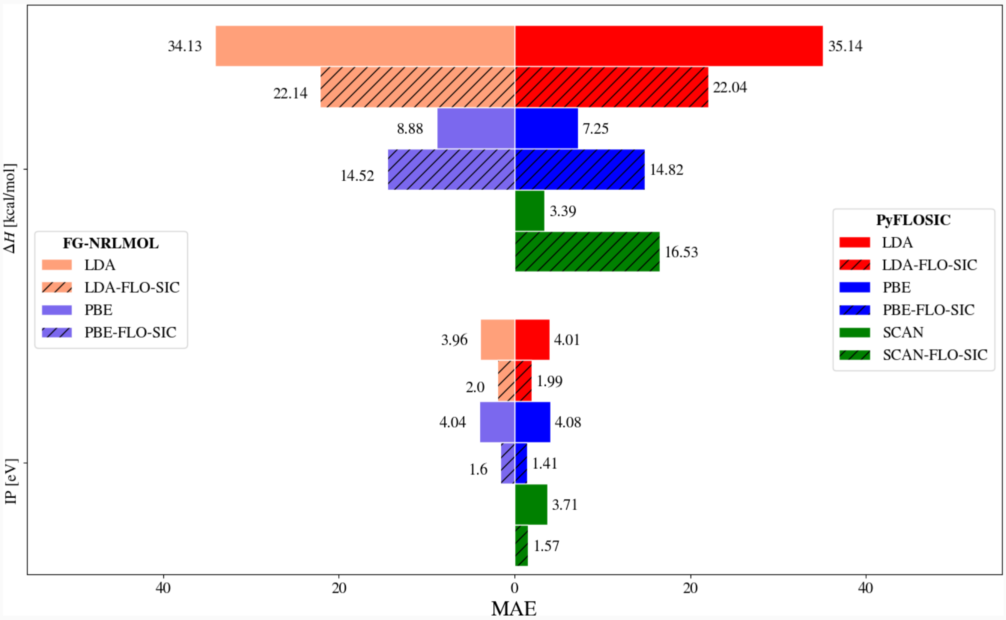

Figure 85: G2-1 errors using the density functional optimized (DFO) basis set for FLO-SIC applied to the LSDA (labeled with LDA), PBE and SCAN functional.

In summary, the FLO-SIC method ontop of LSDA improves enthalpies of formation as well as ionization potentials. FLO-SIC ontop on PBE and SCAN only improves ionization potentials and decreases the quality of the calculated enthalpies of formation. This paradox of SIC [321] is known, and various approaches of local and global scaling of SIC in many body regions [108, 322] are done in the past to overcome this challenge. Additional consideration may provide a generalization of self-interaction correction which might allow also consistent improvements of thermodynamical properties using FLO-SIC ontop of a modern exchange-correlation functional. Overcoming these challenges, which include

1. consistent improvement of properties for any exchange-correlation functional
2. solving the multiple minima issue [299, 323]
3. solving the symmetry breaking related issues [44, 323, 324]
4. overcome the large overestimation of SIC band gaps [324]

might enable to calculate systems such as MOFs with SIC to gain detailed insights in the bonding of materials as well as high numerical accuracy. Alternatively, a more universal electron force field definition may be able to provide similar bonding information with only a fraction of the numerical effort. Nevertheless, the explicit treatment of semi-classical electrons and FODs respectively allows to get further insights in thermodynamical properties (e.g., ionization potentials and enthalpies of formation) with direct structural correlations.

Part IV

SUMMARY

This last part provides the quintessence of all numerical investigations of this thesis.

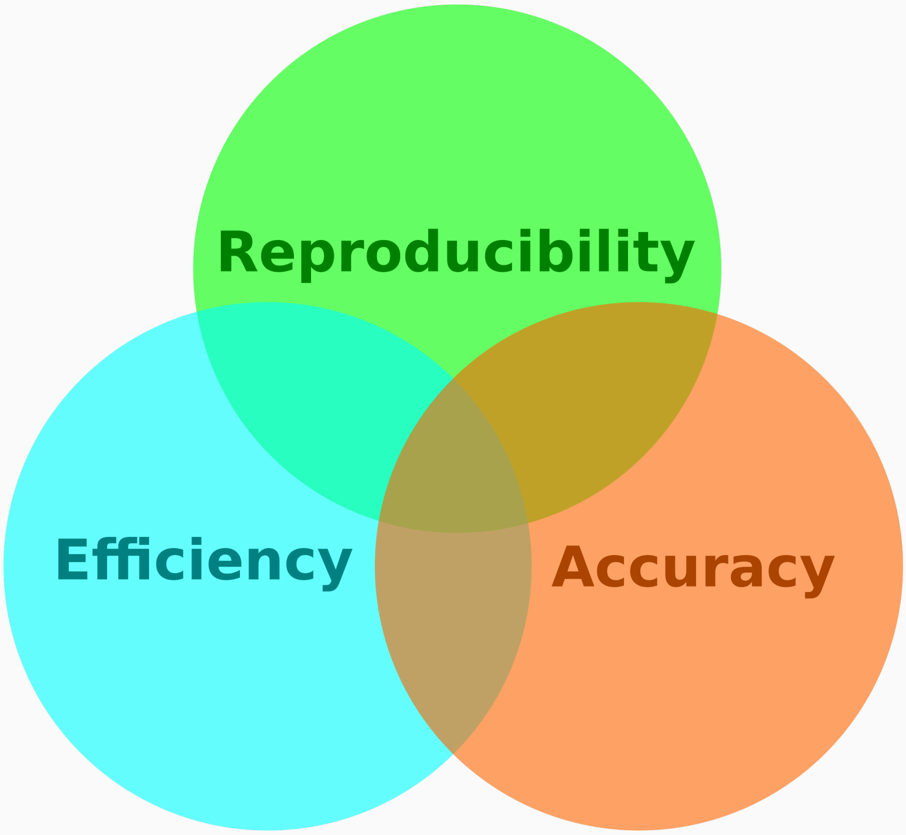

Figure 86: Three pillars of computer science.

10

CONCLUSION

This thesis is concerned with the efficient, accurate and reliable calculation of thermodynamical and related properties. In the first part of this thesis, major theoretical concepts have been introduced (see Chapter 3, Chapter 4, Chaper 5), which are applied to study the battery material class of lithium silicides (see Chapter 6) in part two of this thesis as well as metal-organic frameworks (see Chapter 7) in the third part. In the last main part of this thesis the importance and possibilities of the explicit treatment of electrons besides nuclei has been highlighted and analyzed (see Chapter 8). This thesis presented various workflows applicable to many standard DFT or FF codes to calculate mechanical, elastic and thermodynamical properties.

As highlight the C_p-MD workflow using MEAM force fields has been presented as a useful alternative to the quasi-harmonic approximation applying DFT to calculate thermodynamical properties for lithium silicides. In addition, the proposed T_c-*MD* workflow allowed to calculate melting points and with that a purely theoretical phase diagram for lithium silicides. In case of MOFs, it was highlighted that these materials need to be treated with care as small changes (e.g., pressure and temperature) may introduce significant changes (e.g., orientation of linkers or change of space group). Besides studying mechanical and elastic properties, also the porous nature of these materials has been analyzed. It was shown that the diameter of the probe significantly influences the determined accessible volume.

As the secondary building units (SBUs) of MOFs typically contain metal centers, also magnetic properties of these materials have been investigated. With the idea to treat a SBU as a single molecular magnet (SMM) the possibility of ferromagnetic building was studied by performing a screening through different combinations of transition metals in the two metal center containing building unit of DUT-8(Ni). Reproducible DFT calculations reveal possible ferromagnetic build units M1-[V,V], M1-[Fe,Fe], M1-[Fe,Co], M1-[Fe,Ni] and M1-[Fe,Cu] with M1 being the model system of the SBU.

Two force field based QHA workflows, GULP@FF-QHA and LAMMPS@FF-QHA, have been proposed and used to study thermodynamical properties of MOFs. Thermodynamical instabilities at low temperatures have been found and analyzed for UiO-67, UiO-68 and open@DUT-8(Ni). It was shown that these instabilities are sensitive to pressure changes, while the high temperature behaviour of the isobaric heat capacity from 200 - 400 K is not influenced drastically. For UiO-67 these instabilities are consistent with the ones observed in the pV curves. Thus, these thermodynamical instabilites might be a further hint for the possibility of the existence of conformers of MOFs like UiO-67.

In the last chapter the glue between reasonable accuracy and efficiency has been introduced with the explicit treat of electrons besides nuclei. Fermi-orbital descriptors (FODs), their chemical interpretation, generation and the possibility to connect the electron force field with the Fermi-Löwdin orbital self-interaction correction to speed-up calculations has been introduced. In general, computation of any kind can help to understand physical properties of various systems. Properly chosen force fields can speed up investigations enormously, where standard DFT calculations would deplete numerical resources with no additional effort (e.g., QHA using DFT for large scale systems). As shown for various cases within this thesis, an appropriate combination of different levels of theory can lead to suitable accuracy, reasonable computational time as well as efficient usage of computational resources.

Thus, this thesis concludes with a picture of reliable computer science (see Fig. 86). The numerical quality and outcome of calculations need to justify the numerical effort. This relation describes the interaction between the desired accuracy of numerical results and the efficiency in producing these numerical values using resources sustainably. Numerical results should be reproducible within the level of theory applied and parameter space used for the investigations. Double-checking results with independent implementations reduces errors and increases the reliability of numerical results. Numerical tools should not be used as black boxes, as every theory uses approximations which constrain their usage. To achieve all this science need to be open and codes freely available. Science is the response to human needs, and not about to praise singular human beings. Therefore, scientists should act and work as an open community and not against each other as individual actors.

11

OUTLOOK

Machine Learning and neural networks

In many respects machine learning techniques, i.e., neural networks, can be used in future to speed up force field, density-functional theory and even FLO-SIC calculations. For some force fields, a data set is needed which includes atomic positions, energy and most often also forces for various configurations of the systems of interest. Typically such datasets can be generated using *ab initio* molecular dynamics simulations using DFT. There exist many promising libraries

- TensorFlow [325]
- TensorMol [326]
- Symmetric gradient domain machine learning (sGDML) model [327]
- Atomistic Machine-learning package (Amp) [328]

which enable the usage of machine learning and neural networks in the field of computational physics and chemistry. Typically one uses molecular dynamics calculations to set up the data base for the neural network. One can use any set, thus the structures produced by the EOS and ELASTIC workflow proposed in this work can also be used to set up such a training data sets (see Fig. 87). The example for lithium and silicon shows that these data sets produce machine-learned potentials that give reasonable bulk moduli. The Amp code is able to work with any ASE calculator and the data base can be set up with a trajectory format. Thus, saving data in suitable format will allow the efficient re-usage for the generation of machine-learned potentials.

Further, an advantage of the Amp code is that it produces a machine-learned potential which can be used automatically within ASE. Accordingly, an accurate machine-learned potential can be used within ASE and Phonopy to efficiently calculate thermodynamical and related properties. All workflows summarized in this thesis can also be applied using the trained AMP potential.

In future it might be possible to collect several optimized FOD positions and train a neural network, possibly allowing to predict nearly perfect starting FOD guesses. This step may be limited by the amount of optimized FOD positions that are currently available. A FLO-SIC based molecular dynamics simulation might provide the possibility to obtain a suitable database for such a FOD neural network. For the simple H_2^+ molecule even 40 reference structures provide a good first machine-learned AMP FLO-SIC potential (see Fig. 88).

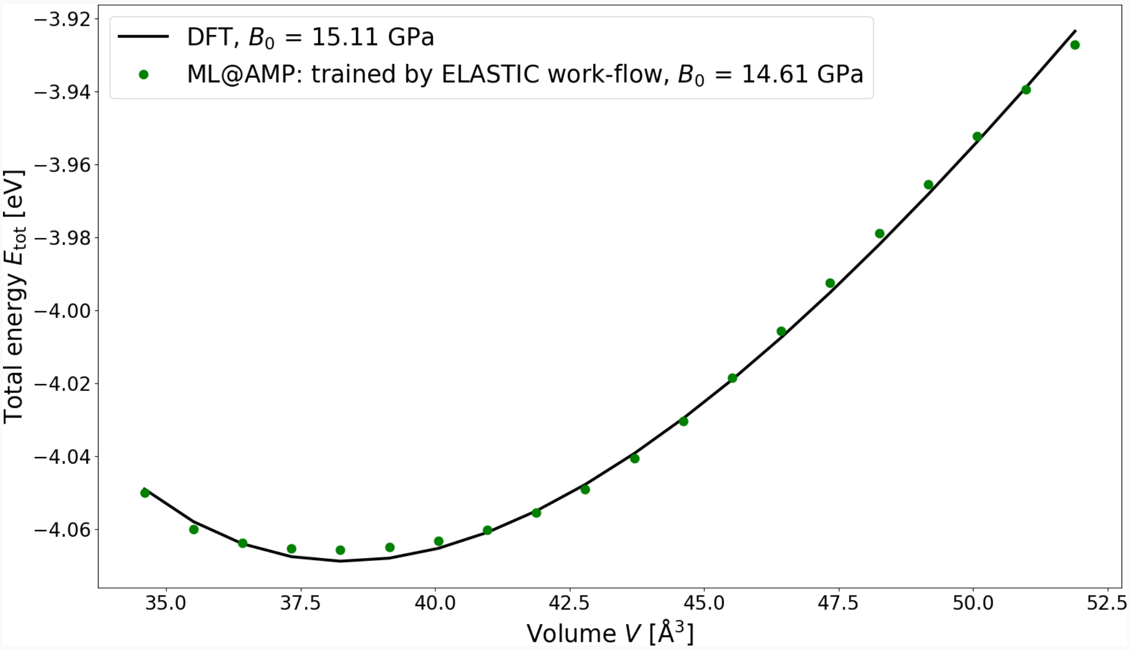

(a) Lithium

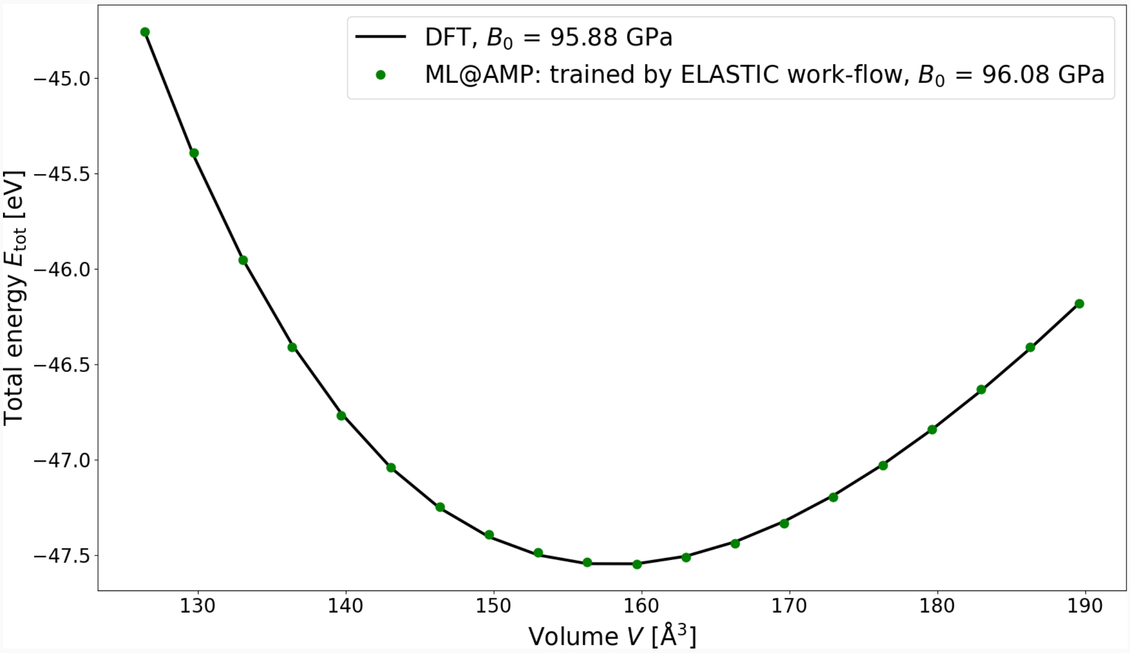

(b) Silicon

Figure 87: Simple machine-learned potentials for lithium and silicion using the AMP code. The DFT calculations were performed with GPAW (kpts = (12,12,12) and $E_{\mathrm{cut}} = 50$ Ry). The data set is generated by all structures used for the EOS workflow and the ELASTIC workflow. The total amount of structures for lithium is 125 and for silicon 35. Each data entry has the geometry and the respective energy and forces of the reference calculation. The AMP code automatically determined that some of the used entries are redundant. The picture was produced by the author using MATPLOTLIB (see Appendix A).

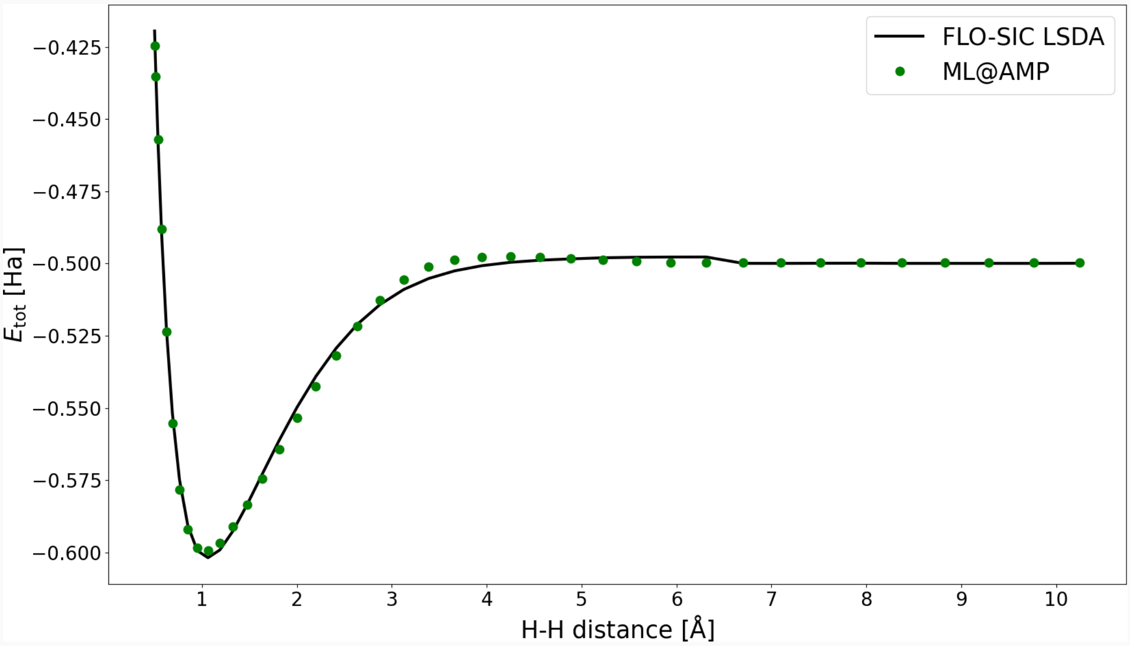

Figure 88: Simple FLO-SIC machine-learned potentials for H_2^+ using the Amp code. The FLO-SIC calculations were performed with PyFLOSIC using LSDA (LDA-PW) as exchange-correlation functional and cc-pVQZ as GTO basis set. The data set is generated by all structures used for the bond-dissociation curve. The total amount of structures for the training data set is 40. Each data entry has the geometry and the respective energy and forces of the reference calculation. The picture was produced by the author using Matplotlib (see Appendix A).

Fermi-orbital descriptor embedding theory

FODs have a clear relation to wavefunctions, which represent orbital densities or the total density itself. Thus, FODs might be a very sparse descriptor representation of the density. It has been shown within this thesis that the electron force field can provide useful starting guesses for FODs which can be used within FLO-SIC. This shows that FODs might relate different levels of theory, ranging from simple force fields to SIC and even high-quality quantum chemistry theories. Given the possibility of such an overall relation, large organic linkers may be treated with an advanced version of the electron force field and active centers like SBUs are treated with FLO-SIC. Such a FOD embedding theory may be very memory and speed efficient as well as reasonably accurate to solve large scale problems that are even bigger than battery materials or MOFs. A first implementation might be based on a similar approach as the multiase package [329] or a QMMM approach [330] combining the ASE calculators of PyFLOSIC and PyEFF for multiscale calculations.

Part V

APPENDIX

A

APPENDIX

A.1 OWN SOFTWARE CONTRIBUTIONS

PyFLOSIC The Python Fermi-Löwdin Orbital Self-Interaction Correction PyFLOSIC code [39] is a new implementation of the Fermi-Löwdin orbital self-interaction correction (FLO-SIC) using the PySCF electronic structure code as a basis. PyFLOSIC allows to apply the FLO-SIC method using any exchange-correlation functional provided by the Libxc library. The author is one of the main authors of PyFLOSIC.

- Code: `https://github.com/pyflosic/pyflosic`

PyEFF The Python Electronic Force Fied PyEFF code [299] is a new implementation of the electron force field using Python as programming language developed by the author during this thesis. While the original eFF code focuses on molecular dynamics, PyEFF concentrates on molecular statics and the usage of semi-classical electron positions within the eFF formulation as starting points for Fermi-orbital descriptors (FODs) used within FLO-SIC.

- Code: `https://github.com/pyflosic/pyeff`

PyCOM The Python Center Of Mass PyCOM routine offers the possibility to calculate FOD starting guesses from the centroids (or center of masses) of orbital densities. These guesses can be used within the FLO-SIC method. PyCOM is part of the PyFLOSIC code.

- Code: `https://github.com/pyflosic/pyflosic`

porE *and* PyPORE The package PyPORE provides a graphical user interface (GUI) for the porE code [241] developed by Kai Trepte and co-developed by the author. The PyPORE GUI offers all features of porE and enables automatic transformation of cif files to porE input. The porE Fortran files can also be used as shared library within Python which allows automated calculations of larger sets of MOFs. The PyPORE GUI is distributed with the porE code. The codes porE and PyPORE are available at github under OpenSource licence (Apache 2.0).

- Code: `https://github.com/kaitrepte/porE`

A.2 SOFTWARE

A.2.1 *Visualization tools*

Matplotlib The Matplotlib package was the general plotting tool applied within this thesis. The package is easy to use. The combination with the NumPy and SciPy packages for plotting, fitting and nicer layouts enables solutions for easy as well as rather complex tasks.

- Code: `https://github.com/matplotlib/matplotlib`

Inkscape The open source inkscape code was mainly used to combine plots produced by Matplotlib with structure visualizations given as png files. The svg file format enables to easily re-use and manipulate produced graphics.

- Code: `https://gitlab.com/inkscape/inkscape`

A.2.2 *Force field codes*

LAMMPS The Large-scale Atomic/Molecular Massively Parallel LAMMPS code is a classical molecular dynamics simulation codes designed to efficiently deal with large scale simulations on parallel computers. In combination with the latgen and phana code LAMMPS can be used for phonon calculations (fix_phonon). In addition to that, LAMMPS provides a module for the calculation of elastic constants. The Python API of LAMMPS in combination with the phonoLAMMPS package can be used to calculate phonons as well. The lammps-interface can be used to convert cif files to LAMMPS input files as well as to generate force field definition files for example for UFF.

- Code: `https://github.com/lammps/lammps`
- Support codes:
  - phana: `https://github.com/lingtikong/phana`
  - latgen: `https://github.com/lingtikong/latgen`
  - phonoLAMMPS : `https://github.com/abelcarreras/phonolammps`
  - lammps-interface: `https://github.com/peteboyd/lammps_interface`

GULP The GULP force field code has a very user-friendly and easy to understand input format and can write cif files as output. GULP offers various features for phonon calculations or can write force constants files which can be used by Phonopy.

- Code: `http://gulp.curtin.edu.au/gulp/`

RASPA2 RASPA2 is a classical simulation code offering molecular dynamics as well as Monte Carlo methods for investigations of MOFs. RASPA2 can calculate porosities, pore size distributions and adsorption isotherms. Besides its various features it offers also a Python package, which allows for a high degree of automation.

- Code: `https://github.com/numat/RASPA2`

A.2.3 *Density functional theory codes*

FG-NRLMOL FG-NRLMOL is a developer version of the NRLMOL code. This code was mainly maintained and developed in Freiberg (FG) by Torsten Hahn. The NRLMOL code is a Gaussian type orbital DFT code, which had the first implementation of the FLO-SIC method by Mark R. Pederson. The NRLMOL code offers various features like a variational mesh, a DFT optimized GTO basis set, various spectral tools (joint density of states (JDOS), IR, RAMAN) and unique features for the calculation of magnetic properties (e.g., magnetic anisotropy). Beginners need a detailed and long introduction to all specific features and the correct usage of the code.

QUANTUM ESPRESSO QUANTUM ESPRESSO (QE) is a program suite of open source computer codes for electronic-structure calculations and materials modeling. QE uses plane waves and pseudo-potentials for DFT calculations. The unified pseudo-potential format UPF is used within QE.

- Code: `https://www.quantum-espresso.org/`
- Pseudo-potentials: `http://theossrv1.epfl.ch/Main/Pseudopotentials`

GPAW For a PYTHON user the GPAW code is a really good starting point to learn an electronic structure code. GPAW can use three completely different basis set implementations, namely the finite difference, the LCAO as well as the plane wave method. Whereas one needs to learn a new input language for various electronic structure codes, the input language of GPAW is simply the PYTHON language. GPAW works hand-in-hand with ASE PYTHON package. At several instances of this thesis the developer branch of Aleksei Ivanov was used. It offers direct minimisation (dm) using an exponential transformation of molecular orbitals in LCAO mode at zero Kelvin as well as a implementation of real- and complex valued SIC.

- Code: `https://wiki.fysik.dtu.dk/gpaw/`
- Aleksei Ivanov's branch: `https://gitlab.com/gpaw/gpaw/merge_requests/470`

PYSCF The PYSCF code is written mostly in PYTHON and only uses C for numerically demanding parts. The PYSCF code uses Gaussian basis functions, for which the main author of the PYSCF code developed a very useful library. Besides DFT with all functionals available from LIBXC, PYSCF offers various quantum chemistry methods starting from Hartree-Fock (HF) over coupled cluster with single, doubles and perturbative triples (CCSD(T)) to more modern methods. All these methods use the same numerical parameter space, which allows for excellent comparisons of different methods. The class architecture of each method is brilliant and allows for an independent development of various methods with the same code. A new class can inherit methods from basic classes (e.g., UHF, UKS), while one only needs to redefine the parts which are different for a new algorithm. The PYSCF code structure allowed for the development of the PYFLOSIC code.

- Code: `https://sunqm.github.io/pyscf/`

A.2.4 *Crystal structure viewer*

VESTA VESTA is a very useful crystal structure viewer, especially for periodic solids. The VESTA code can be download and comes as a pre-compiled executable. By setting up a alias in the .bashrc or .profile file under linux, VESTA can be used as a command line tool. VESTA can also visualize 3-dimensional data (e.g., density as cube files). Besides the nice visualization, VESTA can also be used to calculate powder-diffraction spectra. VESTA has its own file format vesta, thus prepared structures can be saved and used later with the same parameters.

- Code: `http://jp-minerals.org/vesta/en/`

JMOL *and* JSMOL JMOL and JSMOL are open-source Java/Java Script viewer for chemical structures. They can be used as a command line tool. JMOL and JSMOL can read various input formats (e.g., xyz, cif, cube). An advantage of JMOL and JSMOL is that is exists in variants, which can be embedded in homepages.

- Code: `http://jmol.sourceforge.net/`

ASE GUI The command line executable ase GUI comes with the ASE PYTHON package. It is very easy to manipulate and generate molecular structures. The easy to use translation and rotation options of selected groups of atoms helped within this thesis to setup molecules which have not been available from a database or to setup FOD guesses by hand.

- Code: `https://wiki.fysik.dtu.dk/ase/`

A.2.5 *Phonon utilities*

SPGLIB *and* PHONOPY The main developer, i.e., Atsushi Togo, of the PYTHON PHONOPY package also wrote the SPGLIB library, which can be used within PYTHON. The SPGLIB packages allows the automatic analysis of the space group of a periodic solid (e.g., given as cif file). Further, SPGLIB offers the possibility to determine primitive unit cells for any given input. Especially for large systems like battery materials and MOFs the usage of primitive unit cells can enormously speed up calculations as well as save a lot of computational time. PHONOPY can use various codes as energy- and force generators (e.g., QUANTUM ESPRESSO and GPAW) to calculate phonon properties as well as thermodynamic properties within the quasi-harmonic approximation (QHA). This useful design of PHONOPY allowed the straightforward usage of PHONOPY with GULP without having a direct interface.

- Codes:

  `https://atztogo.github.io/spglib/`
  `https://atztogo.github.io/phonopy/`

A.2.6 *IO utilities*

ASE The PYTHON atomic simulation environment ASE offers a wide range of input-output tools for reading, writing or manipulating input and output files for various electronic structure (e.g., GPAW, QUANTUM ESPRESSO, PYSCF) as well as force field codes (e.g., LAMMPS and GULP). If a code is not available the design of a new calculator is quite simple. For this thesis various calculators, which at the time were not available for certain codes (e.g., GULP, EFF, PYEFF, PYFLOSIC), have been designed and used. The ASE package is the most used library for this thesis besides the standard PYTHON packages NUMPY, SCIPY and MATPLOTLIB.

- Code: `https://wiki.fysik.dtu.dk/ase/`

PWTOOLS During his PhD at the Institute of Theoretical Physics in Freiberg, Steve Schmerler started to sum up various PYTHON tools he wrote himself in the so called PWTOOLS package. This tool box is an independent package similar to the ASE package. PWTOOLS provide pre- and post-processing functionality for QUANTUM ESPRESSO, LAMMPS and CP2K. For these codes PWTOOLS offeres the possibility to analyze large molecular dynamics trajectories. For instance, PWTOOLS can efficiently calculate (radial) pair distribution functions. Further, PWTOOLS has its own implementation of the (quasi) harmonic approximation.

- Code: `https://github.com/elcorto/pwtools`

A.3 SYMMETRY ANALYZER BENCHMARK

PLATON

The PLATON codes was used as `/path_to_platon_exe/platon -o <name.>cif`. The commands executed within PLATON were

- M_1 = CALC ADDSYM ε_{ang} ε_{rot} ε_{inv} $\varepsilon_{\text{trans}}$,
- M_2 = CALC ADDSYM EXACT ε_{ang} ε_{rot} ε_{inv} $\varepsilon_{\text{trans}}$,

with M being the method used, ε_{ang} being the angle criterion in search for metrical symmetry of the lattice (internal variable name ang, PLATONs default is 1°), ε_{rot} being the distance criterion for coinciding atoms for non-inversion (pseudo)-symmetry elements (internal variable name d1, PLATONs default 0.25 Å), $\varepsilon_{\text{trans}}$ being the distance criterion for coinciding atoms for (pseudo)-inversion symmetry (internal variable name d2, PLATONs default 0.25 Å) and $\varepsilon_{\text{trans}}$ being the distance criterion for coinciding atoms for (pseudo)-translation symmetry (internal variable name d3, PLATONs default 0.25 Å). The *EXACT* option enforces that all atoms should fit for the given criteria. The authors of AFLOW-SYM [244] proposed new standard values for PLATON, where each tolerance is divided by 100. These proposed values were included in the tolerance benchmark as are various values in between these values. The results of the symmetry tolerance benchmark for the PLATON code are summarized in Tab. 25.

For further symmetry related information for the PLATON code might see

- `http://www.cryst.chem.uu.nl/spek/platon/pl000401.html`

Table 25: PLATON: Symmetry tolerance benchmark for UiO-66 and UiO-67. The minimal tolerance settings ε_{min} and the maximal tolerance settings ε_{max} used within the main part are highlighted. For ε_{rot}, ε_{inv}, and $\varepsilon_{\text{trans}}$ the value for ε_{lat} was used.

		ε_{ang}	ε_{lat}	C_1		C_2		C_3	
				UiO-66	UiO-67	UiO-66	UiO-67	UiO-66	UiO-67
	M_1	1	0.0001	$P1$	$R3$	$P1$	$R3$	$P1$	$R3$
	M_1	1	0.001	$P1$	$R3$	$P1$	$F23$	$F\bar{4}3m$	$F23$
	M_1	1	0.01	$F\bar{4}3m$	$F23$	$F\bar{4}3m$	$F23$	$F\bar{4}3m$	$F23$
	M_1	1	0.1	$F\bar{4}3m$	$F23$	$F\bar{4}3m$	$F23$	$F\bar{4}3m$	$F23$
	M_1	1	1	$Fm\bar{3}m$	$Fm\bar{3}m$	$Fm\bar{3}m$	$Fm\bar{3}m$	$Fm\bar{3}m$	$Fm\bar{3}m$
	M_1	1	0.25	$F\bar{4}3m$	$Fm\bar{3}m$	$Fm\bar{3}m$	$Fm\bar{3}m$	$Fm\bar{3}m$	$Fm\bar{3}m$
	M_1	0.01	0.0025	Im	$F23$	$P1$	$F23$	$F\bar{4}3m$	$F23$
	M_1	0.1	0.025	$F\bar{4}3m$	$F23$	$F\bar{4}3m$	$F23$	$F\bar{4}3m$	$F23$
ε_{min}	M_2	1	0.0001	$P1$	$R3$	$P1$	$R3$	$P1$	$R3$
	M_2	1	0.001	$P1$	$R3$	$P1$	$F23$	$R3m$	$F23$
	M_2	1	0.01	$P1$	$F23$	Im	$F23$	$F\bar{4}3m$	$F23$
	M_2	1	0.1	$F\bar{4}3m$	$F23$	$F\bar{4}3m$	$F23$	$F\bar{4}3m$	$F23$
	M_2	1	1	$Fm\bar{3}m$	$Fm\bar{3}m$	$Fm\bar{3}m$	$Fm\bar{3}m$	$Fm\bar{3}m$	$Fm\bar{3}m$
	M_2	0.1	0.025	$F\bar{4}3m$	$F23$	$F\bar{4}3m$	$F23$	$F\bar{4}3m$	$F23$
ε_{max}	M_2	0.3	0.25	$F\bar{4}3m$	$F23$	$F\bar{4}3m$	$F\bar{4}3m$	$F\bar{4}3m$	$F\bar{4}3m$

SPGLIB

The main tolerance in SPGLIB package is the distance tolerance $\varepsilon_{\text{symprec}}$ (internal variable name symprec) in cartesian coordinates to determine crystal symmetry. The standard value for $\varepsilon_{\text{symprec}}$ is 1e-5. An additional tolerance is the angle tolerance ε_{ang} (internal variable name angle_tolerance) between basis vectors. This tolerance is denoted as experimental feature, and normally it is not recommended to use. The standard value for ε_{ang} is -1.0. For the symmetry benchmark the angle tolerance has been fixed and the distance tolerance was varied (see Tab. 26). A PYTHON script called analyze_symmetry.py utilizing the SPGLIB library was used to perform the symmetry benchmark.

For further information for the SPGLIB package see

- `https://atztogo.github.io/spglib/`

Table 26: SPGLIB: Symmetry tolerance benchmark for UiO-66 and UiO-67. The minimal tolerance settings ε_{min} and the maximal tolerance settings ε_{max} used within the main part are highlighted.

	ε_{ang}	$\varepsilon_{\text{symprec}}$	C_1 UiO-66	C_1 UiO-67	C_2 UiO-66	C_2 UiO-67	C_3 UiO-66	C_3 UiO-67
ε_{min}	1.00000	0.00001	$P1$	$R3$	$P1$	$R3$	$P1$	$R3$
	1.00000	0.00010	$P1$	$R3$	$P1$	$R3$	$P1$	$R3$
	1.00000	0.00100	$P1$	$R3$	$P1$	$R3$	$R\bar{3}m$	$R3$
	1.00000	0.01000	$P\bar{1}$	$F23$	$P\bar{1}$	$F23$	$F\bar{4}3m$	$F23$
	1.00000	0.10000	$F\bar{4}3m$	$F23$	$F\bar{4}3m$	$F23$	$F\bar{4}3m$	$F23$
	1.00000	0.25000	$F\bar{4}3m$	$F23$	$F\bar{4}3m$	$F23$	$F\bar{4}3m$	$F23$
ε_{min}	1.00000	1.00000	$F\bar{4}3m$	$F23$	$F\bar{4}3m$	$F\bar{4}3m$	$F\bar{4}3m$	$F\bar{4}3m$

FINDSYM

The FINDSYM package [243] allows the variation of various tolerance values, the lattice tolerance $\varepsilon_{\mathrm{lat}}$ (internal variable name latticeTolerance), the atomic position tolerance $\varepsilon_{\mathrm{pos}}$ (internal variable name atomicPositionTolerance) and the respective maximal value $\varepsilon_{\mathrm{posmax}}$ (internal variable name atomicPositionMaxTolerance) as well as the occupation tolerance $\varepsilon_{\mathrm{occ}}$ (internal variable name occupationTolerance). The online tool of FINDSYM further allows to adjust other tolerances. For the symmetry benchmark the standard values of FINDSYM were chosen to be the values for minimal tolerance $\varepsilon_{\mathrm{min}}$. These values have been systematically adjusted (see Tab. 27). For the FINDSYM package a Python wrapper called pyfindsym.py was written, which allows to perform the symmetry benchmark automatically for a given cif file.

For further information for the FINDSYM tool might see

- `https://stokes.byu.edu/iso/findsym.php`

Table 27: FINDSYM: Symmetry tolerance benchmark for UiO-66 and UiO-67. The minimal tolerance settings $\varepsilon_{\mathrm{min}}$ and the maximal tolerance settings $\varepsilon_{\mathrm{max}}$ used within the main part are highlighted. Besides for the standard values of FINDSYM ($\varepsilon_{\mathrm{occ}}$ = 0.001, $\varepsilon_{\mathrm{posmax}}$ = 0.33, $\varepsilon_{\mathrm{pos}}$ = 0.001 , $\varepsilon_{\mathrm{lat}}$ = 1e-05), $\varepsilon_{\mathrm{posmax}}$ was set to the value of $\varepsilon_{\mathrm{pos}}$ and $\varepsilon_{\mathrm{occ}}$ to the value of $\varepsilon_{\mathrm{lat}}$. Thus, only the tolerances $\varepsilon_{\mathrm{pos}}$ and $\varepsilon_{\mathrm{lat}}$ are shown.

			C_1		C_2		C_3	
	$\varepsilon_{\mathrm{pos}}$	$\varepsilon_{\mathrm{lat}}$	UiO-66	UiO-67	UiO-66	UiO-67	UiO-66	UiO-67
$\varepsilon_{\mathrm{min}}$	0.001	1e-05	$P1$	$R3$	$P1$	$R3$	$P1$	$R3$
	0.001	0.0001	$P1$	$R3$	$P1$	$R3$	$R3m$	$R3$
	0.01	0.001	$P1$	-	$P1$	$F23$	$F\bar{4}3m$	$F23$
	0.1	0.01	$F\bar{4}3m$	$F23$	$F\bar{4}3m$	$F23$	$F\bar{4}3m$	$F23$
	1	0.1	$F\bar{4}3m$	$F23$	$F\bar{4}3m$	$F\bar{4}3m$	$F\bar{4}3m$	$F\bar{4}3m$
$\varepsilon_{\mathrm{max}}$	1	1	$F\bar{4}3m$	$F23$	$F\bar{4}3m$	$F\bar{4}3m$	$F\bar{4}3m$	$F\bar{4}3m$

AFLOW-SYM

The AFLOW-SYM package [244] has only one generic tolerance $\varepsilon_{\mathrm{sg}}$. The authors of the AFLOW-SYM package [244] also proposed different tolerance values for other symmetry codes (SPGLIB, FINDSYM and PLATON). For the investigations performed within this thesis also these alternative tolerance values provide not the optimal tolerance values. However, also the authors of the AFLOW-SYM package [244] found that the PLATON standard values need to be decreased (they proposed to divide them by 100 each), which is in perfect agreement with the observations of this thesis. For the symmetry benchmark also the tolerance $\varepsilon_{\mathrm{sg}}$ has been varied systematically (see Tab. 28). The AFLOW-SYM package comes with its own PYTHON API, which has been adjusted to perform the symmetry benchmark automatically starting from a cif file.

For further information for the AFLOW-SYM package might see

- `http://materials.duke.edu/awrapper.html`

Table 28: AFLOW-SYM: Symmetry tolerance benchmark for UiO-66 and UiO-67. The minimal tolerance settings $\varepsilon_{\mathrm{min}}$ and the maximal tolerance settings $\varepsilon_{\mathrm{max}}$ used within the main part are highlighted.

	$\varepsilon_{\mathrm{sg}}$	C_1		C_2		C_3	
		UiO-66	UiO-67	UiO-66	UiO-67	UiO-66	UiO-67
$\varepsilon_{\mathrm{min}}$	0.00001	$P1$	$R3$	$P1$	$R3$	$P1$	$R3$
	0.00010	$P1$	$R3$	$P1$	$R3$	$P1$	$R3$
	0.00100	$P1$	$R3$	$P1$	$R3$	$R3m$	$R3$
	0.01000	$P1$	$F23$	$P1$	$F23$	$F\bar{4}3m$	$F23$
$\varepsilon_{\mathrm{max}}$	0.10000	$F\bar{4}3m$	$F23$	$F\bar{4}3m$	$F23$	$F\bar{4}3m$	$F23$

Conclusion

The symmetry benchmark test showed that the codes FINDSYM, Spglib, AFLOW-SYM provide very similar trends varying the tolerances using similar magnitudes. For PLATON only lower tolerances (dividing all lattice related tolerances, $\varepsilon_{\mathrm{rot}}$, $\varepsilon_{\mathrm{inv}}$, and $\varepsilon_{\mathrm{trans}}$, by a factor of 10) provide consistent results with the other tested symmetry codes. In future, the standard values of the discussed symmetry codes (PLATON, FINDSYM, Spglib, AFLOW-SYM) might be optimized using machine learning strategies and a well balanced training data base as well as a systematic comparison of all codes.

BIBLIOGRAPHY

[1] D. R. Hartree. "The Wave Mechanics of an Atom with a Non-Coulomb Central Field. Part I. Theory and Methods." In: *Math. Proc. Camb. Philos. Soc.* 24 (1928), pp. 89–110 (cit. on p. 1).

[2] V. Fock. "Näherungsmethode zur Lösung des quantenmechanischen Mehrkörperproblems." In: *Z. Phys.* 61.1 (1930), pp. 126–148 (cit. on p. 1).

[3] W. Kolos and L. Wolniewicz. "Improved Theoretical Ground-State Energy of the Hydrogen Molecule." In: *J. Chem. Phys.* 49.1 (1968), pp. 404–410 (cit. on p. 1).

[4] P. Hohenberg and W. Kohn. "Inhomogeneous Electron Gas." In: *Phys. Rev.* 136 (3B 1964), B864–B871 (cit. on pp. 1, 12).

[5] W. Kohn and L. J. Sham. "Self-Consistent Equations Including Exchange and Correlation Effects." In: *Phys. Rev.* 140 (4A 1965), A1133–A1138 (cit. on pp. 1, 12).

[6] C. D. Sherrill. "Frontiers in electronic structure theory." In: *J. Chem. Phys.* 132.11 (2010), p. 110902 (cit. on p. 1).

[7] K. Burke. "Perspective on density functional theory." In: *J. Chem. Phys.* 136.15 (2012), p. 150901 (cit. on p. 1).

[8] P. G. Boyd et al. "Force-field prediction of materials properties in metal-organic frameworks." In: *J. Phys. Chem. Lett.* 8.2 (2017), pp. 357–363 (cit. on pp. 1, 21, 37, 47, 88, 104).

[9] J. K. Bristow, D. Tiana, and A. Walsh. "Transferable force field for metal–organic frameworks from first-principles: BTW-FF." In: *J. Chem. Theory Comput.* 10.10 (2014), pp. 4644–4652 (cit. on pp. 1, 37, 87, 100).

[10] S. Bureekaew et al. "MOF-FF–A flexible first-principles derived force field for metal-organic frameworks." In: *Phys. Status Solidi B* 250.6 (2013), pp. 1128–1141 (cit. on p. 1).

[11] J. K. Bristow et al. "A general forcefield for accurate phonon properties of metal–organic frameworks." In: *Phys. Chem. Chem. Phys.* 18.42 (2016), pp. 29316–29329 (cit. on pp. 1, 37, 100, 102, 104, 105).

[12] G. Ceder et al. "Recharging lithium battery research with first-principles methods." In: *MRS Bull.* 36.3 (2011), pp. 185–191 (cit. on p. 1).

[13] F.-X. Coudert and A. H. Fuchs. "Computational characterization and prediction of metal–organic framework properties." In: *Coord. Chem. Rev.* 307 (2016), pp. 211–236 (cit. on p. 1).

[14] J.-R. Li, R. J. Kuppler, and H.-C. Zhou. "Selective gas adsorption and separation in metal-organic frameworks." In: *Chem. Soc. Rev.* 38 (5 2009), pp. 1477–1504 (cit. on p. 1).

[15] F. X. L. i Xamena et al. "MOFs as catalysts: Activity, reusability and shape-selectivity of a Pd-containing MOF." In: *J. Catal.* 250.2 (2007), pp. 294–298 (cit. on p. 1).

[16] J. Lei et al. “Design and sensing applications of metal–organic framework composites.” In: *TrAC, Trends Anal. Chem.* 58 (2014). New Nanobiosensing Techniques and Bioanalysis, pp. 71–78 (cit. on p. 1).

[17] S. M. Cohen. “Modifying MOFs: new chemistry, new materials.” In: *Chem. Sci.* 1.1 (2010), pp. 32–36 (cit. on p. 1).

[18] T. D. Bennett and A. K. Cheetham. “Amorphous metal–organic frameworks.” In: *Acc. Chem. Res.* 47.5 (2014), pp. 1555–1562 (cit. on p. 1).

[19] V. Strobel. *Pold87/academic-keyword-occurrence: First release*. Apr. 2018. DOI: `10.5281/zenodo.1218409`. URL: `https://doi.org/10.5281/zenodo.1218409` (cit. on p. 1).

[20] M. Frisch et al. “Gaussian 09, revision A. 02, vol 19. Gaussian.” In: *Inc., Wallingford* (2009), pp. 227–238 (cit. on pp. 3, 7, 142).

[21] G. Kresse and J. Hafner. “Ab initio molecular dynamics for liquid metals.” In: *Phys. Rev. B* 47.1 (1993), p. 558 (cit. on pp. 3, 7).

[22] G. Kresse and J. Furthmüller. “Efficient iterative schemes for ab initio total-energy calculations using a plane-wave basis set.” In: *Phys. Rev. B* 54.16 (1996), p. 11169 (cit. on pp. 3, 7).

[23] G. Kresse and D. Joubert. “From ultrasoft pseudopotentials to the projector augmented-wave method.” In: *Phys. Rev. B* 59.3 (1999), p. 1758 (cit. on pp. 3, 7).

[24] J. Hafner. “Ab-initio simulations of materials using VASP: Density-functional theory and beyond.” In: *J. Comput. Chem.* 29.13 (2008), pp. 2044–2078 (cit. on pp. 3, 7).

[25] K. Schwarz, P. Blaha, and S. Trickey. “Electronic structure of solids with WIEN2k.” In: *Mol. Phys.* 108.21-23 (2010), pp. 3147–3166 (cit. on pp. 3, 7).

[26] P. Giannozzi et al. “QUANTUM ESPRESSO: a modular and open-source software project for quantum simulations of materials.” In: *J. Phys.: Condens. Matter* 21.39 (2009), p. 395502 (cit. on pp. 3, 7, 122).

[27] J. Enkovaara et al. “Electronic structure calculations with GPAW: a real-space implementation of the projector augmented-wave method.” In: *J. Phys.: Condens. Matter* 22.25 (2010), p. 253202 (cit. on pp. 3, 7, 122).

[28] J. Hutter et al. “cp2k: atomistic simulations of condensed matter systems.” In: *Wiley Interdiscip. Rev. Comput. Mol. Sci.* 4.1 (2014), pp. 15–25 (cit. on p. 3).

[29] J. Kortus and M. R. Pederson. “Magnetic and vibrational properties of the uniaxial $Fe_{13}O_8$ cluster.” In: *Phys. Rev. B* 62.9 (2000), pp. 5755–5759 (cit. on pp. 3, 24, 122).

[30] M. R. Pederson, K. A. Jackson, and W. E. Pickett. “Local-density-approximation-based simulations of hydrocarbon interactions with applications to diamond chemical vapor deposition.” In: *Phys. Rev. B* 44.8 (1991), pp. 3891–3899 (cit. on pp. 3, 24, 122).

[31] M. R. Pederson et al. “Strategies for massively parallel local-orbital-based electronic structure methods.” In: *Phys. Status Solidi (b)* 217.1 (2000), pp. 197–218 (cit. on pp. 3, 24, 122).

[32] M. R. Pederson and K. A. Jackson. "Pseudoenergies for simulations on metallic systems." In: *Phys. Rev. B* 43.9 (1991), pp. 7312–7315 (cit. on pp. 3, 24, 122).

[33] M. R. Pederson and K. A. Jackson. "Variational mesh for quantum-mechanical simulations." In: *Phys. Rev. B* 41.11 (1990), pp. 7453–7461 (cit. on pp. 3, 24, 122).

[34] J. P. Perdew et al. "Atoms, molecules, solids, and surfaces: Applications of the generalized gradient approximation for exchange and correlation." In: *Phys. Rev. B* 46.11 (1992), pp. 6671–6687 (cit. on pp. 3, 24, 122).

[35] D. Porezag. "Development of Ab-Initio and Approximate Density Functional Methods and their Application to Complex Fullerene Systems." PhD thesis. TU Chemnitz, Fakultät für Naturwissenschaften, 1997. URL: `http://archiv.tu-chemnitz.de/pub/1997/0025` (cit. on pp. 3, 24, 122, 123, 142).

[36] F. Neese. "The ORCA program system." In: *Wiley Interdiscip. Rev. Comput. Mol. Sci.* 2.1 (2012), pp. 73–78 (cit. on pp. 3, 122, 142).

[37] J. Lehtola et al. "ERKALE - A flexible program package for X-ray properties of atoms and molecules." In: *J. Comput. Chem.* 33.18 (2012), pp. 1572–1585 (cit. on pp. 3, 7, 8, 142).

[38] Q. Sun et al. "PySCF: the Python-based simulations of chemistry framework." In: *Wiley Interdiscip. Rev. Comput. Mol. Sci.* 8.1 (2018), e1340 (cit. on pp. 3, 7).

[39] S. Schwalbe et al. "PyFLOSIC: Python-based Fermi–Löwdin orbital self-interaction correction." In: *The Journal of Chemical Physics* 153.8 (2020), p. 084104 (cit. on pp. 3, 24, 155).

[40] M. R. Pederson. "Fermi orbital derivatives in self-interaction corrected density functional theory: Applications to closed shell atoms." In: *J. Chem. Phys.* 142.6 (2015), p. 064112 (cit. on pp. 3, 17, 21).

[41] M. R. Pederson, A. Ruzsinszky, and J. P. Perdew. "Communication: Self-interaction correction with unitary invariance in density functional theory." In: *J. Chem. Phys.* 140.12 (2014), p. 121103 (cit. on pp. 3, 17, 21).

[42] Z.-h. Yang, M. R. Pederson, and J. P. Perdew. "Full self-consistency in the Fermi-orbital self-interaction correction." In: *Phys. Rev. A* 95 (5 2017), p. 052505 (cit. on pp. 3, 17).

[43] T. Hahn et al. "Fermi orbital self-interaction corrected electronic structure of molecules beyond local density approximation." In: *J. Chem. Phys.* 143.22 (2015), p. 224104 (cit. on pp. 3, 17).

[44] T. Hahn et al. "Symmetry Breaking within Fermi–Löwdin Orbital Self-Interaction Corrected Density Functional Theory." In: *J. Chem. Theory Comput.* 13.12 (2017), pp. 5823–5828 (cit. on pp. 3, 17, 143).

[45] S. Plimpton, P. Crozier, and A. Thompson. "LAMMPS-large-scale atomic/molecular massively parallel simulator." In: *Sandia National Laboratories* 18 (2007), p. 43 (cit. on pp. 3, 47).

[46] J. D. Gale. "GULP: A computer program for the symmetry-adapted simulation of solids." In: *J. Chem. Soc., Faraday Trans.* 93.4 (1997), pp. 629–637 (cit. on pp. 3, 47).

[47] J. T. Su and W. A. Goddard. “Excited electron dynamics modeling of warm dense matter.” In: *Phys. Rev. Lett.* 99.18 (2007), p. 185003 (cit. on pp. 3, 22, 24, 131).

[48] J. T. Su and W. A. Goddard. “Mechanisms of Auger-induced chemistry derived from wave packet dynamics.” In: *Proc. Natl. Acad. Sci.* 106.4 (2009), pp. 1001–1005 (cit. on pp. 3, 22, 24, 131).

[49] J. T. Su. “An electron force field for simulating large scale excited electron dynamics. Dissertation (Ph.D.), California Institute of Technology.” PhD thesis. 2007. URL: `http://resolver.caltech.edu/CaltechETD:etd-05032007-151410` (cit. on pp. 3, 22, 24, 131).

[50] J. C. Slater. “Atomic shielding constants.” In: *Phys. Rev.* 36.1 (1930), p. 57 (cit. on p. 7).

[51] P. M. Gill. “Molecular integrals over Gaussian basis functions.” In: *Advances in quantum chemistry*. Vol. 25. Elsevier, 1994, pp. 141–205 (cit. on p. 7).

[52] H. B. Schlegel and M. J. Frisch. “Transformation between Cartesian and pure spherical harmonic Gaussians.” In: *Int. J. Quantum Chem.* 54.2 (1995), pp. 83–87 (cit. on p. 7).

[53] *The Elk FP-LAPW Code, http://elk.sourceforge.net/.* (Cit. on p. 7).

[54] K. L. Schuchardt et al. “Basis set exchange: a community database for computational sciences.” In: *J. Chem. Inf. Model.* 47.3 (2007), pp. 1045–1052 (cit. on p. 8).

[55] S. Obara and A. Saika. “Efficient recursive computation of molecular integrals over Cartesian Gaussian functions.” In: *J. Chem. Phys.* 84.7 (1986), pp. 3963–3974 (cit. on p. 8).

[56] M. Head-Gordon and J. A. Pople. “A method for two-electron Gaussian integral and integral derivative evaluation using recurrence relations.” In: *J. Chem. Phys.* 89.9 (1988), pp. 5777–5786 (cit. on p. 8).

[57] E. F. Valeev. *Libint - efficient computation of quantum mechanical matrix elements over Gaussian basis sets, https://github.com/evaleev/libint* (cit. on p. 8).

[58] Q. Sun. “Libcint: An efficient general integral library for Gaussian basis functions.” In: *J. Comput. Chem.* 36.22 (2015), pp. 1664–1671 (cit. on p. 8).

[59] T. Helgaker, P. Jorgensen, and J. Olsen. *Molecular electronic-structure theory*. John Wiley & Sons, 2014 (cit. on p. 8).

[60] T. Kato. “On the eigenfunctions of many-particle systems in quantum mechanics.” In: *Commun. Pure Appl. Math.* 10.2 (1957), pp. 151–177 (cit. on p. 8).

[61] P. Pulay. “Ab initio calculation of force constants and equilibrium geometries in polyatomic molecules.” In: *Mol. Phys.* 17 (1969), pp. 197–204 (cit. on p. 8).

[62] R. Feynman. “Forces in Molecules.” In: *Phys. Rev.* 56 (1939), pp. 340–343 (cit. on p. 8).

[63] S. F. Boys and F. d. Bernardi. “The calculation of small molecular interactions by the differences of separate total energies. Some procedures with reduced errors.” In: *Mol. Phys.* 19.4 (1970), pp. 553–566 (cit. on p. 8).

[64] C. Møller and M. S. Plesset. “Note on an approximation treatment for many-electron systems.” In: *Phys. Rev.* 46.7 (1934), p. 618 (cit. on pp. 8, 12).

[65] J. Čížek. “On the Correlation Problem in Atomic and Molecular Systems. Calculation of Wavefunction Components in Ursell-Type Expansion Using Quantum-Field Theoretical Methods.” In: *J. Chem. Phys.* 45 (1966), pp. 4256–4266 (cit. on pp. 8, 12).

[66] D. J. Singh and L. Nordstrom. *Planewaves, Pseudopotentials, and the LAPW method*. Springer Science & Business Media, 2006 (cit. on p. 9).

[67] C. C. J. Roothaan. “New developments in molecular orbital theory.” In: *Rev. Mod. Phys.* 23.2 (1951), p. 69 (cit. on pp. 11, 17).

[68] J. A. Pople and R. K. Nesbet. “Self-consistent orbitals for radicals.” In: *J. Chem. Phys.* 22.3 (1954), pp. 571–572 (cit. on pp. 11, 17).

[69] C. Kollmar. “A simplified approach to the density functional theory of molecules.” In: *Z. Naturforsch. A* 54.2 (1999), pp. 101–109 (cit. on p. 11).

[70] R. A. Friesner. “Ab initio quantum chemistry: Methodology and applications.” In: *Proc. Natl. Acad. Sci.* 102.19 (2005), pp. 6648–6653 (cit. on p. 12).

[71] C. Ochsenfeld, J. Kussmann, and D. S. Lambrecht. “Linear-scaling methods in quantum chemistry.” In: *Rev. Comp. Ch.* 23 (2007), p. 1 (cit. on p. 12).

[72] A. Sengupta, R. O. Ramabhadran, and K. Raghavachari. “Breaking a bottleneck: Accurate extrapolation to “gold standard” CCSD (T) energies for large open shell organic radicals at reduced computational cost.” In: *J. Comput. Chem.* 37.2 (2016), pp. 286–295 (cit. on p. 12).

[73] J. A. Pople, P. M. Gill, and B. G. Johnson. “Kohn—Sham density-functional theory within a finite basis set.” In: *Chem. Phys. Lett.* 199.6 (1992), pp. 557–560 (cit. on p. 12).

[74] S. Lehtola and H. Jónsson. “Variational, Self-Consistent Implementation of the Perdew-Zunger Self-Interaction Correction with Complex Optimal Orbitals.” In: *J. Chem. Theory Comput.* 10.12 (2014), pp. 5324–5337 (cit. on pp. 12, 17).

[75] J. P. Perdew and K. Schmidt. “Jacob’s ladder of density functional approximations for the exchange-correlation energy.” In: *AIP Conference Proceedings*. Vol. 577. 1. AIP. 2001, pp. 1–20 (cit. on p. 13).

[76] J. P. Perdew and Y. Wang. “Accurate and simple analytic representation of the electron-gas correlation energy.” In: *Phys. Rev. B* 45 (23 June 1992), pp. 13244–13249 (cit. on p. 13).

[77] J. P. Perdew, K. Burke, and M. Ernzerhof. “Generalized gradient approximation made simple.” In: *Phys. Rev. Lett.* 77.18 (1996), p. 3865 (cit. on p. 13).

[78] J. Sun, A. Ruzsinszky, and J. P. Perdew. “Strongly Constrained and Appropriately Normed Density Functional.” In: *Phys. Rev. Lett.* 115 (2015), p. 036402 (cit. on pp. 14, 142).

[79] P. J. Stephens et al. “Ab initio calculation of vibrational absorption and circular dichroism spectra using density functional force fields.” In: *J. Phys. Chem.* 98.45 (1994), pp. 11623–11627 (cit. on p. 14).

[80] L. Goerigk et al. “A look at the density functional theory zoo with the advanced GMTKN55 database for general main group thermochemistry, kinetics and noncovalent interactions.” In: *Phys. Chem. Chem. Phys.* 19.48 (2017), pp. 32184–32215 (cit. on pp. 14, 50).

[81] U. Ekström et al. “Arbitrary-order density functional response theory from automatic differentiation.” In: *J. Chem. Theory Comput.* 6.7 (2010), pp. 1971–1980 (cit. on p. 14).

[82] S. Lehtola et al. “Recent developments in libxc-A comprehensive library of functionals for density functional theory.” In: *SoftwareX* 7 (2018), pp. 1–5 (cit. on pp. 14, 142).

[83] N. Mardirossian and M. Head-Gordon. “Thirty years of density functional theory in computational chemistry: an overview and extensive assessment of 200 density functionals.” In: *Mol. Phys.* 115.19 (2017), pp. 2315–2372 (cit. on p. 14).

[84] J. P. Perdew et al. “Gedanken densities and exact constraints in density functional theory.” In: *J. Chem. Phys.* 140.18 (2014), 18A533 (cit. on p. 14).

[85] Y. Zhao and D. G. Truhlar. “A new local density functional for main-group thermochemistry, transition metal bonding, thermochemical kinetics, and noncovalent interactions.” In: *J. Chem. Phys.* 125.19 (2006), p. 194101 (cit. on p. 14).

[86] Y. Zhao and D. G. Truhlar. “The M06 suite of density functionals for main group thermochemistry, thermochemical kinetics, noncovalent interactions, excited states, and transition elements: two new functionals and systematic testing of four M06-class functionals and 12 other functionals.” In: *Theor. Chem. Acc.* 120.1-3 (2008), pp. 215–241 (cit. on p. 14).

[87] J. P. Perdew et al. “Why density functionals should not be judged primarily by atomization energies.” In: *Period. Polytech. Chem. Eng.* 60.1 (2016), pp. 2–7 (cit. on p. 15).

[88] C. Shahi et al. “Stretched or noded orbital densities and self-interaction correction in density functional theory.” In: *J. Chem. Phys.* 150.17 (2019), p. 174102 (cit. on pp. 15, 17).

[89] B. Santra and J. P. Perdew. “Perdew-Zunger self-interaction correction: How wrong for uniform densities and large-Z atoms?” In: *J. Chem. Phys.* 150.17 (2019), p. 174106 (cit. on p. 15).

[90] J. Vilhena et al. “Violation of a local form of the Lieb-Oxford bound.” In: *Phys. Rev. A* 85.5 (2012), p. 052514 (cit. on p. 16).

[91] J. L. Bao, L. Gagliardi, and D. G. Truhlar. “Self-interaction error in density functional theory: An appraisal.” In: *J. Phys. Chem. Lett.* 9.9 (2018), pp. 2353–2358 (cit. on p. 16).

[92] J. P. Perdew and A. Zunger. “Self-interaction correction to density-functional approximations for many-electron systems.” In: *Phys. Rev. B* 23.10 (1981), p. 5048 (cit. on pp. 17, 19).

[93] R. A. Heaton, J. G. Harrison, and C. C. Lin. “Self-interaction correction for density-functional theory of electronic energy bands of solids.” In: *Phys. Rev. B* 28.10 (1983), p. 5992 (cit. on p. 17).

[94] S. Schwalbe et al. "Fermi-Löwdin orbital self-interaction corrected density functional theory: Ionization potentials and enthalpies of formation." In: *J. Comput. Chem.* 39.29 (2018), pp. 2463–2471 (cit. on pp. 17, 19, 50, 131, 137, 141).

[95] N. I. Hammer et al. "Dipole-bound anions of highly polar molecules: Ethylene carbonate and vinylene carbonate." In: *J. Chem. Phys.* 120.2 (2004), pp. 685–690 (cit. on p. 17).

[96] K. D. Jordan and F. Wang. "Theory of dipole-bound anions." In: *Annu. Rev. Phys. Chem.* 54.1 (2003), pp. 367–396 (cit. on p. 17).

[97] M. R. Pederson et al. "Self-interaction corrections applied to Mg-porphyrin, C_{60}, and pentacene molecules." In: *J. Chem. Phys.* 144.16 (2016), p. 164117 (cit. on p. 17).

[98] Y. Li and J. Krieger. "Construction and application of gradient-expansion approximations for exchange energy with self-interaction correction." In: *Phys. Rev. A* 41.3 (1990), p. 1701 (cit. on p. 17).

[99] J. M. del Campo et al. "Non-empirical improvement of PBE and its hybrid PBE0 for general description of molecular properties." In: *J. Chem. Phys.* 136.10 (2012), p. 104108 (cit. on p. 17).

[100] J. Gázquez et al. "Analysis of the generalized gradient approximation for the exchange energy." In: vol. 1. Feb. 2013, pp. 295–312. ISBN: 978-1-4665-0528-5. DOI: `10.1201/b14048-15` (cit. on p. 17).

[101] J. C. Pacheco-Kato et al. "A PW91-like exchange with a simple analytical form." In: *Chem. Phys. Lett.* 651 (2016), pp. 268–273 (cit. on p. 17).

[102] M. Kick, K. Reuter, and H. Oberhofer. "Intricacies of DFT+ U, not only in a Numeric Atom Centered Orbital Framework." In: *J. Chem. Theory Comput.* (2019) (cit. on p. 17).

[103] F. Aryasetiawan and O. Gunnarsson. "The GW method." In: *Rep. Prog. Phys.* 61.3 (1998), p. 237 (cit. on p. 17).

[104] F. Tran, P. Blaha, and K. Schwarz. "Band gap calculations with Becke–Johnson exchange potential." In: *J. Phys.: Condens. Matter* 19.19 (2007), p. 196208 (cit. on p. 17).

[105] F. Tran and P. Blaha. "Accurate band gaps of semiconductors and insulators with a semilocal exchange-correlation potential." In: *Phys. Rev. Lett.* 102.22 (2009), p. 226401 (cit. on p. 17).

[106] D. Koller, F. Tran, and P. Blaha. "Improving the modified Becke-Johnson exchange potential." In: *Phys. Rev. B* 85.15 (2012), p. 155109 (cit. on p. 17).

[107] A. J. Cohen, P. Mori-Sánchez, and W. Yang. "Insights into current limitations of density functional theory." In: *Science* 321.5890 (2008), pp. 792–794 (cit. on p. 17).

[108] J. P. Perdew et al. "Prescription for the design and selection of density functional approximations: More constraint satisfaction with fewer fits." In: *J. Chem. Phys.* 123.6 (2005), p. 062201 (cit. on pp. 17, 143).

[109] M. R. Pederson and T. Baruah. “Chapter Eight - Self-Interaction Corrections Within the Fermi-Orbital-Based Formalism.” In: *Advances In Atomic, Molecular, and Optical Physics*. Ed. by E. Arimondo, C. C. Lin, and S. F. Yelin. Vol. 64. Academic Press, 2015, pp. 153–180 (cit. on p. 17).

[110] K. Trepte et al. “Analytic Atomic Gradients in the Fermi-Löwdin Orbital Self-Interaction Correction.” In: *J. Comput. Chem.* 40.6 (2019), pp. 820–825 (cit. on p. 17).

[111] J. G. Harrison, R. A. Heaton, and C. C. Lin. “Self-interaction correction to the local density Hartree-Fock atomic calculations of excited and ground states.” In: *J. Phys. B* 16.12 (1983), p. 2079 (cit. on pp. 17, 19).

[112] P. Mori-Sánchez and A. J. Cohen. “The derivative discontinuity of the exchange–correlation functional.” In: *Phys. Chem. Chem. Phys.* 16.28 (2014), pp. 14378–14387 (cit. on p. 18).

[113] G. Borghi et al. “Koopmans-compliant functionals and their performance against reference molecular data.” In: *Phys. Rev. B* 90 (7 Aug. 2014), p. 075135 (cit. on p. 19).

[114] G. Borghi et al. “Variational minimization of orbital-density-dependent functionals.” In: *Phys. Rev. B* 91 (15 Apr. 2015), p. 155112 (cit. on p. 19).

[115] M. R. Pederson, R. A. Heaton, and C. C. Lin. “Local-density Hartree–Fock theory of electronic states of molecules with self-interaction correction.” In: *J. Chem. Phys.* 80.5 (1984), pp. 1972–1975 (cit. on p. 19).

[116] W. L. Luken and D. N. Beratan. “Localized orbitals and the Fermi hole.” In: *Theor. Chim. Acta* 61.3 (1982), pp. 265–281 (cit. on pp. 19, 20, 139).

[117] W. L. Luken. “Properties of the Fermi Hole in Molecules.” In: *Croat. Chem. Acta* 57.6 (1984), pp. 1283–1294 (cit. on p. 19).

[118] J. Foster and S. Boys. “Canonical configurational interaction procedure.” In: *Rev. Mod. Phys.* 32.2 (1960), p. 300 (cit. on p. 20).

[119] C. Edmiston and K. Ruedenberg. “Localized atomic and molecular orbitals.” In: *Rev. Mod. Phys.* 35.3 (1963), p. 457 (cit. on p. 20).

[120] J. Pipek and P. G. Mezey. “A fast intrinsic localization procedure applicable for abinitio and semiempirical linear combination of atomic orbital wave functions.” In: *J. Chem. Phys.* 90.9 (1989), pp. 4916–4926 (cit. on p. 20).

[121] P.-O. Löwdin. “On the non-orthogonality problem connected with the use of atomic wave functions in the theory of molecules and crystals.” In: *J. Chem. Phys.* 18.3 (1950), pp. 365–375 (cit. on p. 20).

[122] P. Gullet, G. Wagner, and A. Slepoy. “Numerical tools for atomistic simulations.” In: *SANDIA Report* 8782 (2003), p. 2003 (cit. on p. 22).

[123] S. Groh and M. Alam. “Fracture behavior of lithium single crystal in the framework of (semi-)empirical force field derived from first-principles.” In: *Modell. Simul. Mater. Sci. Eng.* 23.4 (2015), p. 045008 (cit. on p. 22).

[124] S. Kale et al. “Lewis-inspired representation of dissociable water in clusters and Grotthuss chains.” In: *J. Biol. Phys.* 38.1 (Jan. 2012), pp. 49–59 (cit. on p. 22).

[125] S. Kale and J. Herzfeld. “Natural polarizability and flexibility via explicit valency: The case of water.” In: *J. Chem. Phys.* 136.8 (2012), p. 084109 (cit. on p. 22).

[126] S. Ekesan, S. Kale, and J. Herzfeld. “Transferable pseudoclassical electrons for aufbau of atomic ions.” In: *J. Comput. Chem.* 35.15 (2014), pp. 1159–1164 (cit. on p. 22).

[127] A. Jaramillo-Botero et al. “Large-scale, long-term nonadiabatic electron molecular dynamics for describing material properties and phenomena in extreme environments.” In: *J. Comput. Chem.* 32.3 (2011), pp. 497–512 (cit. on p. 22).

[128] A. A. Frost and R. A. Rouse. “Floating spherical Gaussian orbital model of molecular structure. IV. Hydrocarbons.” In: *J. Am. Chem. Soc.* 90.8 (1968), pp. 1965–1969 (cit. on p. 22).

[129] S. Plimpton. “Fast Parallel Algorithms for Short-Range Molecular Dynamics.” In: *J. Comput. Phys.* 117.1 (1995), pp. 1–19 (cit. on p. 24).

[130] R. J. Angel. “Equations of state.” In: *Rev. Mineral. Geochem.* 41.1 (2000), pp. 35–59 (cit. on p. 26).

[131] F. D. Murnaghan. “Finite deformations of an elastic solid.” In: *Am. J. Math.* 59.2 (1937), pp. 235–260 (cit. on p. 26).

[132] F. Birch. “Finite elastic strain of cubic crystals.” In: *Phys. Rev.* 71.11 (1947), p. 809 (cit. on pp. 26, 56, 93, 96, 98, 99).

[133] P. Vinet et al. “A universal equation of state for solids.” In: *J. Phys. C: Solid State Phys.* 19.20 (1986), p. L467 (cit. on pp. 26, 108, 134).

[134] P. Vinet et al. “Compressibility of solids.” In: *J. Geophys. Res. Solid Earth* 92.B9 (1987), pp. 9319–9325 (cit. on pp. 26, 108, 134).

[135] A. H. Larsen et al. “The atomic simulation environment—a Python library for working with atoms.” In: *J. Phys.: Condens. Matter* 29.27 (2017), p. 273002 (cit. on pp. 27, 47).

[136] S. P. Ong et al. “Python Materials Genomics (pymatgen): A robust, open-source python library for materials analysis.” In: *Comput. Mater. Sci.* 68 (2013), pp. 314–319 (cit. on p. 27).

[137] S. Schmerler. *pwtools*. `https://github.com/elcorto/pwtools`. Accessed: June 12, 2019 (cit. on p. 27).

[138] F. Cardarelli. “Less Common Nonferrous Metals.” In: *Materials Handbook: A Concise Desktop Reference*. Cham: Springer International Publishing, 2018, pp. 317–695 (cit. on p. 27).

[139] R. Golesorkhtabar et al. “ElaStic: A tool for calculating second-order elastic constants from first principles.” In: *Comput. Phys. Commun.* 184.8 (2013), pp. 1861–1873 (cit. on pp. 28, 30).

[140] M. Born. “On the stability of crystal lattices. I.” In: *Math. Proc. Cambridge Philos. Soc.* 36.2 (1940), pp. 160–172 (cit. on p. 29).

[141] R. Hill. “The Elastic Behaviour of a Crystalline Aggregate.” In: *Proc. Phys. Soc. London, Sect. A* 65.5 (1952), p. 349 (cit. on p. 29).

[142] P. T. Jochym and C. Badger. *jochym/Elastic: Maintenance release*. May 2018. DOI: `10.5281/zenodo.1254570`. URL: `https://doi.org/10.5281/zenodo.1254570` (cit. on pp. 30, 31).

[143] A. Dal Corso. "Elastic constants of beryllium: a first-principles investigation." In: *J. Phys.: Condens. Matter* 28.7 (2016), p. 075401 (cit. on p. 31).

[144] M. J. Mehl, B. M. Klein, and D. A. Papaconstantopoulos. "First-principles calculation of elastic properties." In: *Intermetallic Compounds* 1 (1994), pp. 195–210 (cit. on p. 32).

[145] G. Simmons. *Single Crystal Elastic Constants and Calculated Aggregate Properties*. Journal of the Graduate Research Center. Southern Methodist University Press, 1965. URL: `https://books.google.de/books?id=4q5esM1iatMC` (cit. on p. 32).

[146] T. Slotwinski and J. Trivisonno. "Temperature dependence of the elastic constants of single crystal lithium." In: *J. Phys. Chem. Solids* 30.5 (1969), pp. 1276–1278. ISSN: 0022-3697 (cit. on p. 32).

[147] H. C. Nash and C. S. Smith. "Single-crystal elastic constants of lithium." In: *J. Phys. Chem. Solids* 9.2 (1959), pp. 113–118 (cit. on p. 32).

[148] J. J. Hall. "Electronic effects in the elastic constants of n-type silicon." In: *Phys. Rev.* 161.3 (1967), p. 756 (cit. on p. 33).

[149] H. McSkimin and P. Andreatch Jr. "Elastic moduli of silicon vs hydrostatic pressure at 25.0 C and- 195.8 C." In: *J. Appl. Phys.* 35.7 (1964), pp. 2161–2165 (cit. on p. 33).

[150] M. Ganchenkova and R. M. Nieminen. "Mechanical Properties of Silicon Microstructures." In: *Handbook of Silicon Based MEMS Materials and Technologies*. Elsevier, 2015, pp. 253–293 (cit. on p. 33).

[151] A.-B. Chen, A. Sher, and W. Yost. "Chapter 1 Elastic Constants and Related Properties of Semiconductor Compounds and their Alloys." In: *The Mechanical Properties of Semiconductors*. Ed. by K. T. Faber and K. J. Malloy. Vol. 37. Semiconductors and Semimetals. Elsevier, 1992, pp. 1–77 (cit. on p. 33).

[152] J. E. Jones. "On the determination of molecular fields.—I. From the variation of the viscosity of a gas with temperature." In: *Proc. R. Soc. A* 106.738 (1924), pp. 441–462 (cit. on p. 37).

[153] X. Wang et al. "The Lennard-Jones potential: when (not) to use it." In: *Phys. Chem. Chem. Phys.* (2020), pp. - (cit. on p. 37).

[154] R. A. Buckingham. "The classical equation of state of gaseous helium, neon and argon." In: *Proc. R. Soc. A* 168.933 (1938), pp. 264–283 (cit. on p. 37).

[155] A. K. Rappé et al. "UFF, a full periodic table force field for molecular mechanics and molecular dynamics simulations." In: *J. Am. Chem. Soc.* 114.25 (1992), pp. 10024–10035 (cit. on pp. 37, 88).

[156] A. Rappe, K. Colwell, and C. Casewit. "Application of a universal force field to metal complexes." In: *Inorg. Chem.* 32.16 (1993), pp. 3438–3450 (cit. on pp. 37, 88).

[157] D. E. Coupry, M. A. Addicoat, and T. Heine. "Extension of the universal force field for metal–organic frameworks." In: *J. Chem. Theory Comput.* 12.10 (2016), pp. 5215–5225 (cit. on pp. 37, 100).

[158] T. Gruber et al. “Applying the coupled-cluster ansatz to solids and surfaces in the thermodynamic limit.” In: *Phys. Rev. X* 8.2 (2018), p. 021043 (cit. on p. 38).

[159] M. Dove. *Introduction to Lattice Dynamics*. Cambridge Topics in Mineral Physics and Chemistry. Cambridge University Press, 1993. ISBN: 9780521392938 (cit. on pp. 38, 39).

[160] M. Dove. *Structure and Dynamics: An Atomic View of Materials*. Oxford Master Series in Condensed Matter Physics 1. OUP Oxford, 2003. ISBN: 9780198506782 (cit. on p. 39).

[161] S. Schwalbe et al. “Mechanical, elastic and thermodynamic properties of crystalline lithium silicides.” In: *Comput. Mater. Sci.* 134 (2017), pp. 48–57 (cit. on pp. 39, 60).

[162] F. Taubert et al. “Thermodynamic characterization of lithium monosilicide (LiSi) by means of calorimetry and DFT-calculations.” In: *Int. J. Mater. Res.* 108.11 (2017), pp. 942–958 (cit. on pp. 39, 64).

[163] A. Kroupa. “Modelling of phase diagrams and thermodynamic properties using Calphad method - Development of thermodynamic databases.” In: *Comput. Mater. Sci.* 66 (2013), pp. 3–13 (cit. on p. 43).

[164] T. Gruber, S. Bahmann, and J. Kortus. “Metastable structure of $Li_{13}Si_4$.” In: *Phys. Rev. B* 93 (14 2016), p. 144104 (cit. on pp. 43, 54–56, 62, 63).

[165] S. Schmerler and J. Kortus. “*Ab initio* study of AlN: Anisotropic thermal expansion, phase diagram, and high-temperature rocksalt to wurtzite phase transition.” In: *Phys. Rev. B* 89 (6 2014), p. 064109 (cit. on p. 43).

[166] R. M. Martin. *Electronic structure: basic theory and practical methods*. Cambridge university press, 2004 (cit. on pp. 43, 139).

[167] P. Souvatzis et al. “Dynamical stabilization of the body centered cubic phase in lanthanum and thorium by phonon–phonon interaction.” In: *J. Phys.: Condens. Matter* 21.17 (2009), p. 175402 (cit. on p. 44).

[168] C. Campañá and M. H. Müser. “Practical Green’s function approach to the simulation of elastic semi-infinite solids.” In: *Phys. Rev. B* 74 (7 2006), p. 075420 (cit. on p. 44).

[169] L. T. Kong. “Phonon dispersion measured directly from molecular dynamics simulations.” In: *Comput. Phys. Commun.* 182 (2011), pp. 2201–2207 (cit. on p. 44).

[170] L. Kong and L. J. Lewis. “Surface diffusion coefficients: Substrate dynamics matters.” In: *Phys. Rev. B* 77 (16 2008), p. 165422 (cit. on p. 44).

[171] D. Svergun et al. *Small Angle X-Ray and Neutron Scattering from Solutions of Biological Macromolecules*. EBSCO ebook academic collection. OUP Oxford, 2013. ISBN: 9780199639533 (cit. on p. 45).

[172] N. Awasthi. *Phase Stability of Iron-carbon Nanocarbides and Implications for the Growth of Carbon Nanotubes*. Duke University, 2007. ISBN: 9780549708278 (cit. on p. 46).

[173] A. I. Duff et al. “Improved method of calculating *ab initio* high-temperature thermodynamic properties with application to ZrC.” In: *Phys. Rev. B* 91 (21 2015), p. 214311 (cit. on p. 46).

[174] B. Monserrat, N. D. Drummond, and R. J. Needs. “Anharmonic vibrational properties in periodic systems: energy, electron-phonon coupling, and stress.” In: *Phys. Rev. B* 87 (14 2013), p. 144302 (cit. on pp. 46, 83).

[175] I. Errea, M. Calandra, and F. Mauri. “Anharmonic free energies and phonon dispersions from the stochastic self-consistent harmonic approximation: Application to platinum and palladium hydrides.” In: *Phys. Rev. B* 89 (6 2014), p. 064302 (cit. on pp. 46, 83).

[176] O. Hellman et al. “Temperature dependent effective potential method for accurate free energy calculations of solids.” In: *Phys. Rev. B* 87 (10 2013), p. 104111 (cit. on pp. 46, 83).

[177] A. Togo and I. Tanaka. “First principles phonon calculations in materials science.” In: *Scr. Mater.* 108 (2015), pp. 1–5 (cit. on p. 47).

[178] M. A. Addicoat, D. E. Coupry, and T. Heine. “AuToGraFS: automatic topological generator for framework structures.” In: *J. Phys. Chem. A* 118.40 (2014), pp. 9607–9614 (cit. on pp. 47, 88).

[179] J. M. Skelton et al. “Lattice dynamics of the tin sulphides SnS_2, SnS and Sn_2S_3: vibrational spectra and thermal transport.” In: *Phys. Chem. Chem. Phys.* 19.19 (2017), pp. 12452–12465 (cit. on p. 47).

[180] Z.-L. Liu et al. “Phasego 3.0: Automatic analysis of synthesis and decomposition conditions for compounds.” In: *Comput. Phys. Commun.* 209 (2016), pp. 197–198 (cit. on p. 47).

[181] A. Karton. “A computational chemist’s guide to accurate thermochemistry for organic molecules.” In: *Wiley Interdiscip. Rev. Comput. Mol. Sci.* 6.3 (2016), pp. 292–310 (cit. on p. 50).

[182] W. S. Ohlinger et al. “Efficient calculation of heats of formation.” In: *J. Phys. Chem. A* 113.10 (2009), pp. 2165–2175 (cit. on p. 50).

[183] K. A. Peterson, D. Feller, and D. A. Dixon. “Chemical accuracy in ab initio thermochemistry and spectroscopy: current strategies and future challenges.” In: *Theor. Chem. Acc.* 131.1 (2012), p. 1079 (cit. on p. 50).

[184] J. A. Pople et al. “Gaussian-1 theory: A general procedure for prediction of molecular energies.” In: *J. Chem. Phys.* 90.10 (1989), pp. 5622–5629 (cit. on p. 50).

[185] L. A. Curtiss et al. “Gaussian-1 theory of molecular energies for second-row compounds.” In: *J. Chem. Phys.* 93.4 (1990), pp. 2537–2545 (cit. on p. 50).

[186] L. A. Curtiss et al. “Gaussian-2 theory for molecular energies of first-and second-row compounds.” In: *J. Chem. Phys.* 94.11 (1991), pp. 7221–7230 (cit. on p. 50).

[187] L. A. Curtiss et al. “Gaussian-3 (G3) theory for molecules containing first and second-row atoms.” In: *J. Chem. Phys.* 109.18 (1998), pp. 7764–7776 (cit. on p. 50).

[188] L. A. Curtiss, P. C. Redfern, and K. Raghavachari. “Gaussian-4 theory.” In: *J. Chem. Phys.* 126.8 (2007), p. 084108 (cit. on p. 50).

[189] L. Goerigk and S. Grimme. “A general database for main group thermochemistry, kinetics, and noncovalent interactions- assessment of common and reparameterized (meta-) GGA density functionals.” In: *J. Chem. Theory Comput.* 6.1 (2010), pp. 107–126 (cit. on p. 50).

[190] L. Goerigk and S. Grimme. "Efficient and Accurate Double-Hybrid-Meta-GGA Density Functionals-Evaluation with the Extended GMTKN30 Database for General Main Group Thermochemistry, Kinetics, and Noncovalent Interactions." In: *J. Chem. Theory Comput.* 7.2 (2011), pp. 291–309 (cit. on p. 50).

[191] B. J. Lynch and D. G. Truhlar. "Small representative benchmarks for thermochemical calculations." In: *J. Phys. Chem. A* 107.42 (2003), pp. 8996–8999 (cit. on p. 50).

[192] M. Korth and S. Grimme. ""Mindless" DFT benchmarking." In: *J. Chem. Theory Comput.* 5.4 (2009), pp. 993–1003 (cit. on p. 50).

[193] R. A. Mata and M. A. Suhm. "Benchmarking quantum chemical methods: Are we heading in the right direction?" In: *Angew. Chem. Int. Ed.* 56.37 (2017), pp. 11011–11018 (cit. on p. 50).

[194] M. Holzapfel et al. "Nano silicon for lithium-ion batteries." In: *Electrochim. Acta* 52.3 (2006), pp. 973–978 (cit. on p. 53).

[195] C.-M. Wang et al. "In Situ TEM Investigation of Congruent Phase Transition and Structural Evolution of Nanostructured Silicon/Carbon Anode for Lithium Ion Batteries." In: *Nano Lett.* 12.3 (2012), pp. 1624–1632 (cit. on p. 54).

[196] V. Chevrier, J. Zwanziger, and J. Dahn. "First principles study of Li–Si crystalline phases: Charge transfer, electronic structure, and lattice vibrations." In: *J. Alloys Compd.* 496.1 (2010), pp. 25–36 (cit. on pp. 54, 55, 60).

[197] D. Thomas et al. "The heat capacity and entropy of lithium silicides over the temperature range from (2 to 873) K." In: *J. Chem. Thermodyn.* 64 (2013), pp. 205–225 (cit. on pp. 54, 57, 60–62).

[198] Z. Cui et al. "A second nearest-neighbor embedded atom method interatomic potential for Li–Si alloys." In: *J. Power Sources* (2012), pp. 150–159 (cit. on pp. 54, 56, 58, 65).

[199] E. Zintl. "Intermetallische Verbindungen." In: *Angew. Chem.* 52.1 (1939), pp. 1–6 (cit. on p. 55).

[200] R. Nesper and H. G. von Schnering. "Li21Si5, a Zintl phase as well as a Hume-Rothery phase." In: *J. Solid State Chem.* 70.1 (1987), pp. 48–57 (cit. on pp. 55, 56).

[201] R. Nesper. "Structure and chemical bonding in Zintl-phases containing lithium." In: *Prog. Solid State Chem.* 20.1 (1990), pp. 1–45 (cit. on p. 55).

[202] H.-G. Schnering et al. "Structure and properties of Li14Si6/Li/2.33/Si/, the violet phase in the lithium-silicon system." In: *Z. Metallkunde* 71 (1980), pp. 357–363 (cit. on pp. 55, 56).

[203] S. Bahmann and J. Kortus. "EVO - Evolutionary algorithm for crystal structure prediction." In: *Comput. Phys. Commun.* 184.6 (2013), pp. 1618–1625 (cit. on p. 55).

[204] H. Mayer et al. "E9: The New High-Resolution Neutron Powder Diffractometer at the Berlin Neutron Scattering Center." In: *European Powder Diffraction EPDIC 7*. Vol. 378. Materials Science Forum. Trans Tech Publications, 2001, pp. 288–293 (cit. on p. 56).

[205] R. Nesper, H. G. von Schnering, and J. Curda. "Li12Si7, eine Verbindung mit trigonal-planaren Si4-Clustern und isometrischen Si5-Ringen." In: *Chem. Ber.* 119.12 (1986), pp. 3576–3590 (cit. on p. 56).

[206] U. Frank, W. Müller, and H. Schäfer. "Zur Kenntnis der Phase Li13Si4/On the Phase Li13Si4." In: *Z. Naturforsch. A* 30.1-2 (1975), pp. 10–13 (cit. on p. 56).

[207] Y. Kubota et al. "Crystal and electronic structure of Li15Si4." In: *J. Appl. Phys.* 102.5 (2007), p. 053704 (cit. on p. 56).

[208] E. Gladyesh, G. Oleksiv, and P. Kripyake. "New examples of structural type Li22Pb5." In: *Sov. Phys. Crystallogr.* 9.3 (1964), p. 269 (cit. on p. 56).

[209] M. R. Nadler and C. Kempier. "Crystallographic data 186. lithium." In: *Anal. Chem.* 31.12 (1959), p. 2109 (cit. on p. 56).

[210] P. Flubacher, A. J. Leadbetter, and J. A. Morrison. "The heat capacity of pure silicon and germanium and properties of their vibrational frequency spectra." In: *Philos. Mag.* 4.39 (1959), pp. 273–294 (cit. on p. 59).

[211] H. R. Shanks et al. "Thermal Conductivity of Silicon from 300 to 1400° K." In: *Phys. Rev.* 130 (5 1963), pp. 1743–1748 (cit. on p. 59).

[212] T. B. Douglas et al. "Lithium: Heat Content from 0 to 900°, Triple Point and Heat of Fusion, and Thermodynamic Properties of the Solid and Liquid." In: *J. Am. Chem. Soc.* 77.8 (1955), pp. 2144–2150 (cit. on p. 59).

[213] F. Simon and R. C. Swain. "Specific heats at low temperatures." In: *Z. Phys. Chem. Abt. B:* 28 (1935), p. 189 (cit. on p. 59).

[214] R. S. Krishnan, R. Srinivasan, and S. Devanarayanan. *Thermal Expansion of Crystals: International Series in The Science of The Solid State*. Vol. 22. Elsevier, 2013 (cit. on p. 62).

[215] C. J. Wen and R. A. Huggins. "Chemical diffusion in intermediate phases in the lithium-silicon system." In: *J. Solid State Chem.* 37.3 (1981), pp. 271–278 (cit. on p. 66).

[216] S.-N. Luo, A. Strachan, and D. C. Swift. "Nonequilibrium melting and crystallization of a model Lennard-Jones system." In: *J. Chem. Phys.* 120.24 (2004), pp. 11640–11649 (cit. on pp. 67, 69).

[217] W. Zhang, Y. Peng, and Z. Liu. "Molecular dynamics simulations of the melting curve of NiAl alloy under pressure." In: *AIP Adv.* 4.5 (2014), p. 057110 (cit. on pp. 67, 69).

[218] M. Chen et al. "The melting point of lithium: an orbital-free first-principles molecular dynamics study." In: *Mol. Phys.* 111.22-23 (2013), pp. 3448–3456 (cit. on p. 69).

[219] M. Campostrini et al. "Critical behavior of the three-dimensional XY universality class." In: *Phys. Rev. B* 63.21 (2001), p. 214503 (cit. on p. 70).

[220] R. Pathria and P. D. Beale. "12 - Phase Transitions: Criticality, Universality, and Scaling." In: *Statistical Mechanics (Third Edition)*. Ed. by R. Pathria and P. D. Beale. Third Edition. Boston: Academic Press, 2011, pp. 401–469 (cit. on p. 70).

[221] J. M. Honig and J. Spalek. *A primer to the theory of critical phenomena*. Elsevier, 2018 (cit. on p. 70).

[222] R. Boehler. “Melting temperature, adiabats, and Grüneisen parameter of lithium, sodium and potassium versus pressure.” In: *Phys. Rev. B* 27.11 (1983), p. 6754 (cit. on p. 72).

[223] D. Thomas. “Thermodynamische und kinetische Untersuchungen im System Lithium-Silicium.” PhD thesis. TU Bergakademie Freiberg, 2015 (cit. on pp. 72–78).

[224] M. Gayler. “Melting point of high-purity silicon.” In: *Nature* 142.3593 (1938), pp. 478–478 (cit. on p. 72).

[225] R. A. Sharma and R. N. Seefurth. “Thermodynamic properties of the Lithium-Silicon system.” In: *J. Electrochem. Soc.* 123.12 (1976), pp. 1763–1768 (cit. on p. 80).

[226] C. Van der Marel, G. Vinke, and W. Van der Lugt. “The phase diagram of the system lithium-silicon.” In: *Solid State Commun.* 54.11 (1985), pp. 917–919 (cit. on p. 80).

[227] P. Wang et al. “Thermodynamic analysis of the Li–Si phase equilibria from 0 K to liquidus temperatures.” In: *Intermetallics* 42 (2013), pp. 137–145 (cit. on p. 80).

[228] M. Zeilinger et al. “Revision of the Li–Si Phase Diagram: Discovery and Single-Crystal X-ray Structure Determination of the High-Temperature Phase $Li_{4.11}Si$.” In: *Chem. Mater.* 25.22 (2013), pp. 4623–4632 (cit. on p. 80).

[229] M. H. Braga, A. Dębski, and W. Gąsior. “Li–Si phase diagram: Enthalpy of mixing, thermodynamic stability, and coherent assessment.” In: *J. Alloys Compd.* 616 (2014), pp. 581–593 (cit. on p. 80).

[230] S.-M. Liang et al. “Thermodynamics of Li-Si and Li-Si-H phase diagrams applied to hydrogen absorption and Li-ion batteries.” In: *Intermetallics* 81 (2017), pp. 32–46 (cit. on p. 80).

[231] M. Kim et al. “Postsynthetic ligand and cation exchange in robust metal–organic frameworks.” In: *J. Am. Chem. Soc.* 134.43 (2012), pp. 18082–18088 (cit. on p. 85).

[232] A. De Vos et al. “Missing linkers: an alternative pathway to UiO-66 electronic structure engineering.” In: *Chem. Mater.* 29.7 (2017), pp. 3006–3019 (cit. on p. 85).

[233] J. K. Bristow et al. “Free Energy of Ligand Removal in the Metal–Organic Framework UiO-66.” In: *J. Phys. Chem. C* 120.17 (2016), pp. 9276–9281 (cit. on p. 85).

[234] H. V. Doan et al. “Hierarchical Metal–Organic Frameworks with Macroporosity: Synthesis, Achievements, and Challenges.” In: *Nano-Micro Lett.* 11.1 (2019), p. 54 (cit. on p. 85).

[235] A. Togo and I. Tanaka. *`Spglib`: a software library for crystal symmetry search*. 2018. arXiv: `1808.01590 [cond-mat.mtrl-sci]` (cit. on pp. 86, 88, 89).

[236] Q. Yang et al. “CH_4 storage and CO_2 capture in highly porous zirconium oxide based metal–organic frameworks.” In: *Chem. Commun.* 48.79 (2012), pp. 9831–9833 (cit. on pp. 87, 117).

[237] S. M. Rogge et al. “Thermodynamic insight in the high-pressure behavior of UiO-66: effect of linker defects and linker expansion.” In: *Chem. Mater.* 28.16 (2016), pp. 5721–5732 (cit. on pp. 87, 95, 100).

[238] A. A. Yakovenko et al. "Generation and applications of structure envelopes for porous metal–organic frameworks." In: *J. Appl. Crystallogr.* 46.2 (2013), pp. 346–353 (cit. on p. 87).

[239] M. Eddaoudi et al. "Systematic design of pore size and functionality in isoreticular MOFs and their application in methane storage." In: *Science* 295.5554 (2002), pp. 469–472 (cit. on pp. 87, 117).

[240] V. Bon et al. "Exceptional adsorption-induced cluster and network deformation in the flexible metal–organic framework DUT-8 (Ni) observed by in situ X-ray diffraction and EXAFS." In: *Phys. Chem. Chem. Phys.* 17.26 (2015), pp. 17471–17479 (cit. on pp. 87, 117, 120).

[241] K. Trepte and S. Schwalbe. "porE: A code for deterministic and systematic analyses of porosities." In: *Journal of Computational Chemistry* 42.9 (2021), pp. 630–643 (cit. on pp. 88, 94, 115, 116, 119, 155).

[242] A. L. Spek. "Structure validation in chemical crystallography." In: *Acta Crystallogr. D* 65.2 (Feb. 2009), pp. 148–155 (cit. on pp. 88, 89, 116, 117).

[243] H. T. Stokes and D. M. Hatch. "FINDSYM: program for identifying the space-group symmetry of a crystal." In: *J. Appl. Crystallogr.* 38.1 (Feb. 2005), pp. 237–238 (cit. on pp. 88, 89, 162).

[244] D. Hicks et al. "AFLOW-SYM: platform for the complete, automatic and self-consistent symmetry analysis of crystals." In: *Acta Crystallogr. A* 74.3 (May 2018), pp. 184–203 (cit. on pp. 88, 89, 160, 163).

[245] P. G. Yot et al. "Exploration of the mechanical behavior of metal organic frameworks UiO-66(Zr) and MIL-125(Ti) and their NH2 functionalized versions." In: *Dalton Trans.* 45 (10 2016), pp. 4283–4288 (cit. on pp. 92, 93).

[246] L. R. Redfern et al. "Porosity dependence of compression and lattice rigidity in metal–organic framework series." In: *J. Am. Chem. Soc.* 141.10 (2019), pp. 4365–4371 (cit. on pp. 92, 93, 96–98).

[247] M. Mitchell et al. *markummitchell/engauge-digitizer: Version 12.1 Directory dialogs start in saved paths*. Version v12.1. Nov. 2019. DOI: `10.5281/zenodo.3558440`. URL: `https://doi.org/10.5281/zenodo.3558440` (cit. on p. 93).

[248] C. L. Hobday et al. "A Computational and Experimental Approach Linking Disorder, High-Pressure Behavior, and Mechanical Properties in UiO Frameworks." In: *Angew. Chem. Int. Ed.* 55.7 (2016), pp. 2401–2405 (cit. on pp. 96, 97, 99).

[249] K. W. Chapman, G. J. Halder, and P. J. Chupas. "Guest-dependent high pressure phenomena in a Nanoporous metal- organic framework material." In: *J. Am. Chem. Soc.* 130.32 (2008), pp. 10524–10526 (cit. on p. 100).

[250] H. Wu, T. Yildirim, and W. Zhou. "Exceptional mechanical stability of highly porous zirconium metal–organic framework UiO-66 and its important implications." In: *J. Phys. Chem. Lett.* 4.6 (2013), pp. 925–930 (cit. on p. 100).

[251] L.-M. Yang et al. "Computational exploration of newly synthesized zirconium metal–organic frameworks UiO-66,-67,-68 and analogues." In: *J. Mater. Chem. C* 2.34 (2014), pp. 7111–7125 (cit. on p. 100).

[252] B. Mu and K. S. Walton. “Thermal analysis and heat capacity study of metal–organic frameworks.” In: *J. Phys. Chem. C* 115.46 (2011), pp. 22748–22754 (cit. on p. 102).

[253] F. Kloutse et al. “Specific heat capacities of MOF-5, Cu-BTC, Fe-BTC, MOF-177 and MIL-53 (Al) over wide temperature ranges: Measurements and application of empirical group contribution method.” In: *Micropor. Mesopor. Mat.* 217 (2015), pp. 1–5 (cit. on p. 102).

[254] S. A. Moggach, T. D. Bennett, and A. K. Cheetham. “The Effect of Pressure on ZIF-8: Increasing Pore Size with Pressure and the Formation of a High-Pressure Phase at 1.47 GPa.” In: *Angew. Chem. Int. Ed.* 48.38 (2009), pp. 7087–7089 (cit. on p. 115).

[255] D. Ongari et al. “Accurate Characterization of the Pore Volume in Microporous Crystalline Materials.” In: *Langmuir* 33.51 (2017), pp. 14529–14538 (cit. on pp. 115, 117).

[256] A. Bondi. “van der Waals Volumes and Radii.” In: *J. Phys. Chem.* 68 (1964), pp. 441–451 (cit. on p. 115).

[257] L. Sarkisov and A. Harrison. “Computational structure characterisation tools in application to ordered and disordered porous materials.” In: *Mol. Simul.* 37.15 (2011), pp. 1248–1257 (cit. on pp. 116, 117).

[258] D. Dubbeldam, A. Torres-Knoop, and K. S. Walton. “On the inner workings of Monte Carlo codes.” In: *Mol. Simul.* 39.14-15 (2013), pp. 1253–1292 (cit. on pp. 116, 117).

[259] D. Dubbeldam et al. “RASPA: molecular simulation software for adsorption and diffusion in flexible nanoporous materials.” In: *Mol. Simul.* 42.2 (2016), pp. 81–101 (cit. on pp. 116, 117).

[260] T. F. Willems et al. “Algorithms and tools for high-throughput geometry-based analysis of crystalline porous materials.” In: *Micropor. Mesopor. Mat.* 149 (2012), pp. 134–141 (cit. on pp. 116, 117).

[261] S. Chavan et al. “H_2 storage in isostructural UiO-67 and UiO-66 MOFs.” In: *Phys. Chem. Chem. Phys.* **14** (2012), pp. 1614–1626 (cit. on p. 117).

[262] K. Trepte et al. “The origin of the measured chemical shift of ^{129}Xe in UiO-66 and UiO-67 revealed by DFT investigations.” In: *Phys. Chem. Chem. Phys.* 19 (2017), pp. 10020–10027 (cit. on p. 117).

[263] K. Trepte et al. “Theoretical and experimental investigations of ^{129}Xe NMR chemical shift isotherms in metal–organic frameworks.” In: *Phys. Chem. Chem. Phys.* 20 (2018), pp. 25039–25043 (cit. on p. 117).

[264] K. Trepte, S. Schwalbe, and G. Seifert. “Electronic and magnetic properties of DUT-8 (Ni).” In: *Phys. Chem. Chem. Phys.* 17.26 (2015), pp. 17122–17129 (cit. on pp. 117, 120, 122, 123).

[265] S. Schwalbe et al. “Screening for high-spin metal organic frameworks (MOFs): density functional theory study on DUT-8(M_1,M_2) (with M_i = V,...,Cu).” In: *Phys. Chem. Chem. Phys.* 18 (11 2016), pp. 8075–8080 (cit. on pp. 117, 120–125).

[266] N. L. Rosi et al. “Hydrogen Storage in Microporous Metal-Organic Frameworks.” In: *Science* 300.5622 (2003), pp. 1127–1129 (cit. on p. 117).

[267] S. S.-Y. Chui et al. “A Chemically Functionalizable Nanoporous Material $[Cu_3(TMA)_2(H_2O)_3]_n$.” In: *Science* 283.5405 (1999), pp. 1148–1150 (cit. on p. 117).

[268] C. H. Hendon and A. Walsh. “Chemical principles underpinning the performance of the metal–organic framework HKUST-1.” In: *Chem. Sci.* 6 (7 2015), pp. 3674–3683 (cit. on p. 117).

[269] K. T. Butler, C. H. Hendon, and A. Walsh. “Electronic Chemical Potentials of Porous Metal–Organic Frameworks.” In: *J. Am. Chem. Soc.* 136.7 (2014), pp. 2703–2706 (cit. on p. 117).

[270] H. Furukawa et al. “Ultrahigh Porosity in Metal-Organic Frameworks.” In: *Science* 329.5990 (2010), pp. 424–428 (cit. on p. 117).

[271] R. L. Martin, B. Smit, and M. Haranczyk. “Addressing Challenges of Identifying Geometrically Diverse Sets of Crystalline Porous Materials.” In: *J. Chem. Inf. Model.* 52.2 (2012), pp. 308–318 (cit. on p. 117).

[272] M. Pinheiro et al. “Characterization and comparison of pore landscapes in crystalline porous materials.” In: *J. Mol. Graphics Modell.* 44 (2013), pp. 208–219 (cit. on p. 117).

[273] M. Pinheiro et al. “High accuracy geometric analysis of crystalline porous materials.” In: *CrystEngComm* 15 (2013), pp. 7531–7538 (cit. on p. 117).

[274] R. L. Martin and M. Haranczyk. “Construction and Characterization of Structure Models of Crystalline Porous Polymers.” In: *Cryst. Growth Des.* 14.5 (2014), pp. 2431–2440 (cit. on p. 117).

[275] H. Wu, T. Yildrim, and W. Zhou. “Execptional Mechanical Stability of Highly Pourous Zirconium Metal-Organic Framework UiO-66 and Its Important Implications.” In: *J. Phys. Chem. Lett.* 4 (2013), pp. 925–930 (cit. on p. 117).

[276] J. A. Mason, M. Veenstra, and J. R. Long. “Evaluating metal–organic frameworks for natural gas storage.” In: *Chem. Sci.* 5 (2014), pp. 32–51 (cit. on p. 117).

[277] N. Klein et al. “Monitoring adsorption-induced switching by ^{129}Xe NMR spectroscopy in a new metal-organic framework Ni_2(2,6-ndc)$_2$(dabco).” In: *Phys. Chem. Chem. Phys.* 12 (37 2010), pp. 11778–11784 (cit. on p. 120).

[278] H. C. Hoffmann et al. “High-Pressure in Situ ^{129}Xe NMR Spectroscopy and Computer Simulations of Breathing Transitions in the Metal-Organic Framework Ni_2(2,6-ndc)$_2$(dabco) (DUT-8(Ni)).” In: *J. Am. Chem. Soc.* 133.22 (2011), pp. 8681–8690 (cit. on p. 120).

[279] F. Neese. “Prediction of molecular properties and molecular spectroscopy with density functional theory: From fundamental theory to exchange-coupling.” In: *Coord. Chem. Rev.* 253.5–6 (2009). Theory and Computing in Contemporary Coordination Chemistry, pp. 526–563 (cit. on pp. 122, 123).

[280] K. Koepernik and H. Eschrig. “Full-potential nonorthogonal local-orbital minimum-basis band-structure scheme.” In: *Phys. Rev. B* 59 (3 Jan. 1999), pp. 1743–1757 (cit. on pp. 122, 123).

[281] W. Heisenberg. “Mehrkörperproblem und Resonanz in der Quantenmechanik.” In: *Z. Phys.* 38.6-7 (1926), pp. 411–426 (cit. on p. 122).

[282] P. A. M. Dirac. “On the Theory of Quantum Mechanics.” In: *Proc. R. Soc. A* **112**.762 (1926), pp. 661–677 (cit. on p. 122).

[283] J. H. Van Vleck. *The theory of electric and magnetic susceptibilities*. Oxford: Clarendon Press, 1932 (cit. on p. 122).

[284] K. Yamaguchi, Y. Takahara, and T. Fueno. “Ab-initio molecular orbital studies of structure and reactivity of transition metal-oxo compounds.” In: *Applied Quantum Chemistry*. Springer, 1986, pp. 155–184 (cit. on p. 123).

[285] T. Soda et al. “Ab initio computations of effective exchange integrals for H–H, H–He–H and Mn_2O_2 complex: comparison of broken-symmetry approaches.” In: *Chem. Phys. Lett.* 319.3 (2000), pp. 223–230 (cit. on p. 123).

[286] A. P. Ginsberg. “Magnetic exchange in transition metal complexes. 12. Calculation of cluster exchange coupling constants with the Xα-scattered wave method.” In: *J. Am. Chem. Soc.* 102.1 (1980), pp. 111–117 (cit. on p. 123).

[287] L. Noodleman. “Valence bond description of antiferromagnetic coupling in transition metal dimers.” In: *J. Chem. Phys.* 74.10 (1981), pp. 5737–5743 (cit. on p. 123).

[288] L. Noodleman and E. R. Davidson. “Ligand spin polarization and antiferromagnetic coupling in transition metal dimers.” In: *Chem. Phys.* 109.1 (1986), pp. 131–143 (cit. on p. 123).

[289] A. Bencini and D. Gatteschi. “Xα-SW calculations of the electronic structure and magnetic properties of weakly coupled transition-metal clusters. The $[Cu_2Cl_6]^{2-}$ dimers.” In: *J. Am. Chem. Soc.* 108.19 (1986), pp. 5763–5771 (cit. on p. 123).

[290] C. Desplanches et al. “Exchange Coupling of Transition-Metal Ions through Hydrogen Bonding: A Theoretical Investigation.” In: *J. Am. Chem. Soc.* 124.18 (2002), pp. 5197–5205 (cit. on p. 123).

[291] F. Weigend and R. Ahlrichs. “Balanced basis sets of split valence, triple zeta valence and quadruple zeta valence quality for H to Rn: Design and assessment of accuracy.” In: *Phys. Chem. Chem. Phys.* 7 (18 2005), pp. 3297–3305 (cit. on p. 123).

[292] I. Opahle, K. Koepernik, and H. Eschrig. “Full-potential band-structure calculation of iron pyrite.” In: *Phys. Rev. B* 60 (20 Nov. 1999), pp. 14035–14041 (cit. on p. 123).

[293] K. Park and M. R. Pederson. “Effect of extra electrons on the exchange and magnetic anisotropy in the anionic single-molecule magnet Mn_{12}.” In: *Phys. Rev. B* 70 (5 Aug. 2004), p. 054414 (cit. on p. 124).

[294] W. Kołos, K. Szalewicz, and H. J. Monkhorst. “New Born-Oppenheimer potential energy curve and vibrational energies for the electronic ground state of the hydrogen molecule.” In: *J. Chem. Phys.* 84.6 (1986), pp. 3278–3283 (cit. on p. 132).

[295] R. D. Johnson. *NIST Computational Chemistry Comparison and Benchmark Database*. NIST Standard Reference Database Number 101, 18–10–2016. URL: `http://cccbdb.nist.gov/` (cit. on pp. 133, 137).

[296] W. F. Luder. “Electronic structure of molecules (Linnett, JW).” In: *J. Chem. Educ.* 43.1 (1964), pp. 55–56 (cit. on pp. 133, 137, 139).

[297] W. F. Luder. “The electron repulsion theory of the chemical bond. I. New models of atomic structure.” In: *J. Chem. Educ.* 44.4 (1967), p. 206 (cit. on p. 133).

[298] M. Frost et al. “Equation of state and electron localisation in fcc lithium.” In: *J. Appl. Phys.* 123.6 (2018), p. 065901 (cit. on p. 133).

[299] S. Schwalbe et al. “Interpretation and Automatic Generation of Fermi-Orbital Descriptors.” In: *J. Comput. Chem.* 40.32 (2019), pp. 2843–2857 (cit. on pp. 135–137, 143, 155).

[300] P. Atkins and T. Overton. *Shriver and Atkins' Inorganic Chemistry*. Oxford University Press, USA, 2010 (cit. on p. 137).

[301] J. Kraus. *Bachelor thesis: FLOSIC-DFT analysis of chemical bonding: application to diatomic molecules, DOI: 10.13140/RG.2.2.15045.91362*. Sept. 2017. DOI: `10.13140/RG.2.2.15045.91362` (cit. on pp. 137, 139).

[302] E. D. Glendening, C. R. Landis, and F. Weinhold. “Natural bond orbital methods.” In: *Wiley Interdiscip. Rev. Comput. Mol. Sci.* 2.1 (2012), pp. 1–42 (cit. on p. 137).

[303] R. Gillespie. “The valence-shell electron-pair repulsion (VSEPR) theory of directed valency.” In: *J. Chem. Educ.* 40.6 (1963), p. 295 (cit. on p. 137).

[304] T. A. Manz. “Introducing DDEC6 atomic population analysis: part 3. Comprehensive method to compute bond orders.” In: *RSC Adv.* 7.72 (2017), pp. 45552–45581 (cit. on p. 137).

[305] A. Gindulyte et al. “PubChem 2019 update: improved access to chemical data.” In: *Nucleic Acids Res.* 47.D1 (2018), pp. D1102–D1109 (cit. on p. 137).

[306] H. E. Pence and A. Williams. “ChemSpider: An Online Chemical Information Resource.” In: *J. Chem. Educ.* 87.11 (2010), pp. 1123–1124 (cit. on p. 137).

[307] J. Linnett. “Valence-Bond Structures: A New Proposal.” In: *Nature* 187.4740 (1960), p. 859 (cit. on p. 137).

[308] J. Linnett. “A modification of the Lewis-Langmuir octet rule.” In: *J. Am. Chem. Soc.* 83.12 (1961), pp. 2643–2653 (cit. on pp. 137, 139).

[309] J. W. Linnett. *Electronic structure of molecules*. London: Methuen & Co. Ltd., 1964 (cit. on pp. 137, 139).

[310] Jensen, W. B. “Whatever happened to Linnett double-quartet (LDQ) theory?” In: *Educ. Quim.* 28.2 (2017), pp. 74–83 (cit. on pp. 137, 139).

[311] A. C. Cancio, M. Y. Chou, and R. Q. Hood. “Comparative study of density-functional theories of the exchange-correlation hole and energy in silicon.” In: *Phys. Rev. B* 64.11 (2001), p. 115112 (cit. on p. 139).

[312] K. J. Giesbertz, R. van Leeuwen, and U. von Barth. “Towards nonlocal density functionals by explicit modeling of the exchange-correlation hole in inhomogeneous systems.” In: *Phys. Rev. A* 87.2 (2013), p. 022514 (cit. on p. 139).

[313] M. Buijse and E. Baerends. “An approximate exchange-correlation hole density as a functional of the natural orbitals.” In: *Mol. Phys.* 100.4 (2002), pp. 401–421 (cit. on p. 139).

[314] E. Baerends. “Exact exchange-correlation treatment of dissociated H2 in density functional theory.” In: *Phys. Rev. Lett.* 87.13 (2001), p. 133004 (cit. on p. 139).

[315] C. G. Broyden. “The convergence of a class of double-rank minimization algorithms 1. General considerations.” In: *IMA J. Appl. Math.* 6.1 (1970), pp. 76–90 (cit. on p. 141).

[316] R. Fletcher. “A new approach to variable metric algorithms.” In: *Comput. J.* 13.3 (1970), pp. 317–322 (cit. on p. 141).

[317] D. Goldfarb. “A family of variable-metric methods derived by variational means.” In: *Math. Comput.* 24.109 (1970), pp. 23–26 (cit. on p. 141).

[318] D. F. Shanno. “Conditioning of quasi-Newton methods for function minimization.” In: *Math. Comput.* 24.111 (1970), pp. 647–656 (cit. on p. 141).

[319] J. Nocedal. “Updating quasi-Newton matrices with limited storage.” In: *Math. Comput.* 35.151 (1980), pp. 773–782 (cit. on p. 141).

[320] E. Bitzek et al. “Structural Relaxation Made Simple.” In: *Phys. Rev. Lett.* 97 (17 2006), p. 170201 (cit. on p. 141).

[321] J. P. Perdew et al. “Paradox of Self-Interaction Correction: How Can Anything So Right Be So Wrong?” In: *Advances In Atomic, Molecular, and Optical Physics*. Vol. 64. Elsevier, 2015, pp. 1–14 (cit. on p. 143).

[322] O. A. Vydrov et al. “Scaling down the Perdew-Zunger self-interaction correction in many-electron regions.” In: *J. Chem. Phys.* 124.9 (2006), p. 094108 (cit. on p. 143).

[323] S. Lehtola, M. Head-Gordon, and H. Jonsson. “Complex orbitals, multiple local minima, and symmetry breaking in Perdew–Zunger self-interaction corrected density functional theory calculations.” In: *J. Chem. Theory Comput.* 12.7 (2016), pp. 3195–3207 (cit. on p. 143).

[324] M. Stengel and N. A. Spaldin. “Self-interaction correction with Wannier functions.” In: *Phys. Rev. B* 77.15 (2008), p. 155106 (cit. on p. 143).

[325] M. Abadi et al. “TensorFlow: A system for large-scale machine learning.” In: *12th USENIX Symposium on Operating Systems Design and Implementation (OSDI 16)*. 2016, pp. 265–283. URL: `https://www.usenix.org/system/files/conference/osdi16/osdi16-abadi.pdf` (cit. on p. 149).

[326] K. Yao et al. “The TensorMol-0.1 model chemistry: A neural network augmented with long-range physics.” In: *Chem. Sci.* 9.8 (2018), pp. 2261–2269 (cit. on p. 149).

[327] S. Chmiela et al. “sGDML: Constructing accurate and data efficient molecular force fields using machine learning.” In: *Comput. Phys. Commun.* (2019) (cit. on p. 149).

[328] A. Khorshidi and A. A. Peterson. “Amp: A modular approach to machine learning in atomistic simulations.” In: *Comput. Phys. Commun.* 207 (2016), pp. 310–324 (cit. on p. 149).

[329] L. Leukkunen, T. Verho, and O. Lopez-Acevedo. “A Multiscale Code for Flexible Hybrid Simulations Using ASE Framework.” In: *Comput. Sci. Eng.* 16.2 (2013), pp. 54–62 (cit. on p. 151).

[330] A. Dohn et al. “Grid-based projector augmented wave (GPAW) implementation of quantum mechanics/molecular mechanics (QM/MM) electrostatic embedding and application to a solvated diplatinum complex.” In: *J. Chem. Theory Comput.* 13.12 (2017), pp. 6010–6022 (cit. on p. 151).

VERSICHERUNG

Hiermit versichere ich, dass ich die vorliegende Arbeit ohne unzulässige Hilfe Dritter und ohne Benutzung anderer als der angegebenen Hilfsmittel angefertigt habe; die aus fremden Quellen direkt oder indirekt übernommenen Gedanken sind als solche kenntlich gemacht. Die Hilfe eines Promotionsberaters habe ich nicht in Anspruch genommen. Weitere Personen haben von mir keine geldwerten Leistungen für Arbeiten erhalten, die nicht als solche kenntlich gemacht worden sind. Die Arbeit wurde bisher weder im Inland noch im Ausland in gleicher oder ähnlicher Form einer anderen Prüfungsbehörde vorgelegt.

DECLARATION

I hereby declare that I completed this work without any improper help from a third party and without using any aids other than those cited. All ideas derived directly or indirectly from other sources are identified as such. I did not seek the help of a professional doctorate-consultant. Only those persons identified as having done so received any financial payment from me for any work done for me. This thesis has not previously been published in the same or a similar form in Germany or abroad.

Freiberg, October 1, 2021

Sebastian Schwalbe

DANKSAGUNG

An erster Stelle möchte mich bei meinem Doktorvater Prof. Dr. Jens Kortus bedanken, der meine Arbeit ermöglicht, begleitet und mir stets mit Rat und Tat zur Seite stand. Sein allumfassendes aber auch sein spezielles Wissen beispielsweise rund um die Symmetrie von Molekülen oder Festkörpern war und ist stets bewundernswert. Ich bedanke mich auch bei allen Geldgebern die diese Promotion ermöglicht haben. Zu nennen sind hier das Werkstoffe mit neuem Design für verbesserte Lithium-Ionen-Batterien (WeNDeLIB, SPP 1473 DFG) Projekt, die TU Bergakademie Freiberg und das PyFLOSIC DFG Projekt (KO 1924/9-1). Ich bedanke mich insbesondere bei der Deutschen Forschungsgemeinschaft (DFG), die es mir ermöglicht hat mein PyFLOSIC Projekt schon eher zu beginnen. Dies ermöglichte mir meine Arbeit in der Art und Weise fertig zu stellen wie sie heute ist.

Weiter möchte ich allen meiner Mitautoren und Kollegen danken. Jedoch einem meiner besten Freunde, wissenschaftlichen Wegbelegeiter und dem besten Mitautor Dr. Kai Trepte möchte an dieser Stelle ganz besonders danken. Nur durch unsere Zusammenarbeit konnten viele kleine oder auch größere Probleme angegangen und beseitigt werden. Ihm danke ich auch für das Korrekturlesen dieser Arbeit. Besonders möchte ich mich bei Prof. Dr. John P. Perdew bedanken, es war und wird immer eine besondere Ehre für mich sein ihn persönlich kennengelernt zu haben und mit ihm zusammenarbeiten zu dürfen. In meinen Augen ist er die Verkörperung von Wissen und akkurater Physik. Einen weiteren besonderen Dank möchte ich Dr. Susi Lehtola aussprechen, die Entwicklung von PyFLOSIC wäre wohl nie möglich gewesen ohne seine didaktisch herausragenden, inspirierenden und exzellenten Vorarbeiten im Gebiet der Selbstwechselwirkungskorrektur. Auch hier war und ist es ein essentieller, persönlicher und wissenschaftler Höhepunkt ihn persönlich kennenlernen und mit ihm zusammenarbeiten zu dürfen.

Natürlich möchte ich auch meinem Institut für Theoretische Physik (TU Bergakademie Freiberg) danken. Nur in einer vitalen Umgebung kann sinnvolle Arbeit geleistet werden. Ich bedanke mich bei euch eine solche Umgebung zur Verfügung gestellt zu haben. Besonders möchte hier auch Dr. Simon Liebing danken mit dem ich die unterschiedlichsten Tagungen besucht habe und der sich diverse frustrierte Monologe meinerseits beim gemeinsamen Mittagessen anhören mußte. Unserem lokalen Administrator M. Sc. René Wirnata möchte ich insbesondere für das Initialisieren und das Verwalten unseres ShareLatex Servers danken. Viele Artikel, Poster, Vorträge und auch diese Arbeit sind auf diesem Server entstanden. Ein ganz großer Dank gilt auch den besten Studenten die ich in meiner Promotionszeit betreuen durfte, M. Sc. Lenz Fiedler, M. Sc. Jakob Kraus und B. Sc. Wanja Timm Schulze. Ohne die Zusammenarbeit mit M. Sc. Lenz Fiedler würde es PyFLOSIC heute nicht geben. Und ohne die Ausarbeitungen von M. Sc. Jakob Kraus in seinen Abschlußarbeiten wäre unser aller Verständnis der Bedeutung von Fermi-Orbital Deskriptoren (FODs) ein wesentlich geringeres als es heute ist. Das allgemeine Interesse sich weiterzuentwickeln und die darauf basierende Zusammenarbeit mit B. Sc. Wanja Timm Schulze hat mir gezeigt, dass verschiedene Perspektiven neue wissenschaftliche Pfade auch durch steiniges Gelände eröffnen können.

Ich möchte hier auch meinen ehemaligen Grundschullehrern danken, die schon sehr früh das Interesse an Naturwissenschaften in mir geweckt haben und schon sehr früh prophezeit haben, dass es einmal eine solche Arbeit von mir geben werde. Ein allgemeiner Dank gilt allen Entwicklern von freier Software, und den Autoren frei-zugänglicher wissenschaftlicher Lektüre. Ohne euch wäre es nicht möglich gewesen Dinge zu verstehen wie ich sie heute verstehe. Für die Bereitstellung von Rechenzeit bedanke ich mich bei dem ZiH Dresden.

Weiter danke ich meinen besten Freunden Dr. Kai Trepe, M. Sc. Sebastian Borrmann und M. Sc. Martin Polednia für die Existenz unser Freundschaft, die in dunklen Zeiten stets das Licht am Horizont, insgesamt eine Bereicherung und ein unverzichtbarer Teil meines Lebens sind. Aber der größte Dank gilt meinen geliebten Eltern, meiner Mutter Monika Winnemund (geborene Schwalbe) und meinem Vater Frank Winnemund, sowie meinen geliebten Großeltern Annelis Schwalbe, Gerhard Schwalbe, Fred Winnemund und Anita Winnemund, sowie meiner Tante Petra Neubert und Onkel Andreas Neubert. Ohne eure kontinuierliche Unterstützung, Verständnis und den Rückhalt den ihr mir immer gegeben habt wäre diese Arbeit nie möglich gewesen.

ACKNOWLEDGEMENT

At the first place, I want to express my gratitude to my doctoral father Prof. Dr. Jens Kortus, who enabled and guided my thesis and always provided help and advice. His general as well as special knowledge exemplary about symmetries of molecules and solids is marvelous. I thank all funding agencies which enabled this thesis. To mention here the Materials with New Design for Improved Lithium Ion Batteries (WeNDeLIB, SPP 1473 DFG) project, TU Bergakademie Freiberg and the PyFLOSIC DFG project (KO 1924/9-1). Special thanks goes to the German Research Foundation (DFG) allowing me to start my PyFLOSIC project earlier, thus this thesis could be finished to the point it is now.

Further thanks goes to all of my co-authors and colleagues. But to one of my best friends, science companion and the best co-author Dr. Kai Trepte I need to express special gratitude at this place. Only this cooperation allows to tackle and solve little to large problems. I thank him for proof-reading of this thesis. Especially, I want to thank Prof. Dr. John P. Perdew, it was a special honor for me to meet him in person and being able to work with him. In my eyes, he is the embodiment of knowledge and accurate physics. Another special thanks goes to Dr. Susi Lehtola, the development of the PyFLOSIC code would not have been possible without his didactic, inspiring as well as excellent preliminary works in the field of self-interaction correction. It is an essential, personal and scientific highlight to know him in person and working with him.

Obviously, I thank my hosting Institute of Theoretical Physics (TU Berkakademie Freiberg). Only in a vital environment useful achievements can be made. I thank you for providing such an environment to me. Particularly, I thank Dr. Simon Liebing joining me for various conferences and putting up with frustrated monologues during common lunch times. I thank our local administrator Dr. René Wirnata for setting up and maintain our ShareLatex server. Various articles, poster, talks and also this thesis began on this server. A big thanks goes also to the best students I advised during my PhD time, M. Sc. Lenz Fiedler, M. Sc. Jakob Kraus and B. Sc. Wanja Timm Schulze. Without the cooperation with M. Sc. Lenz Fielder the PyFLOSIC code would not exist today. The general interest in developing and the collaboration with B. Sc. Wanja Timm Schulze showed me that different perspectives can open up new scientific paths even through stony terrain. And without the elaborations of M. Sc. Jakob Kraus within his works, our understanding of the meaning of Fermi-orbital descriptors (FODs) would be way less than it is today. In addition, I want to thank my primary school teachers, who early inspired my interest on natural sciences and predicted that such a thesis one day would exist. A general thanks goes to all developers of open source software and the authors of open articles. Without you it wouldn't be possible to gain the knowledge to understand things, like I do today. For granting computational time I thank the ZiH Dresden.

Further, I want to thank my best friends Dr. Kai Trepte, M. Sc. Sebastian Borrmann and M. Sc. Martin Polednia for the existence of our friendship, which enlightened dark times, and overall being an enrichment as well as an absolutely essential part of my life.

But the biggest thanks goes to my beloved parents, my mother Monika Winnemund (born Schwalbe) and my father Frank Winnemund, as well as my beloved grand parents Annelis Schwalbe, Gerhard Schwalbe, Fred Winnemund and Anita Winnemund, and my beloved aunt Petra Neubert and my uncle Andreas Neubert. Without your continuously support, sympathy and backing, you provided me, this work would never be possible.

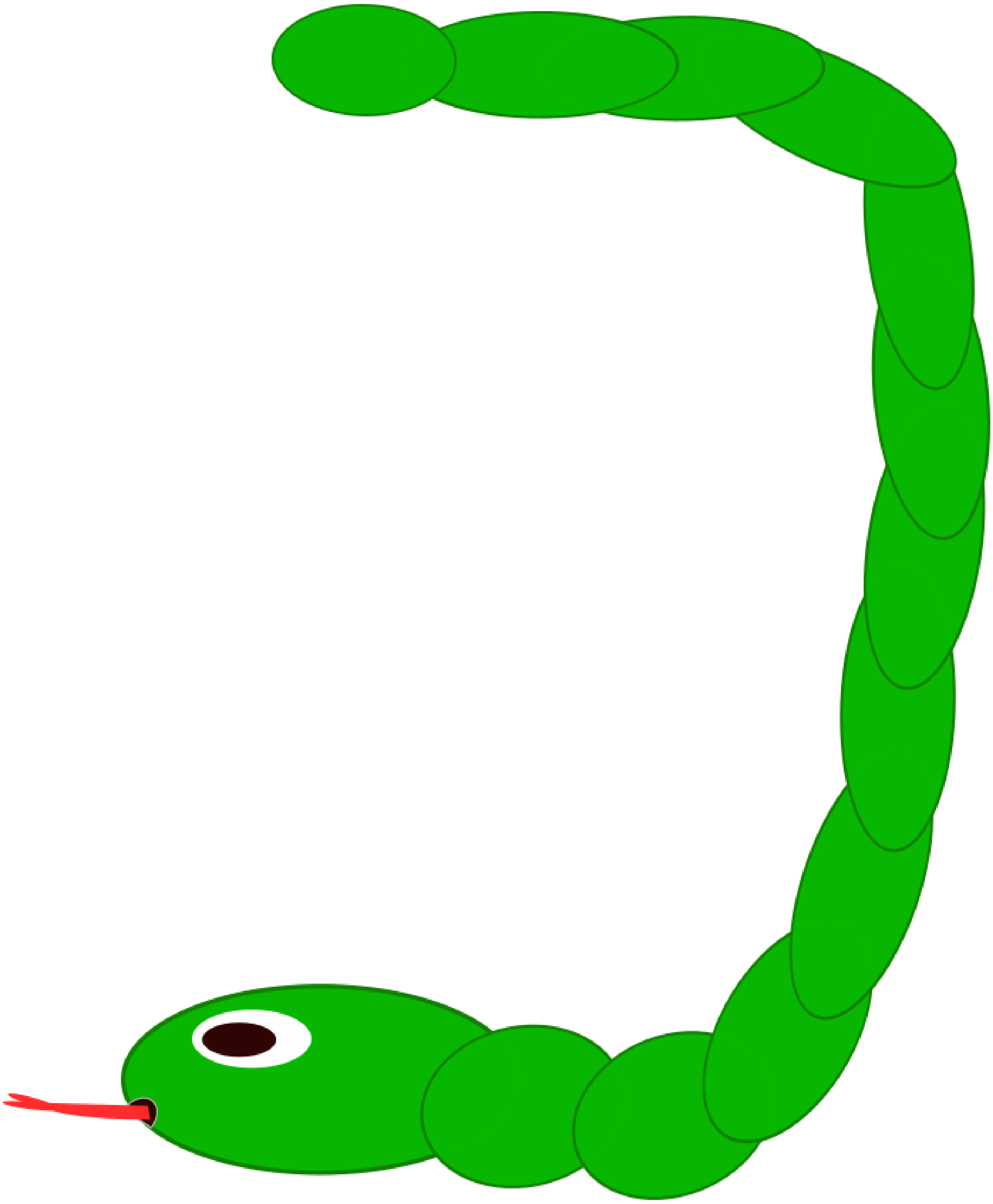

COLOPHON

The author modified the typographical look-and-feel `classicthesis` developed by André Miede and Ivo Pletikosić for typsetting of this thesis. This style itself was inspired by Robert Bringhurst's seminal book on typography *"The Elements of Typographic Style"*. `classicthesis` is available for both LaTeX and LyX:

https://bitbucket.org/amiede/classicthesis/

Final Version as of October 1, 2021 (`classicthesis` version 0.1).